Investigations of incompressible variable-density turbulence in an external acceleration field

Thesis by
Ilana Batya Gat

In Partial Fulfillment of the Requirements for the
degree of
Doctor of Philosophy

CALIFORNIA INSTITUTE OF TECHNOLOGY
Pasadena, California

2018
Defended November 14, 2017

Ilana Batya Gat
ORCID: 0000-0003-0223-0507

ACKNOWLEDGEMENTS

Firstly, I would like to express my deepest gratitude towards my advisor, Professor Paul Dimotakis. Without his unwavering support, help, mentorship, and guidance, this work could not have been done. This work was made possible through his extensive efforts to give me a unique education that I could not have received elsewhere.

I would also like to thank Georgios Matheou for his guidance and help throughout my Caltech tenure, and Daniel Chung for his always helpful input. Additionally, I would like to express my appreciation to Professors Dale Pullin and Dan Meiron for their contributions during our joint group meetings that have ensured my research could withstand tough criticism.

I would also like to thank Professor Beverley McKeon for her extensive help on my side project of co-chairing the Caltech Space Challenge.

The computational aspects of this work were done with help from the Caltech High Performance Computing center, specifically Mark Bartelt, who helped us with the Caltech Zwicky computer cluster, supported by NSF MRI-R2 Award PHY-0060291 and by the Sherman Fairchild Foundation. Computing for this project was also done by a collaboration with Christian Ott with the Blue Waters Sustained-Petascale Computing Project, supported by NSF Awards OCI-0725070 and ACI-1238993, and the state of Illinois. Blue Waters is a joint effort of the University of Illinois at Urbana-Champaign and its National Center for Supercomputing Applications. Simulations performed on Blue Waters were under NSF PRAC award number ACI-1440083. Computations were also done on the Cray Trinity system of the Alliance for Computing at Extreme Scale (ACES), a partnership between Los Alamos National Laboratory and Sandia National Laboratories for the U.S. Dept. of Energy's NNSA.

Additional support for this work was from the DOE Grant DE-NA0002382, the NSF Graduate Research Fellowship Program under Grant DGE-1144469, the Caltech academic program, the Caltech Northrop Chair in Aeronautics, and the AFOSR Grant FA9550-12-1-0461.

I am extremely thankful for the work by Daniel Lang, whose computer expertise is unfathomable. All data storage, visualization, and post-processing were facilitated by a computer cluster of storage, called Lykos, and compute nodes, termed Skepsis,

integrated by Daniel Lang, and developed through support by NSF MRI Grant EIA-0079871, AFOSR DURIP Grant FA9550-10-1-0553, and support by the AFOSR and DOE grants mentioned above.

I would also like to thank Carlos Pantano for noting an additional term in the self-similar mass conservation equation contributed by the diffusion-induced velocity (equation 4.3), and for calculating the stability analysis of this flow.

The general GALCIT community has been a tremendous support system. From my fellow graduate students to all the administrative staff, I am extremely thankful for the jovial reinforcements. Specifically, I would like to thank Dimity Nelson, for all her help and advisement throughout my graduate school life.

I would like to also thank my family. My parents, Linda and Nahum Gat, have been the best support system, and have helped me get where I am today. They have both, at many times, dropped everything to help me after a difficult graduate school day, week, or month. I will forever be indebted to them for their commitment to my success. My siblings, Aviva, Danny, and Joel, have been the comedic relief (and more) to my life. I am grateful for their love and encouragement.

Last, but not least, I would like to dedicate my thesis to my husband, Chris Holmes-Parker. Without his continual support, encouragement, devotion, and love, I could not imagine this thesis ever being written. Thank you, Chris.

ABSTRACT

Of interest to turbulence modeling is the behavior of variable-density flow at high Reynolds numbers — a flow difficult to model. This thesis provides insight into variable-density flow behavior by examining the dynamics and mixing of variable-density turbulence subject to an externally imposed acceleration field. The flow is studied in the zero-Mach-number limit with a series of direct numerical simulations. The flow configuration consists of alternating slabs of high- and low-density fluid in a triply periodic domain. Density ratios in the range of $1.005 \leq R \equiv \rho_1/\rho_2 \leq 10$ are investigated. The flow produces temporally evolving shear layers.

A perpendicular mean density–pressure gradient is maintained as the flow evolves, with multi-scale baroclinic torques generated in the turbulent flow that ensues. For all density ratios studied, the simulations attain Reynolds numbers at the beginning of the fully developed turbulence regime.

An empirical relation for the convection velocity predicts the observed entrainment-ratio and dominant mixed-fluid composition statistics. Two mixing-layer temporal evolution regimes are identified: an initial diffusion-dominated regime with a growth rate $\sim t^{1/2}$ followed by a turbulence-dominated regime with a growth rate $\sim t^3$. In the turbulent regime, composition probability density functions within the shear layers exhibit a slightly tilted ('non-marching') hump, corresponding to the most probable mole fraction. The shear layers preferentially entrain low-density fluid by volume at all density ratios, which is reflected in the mixed-fluid composition.

The mixed-fluid orientations of vorticity, baroclinic torques, density gradients, and pressure gradients are presented. Baroclinic torques, the cross product of the density and pressure gradients, tend to be aligned with positive or negative vorticity direction, with vorticity preferentially aligning with the intermediate eigenvector of the local strain-rate tensor, with some variance.

Abstract adapted from Gat et al., 2017

PUBLISHED CONTENT AND CONTRIBUTIONS

Gat, I., G. Matheou, D. Chung, and P. E. Dimotakis (2017). "Incompressible variable-density turbulence in an external acceleration field". In: *"J. Fluid Mech."* 827, pp. 506–535. DOI: 10.1017/jfm.2017.490.
I.G. updated code, ran all simulations, and analyzed the data to draw various conclusions with co-authors.

– (2016). "Acceleration-driven variable-density turbulent flow". In: *Proceedings of the VIIIth International Symposium on Stratified Flows (ISSF)*. San Diego, CA. Retrieved from http://escholarship.org/uc/item/61d722q6.
I.G. updated code, ran all simulations, and analyzed the data to draw various conclusions with co-authors.

TABLE OF CONTENTS

LIST OF ILLUSTRATIONS

Number *Page*

Chapter 1

BACKGROUND

Turbulent flow occurs all around us, from our atmosphere, to our oceans, to even our stars. Leonardo da Vinci was the first known to attempt turbulence visualization, and sketched a free water jet (Lumley, 1992). He mentioned the eddy motions, alluding to the large to small scale energy transfer, known today as the turbulent energy cascade (translated by Ugo Piomelli, University of Maryland, in Gad-el-Hak, 2000). Over the last 500 years since da Vinci's sketch, much progress has been made to understand those turbulent eddies, however there are still significant knowledge gaps. A couple of difficulties hinder turbulence knowledge advancement: turbulence is a non-linear phenomenon that cannot be described by simple analytical solutions, and the range of scales to understand is large and cannot be readily computed. Experimental data help, however numerical simulations can provide information difficult to experimentally obtain.

The smallest scales in turbulent flows are termed the Kolmogorov length, η, and time, τ_k, scales (Kolmogorov, 1941)

$$\eta \equiv (\nu^3/\epsilon)^{1/4}, \quad \tau_k \equiv (\nu/\epsilon)^{1/2}, \tag{1.1}$$

where ν is the kinematic viscosity and ϵ the specific energy dissipation rate, which can be related to the large-scale velocity, U, and largest-eddy size, δ, by $\epsilon \sim U^3/\delta$ (Taylor, 1935). Large-scale eddies, of order δ, impart energy to the small scales, with $\delta \gg \eta$. Reynolds (1883) realized the birth of these eddies depends on the non-dimensional number $c\rho U/\mu$, where c is a flow length scale, ρ is the density, and μ is the dynamic viscosity, with $\nu = \mu/\rho$. This non-dimensional number is now known as the Reynolds number

$$Re = \frac{U\,\delta}{\nu}, \tag{1.2}$$

which can be used to denote scale separation (Tennekes and Lumley, 1972)

$$\frac{\delta}{\eta} = \frac{Re\,\nu}{U}\left(\frac{\epsilon}{\nu^3}\right)^{1/4} \sim Re^{3/4}, \tag{1.3}$$

i.e., larger *Re* implies larger scale separation, indicative of turbulence. Dimotakis (2000) discovered that the scale separation required for turbulence generation occurs

around $Re \sim 10^4$, termed the mixing transition. At that Reynolds number, $\delta/\eta \sim 10^3$, *i.e.*, the smallest scale will be 0.001δ, and a computer simulation must resolve that entirely. A minimum of (approximately) 1000 grid points in each direction, or 10^9 grid points total are then required to resolve one large eddy in a three-dimensional simulation, needed for turbulence computations. This is the *minimum* order-of-magnitude requirement to attain the turbulence transition. If flow past the transition is to be studied, much finer grid resolutions must be used. Additionally, as Re increases, so do the time steps required. The eddy turn-over time $t_\delta \sim \delta/U$, and the numerical time steps required to resolve one eddy turnover,

$$\frac{t_\delta}{t_k} = \frac{\delta}{U}\left(\frac{\epsilon}{\nu}\right)^{1/2} \sim Re^{1/2} \tag{1.4}$$

or, 100 time steps per eddy turnover for flow at the turbulence transition. These computational requirements prove difficult to meet using direct numerical simulation (DNS) — a numerical simulation in which all contributing scales are resolved.

Large flow scales are problem specific, being affected by flow topology. It has been hypothesized, however, that small scales are possibly less sensitive to flow topology and more amenable to being modeled (Rogallo and Moin, 1984). In light of this hypothesis, large-eddy simulation (LES) was attempted to circumvent the DNS resolution requirements (reviewed in Rogallo and Moin, 1984; Lesieur and Metais, 1996; Ghosal, 1999; Piomelli, 1999; Meneveau and Katz, 2000; Lesieur, 2012, for example). LES resolves the larger scales with models used for the small, unresolved scales. Two noteworthy subgrid-scale (SGS) models are the Smagorinsky model (Smagorinsky, 1963) and the Stretched-Vortex Model (SVM, Pullin and Saffman, 1994; Misra and Pullin, 1997; Voelkl, Pullin, and Chan, 2000). Germano et al. (1991) added a dynamic component to the Smagorinsky model, which was implemented by Moin, Squires, et al. (1991) who also suggested a compressibility-effect augmentation to the Smagorinsky model using the dilatation term expression from Yoshizawa (1986). Moin, Squires, et al. (1991) also introduced a SGS passive scalar flux model. Buoyancy effects in the Smagorinsky model were proposed by Lilly (1962), prior to the publishing of the Smagorinsky model in 1963. However, Lilly (1962) mentions working closely with Smagorinsky, and Smagorinsky (1963) notes that model being implemented by Lilly (1962).

The SVM (Pullin and Saffman, 1994; Misra and Pullin, 1997; Voelkl, Pullin, and Chan, 2000) was also augmented for passive scalar transport (Pullin, 2000; Pullin and Lundgren, 2001) and some compressibility effects (Kosović, Pullin, and Samtaney, 2002). Buoyancy effects were later added (Chung and Matheou, 2014).

Both SGS compressibility model extensions use a density-weighted filter (Favre filter) to obtain the LES equations (Speziale et al., 1988), with the incompressible SGS model (with some augmentations) multiplied by the resolved density field – an outcome of the filtering. These modifications to incompressible SGS models for compressible flows can be problematic when compressibility effects (or variable-density effects) become significant (*e.g.*, Garnier, Adams, and Sagaut, 2009). Small-scale turbulent density variations occur in atmospheric flows, astrophysical flows, and more, and their effects in SGS modeling have proven important, at least for the former (Chung and Matheou, 2014; Matheou and Chung, 2014). SGS models must account for these variable-density effects for true LES predictions.

This work aims to quantify variable-density turbulence effects by studying mixing of two different density fluids with density ratios of $1.005 \leq R \equiv \rho_1/\rho_2 \leq 10$ in the zero-Mach-number limit. An externally imposed uniform-acceleration field acts on the flow, accelerating the two different density fluids, inducing mixing between them. This initialization ensures all mixing and turbulence is a product of variable density, since the flow would remain stationary if $R = 1$ (in the gravitationally accelerating frame).

By partitioning the variable-density effects in this way, this flow is ideal to gain insight into the small-to-large scale variable-density turbulence behavior, and is thus studied using DNS, *i.e.*, the small scales are resolved. This study can be used to inspire variable-density augmentations to SGS models, possibly extending to compressible flow SGS models, allowing for a broader range of turbulent flows to be successfully computed. With the ability to computationally model more diverse flows, a broader range of turbulence questions can be pursued.

Chapter 2

INTRODUCTION

Variable-density turbulent flow responding to an externally imposed acceleration field, such as gravity, is encountered in many contexts, such as inertial confinement fusion, geophysics, astrophysics, compressible turbulence, and combustion, with many similarities to classical shear layers. In the present study, of interest are the flow dynamics resulting from the body force $\rho \boldsymbol{g}$, where ρ is the density of the fluid and $\boldsymbol{g}$ the imposed acceleration field. The action of the body force generates complex multi-scale dynamics. For instance, in a uniform gravitational field, density stratification results in waves, instabilities, and modification of turbulence by stable density stratification or buoyant convection (*e.g.*, Turner, 1979).

In many applications, flows can be treated as incompressible with only small density variations, $\rho'/\rho \ll 1$, and the Boussinesq approximation can adequately describe the flow physics (Gerz, Schumann, and Elghobashi, 1989; Métais and Herring, 1989; Batchelor, Canuto, and Chasnov, 1992; Holt, Koseff, and Ferziger, 1992; Gerz and Yamazaki, 1993; Jacobitz, Sakar, and Van Atta, 1997; Staquet and Godeferd, 1998; Shih et al., 2000; Riley and deBruynKops, 2003; Diamessis and Nomura, 2004; Chung and Matheou, 2012). Boussinesq flows capture the effects of stratification in decaying turbulence (Métais and Herring, 1989; Staquet and Godeferd, 1998; Riley and deBruynKops, 2003), with some studies of unstable stratification, *e.g.*, buoyancy-driven flows of a fluctuating density field (Batchelor, Canuto, and Chasnov, 1992) or stable stratification if a different mechanism, *e.g.*, shear, drives the flow (Gerz, Schumann, and Elghobashi, 1989; Holt, Koseff, and Ferziger, 1992; Jacobitz, Sakar, and Van Atta, 1997; Shih et al., 2000; Diamessis and Nomura, 2004; Chung and Matheou, 2012). Such flows tend to be nearly barotropic, with mean pressure gradients in the direction of, or opposite to, mean density gradients.

Misalignments of pressure and density gradients generate baroclinic torques that can significantly influence the flow dynamics and may be important to include in large-eddy simulation (LES) modeling of high-Reynolds-number turbulent flows. The Boussinesq linearization retains density variations only in accounting for body force in the momentum equation (*e.g.*, Batchelor, Canuto, and Chasnov, 1992),

Chapter adapted from Gat et al., 2017

while ignoring non-hydrostatic baroclinic torques in the vorticity equation.

The present study investigates turbulence in a variable-density flow responding to baroclinic torques. A flow configuration is considered in which two different gas-phase fluids and an externally imposed vertical acceleration field result in initially perpendicular pressure and density gradients. A mean perpendicular density–pressure gradient is maintained as the flow evolves while multi-scale baroclinic torques are generated in the turbulent shear layers that ensue.

The present flow is inspired by flow visualization of a laboratory demonstration by Robert Breidenthal in the late 70s at Caltech (unpublished) witnessed by Professor Paul Dimotakis. The flow was a baroclinically generated shear layer formed between vertically oriented streams of water solutions, whose densities were close, *i.e.*, $\Delta\rho/\rho \ll 1$, with $\Delta\rho = \rho_1 - \rho_2$. Subsequent analysis of this flow by Professor Paul Dimotakis indicated a velocity difference across such a shear layer (circulation per unit shear-layer length) that was linearly increasing in time. This is as opposed to a Kelvin–Helmholtz layer (Chandrasekhar, 1961), for example, whose velocity difference is constant. Prathama and Pantano (2017), who conducted an inviscid linear stability analysis for the studied flow, likened it to an accelerating Kelvin-Helmholtz configuration.

The present study extends the aforementioned baroclinically generated shear layer of water solutions to higher density ratios, renders it in a periodic domain, and employs a direct numerical simulation (DNS) approach. Specifically, simulations with varying free-stream density ratios in the range $1.005 \leq R \equiv \rho_1/\rho_2 \leq 10$ are performed. By way of example, flow with a density ratio of $R = 10$ corresponds to turbulent mixing of argon (Ar) and helium (He). The low-Mach-number approximation of the full equations of motion is used to study this flow whose higher density ratios place it outside the validity of the Boussinesq approximation. For low density ratios, *i.e.*, $R = 1 + \varepsilon$, the flow approaches the Boussinesq approximation for small ε.

The inviscid linear stability analysis of the present study, conducted by Prathama and Pantano (2017), showed that the inviscid flow is unconditionally unstable with small perturbations growing exponentially with quadratic time. This is contrasted with the inviscid linear stability of Kelvin–Helmholtz or Rayleigh–Taylor instabilities, for example, in which small perturbations grow exponentially with linear time (*e.g.*, Drazin and Reid, 2004). Viscous effects in the linear stability of Kelvin–Helmholtz or Rayleigh–Taylor instabilities are shown to hinder growth of small wavelength disturbance (*e.g.*, Bellman and Pennington, 1954). The viscous stability

analysis of the studied flow is still being investigated (Prathama and Pantano, private communications).

The present flow exhibits common attributes with other fundamental variable-density (non-Boussinesq) accelerating flows, including three-dimensional Rayleigh–Taylor instability simulations (*e.g.*, Rayleigh, 1882; Taylor, 1950; Anuchina et al., 1978; Read, 1984; Youngs, 1984, 1989; Cook and Dimotakis, 2001, and others), and also variable-density buoyancy-generated turbulence (Sandoval, 1995, and studies mentioned therein) and later studies (*e.g.*, Livescu and Ristorcelli, 2007, 2008; Livescu, Ristorcelli, et al., 2009; Chung and Pullin, 2010). These studies furthered the work of Sandoval (1995). In the present configuration, the turbulent mixing region grows in the horizontal direction, *i.e.*, perpendicular to the vertical acceleration, whereas in Rayleigh–Taylor-type flows, the mixed-fluid region grows in the vertical direction, *i.e.*, parallel to the acceleration direction. In addition, the present simulations correspond to temporally evolving mixed-fluid regions between two pure-fluid accelerating (free) streams, in contrast to spatially homogeneous buoyancy-generated turbulent flows (*e.g.*, Livescu and Ristorcelli, 2007, 2008; Chung and Pullin, 2010).

This flow exhibits similarities to buoyancy-generated turbulent flows as well as similarities to classical spatially developing shear layers (*e.g.*, Brown and Roshko, 1974, 2012; Bradshaw, 1977; Ho and Huerre, 1984; Dimotakis, 2005, and references therein). In the present flow, however, the vertically accelerating free streams develop temporally growing shear layers. In many experiments on buoyancy-driven free-stream acceleration (*e.g.*, Thorpe, 1968, 1978; Pawlak and Armi, 1998), gravity is inclined with respect to the free-stream flow direction, whereas acceleration is parallel to the free-stream flow direction in the present study.

Similar to Livescu and Ristorcelli (2007) and Chung and Pullin (2010), the present flow is triply periodic. Lack of solid boundaries introduces a degree of freedom and non-uniqueness (Livescu and Ristorcelli, 2007), requiring specification of the mean pressure gradient in place of a far-field boundary condition. The mean pressure gradient sets the flow reference frame (see section 3.2). Expanding on work by Chung and Pullin (2010) who used a zero mid-plane-averaged velocity frame, a zero-mean-momentum reference frame is chosen that also facilitates force accounting.

Motivated by turbulence modeling considerations, *e.g.*, the stretched-vortex subgrid-scale model (Pullin and Saffman, 1994; Misra and Pullin, 1997; Voelkl, Pullin, and Chan, 2000), vorticity alignment statistics are investigated. In uniform-density

flows, statistics of vorticity orientation indicate a preferential alignment with the eigenvector corresponding to the intermediate eigenvalue of the local strain rate tensor (Ashurst, Kerstein, et al., 1987; Ohkitani, 2002; Lüthi, Tsinober, and Kinzelbach, 2005; Guala et al., 2005; Hamlington, Schumacher, and Dahm, 2008; Meneveau, 2011; Verma and Blanquart, 2014). Purely kinematic arguments, based on the Biot–Savart law (as noted by Jiménez, 1992) can explain the vorticity–strain preferential alignment for variable-density turbulence, as for uniform-density turbulence, with some assumptions made.

A main difference between vorticity in uniform- versus variable-density flow are baroclinic torques. As such, baroclinic torque, $\nabla\rho \times \nabla p$, alignment with the local strain rate tensor is investigated, along with the pressure- and density-gradient alignments. As mixing occurs, initially perpendicular pressure- and density-gradients can rotate, affecting baroclinic torques. Passive scalar gradients in turbulent flows have been shown to preferentially align perpendicularly to the local strain rate tensor intermediate eigenvector (Ashurst, Kerstein, et al., 1987; R. S. Miller et al., 1995; Verma and Blanquart, 2014). However, here, density gradients are studied instead of passive scalar gradients. Pressure gradients in homogeneous isotropic turbulence have been shown to align at 45° to the strain rate tensor extensional and contractional eigenvectors, with some variation (Ashurst, Kerstein, et al., 1987; Ashurst, Chen, and Rogers, 1987; Kalelkar, 2006). These relative alignments are investigated and extended to the anisotropic variable-density flow studied.

Governing equations, flow configuration, numerical solution method, and relevant flow parameters are discussed in chapter 3. Analyses of the flow evolution and turbulence, including mixing, energy spectra, and vorticity spectra, are discussed in chapter 4. Orientations of vorticity and baroclinic torques, with reference to density- and pressure-gradient alignments, are presented in chapter 5. Chapter 6 concludes and notes that some attributes of variable-density flows can be mapped to those for uniform-density flows, such as spectral scaling for all density ratios, R, extending to the limit of $R = 1 + \varepsilon$, as $\varepsilon \to 0$, however, other attributes, such mean-flow statistics, cannot. Applications and possible future investigations of this variable-density turbulence study in terms of subgrid-scale modeling are discussed in chapter 7. Further details regarding numerical methods, quality of simulations, and sensitivity to initial conditions are documented in appendices A and B. Appendix C discusses the three-dimensional probability density function calculation, used in chapter 5 for orientation plots.

Chapter 3

PROBLEM FORMULATION

3.1 Governing equations

Absent species sources and sinks, the mass, momentum, and species mass-fraction conservation equations for flow subject to an externally imposed acceleration field, such as gravity, are (Sandoval, 1995; Cook and Dimotakis, 2001; Dimotakis, 2005; Livescu and Ristorcelli, 2007; Chung and Pullin, 2010)

$$\frac{\partial \rho}{\partial t} + \nabla \cdot (\rho \boldsymbol{u}) = 0, \tag{3.1a}$$

$$\frac{\partial \rho \boldsymbol{u}}{\partial t} + \nabla \cdot (\rho \boldsymbol{u}\boldsymbol{u}) = -(\boldsymbol{\Gamma} + \nabla p) - \widehat{\boldsymbol{z}}\, \rho g + \nabla \cdot \boldsymbol{\tau}, \tag{3.1b}$$

$$\frac{\partial \rho Y_\alpha}{\partial t} + \nabla \cdot [\rho Y_\alpha (\boldsymbol{u} + \boldsymbol{v}_\alpha)] = 0. \tag{3.1c}$$

In these equations, ρ is the density of the mixture, $\boldsymbol{u}$ is the velocity vector, p is the pressure, $\boldsymbol{\Gamma}(t)$ is the spatially uniform component of the pressure gradient, g is the magnitude of the acceleration in the $-\widehat{\boldsymbol{z}}$ direction, Y_α is the α-species mass fraction, and $\boldsymbol{v}_\alpha$ is the α-species diffusion velocity (*e.g.*, Dimotakis, 2005). A Newtonian viscous stress tensor and monatomic gases, *i.e.*, zero bulk viscosity (Hirschfelder, Curtiss, and Bird, 1964) are assumed,

$$\boldsymbol{\tau} = \mu \left[\nabla \boldsymbol{u} + (\nabla \boldsymbol{u})^{\mathrm{T}} - \frac{2}{3} (\nabla \cdot \boldsymbol{u}) \mathbf{I} \right], \tag{3.1d}$$

where $\mathbf{I}$ is the identity matrix.

Density, ρ, can be uniquely described in terms of the mass fraction for a binary fluid mixture, $Y(\boldsymbol{x}, t) \equiv Y_1(\boldsymbol{x}, t) = 1 - Y_2(\boldsymbol{x}, t)$, with densities ρ_1 and ρ_2, and $\rho_1 > \rho_2$ (Sandoval, 1995), *i.e.*,

$$\frac{1}{\rho(\boldsymbol{x}, t)} = \frac{Y(\boldsymbol{x}, t)}{\rho_1} + \frac{1 - Y(\boldsymbol{x}, t)}{\rho_2} = \frac{1}{\rho_2} - Y(\boldsymbol{x}, t) \left(\frac{1}{\rho_2} - \frac{1}{\rho_1} \right). \tag{3.2}$$

In the zero-Mach-number limit (incompressible flow) studied here, temperature is uniform (and infinite), decoupling the energy equation.

Chapter adapted from Gat et al., 2016, 2017

Species diffusion velocities, $\boldsymbol{v}_\alpha$, derive from Boltzmann statistics (Hirschfelder, Curtiss, and Bird, 1964; Dimotakis, 2005)

$$\rho Y_\alpha \boldsymbol{v}^\alpha \;=\; \frac{\rho_\alpha}{\rho}\sum_\beta \rho_\beta \mathcal{D}_{\alpha\beta}\boldsymbol{d}^\beta - \frac{\mathcal{D}_\alpha^{(T)}}{T}\nabla T \tag{3.3a}$$

with

$$\boldsymbol{d}^\alpha \equiv \nabla X_\alpha + \frac{1}{p}\left[(X_\alpha - Y_\alpha)\nabla p + \rho Y_\alpha \sum_\beta (Y_\beta \boldsymbol{f}^\beta - \boldsymbol{f}^\alpha)\right], \tag{3.3b}$$

where $\boldsymbol{f}^\alpha$ is the α-species body-force field and X_α is the α-species mole fraction. For a binary mixture,

$$X \;\equiv\; X_1 \;=\; \frac{\rho(\boldsymbol{x},t) - \rho_2}{\rho_1 - \rho_2}\,. \tag{3.3c}$$

In zero-Mach-number flow without velocity magnitude constraints, the sound speed is infinite, yielding an infinite-temperature and infinite-pressure ideal gas flow. This results in the second term in equation 3.3a and the bracketed terms in equation 3.3b tending to zero, with Fickian transport dominating the species diffusion velocity, simplifying equation 3.3a, *i.e.*,

$$\rho\, Y\boldsymbol{v} \;=\; -\rho\,\mathcal{D}\,\nabla Y\,, \tag{3.3d}$$

where $\boldsymbol{v} \equiv \boldsymbol{v}_1$ and $Y\boldsymbol{v} = Y_1\boldsymbol{v}_1 = -Y_2\boldsymbol{v}_2$ for a binary mixture. Combining the conservation equations for mass and species mass fraction yields the density evolution equation,

$$\frac{\mathrm{D}\rho}{\mathrm{D}t} \;=\; \frac{\partial\rho}{\partial t} + \boldsymbol{u}\cdot\nabla\rho \;=\; -\,\rho\,\nabla\cdot\boldsymbol{u} \;=\; \rho\,\nabla\cdot\left(\frac{\mathcal{D}}{\rho}\nabla\rho\right), \tag{3.4}$$

i.e., variable-density flow is not divergence free in the presence of diffusion, even in the zero-Mach-number limit (*e.g.*, Sandoval, 1995; Cook and Dimotakis, 2001; Livescu, 2013).

The simulations assume gas-phase molecular diffusion, *i.e.*, a unity Schmidt number, $Sc \approx 1$, where $Sc \equiv (\mu/\rho)/\mathcal{D}$ is the ratio of the viscous to the species diffusivity. Unity Sc corresponds to molecular diffusivity equaling kinematic viscosity, an approximation for gases. In considering a mixture of two gases treated here as ideal, each would be characterized by its own density, *e.g.*, ρ_1 and ρ_2, with the mixed-fluid density, $\rho(X)$, a function of the mixture mole fraction, $X = [\rho(X) - \rho_2]/[\rho_1 - \rho_2]$. Similarly, while dynamic viscosity would be a function of temperature in each of the two pure fluids, there would be a temperature-dependent dynamic viscosity that would be a function of mixture composition and temperature, *i.e.*, $\mu(X,T)$. This

study assumes an infinite (and uniform) temperature flow, *i.e.*, $\mu(X,T) \rightarrow \mu(X)$. $\mu(X)$ can be determined using known viscosity equations for gas mixtures (*e.g.*, Wilke, 1950), however this can complicate studied equations. The model for the simulations performed adopts the simplifying assumption that $\mu(X) = \mu$ is uniform and constant, ignoring all effects from variable viscosity. A uniform unity Schmidt number is also assumed as an approximation for gas-phase diffusion, yielding a variable diffusion coefficient, *i.e.*, $\mathcal{D}(\boldsymbol{x}, t) = \mu/\rho(\boldsymbol{x}, t)$.

3.2 Flow reference frame

The simulated flow is in a triply periodic cube of volume L^3 with an imposed vertical acceleration field. In this setup, the pressure gradient can be solved up to a constant (in space), $\boldsymbol{\Gamma}(t)$ in equation 3.1b (Livescu and Ristorcelli, 2007). The simulations exploit this degree of freedom to select the flow reference frame. Some authors chose $\boldsymbol{\Gamma}(t)$ to render the flow maximally unstable (Livescu and Ristorcelli, 2007), or to ensure a constant mean velocity (Chung and Pullin, 2010). In the simulations presented here, a different approach is chosen.

To help track forces acting on the flow, $\boldsymbol{\Gamma}(t)$ is selected such that $\mathrm{d}\langle\rho\boldsymbol{u}\rangle/\mathrm{d}t = 0$ in the chosen frame, *i.e.*, a constant volume-averaged momentum. Here, $\langle\rangle$ denotes the domain volume average,

$$\langle * \rangle \;=\; \frac{1}{V}\int_V * \,\mathrm{d}V\,. \tag{3.5}$$

The simulated flow is initially quiescent, with zero initial volume-averaged momentum, *i.e.*, $\langle\rho\boldsymbol{u}\rangle_{t=0} = 0$, yielding zero mean momentum for all time. Ensuring $\mathrm{d}\langle\rho\boldsymbol{u}\rangle/\mathrm{d}t = 0$ then requires

$$\boldsymbol{\Gamma} \;\cong\; -\widehat{z}\,\rho_0 g\,, \tag{3.6}$$

where

$$\rho_0 \;=\; \langle\rho\rangle \;=\; \beta\rho_1 \;+\; (1-\beta)\rho_2\,, \tag{3.7}$$

with β denoting the high-density fluid volume fraction in the domain. For the majority of the simulations shown, $\rho_0 = \frac{1}{2}(\rho_1 + \rho_2)$, *i.e.*, $\beta = 1/2$, with equal volumes of high- and low-density fluid in the domain. See further discussion on initial conditions below in section 3.3 and appendix B.

In the simulated frame of reference, equation 3.6, $\boldsymbol{\Gamma}$ is approximately constant, with the mean density, ρ_0, also remaining constant as the flow evolves. However, local fluctuations can cause small unsteady displacements of the center of mass, requiring

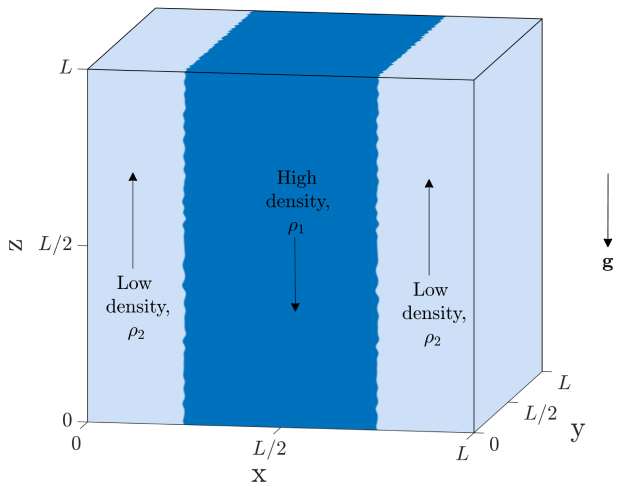

Figure 3.1: Initial density field. High-density fluid (dark blue) moves in the same direction as the acceleration field between regions of low-density fluid (light blue) moving in the opposite direction to the acceleration field. The interface between high- and low-density fluid is initially perturbed in the (y, z)–plane.

the imposition of small variations in $\mathbf{\Gamma}$ to maintain a constant mean momentum. $\mathbf{\Gamma}$ is slightly adjusted at each time step to maintain a zero mean momentum.

3.3 Flow initialization

The flow is initialized with a region of high-density fluid between regions of low-density fluid (figure 3.1). With this initialization, the flow is statistically anisotropic with respect to all three axes but statistically homogeneous in the (y, z)–plane. In the chosen frame, low-density fluid moves opposite to the external uniform acceleration field and high-density fluid moves in the direction of the external uniform acceleration field. In an inertial (laboratory) frame, both fluids would move in the external uniform acceleration field direction (*i.e.*, downwards in figure 3.1).

Transitions at fluid interfaces are initially represented by error functions,

$$\rho(\boldsymbol{x}; t{=}0) \;=\; \frac{1}{2}\left\{\operatorname{erf}\left[\frac{x_\mathrm{i}(\boldsymbol{x}) - x_0}{2\Delta x}\right] - \operatorname{erf}\left[\frac{x_\mathrm{i}(\boldsymbol{x}) - (L - x_0)}{2\Delta x}\right]\right\}(\rho_1 - \rho_2) + \rho_2\,, \quad (3.8a)$$

where $\boldsymbol{x} = (x, y, z)$,

$$x_\mathrm{i}(\boldsymbol{x}) \;=\; x + 20\,\Delta x\,\xi(y, z)\,, \text{ and } x_0 \;=\; (1 - \beta)\,L/2\,. \quad (3.8b)$$

Δx is the grid spacing, L is the periodic cubic domain extent, and $\xi(y, z)$ is the initial scaled perturbation field. Perturbation amplitudes are scaled by $20\,\Delta x$ (equation 3.8b), tying them to grid size to ensure their resolution, with the factor of

20 setting the perturbation amplitude. This yields $20\,\Delta x\,\xi_{\mathrm{RMS}} < 0.44\,\delta_{\mathrm{i}}$ with δ_{i} the initialized shear-layer width. In terms of maximum perturbation amplitude, $20\,\Delta x\ (\xi_{\max} - \xi_{\min}) < 0.034L$. Different perturbations tested had minimal effects on the flow, as discussed in appendix B.

The flow is initialized with $\boldsymbol{u}(\boldsymbol{x}, t{=}0) = 0$, and thus perturbations are only in the density field. The zero-velocity initialization and equation 3.8 do not satisfy the constraints from equation 3.4, *i.e.*, $\nabla \cdot \boldsymbol{u} \neq \nabla \cdot \left(\frac{\mathcal{D}}{\rho}\nabla\rho\right)$, and the density field is not a solution to the self-similar mass conservation equation (discussed later in section 4.1.1). However, the imposition of pressure as a Lagrange multiplier (*e.g.*, Ferziger and Peric, 2012) generates the correct diffusion-induced velocity in the first time step(s). In the zero-Mach-number limit, pressure enters with the dynamic role of ensuring mass conservation by updating the velocity field, as opposed to the thermodynamic pressure relating density and temperature, for example.

Transients from this initial condition decay as the flow evolves. Different initializations were tested with, for example, a hyperbolic tangent (as opposed to an error function) and the full initial solution to equation 3.4, including a non-zero initial velocity field satisfying the mass conservation equation (using the perturbed density field, inducing perturbations in the velocity field). All relaxed to statistically similar states, showing a relative lack of initialization sensitivity of this flow. The initial condition choice used throughout the main text was simple to implement, and left no significant imprint on the flow. Details of the initial perturbation displacements, $\xi(y, z)$, and initial function profile tests are discussed further in appendix B.

3.4 Numerical method

The method of direct numerical simulation (DNS) is used to solve the flow equations. A Fourier pseudo-spectral spatial discretization method is employed (Chung and Pullin, 2010) in a triply periodic cubic domain. A Helmholtz–Hodge decomposition of pressure is implemented following Chung and Pullin (2010). The original code from Chung and Pullin (2010), which was tested and verified, was augmented by Professor Georgios Matheou and further updated (and verified) for this work, see appendix A for numerical method details.

The present simulations maintain a constant volume-averaged momentum in the entire domain, as discussed in section 3.2. The zero volume-averaged momentum constraint is imposed by removing any small mean-momentum fluctuations that ensue at every time step. The semi-implicit Runge–Kutta time stepping method of

Spalart, Moser, and Rogers (1991) is used.

The computational domain is discretized with $n^3 = 1024^3$ cells for the majority of the simulations shown. If no resolution is indicated, the results are for 1024^3 runs. Simulations performed with a 512^3 resolution are labeled as such. Simulations are resolved to $k_{\max}\eta_{\min} > 1.5$, where $k_{\max}$ is the maximum resolved wavenumber and $\eta_{\min}$ is the minimum plane-averaged Kolmogorov length scale (see appendix A).

3.5 Flow characteristics

The flow in the cubic computational domain is scaled as

$$L = 4\pi \tag{3.9a}$$

with times scaled by the characteristic time

$$\tau = 2\pi\sqrt{\frac{\ell}{\mathcal{A}g}}, \tag{3.9b}$$

with ℓ being the initial horizontal distance between the free-stream midpoints, or half the domain width in the studied configuration,

$$\ell = \frac{L}{2}. \tag{3.9c}$$

$$\mathcal{A} = \frac{R-1}{R+1} \tag{3.9d}$$

is the Atwood number, with

$$R \equiv \frac{\rho_1}{\rho_2} \tag{3.9e}$$

the density ratio of high- to low-density fluid. The mean density is set to $\rho_0 = 1$ (*cf.* equation 3.7), which selects the values of ρ_1 and ρ_2, given the volume fraction of high-density fluid, β, and the density ratio, R.

Two-dimensional slices in the $(\widehat{x}, \widehat{z})$–plane are shown in figure 3.2 for flow with $R = 1.05$ at various non-dimensional times to illustrate flow evolution. The flow initially is dominated by molecular diffusion, followed by an unsteady regime characterized by eddy roll-ups. At later times, the flow becomes turbulent, and eventually homogenizes (because of domain periodicity).

Figure 3.3 displays slices of the density field for density ratios: $R = 1.4$, 2, 5, and 10, with $\beta = 1/2$. Only half the domain slice in x is shown. Figure 3.3a depicts the flow for those density ratios at the same non-dimensional time, t/τ. The flow

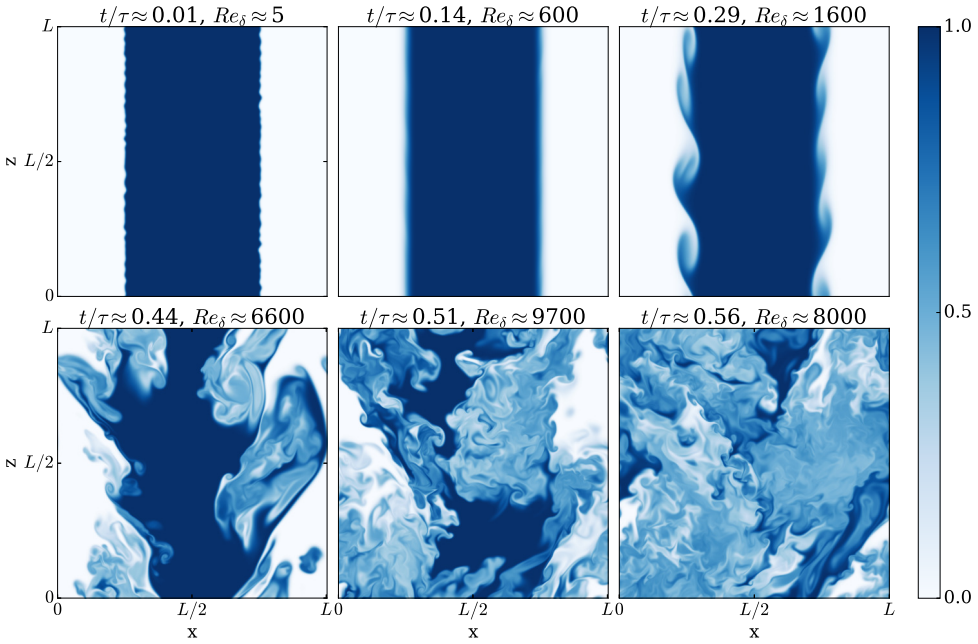

Figure 3.2: Two-dimensional slices of high-density fluid mole-fraction for $R = 1.05$. Reynolds numbers based on shear-layer width, δ.

is initially dominated by diffusion, with growing unsteadiness eventually leading to turbulence. In this turbulent regime, flow realizations are best compared at the same Reynolds number as opposed to the same dimensionless time.

An outer-scale Reynolds number is used in this discussion, based on the shear-layer width, δ, the vertical velocity difference across the shear layer, ΔW, and the mean density within the shear layer, $\overline{\rho}$, as described in section 4.1. Flow realizations for $R = 1.4$, 2, and 5 in figure 3.3b are at $Re_\delta \approx 8500$, at the outset of fully developed turbulence, as further discussed in section 4.1. The flow for $R = 10$ is displayed at $Re_\delta \approx 7700$, the highest Reynolds number attained at that (highest) density ratio.

Flow statistics in the fully developed turbulent regime, which generally begins at approximately $Re_\delta \sim 10^4$ (Dimotakis, 2000), exhibit relatively low sensitivity to Reynolds number. The flow discussed here enters this regime at comparable outer flow Reynolds numbers, as also discussed in section 4.1.

Shear layers eventually encroach across a pure free stream, *e.g.*, figure 3.2 and $R = 5$, 10 slices in figure 3.3b in which the shear layers straddle the low-density stream. Flow simulations are terminated once mixed fluid extends across either pure free stream, except for $R = 1.05$, with which we assessed very late-time flow behaviors.

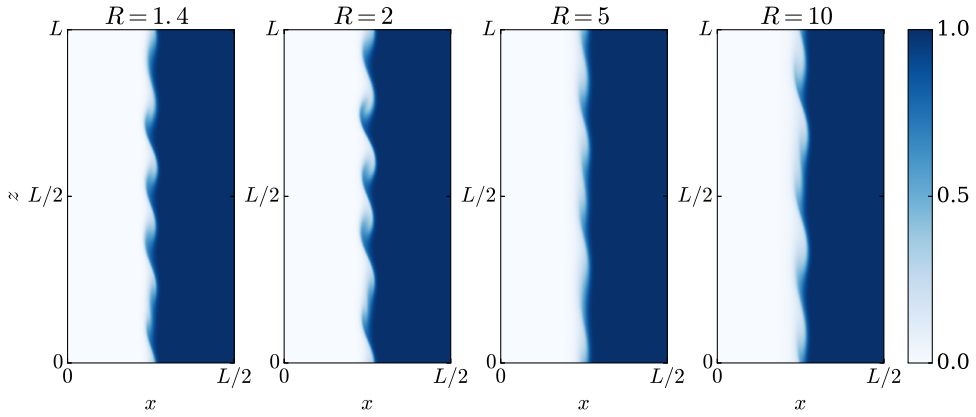

(a)

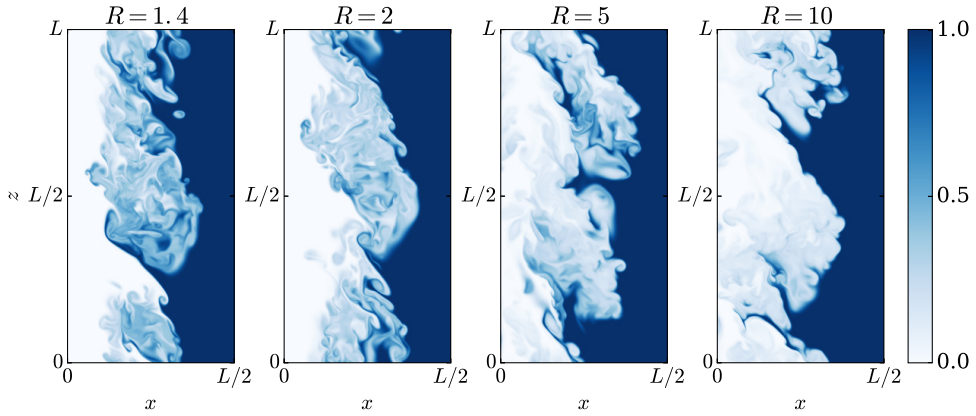

(b)

Figure 3.3: High-density fluid mole fractions for R = 1.4, 2, 5, and 10. Dark color indicates X = 1 (pure high-density fluid) and white indicates X = 0 (pure low-density fluid). (*a*) Flow slices at the same time, $t/\tau \approx 0.2$, when shear-layer growth is dominated by diffusion. (*b*) Flow slices at later (and different) times, at $Re_\delta \approx 8500$, except for R = 10 flow that is displayed at $Re_\delta \approx 7700$.

Chapter 4

FLOW ANALYSIS

4.1 Bulk flow statistics

Mean-flow statistics of the studied setup are described below.

4.1.1 Shear-layer width growth

The mixed-fluid region width definition proposed by Koochesfahani and Dimotakis (1986) is adopted, wherein the 'mixed-fluid' transverse extent, *i.e.*, the shear-layer width, $\delta(t)$, is based on a 1% criterion, or the largest transverse extent in x that spans all locations with fluid mass fractions in the range

$$0.01 \; < \; Y(\boldsymbol{x}, t) \; < \; 0.99\,, \tag{4.1}$$

calculated pointwise at each (y, z) location for both shear layers to obtain a $\delta(y, z; t)$, the average value for both shear layers at each (y, z) location in the flow, which is further averaged to obtain $\delta(t) \equiv \langle \delta(y, z; t) \rangle_{y,z}$. Fluid is considered 'mixed' if, pointwise, equation 4.1 is satisfied, with the shear-layer width, $\delta(t)$ representing the average of the largest transverse mixed-fluid extents for each shear layer at every (y, z) location.

Rewriting equation 3.4 with $Sc = 1$ (uniformly), *i.e.*, $\mathcal{D}(\boldsymbol{x}, t) = \mu/\rho(\boldsymbol{x}, t)$, where μ is approximated as uniform, allows both sides the equation to be expressed as functions of $1/\rho$, which helps elucidate the shear-layer growth behavior, *i.e.*,

$$\frac{\mathrm{D}}{\mathrm{D}t}\left(\frac{1}{\rho}\right) \; = \; \mu \frac{1}{\rho} \nabla^2 \left(\frac{1}{\rho}\right). \tag{4.2}$$

Diffusion induces a contribution to the initial velocity field, and for the unperturbed case, $\boldsymbol{u} = \widehat{\boldsymbol{x}}\, u(x, t)$ and $\rho = \rho(x, t)$ (Sandoval, 1995; Cook and Dimotakis, 2001),

$$u(x, t) \; \approx \; u_{\mathrm{D}}(x, t) \; = \; \mu \, \frac{\partial}{\partial x} \left[\frac{1}{\rho(x, t)} \right] . \tag{4.3}$$

The convective term initially satisfies the equation,

$$\boldsymbol{u} \cdot \nabla \left(\frac{1}{\rho}\right) \; = \; \mu \left[\frac{\partial}{\partial x} \left(\frac{1}{\rho(x, t)} \right) \right]^2 . \tag{4.4}$$

Chapter adapted from Gat et al., 2016, 2017

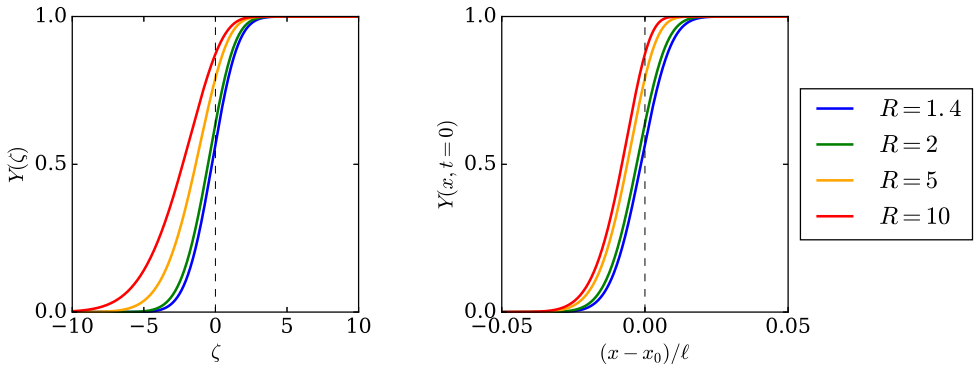

Figure 4.1: Mass-fraction solutions to the self-similar mass conservation equation (4.5) for four density ratios. Left: plot of $Y(\zeta)$, with dashed line at $\zeta = 0$ shown for reference. Right: plot of $Y(x, t{=}0)$ with dashed line at $(x - x_0)/\ell = 0$.

Defining $f(\zeta) = \rho_0/\rho(x,t)$, with $\zeta = (x - x_0)/\sqrt{t\,\mu/\rho_0}$, equation 4.2 becomes

$$f(\zeta)f''(\zeta) + \frac{\zeta}{2}f'(\zeta) - [f'(\zeta)]^2 \;=\; 0\,, \tag{4.5}$$

with boundary conditions of $f(\zeta{\to}\infty) \to \rho_0/\rho_1$ and $f(\zeta{\to}-\infty) \to \rho_0/\rho_2$, which admits similarity solutions. Equation 4.5 indicates that the relevant length scale in the diffusive regime is $\sqrt{t\,\mu/\rho_0}$; the shear layer would grow as $\sim \sqrt{t}$ in this regime. However, to avoid gradient singularities, flows are initialized with a small width, corresponding to an effective initial time, t_i, in each case.

The solution to equation 4.5 is density ratio dependent, as dictated by the boundary conditions. Figure 4.1 displays solutions to equation 4.5, obtained numerically with Mathematica's shooting method, in terms of mass fractions, where

$$f(\zeta) \;=\; \frac{\rho_0}{\rho_2} - \left(\frac{\rho_0}{\rho_2} - \frac{\rho_0}{\rho_1}\right) Y(\zeta) \;\to\; Y(\zeta) \;=\; \frac{\dfrac{\rho_0}{\rho_2} - f(\zeta)}{\dfrac{\rho_0}{\rho_2} - \dfrac{\rho_0}{\rho_1}}\,. \tag{4.6}$$

Figure 4.1, left, displays solutions of equation 4.5 in terms of the self-similar variable, ζ. Figure 4.1, right, displays solutions at the initial times, t_i, *i.e.*, $Y(x, t{=}0)$, where x is offset by x_0 to match initial conditions. Profiles are asymmetric, with longer tails extending into the lower-density fluid.

In the present simulations, the initial velocity field is set to zero everywhere, *i.e.*, $\boldsymbol{u}(\boldsymbol{x}, t{=}0) = 0$. However, initially, a non-zero initial diffusion-induced velocity field is required (*cf.* equation 4.3 and figure 4.2), with non-zero components in all

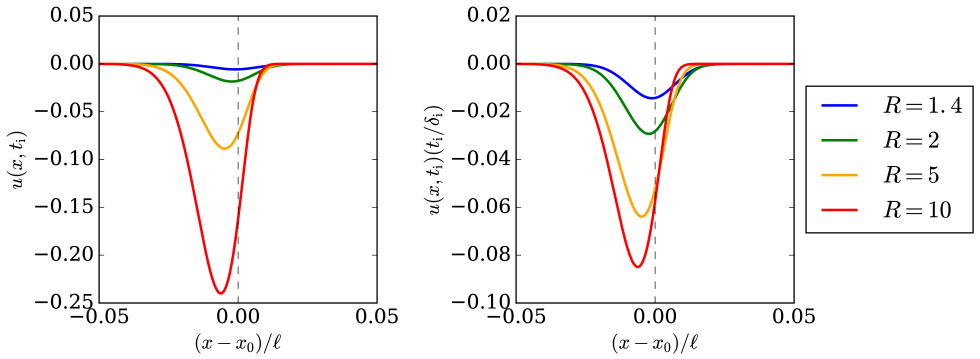

Figure 4.2: Initial diffusion velocity based on initial profile solution (4.5) for four density ratios. Left: plot of dimensional, right: plot of non-dimensional $u(x, t_i)$, with dashed line at $(x - x_0)/\ell = 0$ for reference.

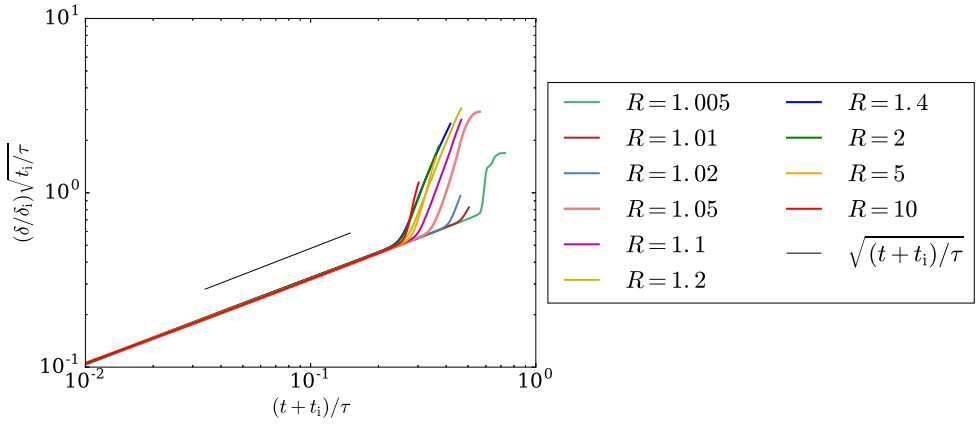

Figure 4.3: Non-dimensionalized shear-layer widths, $(\delta/\delta_i)\sqrt{t_i/\tau}$, versus time (colored lines) with the black line for slope reference.

directions induced by the perturbed density field. This initial non-zero diffusion-induced velocity field (figure 4.2 for the one-dimensional case) was shown to have little impact on the flow and omitted in the majority of the simulations. Appendix B discusses this and other initial condition choices.

The self-similar mass conservation equation predicts shear-layer widths that grow in the diffusive regime as

$$\frac{\delta(t)}{\delta_i} = \left(\frac{t + t_i}{t_i}\right)^{1/2}, \tag{4.7a}$$

with $\delta_i = \delta(t{=}0)$, as set by the initial conditions. This growth is independent of τ in the local diffusive regime, the characteristic time in equation 3.9b, as confirmed in figure 4.3 that displays the temporal shear-layer width growth for the density ratios

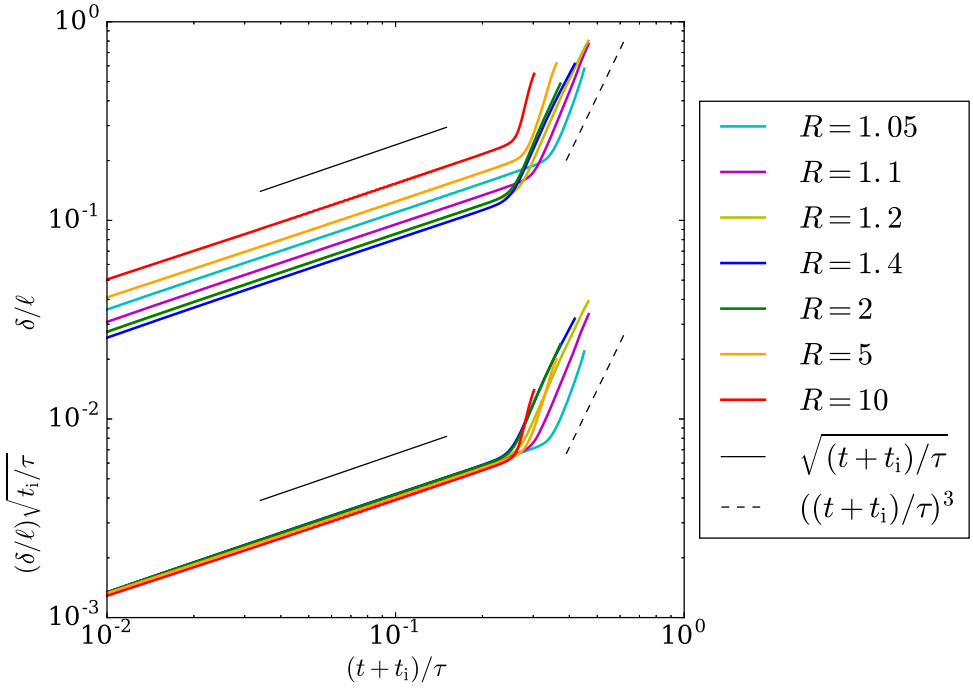

Figure 4.4: Shear-layer widths versus time, for seven density ratios (colored lines). Black lines denote approximate reference slopes. Top lines are non-dimensionalized by domain width. Bottom lines scale non-dimensionalized shear-layer widths with $\sqrt{t_i/\tau}$.

studied, non-dimensionalized with δ_i.

Following transitions to the second regime, shear-layer widths grow in time as

$$\frac{\delta(t)}{\delta_{tr}} \simeq \left(\frac{t+t_i}{t_{tr}+t_i}\right)^3, \tag{4.7b}$$

in which the two asymptotic (diffusive and unsteady) regimes cross at t_{tr} (figure 4.4), with t_{tr} an implicit function of τ. Transitions to the second regime for each flow vary somewhat. However, no systematic dependence of the transition time on flow parameters or initial perturbations is observed, as discussed further in appendix B. Viscosity for the lower-R simulations ($R < 1.05$) was set higher relative to the larger-R simulations, which may have affected their transition times from the diffusion-dominated regime, and are not depicted in figure 4.4.

Figure 4.4 displays shear-layer widths plotted as δ/ℓ (lines on top), and shear-layer widths further scaled with $\sqrt{t_i/\tau}$ (lines on bottom). The shear-layer width is initialized as, δ_i, corresponding to a t_i, which then scales shear-layer width growth

in the diffusive regime. Shear-layer width growth in the unsteady flow regime scales with ℓ, rather than δ_i, and plotted accordingly in figure 4.4.

In the present study, shear-layer widths in the turbulent regime are observed to grow approximately proportional to the cube of time. Modulo variations in the high-Lyapunov-exponent turbulent regime, this near-cubic time dependence of the shear-layer width emerges as a relatively robust and novel result. Professor Paul Dimotakis proposed an explanation in terms of dimensional analysis and similarity. The time derivative of the shear-layer widths, *i.e.*, $\mathrm{d}\delta/\mathrm{d}t$, or in terms of the scaled time, t/τ, is given by

$$\frac{\mathrm{d}\delta}{\mathrm{d}(t/\tau)} \simeq \Lambda(t;\tau,R,g), \tag{4.8a}$$

where Λ is a function with units of length. Using dimensional analysis and incorporating density ratio, R, similarly to its incorporation in Rayleigh–Taylor flow length scales, leads to

$$\frac{\mathrm{d}\delta}{\mathrm{d}(t/\tau)} \propto \mathcal{A}\, g\, t^2, \tag{4.8b}$$

i.e., the relevant length scale based on the reduced acceleration, $\mathcal{A}\, g$, with $\mathcal{A} = \mathcal{A}(R)$ the Atwood number (equation 3.9d). Dividing both sides by ℓ then yields,

$$\frac{\mathrm{d}(\delta/\ell)}{\mathrm{d}(t/\tau)} \propto \frac{t^2}{\ell/(\mathcal{A}\, g)} \simeq C_\delta \left(\frac{t}{\tau}\right)^2, \tag{4.8c}$$

as observed, modulo virtual origins in time and δ. Rescaling ℓ, *i.e.*, $\ell \to \lambda\,\ell$, only redefines the proportionality constant, *i.e.*, $C_\delta \to \lambda^{1/2} C_\delta$, leaving the predicted quadratic growth rate time dependence unaltered.

A comparison of this behavior with the growth of the time-dependent vertical extent of the mixed-fluid region in Rayleigh–Taylor (RT) flow, $h_\mathrm{RT}(t)$, is of interest. RT flow also evolves in response to an externally imposed acceleration field, g, such as gravity, and possesses the same acceleration-induced length scale, $\mathcal{A}\, g\, t^2$. RT flow, however, has no characteristic time scale akin to τ that is imposed on its dynamics. In the present flow, τ scales the time dependence, as seen in figure 4.4 and in other time-dependent statistics discussed below. Equivalently, RT flow does not possess a time-independent length scale akin to ℓ, in terms of which the characteristic time τ is defined (equation 3.9b).

In RT flow, the vertical extent of the mixed-fluid region grows at a rate that is linear in time, *i.e.*, $\mathrm{d}h_\mathrm{RT}/\mathrm{d}t \propto \mathcal{A}\, g\, t$. Vertical velocities also grow linearly in time in the present flow, as shown and discussed below. The difference is that the quadratic growth rate of the shear-layer width $\delta(t)$ is of a *horizontal* extent (perpendicular to

the acceleration field), versus the *vertical* extent (parallel to the acceleration field), h_{RT}, in RT flow.

As defined here and as demonstrated to scale time-dependent results in the present flow, the time scale, τ (defined by equation 3.9b), can be recognized as the period of a simple pendulum of length ℓ, in a reduced acceleration/gravity field, $\mathcal{A}\, g$, inferred from figure 3.2. The pendulum length, ℓ, in the definition of τ is the distance to the two mid-span points in the two free streams, independently of β, the horizontal span of the high-density fluid.

The high-density fluid responds here by initially accelerating in the direction of the uniform acceleration field (downwards in figure 3.1), while the low-density fluid accelerates opposite to it (upwards in figure 3.1), akin to the motion of an initially horizontal pendulum. Periodic boundary conditions on the top and bottom surfaces, however, prevent stable stratification at later times, corresponding to a vertical orientation of an equivalent pendulum, and yielding a homogeneous mixture for long times. Nevertheless, the initial phase of what would be an overturning motion is unimpeded by the boundary conditions and the pendulum period emerges as a characteristic time scale.

Shear-layer growth rates in figure 4.4 suggest that C_δ increases with R. Flows with $R = 5$ and $R = 10$ density ratio did not reach scaled times that were as large in their late-time asymptotic state as for lower density ratios; their free streams were encroached earlier, as discussed above towards the end of section 3.5. Wider free streams (higher grid resolution) for those density ratios may have allowed a similar asymptotic state to be attained, as suggested in $R < 5$ flows.

The present flow is relevant to RT flow. Shear layers investigated here correspond to sheared regions formed between descending high-density fluid "spikes" and ascending low-density fluid "bubbles" in RT flow. The rapidly growing shear layers reported here would be expected to encroach across the supply of pure fluids in RT flow, leading to a later growth phase in the vertical extent of that flow that may, eventually, be slower.

4.1.2 Free-stream velocity difference across the shear layer

The externally imposed acceleration (gravity) field induces a hydrostatic pressure field, which initially is the sole pressure field component,

$$\boldsymbol{\Gamma} + \nabla p \;\simeq\; -\widehat{z}\,\rho_0 g\,, \tag{4.9}$$

simplifying equation 3.1b for the free-stream velocity, *i.e.*,

$$\frac{\mathrm{D}\boldsymbol{U}}{\mathrm{D}t} \simeq -\widehat{\boldsymbol{z}}\, g \left(1 - \frac{\rho_0}{\rho}\right), \tag{4.10}$$

ignoring viscous terms that are small compared to the pressure and acceleration terms. This analysis applies to the free-stream velocity field, $\boldsymbol{U}$, as opposed to the space-time-dependent velocity in the entire domain, $\boldsymbol{u}(\boldsymbol{x}, t)$.

The free-stream velocity field is dominated by its $\widehat{\boldsymbol{z}}$ component, even at late times, which is a function of x — the coordinate across the shear-layer thickness. Thus,

$$\frac{\mathrm{D}\boldsymbol{U}}{\mathrm{D}t} = \frac{\partial \boldsymbol{U}}{\partial t} + (\boldsymbol{U}\cdot\nabla)\,\boldsymbol{U} \approx \widehat{\boldsymbol{z}}\,\frac{\partial W}{\partial t} + \widehat{\boldsymbol{z}}\,W\,\frac{\partial W(x)}{\partial z} = \widehat{\boldsymbol{z}}\,\frac{\partial W}{\partial t} \tag{4.11}$$

with the free-stream velocity field, $\boldsymbol{U} = (0, 0, W)$. Integrating this equation yields

$$W(x,t) = -g\,t\left[1 - \frac{\rho_0}{\rho(x)}\right], \tag{4.12}$$

which represents the free-stream velocities, ignoring viscous effects and pressure fluctuations at the fluid interface. We note that $\langle \rho W\rangle = -gt\,(\langle\rho\rangle - \rho_0) = 0$ since $\langle\rho\rangle = \rho_0$, satisfying the zero-mean-momentum constraint discussed in section 3.2. The difference between the free-stream velocities is then a linear function of time, *i.e.*,

$$\begin{aligned}\Delta W = |W_1 - W_2| &= g\,t\left(\frac{\rho_0}{\rho_2} - \frac{\rho_0}{\rho_1}\right)\\ &= \mathcal{A}\,g\,t\,\frac{(R+1)}{R}\left[(R-1)\,\beta + 1\right],\end{aligned} \tag{4.13a}$$

where, as before, β is the volume fraction of high-density fluid in the periodic domain. Scaling the right-hand side by τ/ℓ yields

$$\Delta W = \frac{(2\pi)^2\,(R+1)\,[(R-1)\beta + 1]}{(\tau/\ell)\,R}\left(\frac{t}{\tau}\right), \tag{4.13b}$$

or

$$\frac{\mathrm{d}\,\Delta W}{\mathrm{d}(t/\tau)} = \frac{(2\pi)^2\,(R+1)\,[(R-1)\beta + 1]}{(\tau/\ell)\,R}. \tag{4.13c}$$

For the common $\beta = 1/2$ case, this becomes

$$\frac{\mathrm{d}\,\Delta W}{\mathrm{d}(t/\tau)} = \frac{[2\pi\,(R+1)]^2}{2\,(\tau/\ell)\,R}. \tag{4.13d}$$

Figure 4.5 displays the simulated values of ΔW, confirming the analytical solution in equation 4.13b and 4.13d. Plots shown are for $\beta = 1/2$. The results were tested and

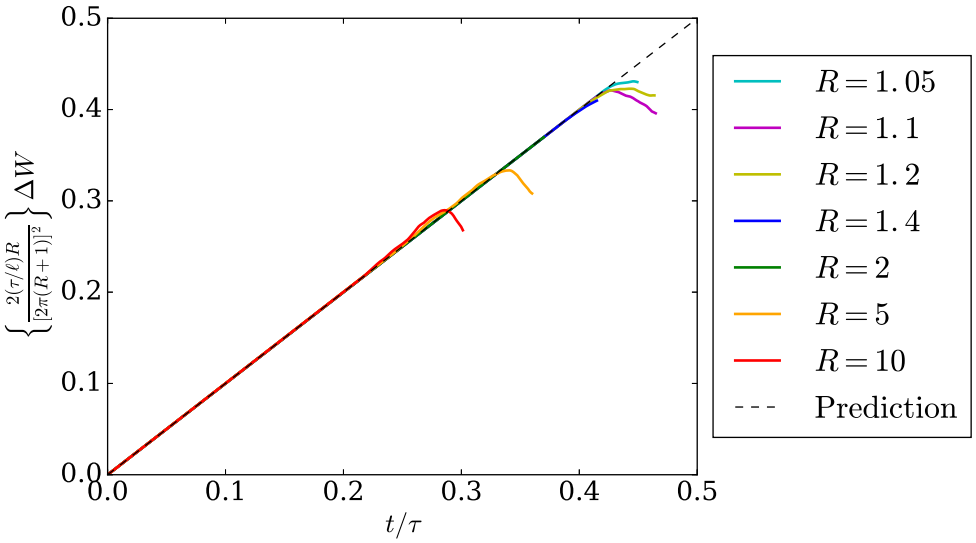

Figure 4.5: Scaled free-stream velocity differences, ΔW, for $\beta = 1/2$ and various density ratios. Dashed black line plots the prediction of equation 4.13b.

also hold for $\beta = 1/4$, $1/3$, $2/3$, and $3/4$, but are not shown for brevity. Late-time deviations occur when shear layers bridge across a free-stream extent.

Returning to the discussion of RT flow, we note that vertical velocities here are also proportional to time, so the vertical separation between two free-stream points across a shear layer would increase as t^2, as does the vertical extent in RT flow.

4.1.3 Mean shear-layer density

Equation 4.5 shows that, in the viscous diffusive regime, $\overline{\rho}$, the mean fluid density within the shear layer is a function of $\zeta = (x - x_0)/\sqrt{t\,\mu/\rho_0}$, *i.e.*, the density field shape throughout the diffusive regime depends only on the self-similarity variable, ζ. The density profile width will increase with time without changing the mean density within the shear layer. This allows the mean density to be predicted from equation 4.5, for one-dimensional unperturbed flow.

An empirical relation for the mean density within the shear layer can also be obtained through the entrainment ratio. The volumetric entrainment ratio, E_v, is the ratio of entrained volume of high- to low-speed fluid in the mixing region. For a temporally growing shear layer, E_v can be represented by the ratio of induction velocities, v_{i1} and v_{i2} (Dimotakis, 1986),

$$E_v = \frac{X_2(\overline{\rho})}{X_1(\overline{\rho})} = -\frac{v_{i2}}{v_{i1}}, \tag{4.14}$$

where X_α are the species mole fractions, or volume fractions, with $\rho_\alpha X_\alpha = \rho Y_\alpha$. The induction velocities, v_{i1} and v_{i2}, are in opposing directions, introducing a minus sign in their ratio. Professor Daniel Chung noted these induction velocities can be defined as $v_{i1} = \mathrm{d}\langle x_{0.99}\rangle_{y,z,L/R}/\mathrm{d}t$ and $v_{i2} = \mathrm{d}\langle x_{0.01}\rangle_{y,z,L/R}/\mathrm{d}t$, with $\langle x_{0.99}\rangle_{y,z,L/R}$ and $\langle x_{0.01}\rangle_{y,z,L/R}$ marking the mean left, L, and right, R, shear-layer boundaries (figure 3.1) in terms of mass fraction (equation 4.1), averaged over (y, z).

The entrainment ratio can be related to the ratio of apparent velocities in the convective frame with the Dimotakis (1986) ansatz, *i.e.*,

$$E_v = \frac{X_2(\overline{\rho})}{X_1(\overline{\rho})} = -\frac{v_{i2}}{v_{i1}} = \frac{W_2 - W_\mathrm{c}}{W_\mathrm{c} - W_1}, \tag{4.15}$$

where W_c is the mean convective velocity of the large-scale shear-layer turbulent structures. With equation 4.15, $\overline{\rho}$, the mean density within the shear layer is predicted by

$$X(\overline{\rho}) = X_1(\overline{\rho}) = \frac{1}{E_v + 1} = \frac{\overline{\rho} - \rho_2}{\rho_1 - \rho_2}, \tag{4.16}$$

where $X = X_1$.

In the present simulations, an empirical relation for the convection velocity, W_c, is indicated by correlations of spatial eddy locations over time and the evolution of the (y, z)-averaged vertical velocity. An expression for W_c is obtained for $\beta = 1/2$ using a relation for convection velocities of temporally growing shear layers (Dimotakis, 1986),

$$W_\mathrm{c} = \frac{1 + r\sqrt{R}}{1 + \sqrt{R}}, \tag{4.17}$$

where r is the free-stream velocity ratio, *i.e.*,

$$\frac{W_\mathrm{c}}{\Delta W} = \frac{(W_1 + W_2)/\Delta W}{2\sqrt{R} + 3} = \frac{R - 1}{(2\sqrt{R} + 3)(R + 1)}. \tag{4.18}$$

Figure 4.6 displays the mean density within the shear layers derived from the simulations (solid lines), compared to the empirical relation for $\overline{\rho}$ (dashed lines) for $\beta = 1/2$. The empirical relation for $\overline{\rho}$ is derived using the volumetric entrainment-ratio definition (equation 4.15) with equation 4.16 noting the vertical velocities, W_1, W_2, and W_c from equations 4.12 and 4.18. Values of $\overline{\rho}$ from simulations are calculated using the shear-layer 1% criterion (4.1) at each (y, z)-plane for both shear layers, and averaging. After an initial transient, as mentioned in section 3.3, the mean shear-layer density is seen to relax to approximately the same value independently of initial conditions. These values also match well with the predicted mean

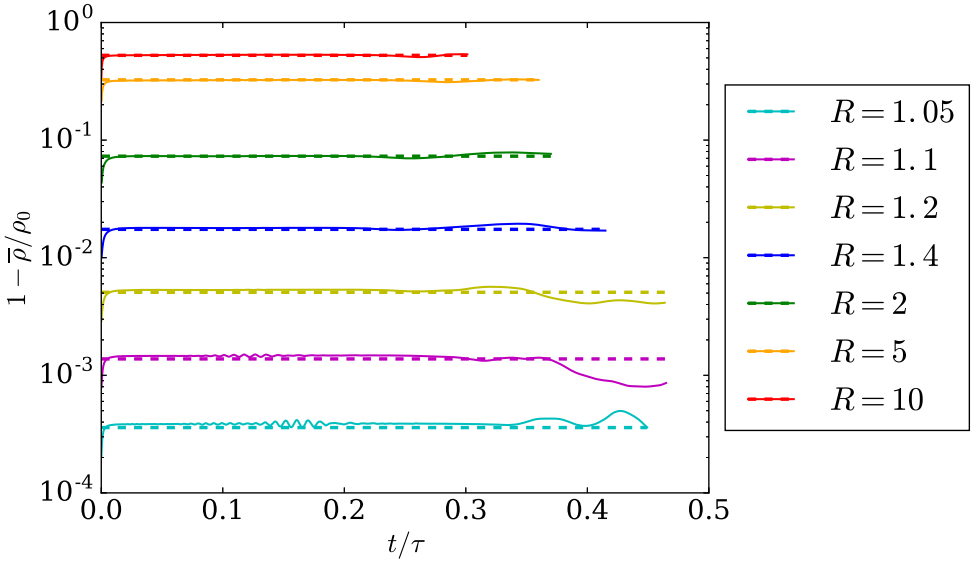

Figure 4.6: Mean density within the shear layers for seven density ratios. Solid lines show flow simulation results and dashed lines display the constant value of the empirical results (equations 4.15, 4.16, and 4.18).

density from equation 4.5. At late times, mean shear-layer densities deviate from the constant $\overline{\rho}$ after pure fluid is depleted. The flow exhibits a small deviation from the predicted $\overline{\rho}$ at t/τ values corresponding to the transition to the second flow regime (figure 4.4).

In the present flow, W_c depends on the reference frame and β, the ratio of heavy to light fluid in the computational domain. The expression for W_c above was extended empirically to capture the dependence on β:

$$\begin{aligned} \frac{W_c}{\Delta W} &= \frac{\left[(1-\beta)^2 W_1 + \beta^2 W_2\right]/\Delta W}{\beta R^\beta + 3(1-\beta)/2} \\ &= \frac{\beta^3 R - (1-\beta)^3}{\left[\beta R^\beta + 3(1-\beta)/2\right]\left[(R-1)\beta + 1\right]}, \end{aligned} \tag{4.19}$$

which agrees with equation 4.18 for $\beta = 1/2$ and was obtained similarly by comparing simulations of the same R but different β values. We offer no theoretical explanation for it, however.

Figure 4.7 displays the comparison of equation 4.19 (in conjunction with equations 4.15 and 4.16 to obtain $\overline{\rho}$) with the simulation $\overline{\rho}$ for $R = 5$ for various β values. These equations yield similar $\overline{\rho}$ values to the simulations (and the analytical solution

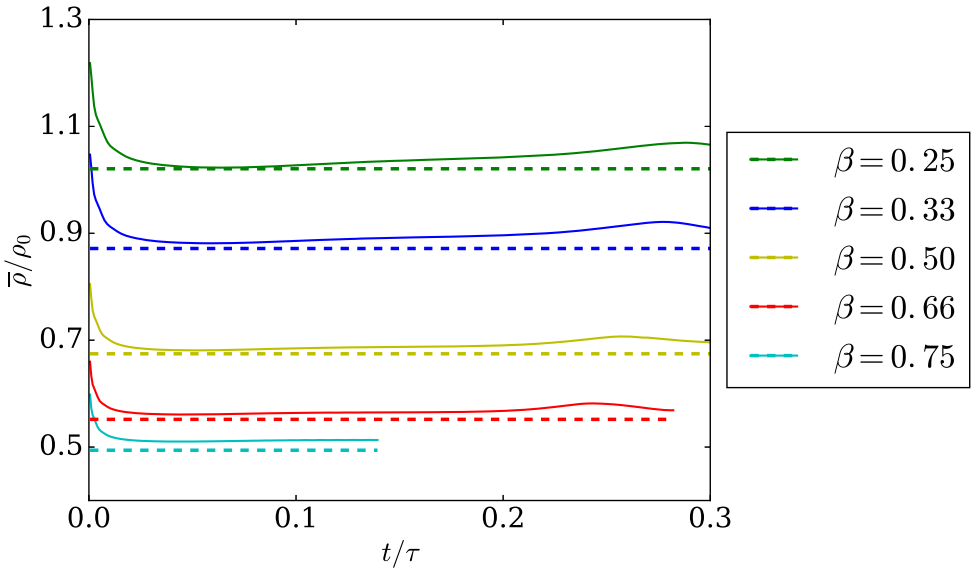

Figure 4.7: Mean densities within $R = 5$ shear layers, simulated for five β values on 512^3 grids. Solid lines show flow simulation results. Dashed lines display the empirical expression value. Small deviations from late-time predictions coincide with diffusive-to-unsteady flow transitions, as also seen in figure 4.6. Note different y-axis here versus that in figure 4.6.

to equation 4.5) and equation 4.19 approximately matches the mean velocity of the shear layer, as it should in this case.

Equation 4.19 indicates that for $\beta \geq 1/2$, $W_c > 0$ for all R. However, for $\beta < 1/2$, there are density ratios for which the convective velocity is negative (downward) in the zero-mean-momentum reference frame. For example, for $\beta = 1/3$, $W_c < 0$ if $R < 7$, and for $\beta = 1/4$, $W_c < 0$ if $R < 26$, which includes all R values investigated. Flow animations also support this conclusion.

4.1.4 Reynolds number

Figure 4.8 shows the evolution of the Reynolds number, $Re_\delta = \overline{\rho}\,\delta\Delta W/\mu$, based on outer-scale variables. The two asymptotic flow regimes, diffusive and unsteady/turbulent, are evident. Some of the curves in figure 4.8 may suggest the beginning of a third regime at late times. However, this occurs when a free-stream fluid is depleted and shear layers no longer grow freely.

Profiles of the mean kinetic energy in the shear layer (figure 4.9) become nearly Reynolds-number independent for $Re_\delta \gtrsim 8000$, characteristic of behavior past the mixing transition (Dimotakis, 2000). These results are taken at x locations

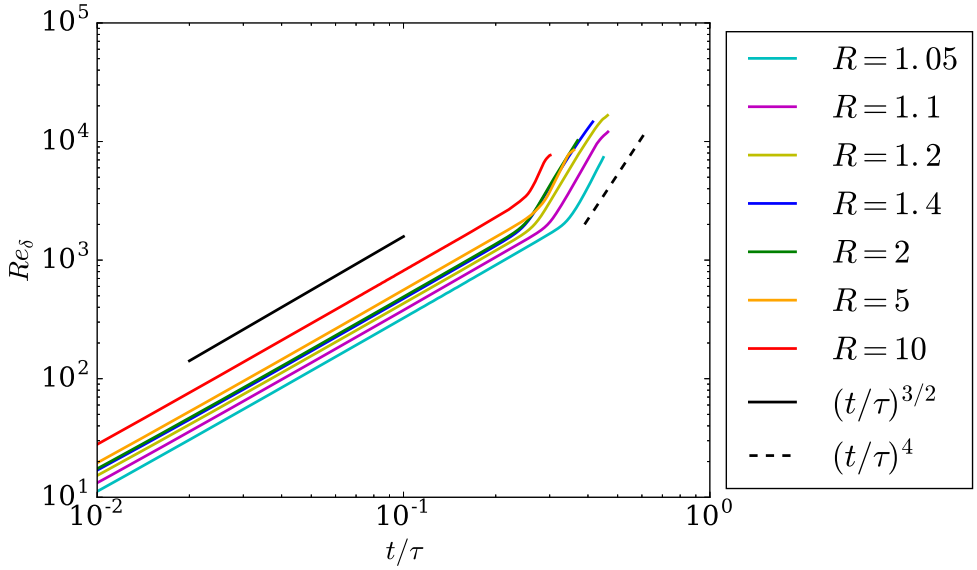

Figure 4.8: Reynolds-number evolution. Colored lines display information from the numerical simulations and black lines (solid and dashed) denote reference slopes.

with $\langle\rho\rangle_{y,z} \approx 1$, where $\langle\rho\rangle_{y,z}$ denotes the mean density averaged over (y, z). The data have been non-dimensionalized by $\epsilon^{-1/4}\,\nu^{-5/4}$. The kinematic viscosity is $\nu = \mu/\langle\rho\rangle_{y,z}$, and $\epsilon = 2\nu\,\langle \boldsymbol{D} : \boldsymbol{D}\rangle_{y,z}$ is the specific kinetic energy dissipation rate, where $\boldsymbol{D} = \boldsymbol{s} - (\nabla \cdot \boldsymbol{u})\,\mathbf{I}/3$ is the traceless strain rate tensor, $\boldsymbol{s} = \left(\nabla\boldsymbol{u} + \nabla\boldsymbol{u}^{\mathrm{T}}\right)/2$ is the strain rate tensor, and ":" implies the double dot product. Quantities are averaged over (y, z)–planes at the same x locations as the data shown in figure 4.9. Kinematic viscosity is used to non-dimensionalize the mean kinetic energy in figure 4.9; however, kinematic viscosity is constant over all Re_δ plotted since the results are at particular x locations where $\langle\rho\rangle_{y,z} \approx 1$, resulting in constant ν with increasing Re_δ. The plateau at high-Reynolds-numbers is not an artifact of viscosity, as expected in the turbulent regime. However, viscosity affects the kinetic energy in the initial diffusive regime, and is used to better collapse initial data.

As the flow becomes unsteady, shear-layer width, δ, growths transition from $t^{1/2}$ to t^3 dependencies, which is also seen in the Re_δ growth transitions from $t^{3/2}$ to t^4 (figure 4.8). This transition occurs between approximately $Re_\delta \sim 1000 \rightarrow 3000$, which is also seen in figure 4.9, with the mean kinetic energy increasing from approximately $3 \rightarrow 100$ over $Re_\delta \sim 1000 \rightarrow 3000$. As the shear layers complete the transition to the t^3 growth regime, the mean kinetic energy slope stabilizes, becoming (more) level when $Re_\delta \sim 8000$ is (approximately) attained (figure 4.9).

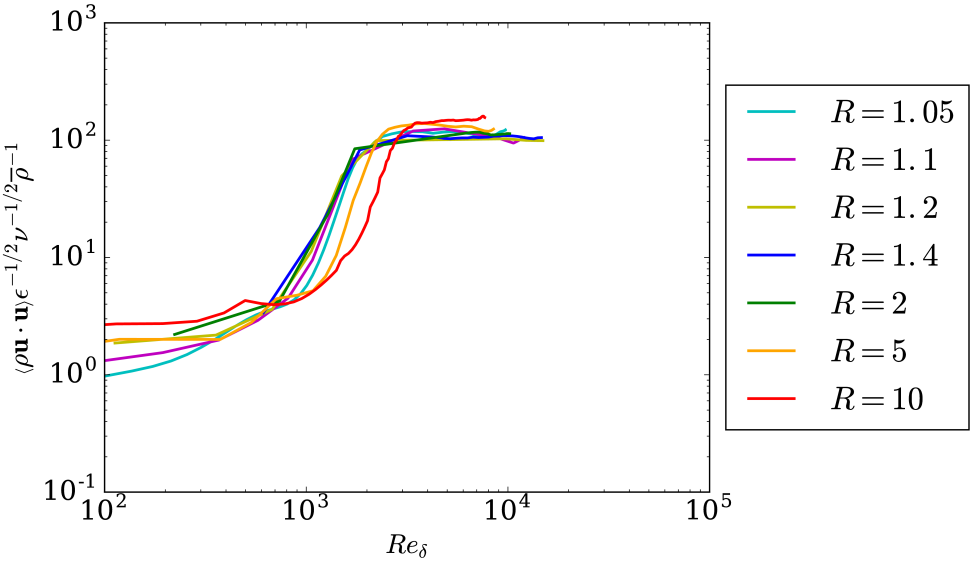

Figure 4.9: Mean kinetic energy at x locations in the shear layer where $\langle \rho \rangle_{y,z} \approx 1$, versus Re_δ.

The unsteady shear-layer growth rate is unchanged at $Re_\delta \sim 8000$, and Re_δ grows consistently through this turbulence transition (figure 4.8 shows no changes at the transitional $Re_\delta \sim 8000$).

4.2 Statistics in mixed-fluid regions

Mixed fluid characteristics are seen to be less sensitive to initial and boundary conditions than the mean-flow statistics. The flow studied produces shear layers with similar mixing characteristics to other shear layer flows.

4.2.1 Entrainment ratio

Shear-layer entrainment ratios are studied following the analysis of experiments by Koochesfahani and Dimotakis (1986), who analyze mixture fraction probability density function (p.d.f.) behavior in spatially developing shear layers. Koochesfahani and Dimotakis (1986) find that mole fraction values in a liquid-phase flow at Reynolds numbers beyond the mixing transition exhibit a 'non-marching' or 'slightly tilted' hump in the shear-layer composition p.d.f. across the transverse extent of the mixing region, representing the prevalent mole fraction within the shear layer. The results of a similar analysis are shown in figure 4.10.

This work discusses temporally developing gas-phase ($Sc = 1$) shear layers subject to an imposed acceleration field, whereas Koochesfahani and Dimotakis (1986)

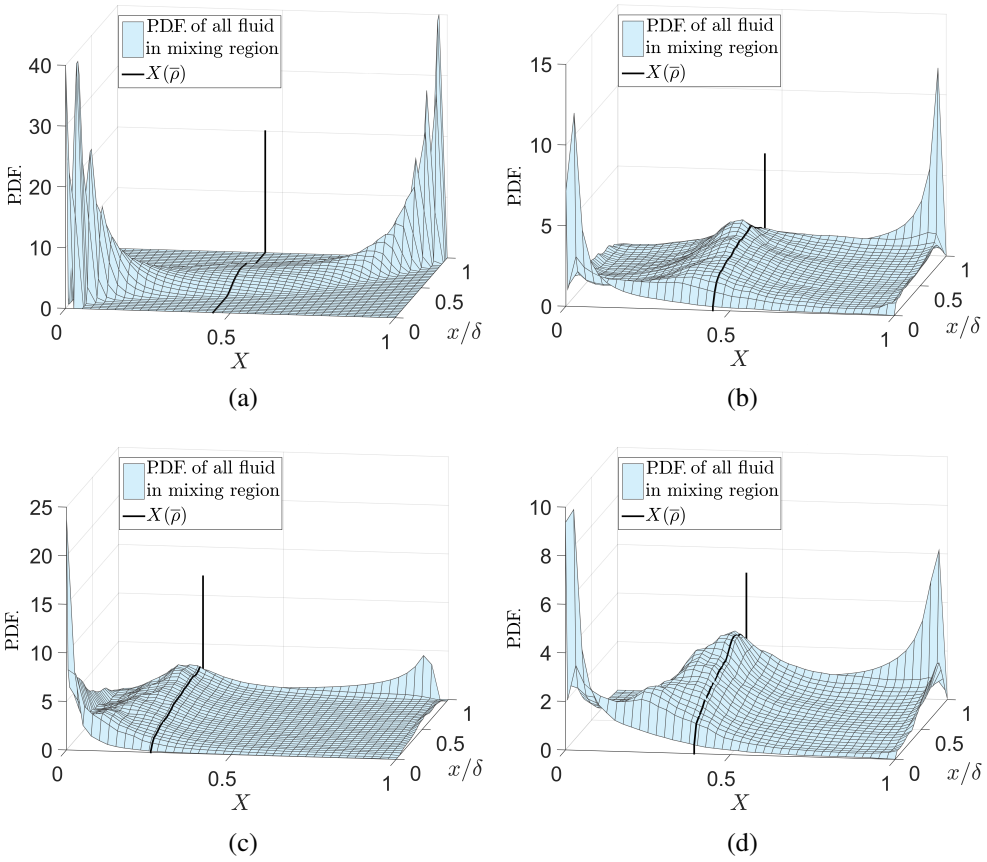

Figure 4.10: Mole fraction p.d.f.s across the shear layer. (*a*) Data for $R = 1.4$ in the diffusion-dominated regime at $t/\tau = 0.18$. (*b*) Data for the same flow as (*a*), but at a later time, in the turbulence-dominated regime at $t/\tau = 0.35$. (*c*) Data for $R = 5$ flow in the unsteady/turbulent regime at $t/\tau = 0.34$. (*d*) Data for $R = 2$ flow at $t/\tau = 0.37$, when $Re_\delta > 10{,}000$. Solid black lines mark $X(\overline{\rho})$.

experimentally investigated spatially developing shear layers with constant and uniform free-stream velocities across liquid-phase shear layers ($Sc \sim 10^3$). The Schmidt number, Sc, represents the ratio of kinematic viscosity to molecular diffusion, which affects mixing. A large liquid Schmidt number corresponds to large kinematic viscosity with respect to molecular diffusivity, versus the two being approximately equal in a gas. However, behavior similar to that reported by Koochesfahani and Dimotakis (1986) is found in the present flow.

Figure 4.10a shows the p.d.f. of high-density fluid mole fraction, X, across the shear layer for $R = 1.4$ early in the simulation ($t/\tau = 0.18$), in the diffusion-dominated regime. The expected 'marching p.d.f.' is observed in this regime. Figure 4.10b displays the shear-layer mole fraction p.d.f. later, for the same ($R = 1.4$) simulation,

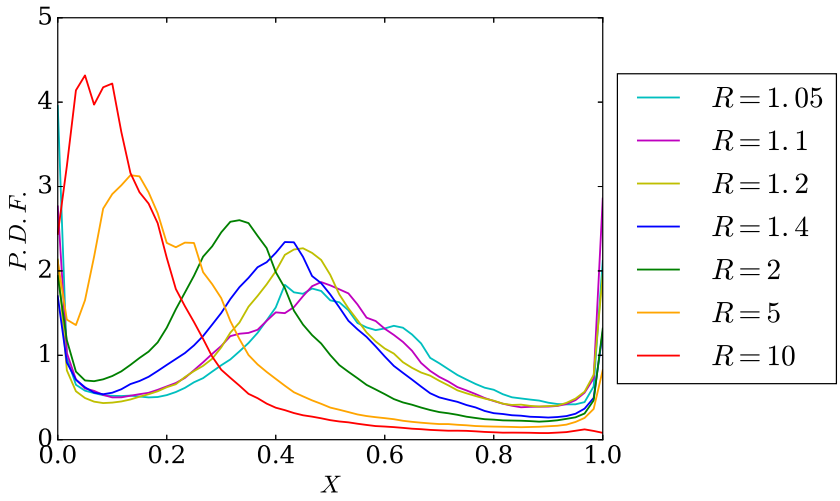

Figure 4.11: One-dimensional p.d.f.s half-way across the shear layer ($x/\delta = 0.5$) for various density ratios at times corresponding to $Re_\delta \approx 8500$. The p.d.f. for the $R = 10$ simulation is displayed at $Re_\delta \approx 7700$.

in the unsteady/turbulent regime. In this regime, a prevalent mole fraction ('non-marching') p.d.f. is observed. However, the most probable mole fraction is not exactly the mean mole fraction of mixed fluid within the shear layer, indicated by the black line, although they are close. Asymmetric composition excursions away from the most probable values yield most probable mole-fraction values away from the mean, as the p.d.f.s indicate and as is shown in figure 4.11.

Non-marching p.d.f.s are observed at all density ratios in the turbulent regime, with a hump location and degree of tilt a function of R. Figure 4.10c shows this in terms of the shear-layer mole fraction p.d.f. for the $R = 5$ simulations in the turbulent regime. Figure 4.10d displays the same behavior for the $R = 2$ simulations at even later times, for $Re_\delta > 10{,}000$ attained for this flow.

The shear layers entrain more low-density high-speed fluid than high-density low-speed fluid, by volume, at amounts that increase with R (Dimotakis, 1986). This is consistent with the solution to the self-similar mass conservation equation, shown in figure 4.1, with asymmetric p.d.f.s (figure 4.11), and has also been observed in buoyancy-driven flows (Livescu and Ristorcelli, 2008). Additionally, similarly to spatially developing liquid-phase shear layers ($Sc \sim 10^3$), the simulated temporally developing gas-phase shear layers ($Sc = 1$ here) also exhibit a constant (in time) most probable mole fraction ('non-marching' hump). This is not commonly reported for gas-phase shear-layer experiments (Meyer, Dutton, and Lucht, 2006). Marching versus non-marching p.d.f.s have been reported to depend on initial conditions

(Rogers and Moser, 1994; Mattner, 2011), in particular, the dimensionality of the initial disturbances, *i.e.*, two- versus three-dimensional (Slessor, Bond, and Dimotakis, 1998). Initial disturbances in this study more closely correspond to the three-dimensional initial perturbations of Slessor, Bond, and Dimotakis (1998), for which they report marching p.d.f.s, however Slessor, Bond, and Dimotakis (1998) report non-marching p.d.f.s for other initial perturbations. For all initial conditions explored in this work (appendix B), non-marching slightly tilted p.d.f. behavior was ubiquitous in the non-diffusive unsteady growth regimes.

4.2.2 Spectra

For uniform-density flows at finite Reynolds numbers, kinetic energy spectra scale as $k^{-5/3+q}$, with $q \to 0$ with increasing Reynolds numbers (Kolmogorov, 1941, 1962; Mydlarski and Warhaft, 1996). Similar behavior is observed for variable-density flows at low density ratios (*e.g.*, Batchelor, Canuto, and Chasnov, 1992; Livescu and Ristorcelli, 2008; Chung and Matheou, 2012). However, for variable-density flow, the kinetic energy, as opposed to the specific kinetic energy, is important.

For notational purposes, the spectrum of a field is denoted as S and the spectrum of the fluctuating specific kinetic energy (or the velocity) by $S_{\boldsymbol{u}'\cdot\boldsymbol{u}'} = S_{u'u'} + S_{v'v'} + S_{w'w'}$, where $\boldsymbol{u}' = (u', v', w')$, omitting the factor of $1/2$. Spectra shown are spatial one-dimensional spectra along the z direction, at particular x locations, averaged in y. We compare the fields at x values corresponding to $\langle\rho\rangle_{y,z} \approx 1$, where $\langle\rho\rangle_{y,z}$ denotes the mean density averaged over (y, z) at x locations where the spectra are calculated. The one-dimensional spectra in the streamwise velocity direction are shown since they are the most prevalent in turbulence research, especially for measurements. Additionally, others have shown that the full three-dimensional spectra can collapse to one dimension, allowing for one-dimensional spectra to be analyzed, without loss of generality (Pullin and Saffman, 1994; Chung and Matheou, 2014).

Specific kinetic energy spectra shown are the Fourier transforms of the velocity field autocorrelations (noted as an overbar in the equation below), averaged in y and at the corresponding values of x in the two shear layers (*cf.* figure 3.1).

$$\begin{aligned} S_{\boldsymbol{u}'\cdot\boldsymbol{u}'}(k_3; x, t) &= \left\langle \int_{-\infty}^{\infty} \overline{\boldsymbol{u}'(\boldsymbol{x} + \widehat{\boldsymbol{z}}z', t) \cdot \boldsymbol{u}'(\boldsymbol{x}, t)}\, e^{-ik_3 z'} \mathrm{d}z' \right\rangle_y \\ &= \left\langle \int_{-\infty}^{\infty} \int_{\boldsymbol{x}} \boldsymbol{u}'(\boldsymbol{x} + \widehat{\boldsymbol{z}}z', t) \cdot \boldsymbol{u}'(\boldsymbol{x}, t)\, e^{-ik_3 z'}\, \mathrm{d}\boldsymbol{x}\, \mathrm{d}z' \right\rangle_y \\ &= \left\langle |\mathcal{F}_z\{u(\boldsymbol{x}, t)\}|^2 + |\mathcal{F}_z\{v(\boldsymbol{x}, t)\}|^2 + |\mathcal{F}_z\{w(\boldsymbol{x}, t)\}|^2 \right\rangle_y \end{aligned} \tag{4.20}$$

In the limit of $R \rightarrow 1$, the kinetic energy spectrum must yield the specific kinetic energy spectrum, multiplied by the (near-)uniform density. The scaled spectrum, $S_{j'\cdot j'}/\overline{\rho}$, is calculated based on the field $\boldsymbol{j} \equiv \rho^{1/2}\boldsymbol{u}$, as proposed by Kida and Orszag (1992). The kinetic energy spectrum is then computed conventionally. After division by $\overline{\rho}$, results should converge to specific kinetic energy spectra in the limit of $R \rightarrow 1$.

To facilitate comparisons and as suggested above, figure 4.12a plots specific kinetic energy spectra (solid lines), $S_{\boldsymbol{u}'\cdot\boldsymbol{u}'}$, and kinetic energy spectra divided by $\overline{\rho}$ (dashed lines), $S_{\boldsymbol{j}'\cdot\boldsymbol{j}'}/\overline{\rho}$, non-dimensionalized by $\epsilon^{-1/4}\,\nu^{-5/4}$. The specific kinetic energy dissipation rate is $\epsilon = 2\nu\,\langle \boldsymbol{D} : \boldsymbol{D}\rangle_{y,z}$ and $\nu = \mu/\langle\rho\rangle_{y,z}$ is a kinematic viscosity, with both averaged over (y,z)–planes at the same x locations, where $\boldsymbol{D}$ is the traceless strain rate tensor.

The panels in figure 4.12 display spectra at different times, corresponding to similar Reynolds numbers of $Re_\delta \approx 8500$ for six simulations, with $Re_\delta \approx 7700$ for the $R = 10$ simulation, the largest Reynolds number attained at that density ratio. Spectra are plotted versus wavenumber, k_z, scaled with η, where $\eta = (\nu^3/\epsilon)^{1/4}$, the plane-averaged Kolmogorov length scale.

Figure 4.12a reveals approximately one decade of power-law scaling. Including density in the autocorrelation through the $\boldsymbol{j}$ dynamic variable has only a small effect on the spectra and does not alter their power-law scaling. The two sets of spectra are similar, as also reported by Kida and Orszag (1992) in their investigation of smaller density variations, *i.e.*, $\rho'/\overline{\rho} \leq 0.18$, in simulations of compressible turbulence. The close match between kinetic energy and specific kinetic energy spectra is not attributable to statistical independence between the density and velocity fields. As evident from the flow geometry, this is not expected.

Figure 4.12b displays non-dimensionalized vorticity spectra, $S_{\boldsymbol{\omega}'\cdot\boldsymbol{\omega}'}$ (solid lines), and non-dimensionalized specific vorticity spectra, $S_{(\boldsymbol{\omega}/\rho)'\cdot(\boldsymbol{\omega}/\rho)'}$ (dashed lines). As with kinetic energy, including density in the vorticity spectra has a small effect, albeit a slightly larger effect than for kinetic energy.

The specific vorticity, $\boldsymbol{\omega}/\rho$, transport equation can be derived from the curl of the non-conservative form of the momentum equation, *i.e.*, the curl of

$$\frac{\partial \boldsymbol{u}}{\partial t} + (\boldsymbol{u}\cdot\nabla)\,\boldsymbol{u} \;=\; -\frac{1}{\rho}\,(\boldsymbol{\Gamma} + \nabla p) - \widehat{\boldsymbol{z}}\,g + \frac{1}{\rho}\nabla\cdot\boldsymbol{\tau}\,. \tag{4.21}$$

$\boldsymbol{\Gamma} \cong \widehat{\boldsymbol{z}}\,\rho_0 g$, as discussed in section 3.2, with $\boldsymbol{\Gamma}/\rho \cong \widehat{\boldsymbol{z}}\,(\rho_0/\rho)\,g$, a function of $\boldsymbol{x}$, which remains after the curl is taken. However, the body force term, $-\widehat{\boldsymbol{z}}\,\rho g$ when

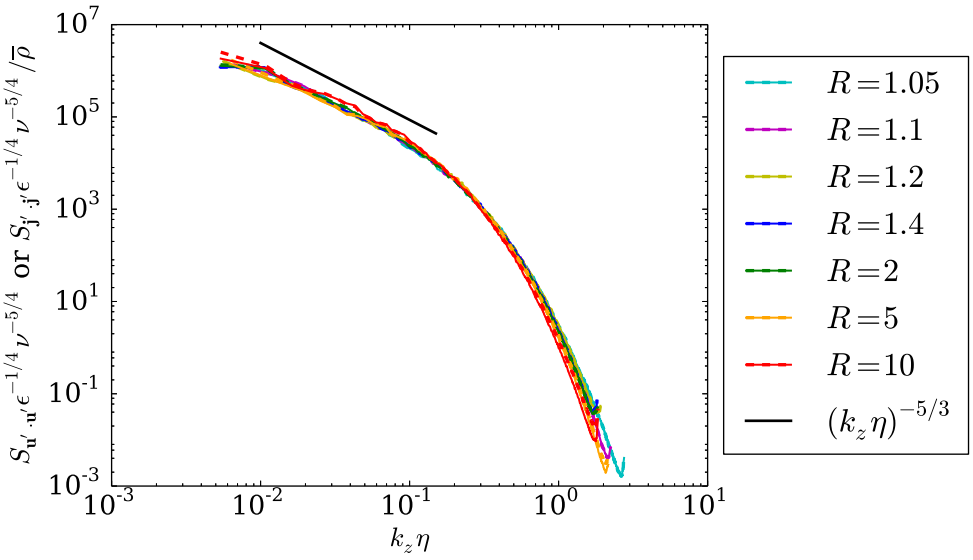

(a)

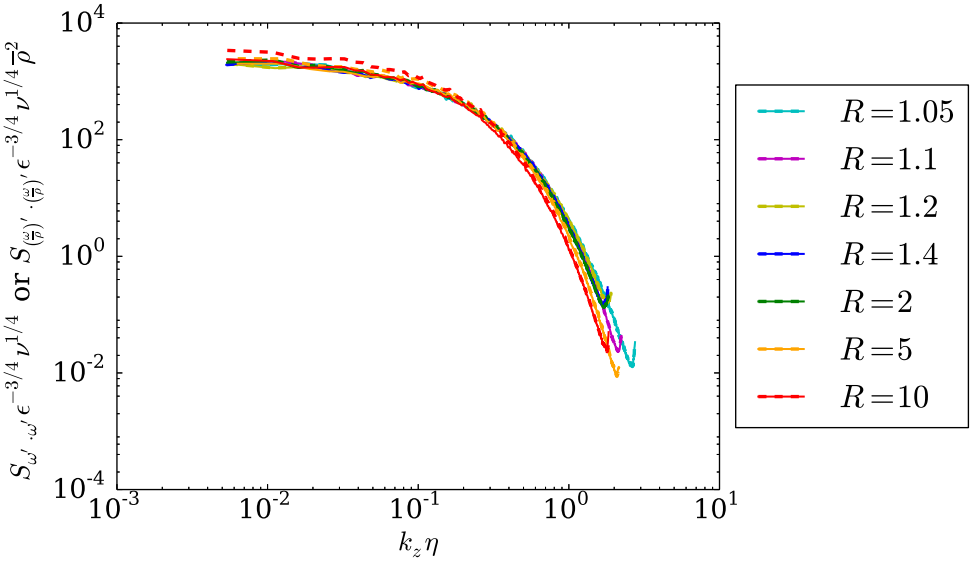

(b)

Figure 4.12: Spectra for seven density ratios at times corresponding to $Re_\delta \approx 8500$. Spectra for $R = 10$ are displayed at $Re_\delta \approx 7700$. (*a*) Specific kinetic energy (solid lines) and kinetic energy (dashed lines) spectra, (*b*) Vorticity (solid lines) and specific vorticity (dashed lines) spectra.

divided by density, is uniform and does not appear in the vorticity equation. Taking the curl of equation 4.21 yields

$$\frac{\partial \boldsymbol{\omega}}{\partial t} + (\boldsymbol{u} \cdot \nabla)\,\boldsymbol{\omega} \;=\; \boldsymbol{\omega} \cdot \boldsymbol{s} \;-\boldsymbol{\omega}\,(\nabla \;\cdot\; \boldsymbol{u}) - \nabla\left(\frac{1}{\rho}\right) \times (\boldsymbol{\Gamma} + \nabla p) + \nabla \times \left(\frac{1}{\rho} \nabla \;\cdot\; \boldsymbol{\tau}\right) . \quad (4.22)$$

Multiplying the above equation by $1/\rho$, and using conservation of mass (equation 3.1a) yields

$$\frac{\mathrm{D}}{\mathrm{D}t}\left(\frac{\boldsymbol{\omega}}{\rho}\right) \;=\; \left(\frac{\boldsymbol{\omega}}{\rho}\right) \cdot \boldsymbol{s} \;+\; \frac{1}{\rho}\left[-\nabla\left(\frac{1}{\rho}\right) \times (\boldsymbol{\Gamma} + \nabla p) + \nabla \times \left(\frac{1}{\rho} \nabla \;\cdot\; \boldsymbol{\tau}\right)\right], \quad (4.23)$$

where $\boldsymbol{s} = \left(\nabla \boldsymbol{u} + \nabla \boldsymbol{u}^{\mathrm{T}}\right)/2$ is the local strain rate tensor, $\boldsymbol{\tau}$ is the viscous stress tensor, and $-\nabla\left(\frac{1}{\rho}\right) \times (\boldsymbol{\Gamma} + \nabla p)$ is the baroclinic torque. In this formulation, no dilatation term appears and density enters through its reciprocal, motivating the investigation of specific vorticity in figure 4.12b.

The mean pressure gradient, $\boldsymbol{\Gamma}$, remains in the baroclinic torque term, and represents the hydrostatic pressure gradient component. In the limit of the Boussinesq approximation, only the hydrostatic component of the pressure gradient contributes to the baroclinic torque. With the above formulation, baroclinic torques limits to the Boussinesq approximation as $R \to 1$.

To explore the spectral dependence on Reynolds number, figure 4.13 displays one-dimensional kinetic energy spectra for $R = 1.4$ at various Reynolds numbers. These are compensated (multiplied by $(k_z \ell)^{5/3-q}$, with $q = 0.3$) and exhibit very small slopes over about a decade, with slopes slightly decreasing with increasing Reynolds number, terminating with the viscous attenuation at small scales, *i.e.*, progressively higher wavenumbers. The value $q = 0.3$ was set to achieve nearly horizontal lines for the larger Reynolds numbers and is consistent with findings by Mydlarski and Warhaft (1996), who show that $q \to 0$ as $Re \to \infty$. Figure 4.13 demonstrates the larger-scale wavenumber separation with increasing Reynolds number, as expected.

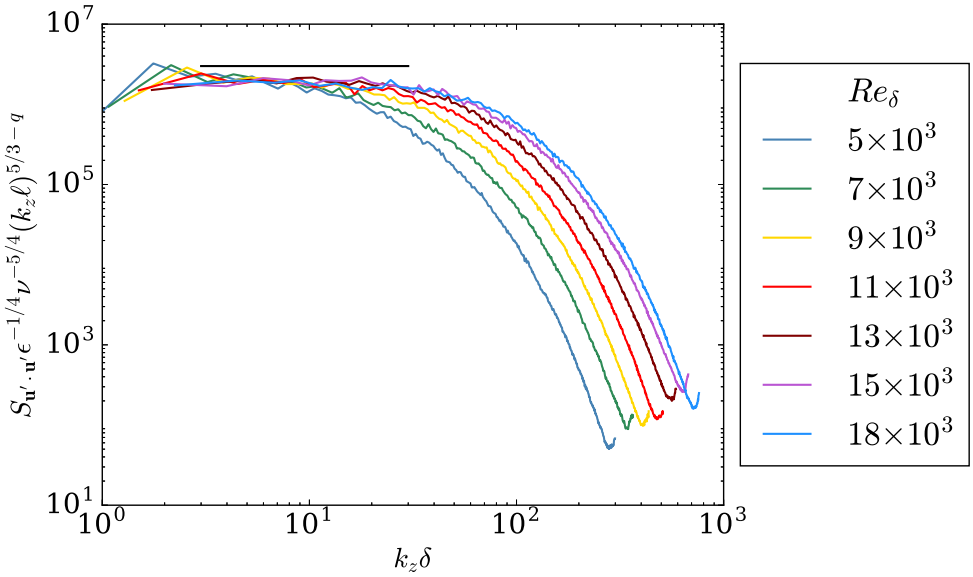

Figure 4.13: One-dimensional compensated spectra in z for flow for a single density ratio, $R = 1.4$, at various Reynolds numbers. Note the different x axis, which is scaled by the (outer-scale) shear-layer width, $\delta(t)$, as opposed to the inner-scale of η in figure 4.12. Spectra are multiplied by $(k_z\ell)^{5/3-q}$, where $\ell = L/2$ half the computational domain width, and $q = 0.3$. The black horizontal line is for reference.

Chapter 5

VECTOR ORIENTATIONS RELATED TO TURBULENCE MODELING

When direct numerical simulation (DNS) is not feasible, *i.e.*, the range of scales to resolve is too large, large-eddy simulation (LES) can be used. LES is a type of turbulence modeling where large scales are resolved, with scales below a cutoff wavelength unresolved and modeled. The smaller scales contain a small fraction of the turbulent kinetic energy and can be more amenable to modeling (Tennekes and Lumley, 1972; Pope, 2004). Additionally, the uniqueness of bulk-flow properties versus the less unique mixed-fluid characteristics, seen in chapter 4, confirms the premise that small scales are not as flow specific as large-scale quantities.

The LES equations are obtained by filtering the governing equations (3.1) using a density weighted filter (Favre filtering) with a filtered field, $\tilde{f}$

$$\widetilde{f} = \frac{\overline{\rho f}}{\overline{\rho}}, \tag{5.1}$$

where here the $\overline{()}$ indicates a filtering

$$\overline{f} \equiv \int G(\boldsymbol{x} - \boldsymbol{x}') f(\boldsymbol{x}') \, \mathrm{d}\boldsymbol{x}' \tag{5.2}$$

with a filter function $G(\boldsymbol{x})$ (Leonard, 1975). This form of variable-density filtering for LES was first proposed for compressible turbulence by Speziale et al. (1988) and tested by Zang, R. B. Dahlburg, and J. P. Dahlburg (1992), and can be used for the incompressible variable-density flow studied.

The filtered conservation of mass, momentum, and species transport for a binary mixture are obtained by filtering equations 3.1 using equation 5.2, and applying the Favre filter definition (equation 5.1). All fields that are not separable with this filtering method, such as the convection term $\overline{\rho}\widetilde{\boldsymbol{u}}\widetilde{\boldsymbol{u}}$, are separated with the closure terms representing the differences, with

$$\frac{\partial \overline{\rho}}{\partial t} + \nabla \cdot (\overline{\rho}\,\widetilde{\boldsymbol{u}}) = 0, \tag{5.3a}$$

$$\frac{\partial \overline{\rho}\,\widetilde{\boldsymbol{u}}}{\partial t} + \nabla \cdot (\overline{\rho}\,\widetilde{\boldsymbol{u}}\,\widetilde{\boldsymbol{u}}) = -(\boldsymbol{\Gamma} + \nabla \overline{p}) - \widehat{\boldsymbol{z}}\,\overline{\rho} g + \nabla \cdot \widetilde{\boldsymbol{\tau}} - \nabla \cdot \boldsymbol{T}, \tag{5.3b}$$

$$\frac{\partial \overline{\rho}\,\widetilde{Y}}{\partial t} + \nabla \cdot \left(\overline{\rho}\,\widetilde{Y}\,\widetilde{\boldsymbol{u}}\right) = \nabla \cdot \left(\overline{\rho}\widetilde{\mathcal{D}} \nabla \widetilde{Y}\right) - \nabla \cdot \boldsymbol{c}\,. \tag{5.3c}$$

In this description, $\overline{\rho}$ is the filtered density (equation 5.2), as opposed to the mean density within the shear layer, and $\boldsymbol{\tau}$ is the viscous stress tensor (equation 3.1d). $\boldsymbol{\Gamma}$ is uniform in space, *i.e.*, $\overline{\boldsymbol{\Gamma}} = \boldsymbol{\Gamma}$. $\widetilde{\mathcal{D}}$ is the filtered species diffusivity, which for unity Schmidt number $\widetilde{\mathcal{D}} = \overline{\mu}/\overline{\rho}$, where viscosity is denoted as a resolved-scale quantity since it could be variable at the subgrid scale (SGS). The subgrid closure terms for the stress tensor, $\boldsymbol{T}$, and scalar transport flux, $\boldsymbol{c}$, are

$$\boldsymbol{T} = \overline{\rho}\left(\widetilde{\boldsymbol{u}\boldsymbol{u}} - \widetilde{\boldsymbol{u}}\,\widetilde{\boldsymbol{u}}\right) - \left(\overline{\boldsymbol{\tau}} - \widetilde{\boldsymbol{\tau}}\right) \tag{5.3d}$$

$$\boldsymbol{c} = \overline{\rho}\left(\widetilde{Y\boldsymbol{u}} - \widetilde{Y}\,\widetilde{\boldsymbol{u}}\right) - \overline{\rho}\left(\widetilde{\mathcal{D}\nabla Y} - \widetilde{\mathcal{D}}\nabla\widetilde{Y}\right) \tag{5.3e}$$

with (Chung, 2009)

$$\frac{1}{\overline{\rho}(\boldsymbol{x},t)} = \frac{1}{\rho_2} - \widetilde{Y}(\boldsymbol{x},t)\left(\frac{1}{\rho_2} - \frac{1}{\rho_1}\right), \tag{5.3f}$$

where, again, the energy equation is decoupled for this uniform temperature incompressible flow, with variable-density effects only from species mixing, as opposed to Mach number variable-density effects in compressible flow. We note that these equations are exact, under the assumptions of a DNS (*i.e.*, infinite-temperature, infinite-pressure incompressible flow).

Using equation 5.3f in 5.3c with 5.3a yields the filtered density evolution equation for unity Schmidt number

$$\frac{\partial\overline{\rho}}{\partial t} + \widetilde{\boldsymbol{u}}\cdot\nabla\overline{\rho} = \overline{\rho}\,\nabla\cdot\left(\frac{\overline{\mu}}{\overline{\rho}^2}\nabla\overline{\rho}\right) + \frac{\overline{\rho}}{\rho_r}\,\nabla\cdot\boldsymbol{c}\,, \tag{5.3g}$$

where

$$\rho_r = \frac{1}{\dfrac{1}{\rho_1} - \dfrac{1}{\rho_2}}\,. \tag{5.3h}$$

The above variable-density filtering method, although providing a closed mass conservation equation (*i.e.*, no mass conservation terms need to be modeled), results in a density correlated velocity field, $\overline{\rho\boldsymbol{u}}/\overline{\rho}$, which cannot be mapped to a filtered velocity field $\overline{\boldsymbol{u}}$ in variable-density flow. Sidharth, Kartha, and Candler (2016) investigated using only the filter function in equation 5.2, *i.e.*, not the density weighted Favre filter (equation 5.1), however, this increases the number of unclosed terms to be modeled, and introduces triple correlations of fields to be solved. In the discussion below, Favre-filtered fields are used, noting that $\widetilde{\boldsymbol{u}} \neq \overline{\boldsymbol{u}}$ unless $R = 1$, for this incompressible flow.

Modeling $\boldsymbol{T}$ and $\boldsymbol{c}$ can change flow predictions by adding or dissipating small-scale energy. Small-scale dissipation is seen from the filtered kinetic energy equation, $\widetilde{K} = \overline{\rho}\,|\widetilde{\boldsymbol{u}}|^2/2$, which is obtained by dotting $\widetilde{\boldsymbol{u}}$ with equation 5.3b,

$$\begin{aligned}\frac{\partial \widetilde{K}}{\partial t} + \nabla \cdot \left(\widetilde{K}\,\widetilde{\boldsymbol{u}}\right) \;=\; & -\,\boldsymbol{\Gamma}\cdot\widetilde{\boldsymbol{u}} - \nabla\cdot(\overline{p}\,\widetilde{\boldsymbol{u}}) + \overline{p}\,\nabla\cdot\widetilde{\boldsymbol{u}} - \widehat{\boldsymbol{z}}\cdot\widetilde{\boldsymbol{u}}\,\overline{\rho}g \\ & + \nabla\cdot(\widetilde{\boldsymbol{\tau}}\cdot\widetilde{\boldsymbol{u}} - \boldsymbol{T}\cdot\widetilde{\boldsymbol{u}}) - \widetilde{\boldsymbol{\tau}} : \nabla\widetilde{\boldsymbol{u}} + \boldsymbol{T} : \nabla\widetilde{\boldsymbol{u}}\,,\end{aligned} \tag{5.4}$$

where ":" implies the double dot product. SGS kinetic energy enters through $\boldsymbol{T} : \nabla\widetilde{\boldsymbol{u}}$, which can be written as $\boldsymbol{T} : \widetilde{\boldsymbol{s}}$, where $\boldsymbol{s}$ is the strain rate tensor with eigenvalues, s_i, ordered as $s_1 > s_2 > s_3$ in the discussion below.

$\boldsymbol{T} : \widetilde{\boldsymbol{s}}$ measures the time rate of change of kinetic energy from the SGS. A positive value results in kinetic energy being added from the SGS to the resolved scales, a process called backscatter, and a negative value represents SGS kinetic energy dissipation. Backscatter exists in turbulent flows (*e.g.*, Piomelli et al., 1991; Meneveau and Katz, 2000; Pope, 2004); however *a priori* studies of isotropic turbulence have shown that in the mean, the kinetic energy is transfered to the SGS from the resolved scales (*e.g.*, Domaradzki, Liu, and Brachet, 1993). Many SGS models thus limit backscatter and ensure energy transfers only from the large to small scales, in an effort to provide the correct mean dissipation (Meneveau and Katz, 2000). In this manner, the Smagorinsky model (Smagorinsky, 1963; Moin, Squires, et al., 1991; Germano et al., 1991) assumes that

$$\boldsymbol{T} : \widetilde{\boldsymbol{s}} \;=\; -\,2\,\overline{\rho}\,\nu_T\,\widetilde{\boldsymbol{s}} : \widetilde{\boldsymbol{s}}, \tag{5.5}$$

where ν_T is an eddy viscosity calculated from the strain rate tensor and other parameters either set based on the flow, or calculated dynamically. With the Smagorinsky model, $\boldsymbol{T} : \widetilde{\boldsymbol{s}} < 0$, and flow is modeled with no backscatter.

The Stretched-Vortex Model (SVM, Pullin and Saffman, 1994; Misra and Pullin, 1997; Voelkl, Pullin, and Chan, 2000; Kosović, Pullin, and Samtaney, 2002) postulates that a distribution of vortex tubes exists at the subgrid scale. An ensemble average of the distribution, which is modeled by delta functions, is used to compute the SGS stress tensor

$$\boldsymbol{T} \;=\; \overline{\rho}\,K\,(\mathbf{I} - \boldsymbol{e}^v\boldsymbol{e}^v)\,, \tag{5.6}$$

where here $\overline{\rho}$ is the resolved-scale density, K is the SGS kinetic energy and $\boldsymbol{e}^v$ is the unit vector in the direction of the SGS ensemble average of vortex tubes (denoted with the superscript v), termed the vortex tube alignment. Note $\boldsymbol{e}^v$ enters only as an

outer product with itself; the same result is obtained if $\boldsymbol{e}^v \rightarrow -\boldsymbol{e}^v$. The ± unknown in solving for the direction of $\boldsymbol{e}^v$ (discussed in section 5.1) does not affect the model.

Using equation 5.6 to model the SGS contribution to the kinetic energy rate of change, $\boldsymbol{T} : \widetilde{\boldsymbol{s}}$,

$$\boldsymbol{T} : \widetilde{\boldsymbol{s}} = \overline{\rho} K \left(\mathbf{I} - \boldsymbol{e}_s^v \boldsymbol{e}_s^v \right) : \widetilde{\boldsymbol{\Lambda}}, \tag{5.7}$$

where $\boldsymbol{e}_s^v$ is the vortex tube alignment in the strain rate field eigenvector frame, *i.e.*, $\boldsymbol{e}_s^v$ is $\boldsymbol{e}^v$ rotated by the strain rate tensor eigenvectors, and $\widetilde{\boldsymbol{\Lambda}}$ only has diagonal components of $(\widetilde{s}_1, \widetilde{s}_2, \widetilde{s}_3)$, the eigenvalues of the resolved strain rate tensor, $\widetilde{\boldsymbol{s}}$. The alignment of $\boldsymbol{e}_s^v$ was studied extensively (Misra and Pullin, 1997), and was found to have little effect in homogeneous isotropic turbulence (Kosović, Pullin, and Samtaney, 2002). Many authors choose $\boldsymbol{e}_s^v$ to align with $\widehat{\widetilde{\boldsymbol{s}}}_1$, the most extensional eigenvector of the resolved strain rate tensor, as that is the simplest model (Voelkl, Pullin, and Chan, 2000), which ensures no backscatter for incompressible single-fluid flow. Assuming single-fluid incompressible flow, *i.e.*, $\widetilde{s}_1 + \widetilde{s}_2 + \widetilde{s}_3 = 0$, and using the alignment of $\boldsymbol{e}_s^v \parallel \widehat{\widetilde{\boldsymbol{s}}}_1$,

$$\boldsymbol{T} : \widetilde{\boldsymbol{s}} = -\overline{\rho} K \widetilde{s}_1 < 0 \tag{5.8}$$

ensuring no backscatter, as discussed by Professor Dale Pullin in private communications. In a variable-density flow, $\widetilde{s}_1 + \widetilde{s}_2 + \widetilde{s}_3 \neq 0$, and while still assuming $\boldsymbol{e}_s^v \parallel \widehat{\widetilde{\boldsymbol{s}}}_1$,

$$\boldsymbol{T} : \widetilde{\boldsymbol{s}} = \overline{\rho} K (\widetilde{s}_2 + \widetilde{s}_3), \tag{5.9}$$

which cannot be related exactly to $\widetilde{s}_1$, as it can in divergence-free flow. Even though $\widetilde{s}_3 < 0$, depending on the relative magnitudes of $|s_3|$ and $|s_2|$, there could be locations with $\boldsymbol{T} : \widetilde{\boldsymbol{s}} > 0$, introducing backscatter.

Effects of subgrid-scale vorticity alignment assumptions are investigated by considering the total vorticity field, resolved and unresolved, with the specific vorticity depicted in figure 5.1. As illustrated, this variable-density flow exhibits worm-like structures in the turbulent regime also reported previously in uniform-density flows (*e.g.*, Siggia, 1981; Kerr, 1985; She, Jackson, and Orszag, 1990; Jiménez et al., 1993; Sreenivasan and Antonia, 1997; Moin and Mahesh, 1998; Pullin and Saffman, 1998, and references therein), with seemingly random orientations. However, this flow does not evolve to a statistically isotropic vorticity field. To study the orientations of vorticity (and other vector) fields, figures of three-dimensional magnitude density functions, $\mathcal{R}$, of locations in the flow where the local fluid is mixed within the compositional bounds of equation 4.1 are used, where $\mathcal{R}$ represents magnitudes

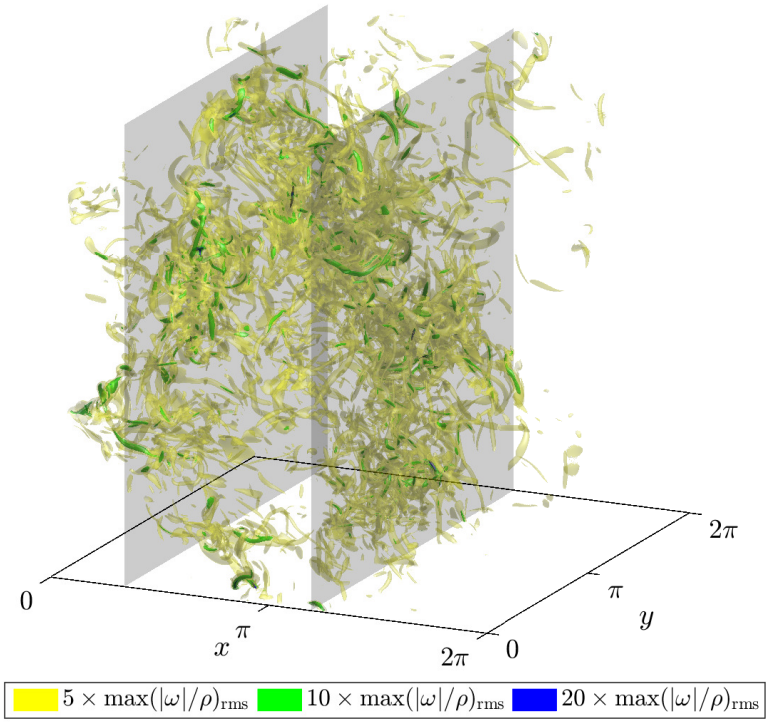

Figure 5.1: Non-dimensional specific vorticity magnitude, $(\overline{\rho}\,\delta/\Delta W)\,|\boldsymbol{\omega}|\,/\rho$, surfaces in the top-left-front eighth of the domain for $R = 1.4$, in the turbulent regime at $t/\tau = 0.41$ and $Re_\delta \approx 15{,}000$. Colors depict surfaces of constant specific vorticity magnitude. Yellow displays the specific vorticity contour for 5 times the maximum root mean square (r.m.s.) value within the displayed domain, green displays the contour encompassing 10 times the r.m.s. maximum within the domain shown, and blue displays the surface at 20 times the r.m.s. maximum. Grey planes mark the mean shear-layer 1%-boundaries (equation 4.1).

multiplied by the joint three-dimensional p.d.f. Integrating $\mathcal{R}$ in three-dimensions yields the mean magnitude of the studied vector in the mixed-fluid region (as opposed to unity, which is obtained when integrating the three-dimensional p.d.f., not multiplied by magnitudes). A guide to read such plots is in section 5.1 below, with the p.d.f. calculation methodology described in appendix C. This chapter continues with the vorticity alignment analysis in section 5.2, followed by baroclinic torque alignments in section 5.3.

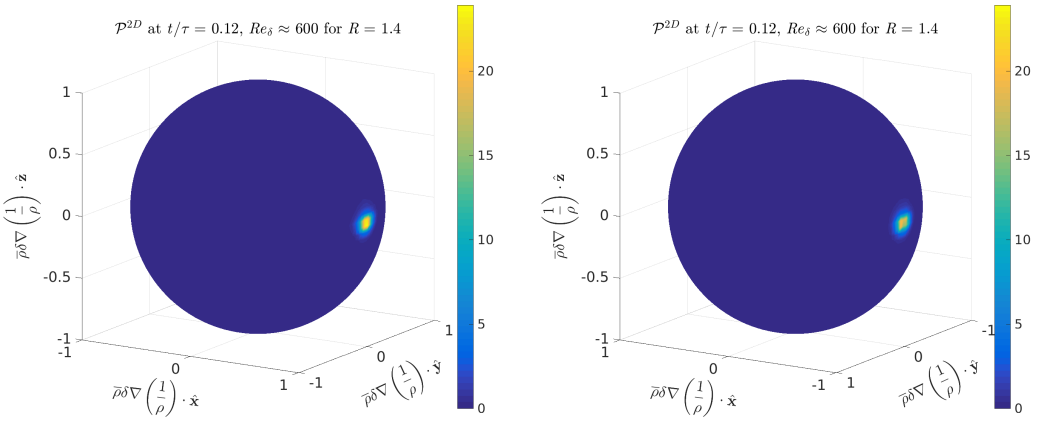

(a) (b)

Figure 5.2: $\mathcal{P}^{2D}$ of $\overline{\rho}\delta\nabla(1/\rho)$ of mixed fluid (equation 4.1) for $R = 1.4$ shown from two angles, to display gradients from both shear layers, at the beginning of the simulation. Note the (x, y)–axis directions in (a) versus (b), with the latter shown at a 180° rotation around $\widehat{\boldsymbol{z}}$ from the former, seen by the $\overline{\rho}\delta\nabla(1/\rho)\cdot\widehat{\boldsymbol{x}}$ direction ranging from $-1 \rightarrow 1$ in (a) versus (b), in which $\overline{\rho}\delta\nabla(1/\rho)\cdot\widehat{\boldsymbol{x}}$ ranges from $1 \rightarrow -1$ when read from left to right. The $\overline{\rho}\delta\nabla(1/\rho)\cdot\widehat{\boldsymbol{y}}$ axis also ranges from $-1 \rightarrow 1$ in (a) versus (b), in which $\overline{\rho}\delta\nabla(1/\rho)\cdot\widehat{\boldsymbol{y}}$ ranges from $1 \rightarrow -1$ when read from left to right.

5.1 Magnitude density function, $\mathcal{R}$

Consider the initial density field in figure 3.1 of two shear layers, a "left shear layer" centered at $x = L/4$, and a "right shear layer" centered at $x = 3L/4$.

$$\nabla\left(\frac{1}{\rho}\right)\begin{cases}\text{Left} & \parallel -\widehat{\boldsymbol{x}}\\ \text{Right} & \parallel +\widehat{\boldsymbol{x}}\end{cases} \tag{5.10}$$

The two-dimensional p.d.f. ($\mathcal{P}^{2D}$, equation C.2) of this field is shown in figure 5.2, which displays the same field from two views in order to show all data, since the left and right shear layers have specific volume gradients in opposite directions. $\nabla(1/\rho)$ has variance in its alignment with $\pm\widehat{\boldsymbol{x}}$ because of initial perturbations and diffusivity. For these statistics, only "mixed fluid" is considered, *i.e.*, fluid that obeys the criterion in equation 4.1. Specific volume gradients, $\nabla(1/\rho)$, shown are non-dimensionalized by $\overline{\rho}\delta$, the mean density within the shear layer multiplied by the shear layer width.

This same data as 5.2 can be viewed as the full three-dimensional p.d.f., $\mathcal{P}$, shown in figure 5.3.

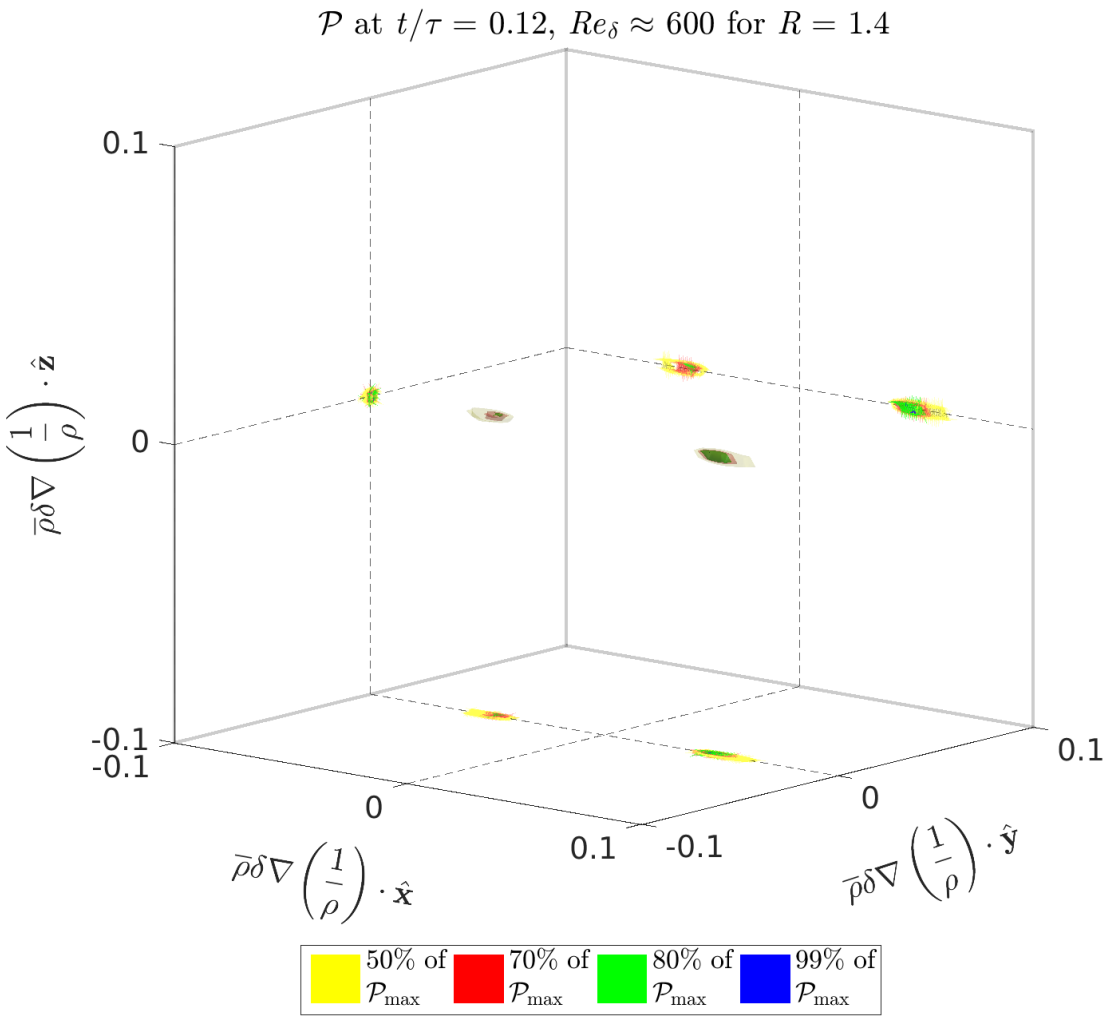

Figure 5.3: Non-dimensional specific volume gradient $\mathcal{P}$ isosurfaces of mixed fluid (equation 4.1) for $R = 1.4$ early in the simulation. Data compiled from simulations are in the plot center, with two-dimensional projections of that data on bounding surfaces. Plot displays that non-dimensional specific volume gradients align with $\pm\widehat{\boldsymbol{x}}$, with a most probable magnitude of approximately 0.05. The most probable vector is one starting from the origin, reaching out to colored isosurfaces in center, with a magnitude of 0.05 in $\pm\widehat{\boldsymbol{x}}$.

The three-dimensional surfaces in the center of figure 5.3 are isosurfaces of constant probability density, with their projections shown on the bounding planes. Yellow-colored surfaces mark the surface locus corresponding to 50% of the maximum probability density, $\mathcal{P}_{\max}$, *i.e.*, the volume enclosed by the yellow isosurface represents the portion of the vector space with a probability density in the interval between $0.5\,\mathcal{P}_{\max}$ and $\mathcal{P}_{\max}$. Red isosurfaces mark 70% of the maximum probability density value, *i.e.*, have a probability density value of a vector within the volume bounded by between $0.7\,\mathcal{P}_{\max}$ and $\mathcal{P}_{\max}$. The green surface encompasses 80% of the maximum probability density, between $0.8\,\mathcal{P}_{\max}$ and $\mathcal{P}_{\max}$, and the blue surface encloses the 99% boundary, *i.e.*, vector values whose p.d.f. value is between $0.99\,\mathcal{P}_{\max}$ and $\mathcal{P}_{\max}$.

Two-dimensional contours are projected on the bounding planes of figure 5.3 to display additional information in the same plot. Each planar contour outlines the projection of the same colored three-dimensional isosurface on that plane. Gray dashed lines reference origin projections, with gray solid lines marking plot boundaries for reference.

To summarize, figure 5.3 shows that the vector field $\overline{\rho}\delta\nabla\,(1/\rho)$ has a maximum probability of pointing with $\pm\widehat{\boldsymbol{x}}$, with a magnitude of roughly 0.05. The isosurfaces mark the magnitude and direction. The most probable vector would be one that starts from the origin (center of plot) and reaches out to the colored isosurfaces. Figure 5.3 displays, essentially, the contours from figure 5.2, expanded from the unit-sphere projection to display most-probable magnitude as well as direction.

Both shear layers are initialized similarly (with the same set of wavenumbers perturbed yet different random number fields). Turbulence is a random process, and all instances that occur in the left shear layer could occur in the right shear layer, if simulations were performed numerous times with varying random number perturbations. Statistics from the left shear layer should not be treated separately from the right, *i.e.*, the flow is essentially symmetric.

Data from left and right shear layers can be partitioned, shown in figure 5.4. The center of the largest horizontal extent of unmixed fluid is considered the boundary, which is found independently at each (y, z) location. At early times, figure 5.4a, the partitions are relatively straight lines at $x = 0, L$ and $x = L/2$. At later times, figure 5.4b, the lines jaggedly follow the mixing behavior. This method would not work once the two shear layers have met, and a different partitioning system would need to be constructed.

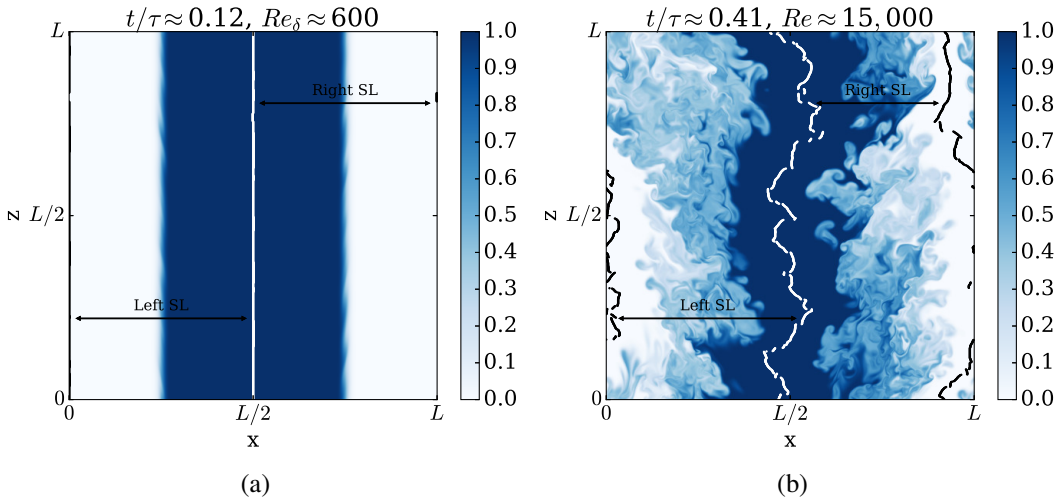

Figure 5.4: Two-dimensional slices of high-density fluid mole-fraction for $R = 1.4$. Vertical black and white lines denote partitions between fluid in the left versus right shear layers. Only mixed fluid within each partition is considered the shear layer. Early time behavior is shown in (*a*) versus late-time behavior (*b*).

Figure 5.5 displays the early-time specific volume gradient $\mathcal{P}$ for $R = 1.4$ with the right and left shear layers separated (figures 5.5a and 5.5b respectively). The two vector fields are fairly similar – essentially statistical mirror images of each other – with some statistical variation, as expected in a flow with slightly different randomized perturbations. They are also slightly different than those in figure 5.3 because of normalizations by themselves versus the combined $\mathcal{P}$. In light of the statistical similarity, rotating the left shear layer around $\widehat{\boldsymbol{z}}$ such that $\widehat{\boldsymbol{x}} \rightarrow -\widehat{\boldsymbol{x}}$ and $\widehat{\boldsymbol{y}} \rightarrow -\widehat{\boldsymbol{y}}$, for example, allows the two data sets to combine, shown in figure 5.6a. Statistics in the text below combine both shear layers since again, the two shear layers are representing the same dynamics and should not be treated differently.

Many vectors studied in this work have skewed p.d.f.s resulting in most-probable magnitudes differing from mean magnitudes of the vector fields. To display a more accurate depiction of the mean magnitude, $\mathcal{R}$ isosurfaces of the same data in figure 5.6a are displayed in figure 5.6b. $\mathcal{R}$ represents, essentially, a distribution of magnitudes, or magnitudes multiplied by the three-dimensional p.d.f. (equation C.4 in appendix C). Integration of $\mathcal{P}$ in three dimensions yields unity, whereas integration of $\mathcal{R}$ in three dimensions yields the mean magnitude of the vector. $\mathcal{R}$ is the quantity most commonly displayed throughout this work.

Many of the $\mathcal{R}$ plots in this work are in the local strain rate tensor, $\boldsymbol{s}$, eigenvector

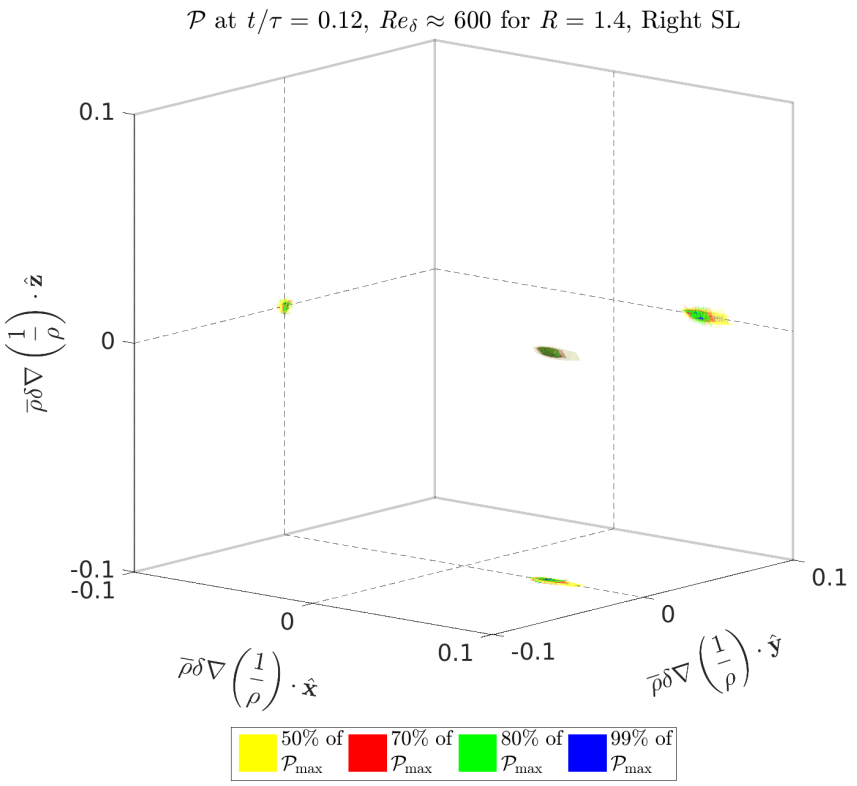

(a)

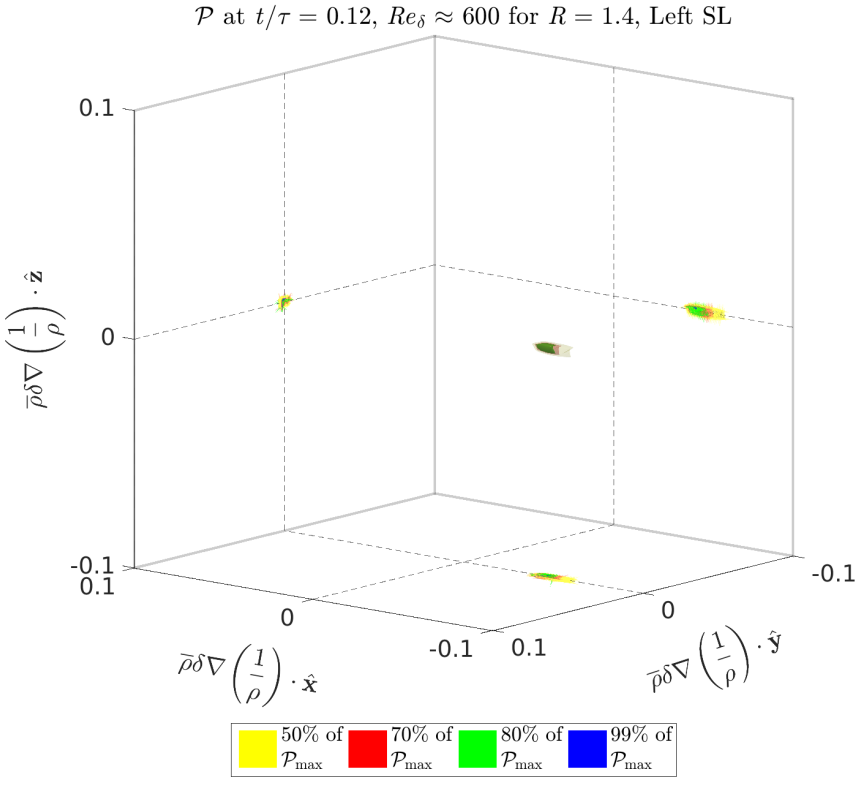

(b)

Figure 5.5: Non-dimensional specific volume gradient $\mathcal{P}$ isosurfaces of mixed fluid (equation 4.1) for $R = 1.4$ early in the simulation. (a) Data from the right shear layer versus (b) data from the left shear layer. Note the different (x, y)-axis directions in the two figures, with (b) shown at a 180° rotation around $\widehat{z}$ from (a).

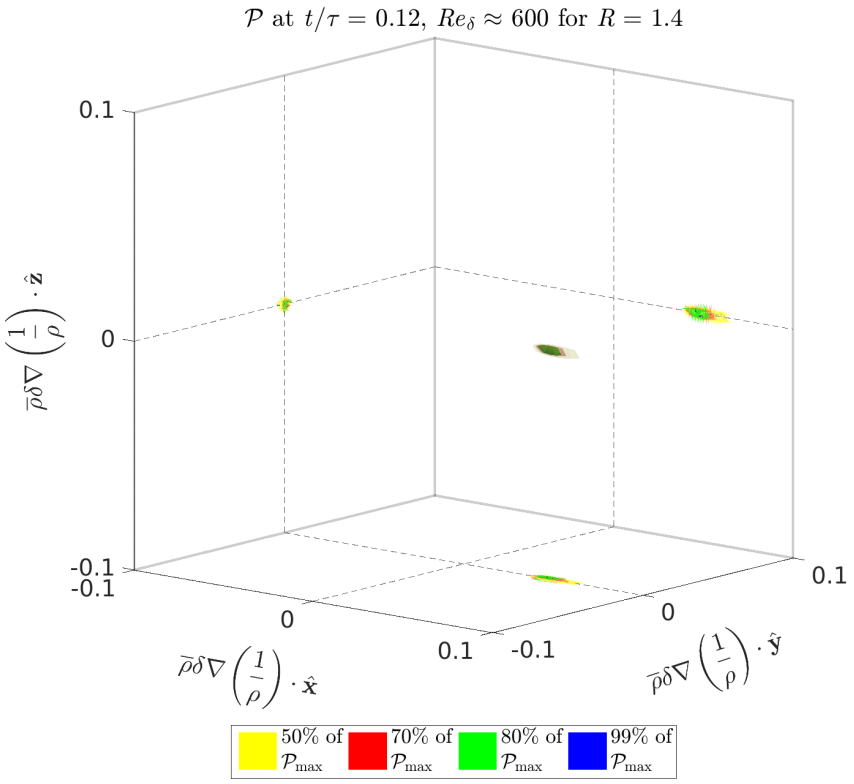

(a)

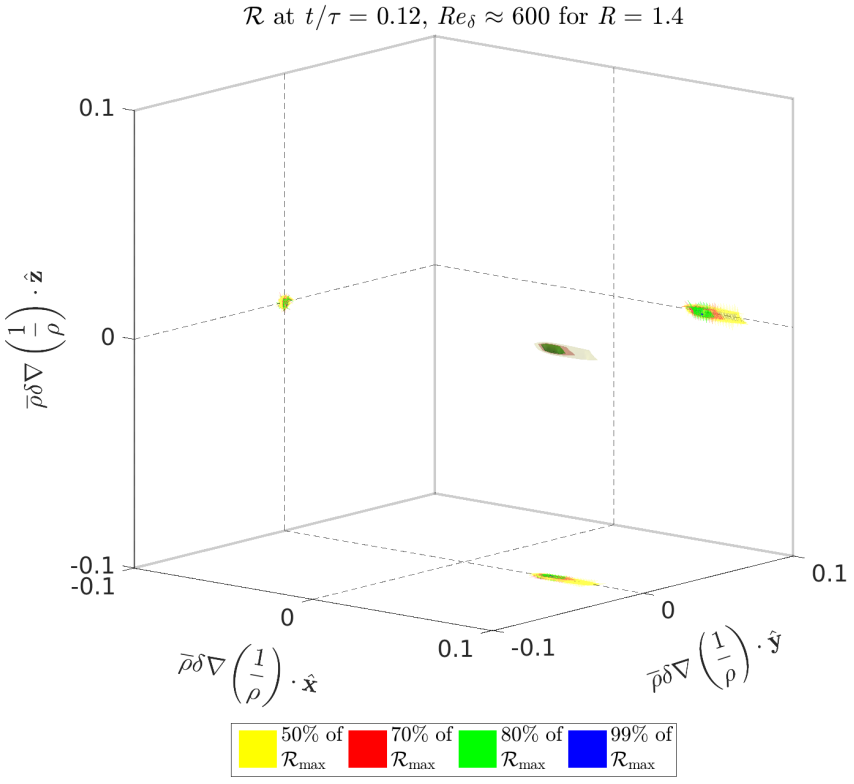

(b)

Figure 5.6: Non-dimensional specific volume gradient (*a*) $\mathcal{P}$ and (*b*) $\mathcal{R}$ isosurfaces of mixed fluid (equation 4.1) for $R = 1.4$ early in the simulation, with the left shear layer rotated such that data from both shear layers align.

basis. In terms of the specific volume gradient,

$$\overline{\rho}\delta\nabla\left(\frac{1}{\rho}\right) = \overline{\rho}\delta\left[\nabla\left(\frac{1}{\rho}\right)\cdot\widehat{\boldsymbol{s}}_1, \nabla\left(\frac{1}{\rho}\right)\cdot\widehat{\boldsymbol{s}}_2, \nabla\left(\frac{1}{\rho}\right)\cdot\widehat{\boldsymbol{s}}_3\right]. \tag{5.11}$$

The notation $s_1 > s_2 > s_3$ is used, where s_i are the eigenvalues of the local strain rate tensor, and $\widehat{\boldsymbol{s}}_i$ are the eigenvectors. Vectors are discussed in terms of $\boldsymbol{s} = \left(\nabla\boldsymbol{u} + \nabla\boldsymbol{u}^{\mathrm{T}}\right)/2$, and not the traceless strain rate tensor, $\boldsymbol{D} = \boldsymbol{s} - (\nabla\cdot\boldsymbol{u})\,\mathbf{I}/3$ since $\boldsymbol{s}$ is what enters naturally in the vorticity evolution equation (4.23). $\boldsymbol{D}$ and $\boldsymbol{s}$ have the same eigenvectors, with their eigenvalues differing by $-(\nabla\cdot\boldsymbol{u})\,\mathbf{I}/3$.

Strain rate tensor eigenvectors, $\widehat{\boldsymbol{s}}_i$, can only be defined within a ± sign. As such, they define a line space, but not necessarily a line direction (Ashurst, Kerstein, et al., 1987). To circumvent this ambiguity, some authors have chosen to discuss absolute values of vector dot products with $\widehat{\boldsymbol{s}}_i$ (*e.g.*, Ashurst, Kerstein, et al., 1987; Ashurst, Chen, and Rogers, 1987; Jiménez, 1992; Hamlington, Schumacher, and Dahm, 2008). In this work, we aim to understand vector field alignments with the three-dimensional Cartesian space, with the strain rate tensor eigenvector space, and with each other. However, the vector fields explored in this work have a more inherent alignment in strain rate tensor eigenvector coordinates than in Cartesian coordinates, especially in the turbulent regime. Alignments are thus shown with each other and the strain rate eigenvector frame together in one plot. To do this, the ± ambiguity of the strain rate tensor eigenvectors are exploited by choosing signs of $\widehat{\boldsymbol{s}}_i$ to show alignment of vectors with $\widehat{\boldsymbol{s}}_i$, but also with each other. This can be done since the strain rate tensor eigenvectors have an inherent alignment with the flow, which itself has an alignment in Cartesian space (in the mean), allowing the direction of the strain rate tensor eigenvectors to be chosen with respect to Cartesian space or, possibly with known vector directions themselves.

Strain rate tensor eigenvector alignments with a Cartesian frame have been seen previously, for example, in a turbulent atmospheric boundary layer by Higgins, Parlange, and Meneveau (2003), who show absolute values of dot products between the filtered strain rate tensor eigenvectors and the mean flow coordinate system (in Cartesian space) to illustrate the preferred directions. In this work, the preferred directions are exploited to choose signs of the strain rate tensor eigenvectors. This is done such that vectors, like vorticity, can be related to others, like baroclinic torques. For example, if baroclinic torques were aligned oppositely to vorticity, but only the absolute value in the strain rate frame was plotted, this information would be lost. If we were only relating vorticity to $\widehat{\boldsymbol{s}}_i$, for example, this exploitation would

not be needed, and the absolute value of the dot products would be sufficient. The full three-dimensional space is only used here to relate vectors with each other and also with $\widehat{\boldsymbol{s}}_i$.

Some authors have shown the dot product of vorticity with $\widehat{\boldsymbol{s}}_i$ (without the absolute value), however the plots are symmetric (*e.g.*, Vincent and Meneguzzi, 1991; Horiuti, 2003; Verma and Blanquart, 2014). In those cases, the same information could be conveyed more concisely with absolute values. As discussed below, the signs of $\widehat{\boldsymbol{s}}_i$ are chosen specifically, avoiding this issue. There are some symmetries, however the prominent direction of a vector with $\widehat{\boldsymbol{s}}_i$ is not symmetrical in this work, with positive and negative values representing positivity and negativity with respect to Cartesian coordinates, for example.

In short, the three-dimensional space octants in the strain rate tensor eigenvector frame are not independent, but all octants are shown to represent how flow quantities align with respect to each other. In this manner, a vector shown (in this work) to align with $-\widehat{\boldsymbol{s}}_2$, for example, could have been said to align with $+\widehat{\boldsymbol{s}}_2$, since $\widehat{\boldsymbol{s}}_2$ represents a line, not a direction, but the negative sign is the chosen direction here. The vector field would just be shown to align with $-\widehat{\boldsymbol{s}}_2$ for comparison purposes. However, in this work, a vector shown to align with $-\widehat{\boldsymbol{s}}_2$ compared to a vector shown to align with $+\widehat{\boldsymbol{s}}_2$ are in fact aligned oppositely, even in Cartesian space.

To decide the optimal sign for each $\widehat{\boldsymbol{s}}_i$ (while maintaining a right-handed coordinate frame), consider the initialized profile of heavy fluid moving downwards and light fluid upwards (figure 3.1). The strain rate tensor is approximately

$$\boldsymbol{s} \approx \begin{bmatrix} 0 & 0 & \pm a \\ 0 & 0 & 0 \\ \pm a & 0 & 0 \end{bmatrix}, \tag{5.12}$$

where $a = \left|\frac{\mathrm{d}W(x,t)}{\mathrm{d}x}\right|$ with $+a$ in the right shear layer, and $-a$ in the left. For both shear layers, the eigenvalues, $s_i = (a, 0, -a)$, with differing eigenvectors. For the left shear layer,

$$\widehat{\boldsymbol{s}}_{1,Left} = \begin{bmatrix} -\frac{1}{\sqrt{2}} \\ 0 \\ \frac{1}{\sqrt{2}} \end{bmatrix}, \quad \widehat{\boldsymbol{s}}_{2,Left} = \begin{bmatrix} 0 \\ -1 \\ 0 \end{bmatrix}, \quad \widehat{\boldsymbol{s}}_{3,Left} = \begin{bmatrix} \frac{1}{\sqrt{2}} \\ 0 \\ \frac{1}{\sqrt{2}} \end{bmatrix} \tag{5.13a}$$

and the right shear layer,

$$\widehat{\boldsymbol{s}}_{1,Right} = \begin{bmatrix} \frac{1}{\sqrt{2}} \\ 0 \\ \frac{1}{\sqrt{2}} \end{bmatrix}, \quad \widehat{\boldsymbol{s}}_{2,Right} = \begin{bmatrix} 0 \\ 1 \\ 0 \end{bmatrix}, \quad \widehat{\boldsymbol{s}}_{3,Right} = \begin{bmatrix} -\frac{1}{\sqrt{2}} \\ 0 \\ \frac{1}{\sqrt{2}} \end{bmatrix}. \tag{5.13b}$$

With the chosen ± signs above, noting both the left and right strain rate eigenvectors are in a right-handed coordinate frame, and using equations 5.10 and 5.13,

$$\begin{aligned} \nabla\left(\frac{1}{\rho}\right)_{Left} &= \left[\nabla\left(\frac{1}{\rho}\right)\cdot\widehat{\boldsymbol{s}}_{1,Left}, \nabla\left(\frac{1}{\rho}\right)\cdot\widehat{\boldsymbol{s}}_{2,Left}, \nabla\left(\frac{1}{\rho}\right)\cdot\widehat{\boldsymbol{s}}_{3,Left}\right] \\ &\rightarrow \nabla\left(\frac{1}{\rho}\right)_{Left} \parallel \frac{1}{\sqrt{2}}\left(\widehat{\boldsymbol{s}}_1 - \widehat{\boldsymbol{s}}_3\right) \end{aligned} \tag{5.14a}$$

$$\begin{aligned} \nabla\left(\frac{1}{\rho}\right)_{Right} &= \left[\nabla\left(\frac{1}{\rho}\right)\cdot\widehat{\boldsymbol{s}}_{1,Right}, \nabla\left(\frac{1}{\rho}\right)\cdot\widehat{\boldsymbol{s}}_{2,Right}, \nabla\left(\frac{1}{\rho}\right)\cdot\widehat{\boldsymbol{s}}_{3,Right}\right] \\ &\rightarrow \nabla\left(\frac{1}{\rho}\right)_{Right} \parallel \frac{1}{\sqrt{2}}\left(\widehat{\boldsymbol{s}}_1 - \widehat{\boldsymbol{s}}_3\right), \end{aligned} \tag{5.14b}$$

i.e., both shear-layer specific volume gradients align similarly in the strain rate frame allowing them to be combined, since again, the two shear layers should not be treated independently. In the strain rate tensor frame, no rotation is needed to collapse the two shear layers; they collapse naturally in the strain rate tensor eigenvector frame. Next, in terms of vorticity, the curl of equation 4.12 yields the initial vorticity field

$$\boldsymbol{\omega} = -\widehat{\boldsymbol{y}}\,\rho_0\, g\, t \frac{\mathrm{d}}{\mathrm{d}x}\left(\frac{1}{\rho}\right), \tag{5.14c}$$

i.e.,

$$\boldsymbol{\omega} \begin{cases} \text{Left} & \parallel +\widehat{\boldsymbol{y}} \\ \text{Right} & \parallel -\widehat{\boldsymbol{y}} \end{cases} \tag{5.14d}$$

prior to the left shear layer Cartesian rotation, or, in the strain rate frame,

$$\boldsymbol{\omega} \begin{cases} \text{Left} & \parallel -\widehat{\boldsymbol{s}}_2 \\ \text{Right} & \parallel -\widehat{\boldsymbol{s}}_2 \end{cases}. \tag{5.14e}$$

Lastly, the pressure gradient, $\boldsymbol{\Gamma} + \nabla p \parallel -\widehat{\boldsymbol{z}}$ initially, and with the chosen signs of the strain rate tensors,

$$\boldsymbol{\Gamma} + \nabla p \begin{cases} \text{Left} & \parallel -\dfrac{1}{\sqrt{2}}\left(\widehat{\boldsymbol{s}}_1 + \widehat{\boldsymbol{s}}_3\right) \\ \text{Right} & \parallel -\dfrac{1}{\sqrt{2}}\left(\widehat{\boldsymbol{s}}_1 + \widehat{\boldsymbol{s}}_3\right) \end{cases}. \tag{5.14f}$$

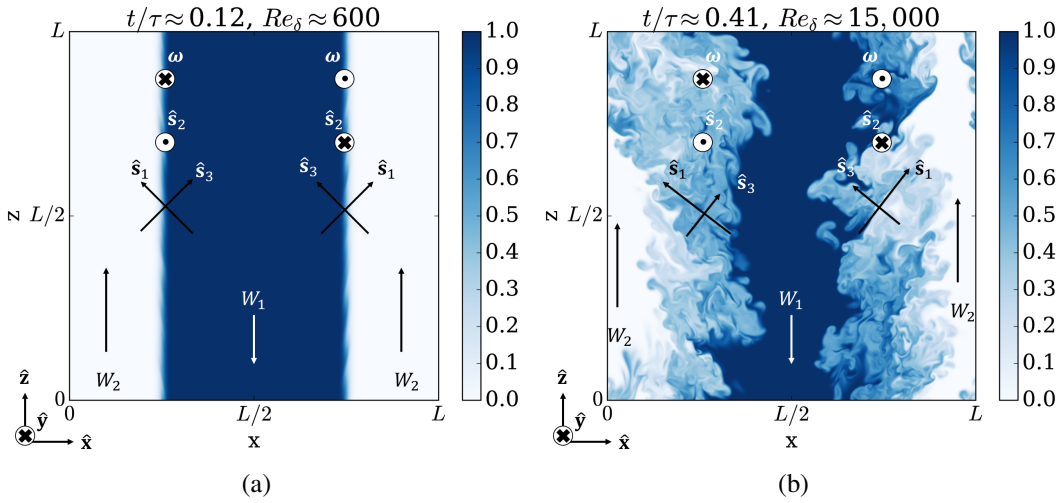

(a) (b)

Figure 5.7: Two-dimensional slices of high-density fluid mole-fraction for $R = 1.4$ (slices also shown in figure 5.4). Estimated depictions of the (mean) strain rate eigenvectors are shown, with the direction of two free streams also labeled, $W_{1,2}$. Vectors pointing into the page are labeled as a circle inscribed with an "x," with vectors pointing out of the page referenced as a circle inscribed with a dot. Early time behavior is shown in (a) versus late-time behavior (b).

With the above methodology, relevant directions for both shear layers align and the two are treated similarly, as discussed above. The ± sign choice of the eigenvectors is aided by the continual anisotropy of this flow, with a mean pressure gradient always aligning in $-\widehat{z}$, and a mean density gradient in $\pm\widehat{x}$, inducing a mean strain field. This allows additional information to be transmitted in these plots, such as vector field alignments with respect to the initial vorticity direction, which is set to be in $-\widehat{s}_2$, or with gravity. A depiction of these chosen signs referenced in the flow setup in shown in figure 5.7a, prior to the left shear layer being rotated in $\widehat{z}$. In the flow configuration with the chosen eigenvector signs, $\widehat{s}_1$ will point from the heavy to light fluid in an upwards fashion, with $\widehat{s}_3$ pointing from light to heavy, also in an upwards fashion (in $\widehat{z}$). The intermediate eigenvector, $\widehat{s}_2$ will have the opposite direction (approximately) as $\boldsymbol{\omega}$. Figure 5.7a helps illustrate that density gradients, for example, will be at approximately 45° to $\widehat{s}_1$ and $-\widehat{s}_3$, since those eigenvectors align approximately at 45° angles to the interface between the two free-stream fluids, as also calculated in equations 5.14a and 5.14b.

Figure 5.7b shows a similar diagram as figure 5.7a, but at much later times. At these later times, pointwise, $\widehat{s}_1$ and $\widehat{s}_3$ will no longer be as obviously aligned from heavy

to light fluid. However, there is still a mean strain and contraction that can be seen by the shear layer shape, and referenced by the $\widehat{s}_1$ and $\widehat{s}_3$ vectors drawn. This mean strain and contraction is felt pointwise in the shear layer, and although the strain rate tensor eigenvectors will no longer be as nicely aligned as they were initially, there are some late-time estimations that can be made, which are discussed below.

$\mathcal{P}$ and $\mathcal{R}$ of the specific volume gradient for $R = 1.4$ at early times in the strain rate eigenvector frame are shown in figure 5.8. Here, the isosurfaces spread over larger magnitudes than in the Cartesian frame. This is caused by the data being more concentrated in angles *i.e.*, $\mathcal{P}^{2D}_{\max}$ is larger in the strain rate frame than in Cartesian space, however $\mathcal{P}^{3D}_{\max}$ is smaller in the strain rate frame than in Cartesian space, *i.e.*, the data aligns more tightly with the strain rate frame than the Cartesian counterpart. Note also that figure 5.8 shows specific volume gradients aligning at 45° to $\widehat{s}_1$ and $-\widehat{s}_3$, exactly as expected from equations 5.14a and 5.14b.

The simplistic assumptions of equation 5.12 for the strain rate tensor do not hold for all times, as seen in figure 5.7b. As fluid entrained into the shear layer becomes turbulent, positive and negative density gradients can exist in both shear layers. As long as there is free-stream fluid on both sides of the shear layer, the maximum strain, $\widehat{s}_1$, will be a line stretching from the free-stream heavy to free-stream light fluid angled upwards in $\widehat{z}$, as the chosen sign, with some local variations. The maximum compression will be from the free-stream light to the free-stream heavy fluid, also in an upwards direction, with consistent signs as equations 5.13, with local variations. Additionally, the flow configuration imparts a vorticity that is inherently aligned (somewhat) with $-\widehat{s}_2$, with the minus sign as the chosen direction, and will not flip to be aligned with $+\widehat{s}_2$, although it may depart from perfect alignment. A similar note can be made in terms of $\boldsymbol{\omega}$ and $\widehat{y}$. To ensure consistent signs in $\widehat{s}_i$, first

$$\operatorname{sign}(\widehat{s}_2 \cdot \widehat{y}) = -\operatorname{sign}(\boldsymbol{\omega} \cdot \widehat{y}) \,. \tag{5.15}$$

which allows consistent alignment of $\boldsymbol{\omega}$ with $\widehat{s}_2$, prior to the left shear layer rotation in Cartesian coordinates. This fixes the sign of $\widehat{s}_2$. Next, if in the rotated Cartesian frame (*i.e.*, the left shear layer has $\widehat{x} \to -\widehat{x}$),

$$\widehat{s}_1 \cdot \widehat{x} < 0 \qquad \text{and} \qquad \widehat{s}_1 \cdot \widehat{z} < 0 \tag{5.16}$$

$$\implies \quad \widehat{s}_1 \to -\widehat{s}_1 \tag{5.17}$$

and $\widehat{s}_3$ is updated as needed to ensure a right-handed coordinate frame.

This methodology ensures $\boldsymbol{\omega} \cdot \widehat{s}_2 < 0$ and that $\boldsymbol{\Gamma} \cdot (\widehat{s}_1 + \widehat{s}_3) < 0$ which provides a consistent orientation for the data projected into the strain rate eigenvector frame.

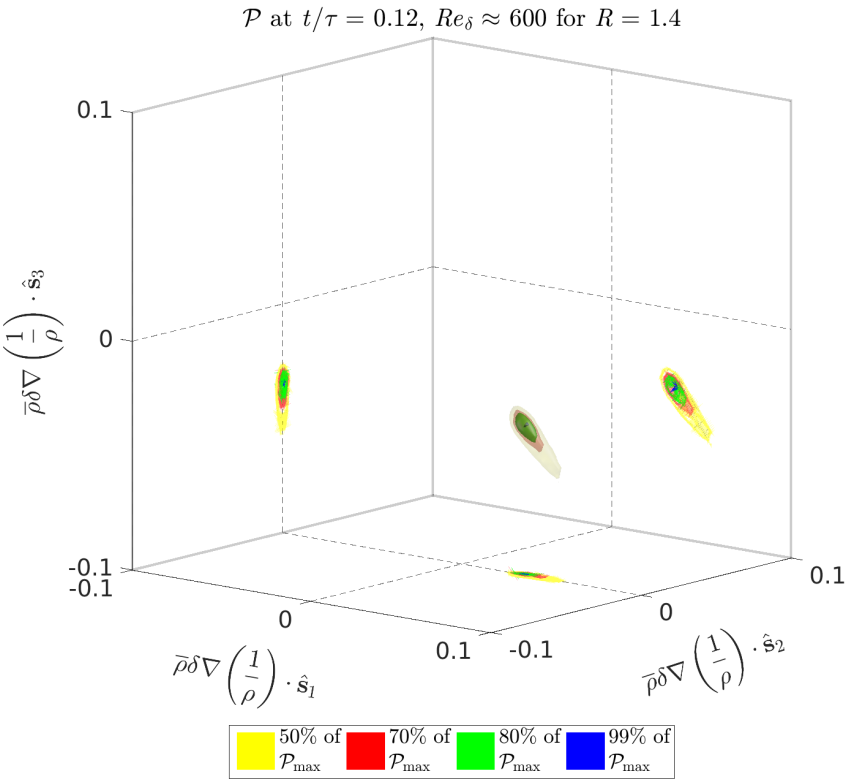

(a)

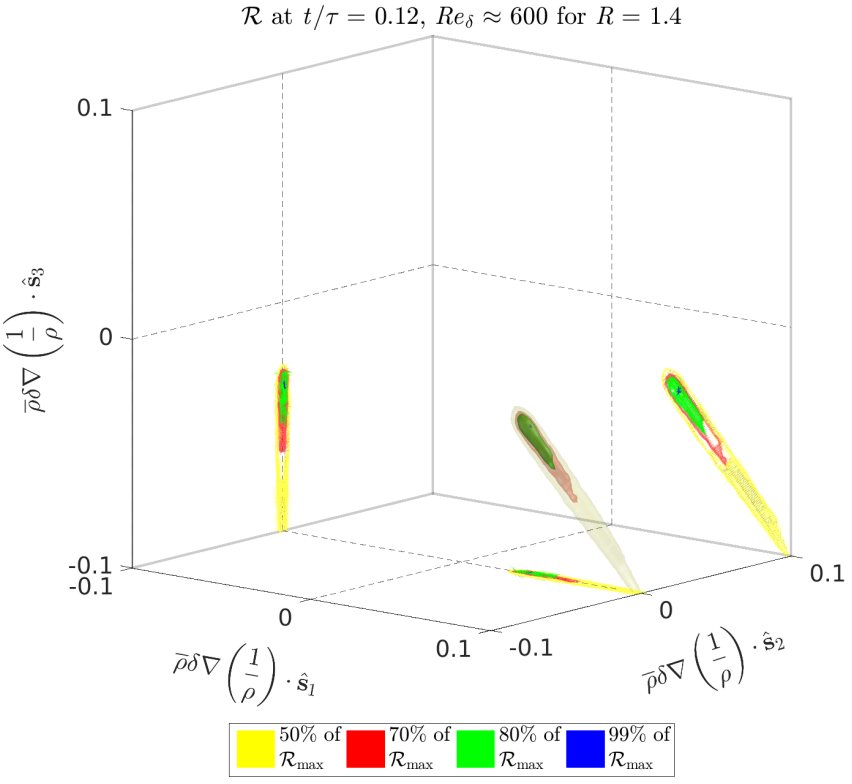

(b)

Figure 5.8: Non-dimensional specific volume gradient (*a*) $\mathcal{P}$ and (*b*) $\mathcal{R}$ isosurfaces of mixed fluid (equation 4.1) for $R = 1.4$ early in the simulation. Data shown is same data in figure 5.6, but in the local strain rate frame.

In short, the degeneracies of the strain rate tensor eigenvector directions are exploited with the strong anisotropy of the studied flow, to relate flow quantities in the ambiguous strain rate eigenvector frame. Note, however, that symmetries are seen, for example in $\pm\widehat{\boldsymbol{s}}_2$ in figure 5.8, because of the strain rate tensor eigenvector degeneracy, but there are no symmetries in the most prominent direction of $\nabla(1/\rho)$.

5.2 Vorticity alignment

Returning to the vorticity field alignment, figures 5.9 and 5.10 display $\mathcal{R}$ isosurfaces of the vorticity field and its evolution in Cartesian coordinates for $R = 1.4$ in the diffusive regime (figure 5.9) through the unsteady transition (figure 5.10). As the flow becomes unsteady, variations start to become anisotropic. Late-time vorticity $\mathcal{R}$ isosurfaces for $R = 1.4$ and $R = 10$ are shown in figures 5.11a and 5.11b respectively, further illustrating the strong anisotropy referenced above. Such anisotropy is common in flows with a driving force, *e.g.*, gravity (Cook and Dimotakis, 2001; Livescu and Ristorcelli, 2007, 2008). As apparent from figure 5.11, although $\boldsymbol{\omega} \cdot \widehat{\boldsymbol{y}} < 0$ generally, the alignments with $\widehat{\boldsymbol{x}}$ and $\widehat{\boldsymbol{z}}$ have significant variations, as opposed to the alignment in the initial diffusive regime, which is more tightly aligned with $-\widehat{\boldsymbol{y}}$ (figure 5.9). In the diffusive regime, $\boldsymbol{\omega}$ is simply the curl of equation 4.12, yielding an initial $\boldsymbol{\omega} \parallel -\widehat{\boldsymbol{y}}$ (equation 5.14c) in both shear layers with the rotated $(\widehat{\boldsymbol{x}}, \widehat{\boldsymbol{y}})$–plane discussed in section 5.1 above.

To investigate vorticity alignment with the strain rate tensor, note that, using the Biot-Savart relation, vorticity can be used to express the velocity gradient tensor (Jiménez, 1992)

$$\nabla \boldsymbol{u}(\boldsymbol{x}, t) = \frac{1}{4\pi} \nabla \int_{\boldsymbol{x}'} \boldsymbol{\omega}(\boldsymbol{x}', t) \times \frac{\boldsymbol{x} - \boldsymbol{x}'}{|\boldsymbol{x} - \boldsymbol{x}'|^3} \, \mathrm{d}^3\boldsymbol{x}' + \nabla (\nabla \phi) \,, \tag{5.18}$$

where $\nabla\phi$ represents the irrotational component. Integrating the first term in the right hand side of the above equation by parts and assuming that $\boldsymbol{\omega}(\boldsymbol{x} \to \pm\infty) \to 0$ yields

$$\nabla \boldsymbol{u}(\boldsymbol{x}, t) = -\frac{1}{4\pi} \int_{\boldsymbol{x}'} \frac{1}{|\boldsymbol{x} - \boldsymbol{x}'|^3} \left\{ (\boldsymbol{x} - \boldsymbol{x}') \times [\nabla \boldsymbol{\omega}(\boldsymbol{x}', t)] \right\} \mathrm{d}^3\boldsymbol{x}' + \nabla (\nabla \phi) \,, \tag{5.19}$$

where $\boldsymbol{x}$ can represent any orthogonal coordinate system. For now, the coordinate frame will be kept general, denoted by $\boldsymbol{x} = (x_1, x_2, x_3)$. Jiménez (1992) noted that if $\boldsymbol{\omega}(\boldsymbol{x}) = \omega_0(\boldsymbol{x})\widehat{\boldsymbol{x}}_2$, and $\partial\omega_0/\partial x_1 \approx \partial\omega_0/\partial x_3 \gg \partial\omega_0/\partial x_2$, with $\phi \neq \phi(\boldsymbol{x})$, then

$$\nabla \boldsymbol{u} = \begin{bmatrix} \checkmark & 0 & \checkmark \\ 0 & 0 & 0 \\ \checkmark & 0 & \checkmark \end{bmatrix}, \tag{5.20}$$

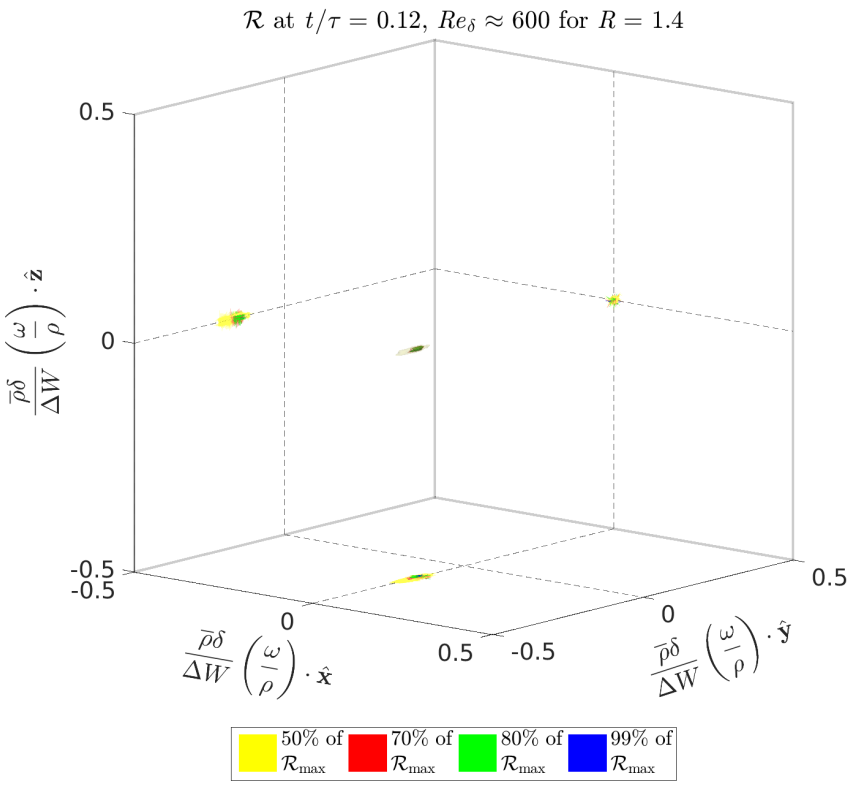

(a)

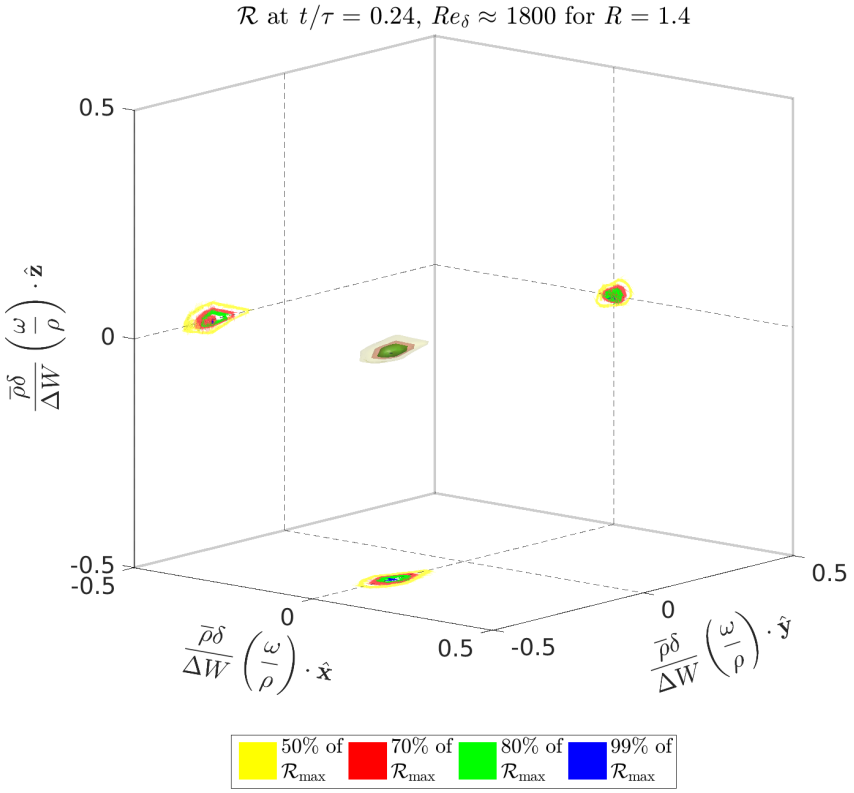

(b)

Figure 5.9: Non-dimensional specific vorticity $\mathcal{R}$ isosurfaces of mixed fluid (equation 4.1) in Cartesian coordinates for $R = 1.4$ at (*a*) $t/\tau = 0.12$ and (*b*) $t/\tau = 0.24$ *i.e.*, early in the flow development.

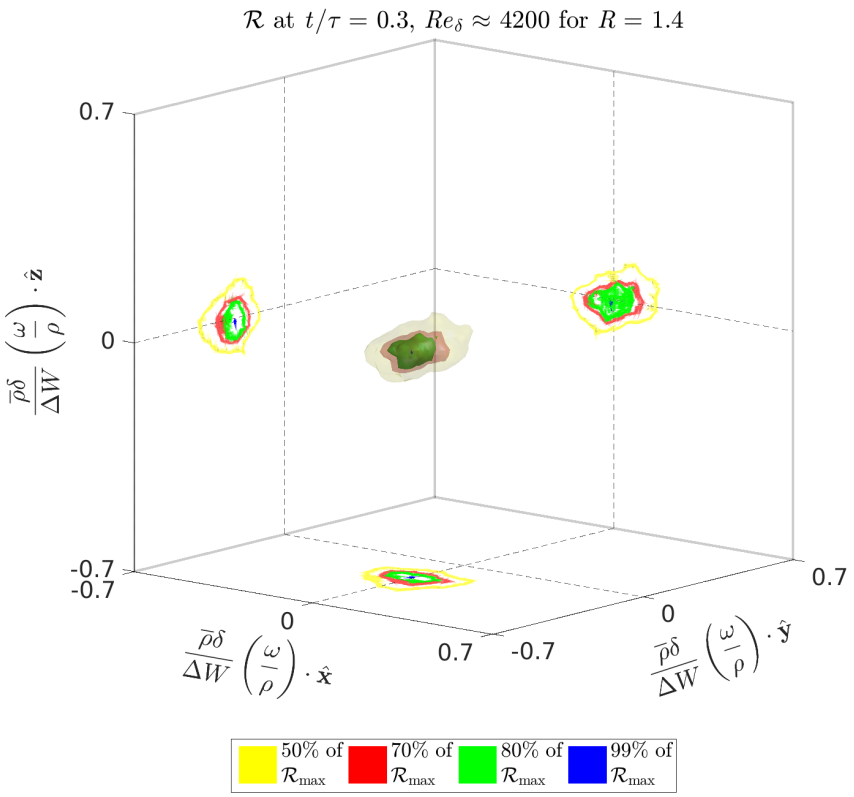

(a)

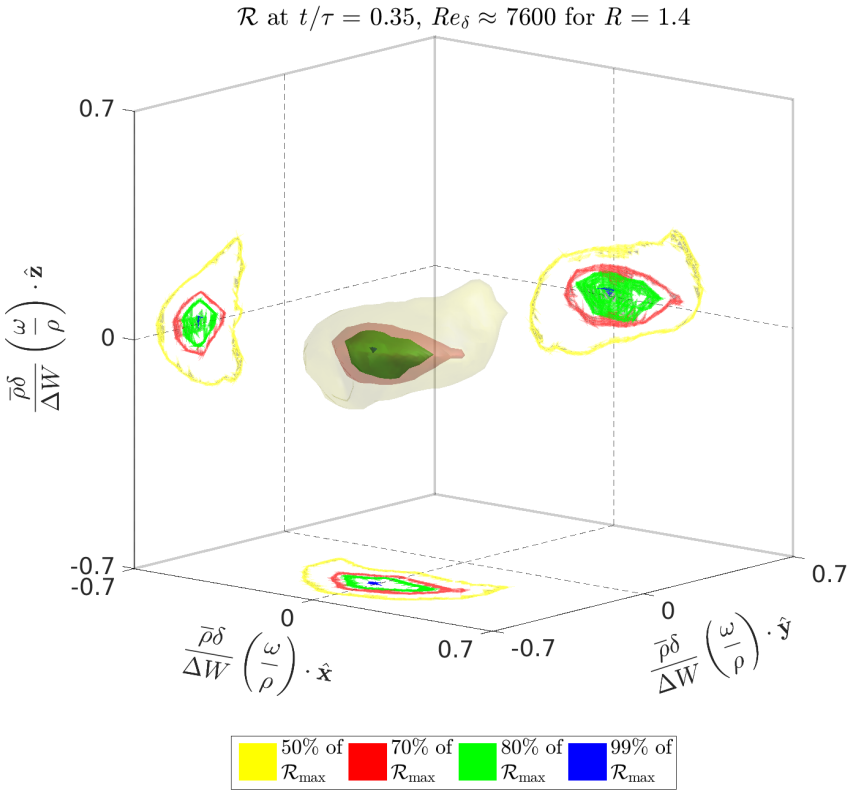

(b)

Figure 5.10: Non-dimensional specific vorticity $\mathcal{R}$ isosurfaces of mixed fluid (equation 4.1) in Cartesian coordinates for $R = 1.4$ at (*a*) $t/\tau = 0.3$ and (*b*) $t/\tau = 0.35$ *i.e.*, around the unsteady regime transition.

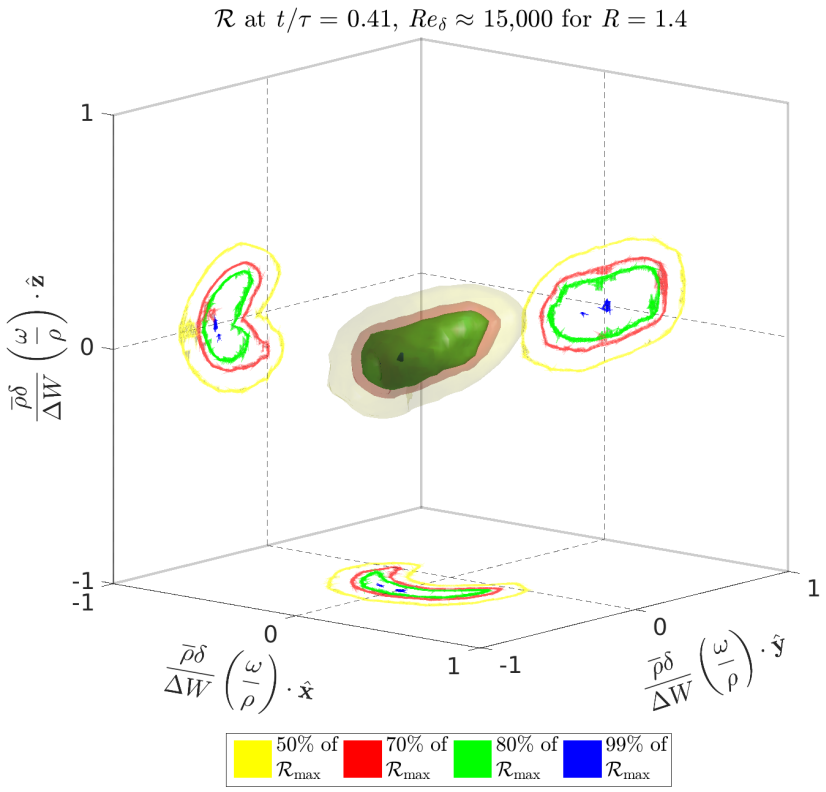

(a)

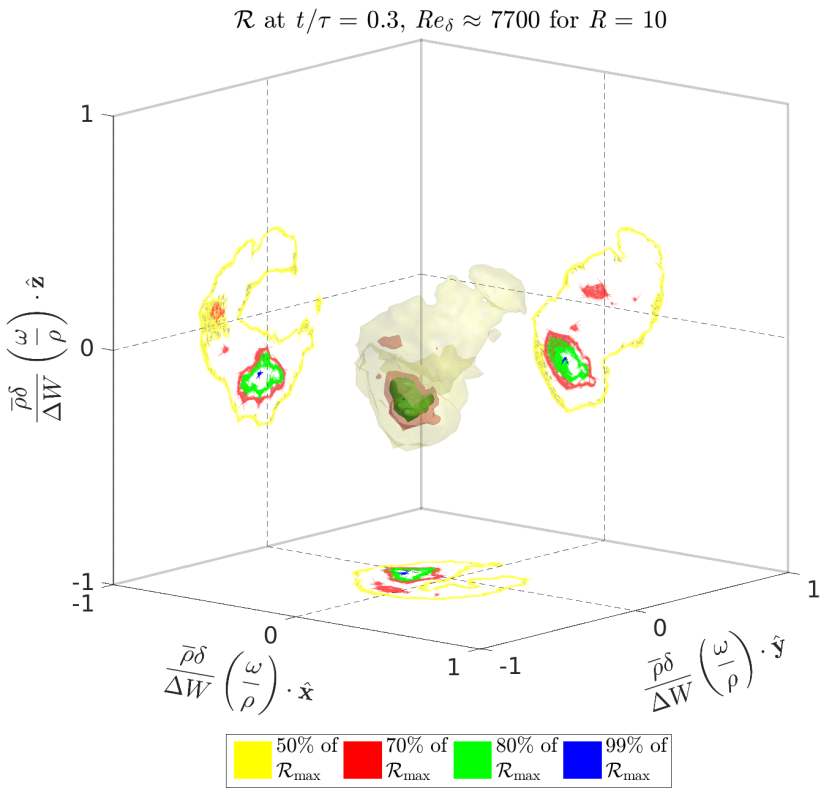

(b)

Figure 5.11: Non-dimensional specific vorticity $\mathcal{R}$ isosurfaces of mixed fluid (equation 4.1) in Cartesian coordinates for (*a*) $R = 1.4$ at a Reynolds number within the fully developed turbulent regime, $Re_\delta \approx 15{,}000$, at $t/\tau = 0.41$, and (*b*) $R = 10$, $Re_\delta \approx 7700$, at $t/\tau = 0.3$.

where only locations with a check-mark are non-zero. The strain rate tensor eigenvectors of the above velocity gradient tensor will have $\widehat{\boldsymbol{s}}_2 = \widehat{\boldsymbol{x}}_2$, *i.e.*, $\widehat{\boldsymbol{s}}_2 \parallel \boldsymbol{\omega}$.

The only assumptions to obtain this result are that

1. $\partial\omega_0/\partial x_1 \approx \partial\omega_0/\partial x_3 \gg \partial\omega_0/\partial x_2$
2. $\phi \neq \phi(\boldsymbol{x})$

with no assumptions on uniform-density versus variable-density flow. This mathematical relation that $\boldsymbol{\omega} \parallel \widehat{\boldsymbol{s}}_2$ has been observed to hold in previous work for uniform-density flows (*e.g.*, Ashurst, Kerstein, et al., 1987; Ohkitani, 2002; Lüthi, Tsinober, and Kinzelbach, 2005; Guala et al., 2005; Hamlington, Schumacher, and Dahm, 2008; Meneveau, 2011; Verma and Blanquart, 2014). Kinematic arguments can also be made to justify the alignment of $\boldsymbol{\omega}$ with $\widehat{\boldsymbol{s}}_2$ for uniform-density vorticity, as noted by Professor Paul Dimotakis. Outside viscous cores of one of many vortex tubes reported to occur in turbulent flow (She, Jackson, and Orszag, 1990; Vincent and Meneguzzi, 1991), the dominant azimuthal velocity decreases like $1/r$, being highest at the viscous-core boundary. Following fluid elements spaced radially from the vortex tube, an element closest to the core will move faster than one farther away. This results in a stretching motion at 45° to the radius vector, which marks the direction of the eigenvector corresponding to the most extensional eigenvalue of the local strain rate tensor. Elements starting diagonally spaced with those farther from the vortex tube ahead of those closer, will end up on similar radial lines. These elements, however, contract in this direction: the direction of the contractional eigenvector of the local strain rate tensor, at −45° to the radius vector.

A consequence of the argument above is that $\widehat{\boldsymbol{s}}_1$ and $\widehat{\boldsymbol{s}}_3$ (the local eigenvectors corresponding to the most extensional and contractional eigenvectors of the local strain rate tensor, respectively) are in the plane perpendicular to the local vorticity. The intermediate eigenvector, $\widehat{\boldsymbol{s}}_2$, is perpendicular to $\widehat{\boldsymbol{s}}_1$ and $\widehat{\boldsymbol{s}}_3$, and thus points in the direction of $\pm\boldsymbol{\omega}$. This explains why, for uniform-density flow, vorticity aligns with $\widehat{\boldsymbol{s}}_2$, or more accurately, why the $(\widehat{\boldsymbol{s}}_1, \widehat{\boldsymbol{s}}_3)$–plane is preferentially perpendicular to $\boldsymbol{\omega}$.

The discussions above suggest that vorticity aligns with the intermediate eigenvector of the strain rate field induced by vorticity itself, *i.e.*, the self strain rate field of a vortex element. Returning to the mathematical argument (equations 5.18 through

5.20), the second assumption, that $\phi \neq \phi(\boldsymbol{x})$, could be lifted to represent background strain. Using the initial diffusive velocity to represent $\nabla\phi$,

$$\nabla\phi \;=\; -\mu\nabla\left(\frac{1}{\rho}\right) \tag{5.21}$$

with $\nabla(1/\rho) \perp \widehat{\boldsymbol{s}}_2$ (see sections 5.1 and 5.3.1), then the non-zero components of $\nabla\boldsymbol{u}$ are unchanged, leaving $\boldsymbol{\omega} \parallel \widehat{\boldsymbol{s}}_2$. Hamlington, Schumacher, and Dahm (2008) note that vorticity may align with the most extensional eigenvector of the imposed background strain rate field, which could occur if $\nabla\phi \not\perp \widehat{\boldsymbol{s}}_2$. However this is not the case for the studied flow. Deviations from $\widehat{\boldsymbol{s}}_2 \parallel \boldsymbol{\omega}$ in the studied flow could be from $\partial\omega_0/\partial x_2$ being of order $\partial\omega_0/\partial x_{1,3}$.

It has been argued that $\boldsymbol{\omega} \parallel \widehat{\boldsymbol{s}}_2$, and the alignment of the SGS vorticity, $\boldsymbol{\omega}'$, or $\boldsymbol{e}_s^v$, is now discussed. First, return to the uniform-density case with $\widetilde{\boldsymbol{u}} \rightarrow \overline{\boldsymbol{u}}$, and switch to index notation for clarity. Filtering equation 5.18, dividing by two, and adding the transpose to obtain the resolved strain rate tensor, $\overline{s}_{ij}$, yields

$$\overline{s}_{ij} \;=\; -\frac{1}{8\pi}\int_{\boldsymbol{x}'}\left\{\varepsilon_{ikl}\overline{\frac{r_k}{|\boldsymbol{r}|^3}\frac{\partial\omega_l(\boldsymbol{x}',t)}{\partial x_j'}} + \varepsilon_{jkl}\overline{\frac{r_k}{|\boldsymbol{r}|^3}\frac{\partial\omega_l(\boldsymbol{x}',t)}{\partial x_i'}}\right\}\mathrm{d}^3\boldsymbol{x}', \tag{5.22}$$

where $\boldsymbol{r} = \boldsymbol{x} - \boldsymbol{x}'$, ε_{ijk} is the Levi-Civita symbol, and $\boldsymbol{s} = \overline{\boldsymbol{s}} + \boldsymbol{s}'$. It has been shown that $\boldsymbol{\omega} \parallel \widehat{\boldsymbol{s}}_2$. Using the same assumptions as before, now with equation 5.22, it can be argued that $\boldsymbol{\omega} \parallel \widehat{\overline{\boldsymbol{s}}}_2$, or that $\widehat{\overline{\boldsymbol{s}}}_2 \parallel \widehat{\boldsymbol{s}}_2$. The SGS strain rate tensor, $\boldsymbol{s}'$, is then

$$\begin{aligned} s_{ij}' \;=\; -\frac{1}{8\pi}\int_{\boldsymbol{x}'}\Bigg\{ & \varepsilon_{ikl}\left[\frac{r_k}{|\boldsymbol{r}|^3}\frac{\partial\overline{\omega}_l(\boldsymbol{x}',t)}{\partial x_j'} + \frac{r_k}{|\boldsymbol{r}|^3}\frac{\partial\omega_l'(\boldsymbol{x}',t)}{\partial x_j'} - \overline{\frac{r_k}{|\boldsymbol{r}|^3}\frac{\partial\omega_l(\boldsymbol{x}',t)}{\partial x_j'}}\right] \\ & + \varepsilon_{jkl}\left[\frac{r_k}{|\boldsymbol{r}|^3}\frac{\partial\overline{\omega}_l(\boldsymbol{x}',t)}{\partial x_i'} + \frac{r_k}{|\boldsymbol{r}|^3}\frac{\partial\omega_l'(\boldsymbol{x}',t)}{\partial x_i'} - \overline{\frac{r_k}{|\boldsymbol{r}|^3}\frac{\partial\omega_l(\boldsymbol{x}',t)}{\partial x_i'}}\right]\Bigg\}\,\mathrm{d}^3\boldsymbol{x}'. \end{aligned} \tag{5.23}$$

The SVM assumes that $\boldsymbol{\omega}' \parallel \widehat{\overline{\boldsymbol{s}}}_1$. Rotating the above equation to the resolved strain rate field eigenvector frame, and noting that the terms involving $\boldsymbol{\omega}$ and $\overline{\boldsymbol{\omega}}$ will align with $\widehat{\overline{\boldsymbol{s}}}_2$, then

$$|\nabla\boldsymbol{\omega}'| \;\ll\; |\nabla\overline{\boldsymbol{\omega}}| \;\approx\; |\nabla\boldsymbol{\omega}| \tag{5.24}$$

must hold to use the assumption that the SGS vorticity, $\boldsymbol{\omega}' \parallel \widehat{\overline{\boldsymbol{s}}}_1$ in the SVM. If it does not hold, then $\overline{\boldsymbol{s}} + \boldsymbol{s}' = \boldsymbol{s}$ would produce a $\widehat{\boldsymbol{s}}_2 \not\parallel \widehat{\overline{\boldsymbol{s}}}_2$, contradicting the equations above, and thus invalid. With $\boldsymbol{\omega}' \parallel \widehat{\overline{\boldsymbol{s}}}_1$ and not $\parallel \widehat{\overline{\boldsymbol{s}}}_2$, there will still be slight misalignments between $\widehat{\overline{\boldsymbol{s}}}_2$ and $\widehat{\boldsymbol{s}}_2$, and thus, misalignments between $\boldsymbol{\omega}$ and $\widehat{\boldsymbol{s}}_2$, even if 5.24 holds. The only guarantee for $\widehat{\boldsymbol{s}}_2 \parallel \widehat{\overline{\boldsymbol{s}}}_2$ is if $\boldsymbol{\omega}' \parallel \widehat{\overline{\boldsymbol{s}}}_2$.

This chapter examines how well vorticity aligns with the intermediate eigenvalue of the local strain rate tensor, introducing the variable-density affects by studying the specific vorticity (equation 4.23). Figures 5.12 and 5.13 depict specific vorticity $\mathcal{R}$ isosurfaces for four density ratios. $R = 1.4$ and 10 data are the same as in figure 5.11, but in a different frame. These illustrate that (specific) vorticity is preferentially aligned with the *negative* of the intermediate strain rate eigenvector in the variable-density flow investigated. The negative sign alignment is purely based on the chosen eigenvector signs (discussed in section 5.1), but is important to note when comparing to other vector fields below. Additionally, there is a symmetry seen in figures 5.12 and 5.13 in the $\widehat{\boldsymbol{s}}_1$ and $\widehat{\boldsymbol{s}}_3$ directions because the octants in the strain rate tensor eigenvector frame are not unique.

Note that the degree of alignment of $\boldsymbol{\omega}$ with $\widehat{\boldsymbol{s}}_2$ tightens as R increases. For example, vorticity in the $R = 1.4$ case at a $Re_\delta \approx 8000$ (closer to the Reynolds number the $R = 10$ case is displayed) looks very similar to figure 5.12a, *i.e.*, not as tightly aligned as is the $R = 10$ case in figure 5.13b. This can be explained by one or both of our assumptions on vorticity alignment (that $\partial\omega_0/\partial x_1 \approx \partial\omega_0/\partial x_3 \gg \partial\omega_0/\partial x_2$ and $\nabla\phi \perp \widehat{\boldsymbol{s}}_2$) weakening with smaller R. The second assumption, based on equation 5.21, holds, as discussed in section 5.3.1. The first assumption, then, must be affected by density ratio, R. The variability in vorticity alignment seen with the lower-R cases is consistent with vorticity alignment in uniform-density flows (*e.g.*, Verma and Blanquart, 2014). A larger variability is observed in the $\widehat{\boldsymbol{s}}_1$ direction than in the $\widehat{\boldsymbol{s}}_3$ direction because the strain rate field stretches vorticity along $\widehat{\boldsymbol{s}}_1$ and contracts it along $\widehat{\boldsymbol{s}}_3$.

Conditional three-dimensional $\mathcal{R}$ isosurfaces of specific vorticity based on the sign of the intermediate eigenvalue of the local strain rate tensor, s_2, are shown in figures 5.14 and 5.15 for $R = 1.4$ and $R = 10$ in the local strain rate tensor eigenvector frame. Figure 5.14 displays conditional $\mathcal{R}$ isosurfaces for locations within the shear layer with $s_2 > 0$, while figure 5.15 displays the conditional $\mathcal{R}$ isosurfaces for locations with $s_2 < 0$. In all of these variable-density simulations, approximately 75% of the data points have $s_2 > 0$, as reported previously (Ashurst, Kerstein, et al., 1987; Nomura and Elghobashi, 1992; Lund and Rogers, 1994).

Locations with a negative intermediate eigenvalue exhibit more variability in the $(\widehat{\boldsymbol{s}}_1, \widehat{\boldsymbol{s}}_3)$–plane, whereas the dominating positive intermediate-eigenvalue statistics exhibit a smaller variability. These results are seemingly inconsistent with the 'lasagna' ($s_2 > 0$) versus 'spaghetti' ($s_2 < 0$) descriptions of stretching that suggest

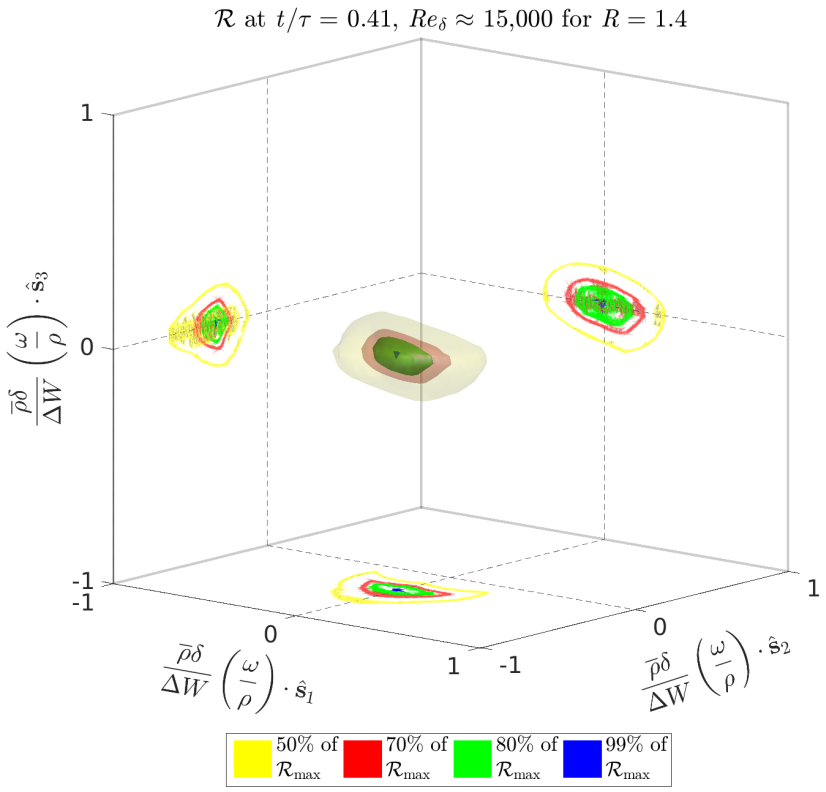

(a)

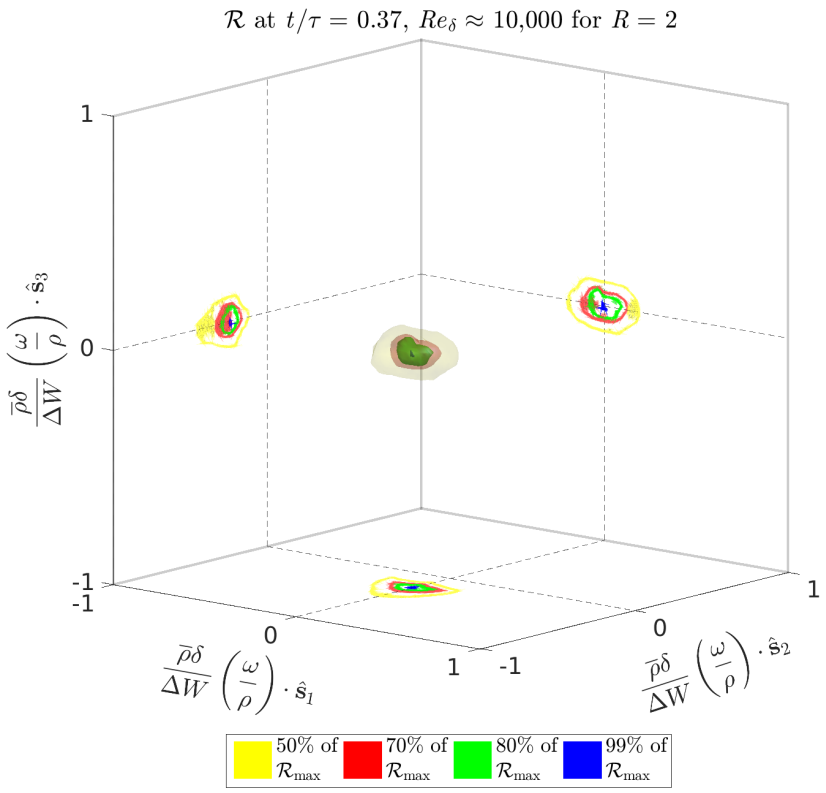

(b)

Figure 5.12: Non-dimensional specific vorticity $\mathcal{R}$ isosurfaces of mixed fluid (equation 4.1) in the local strain rate tensor eigenvector coordinate system for (*a*) $R = 1.4$ and (*b*) $R = 2$ at Reynolds numbers within the fully developed turbulent regime.

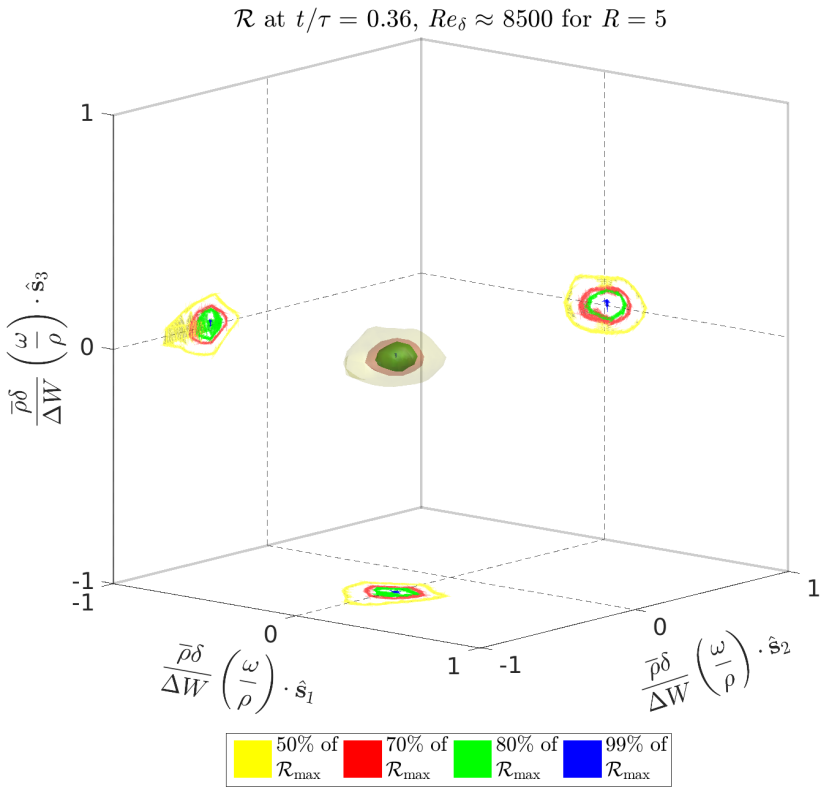

(a)

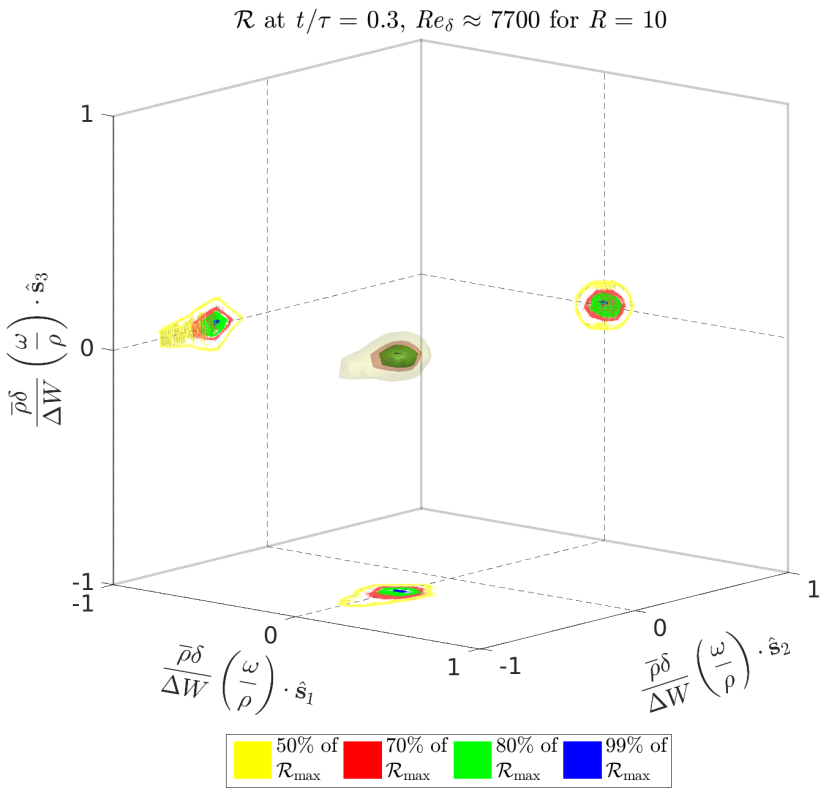

(b)

Figure 5.13: Non-dimensional specific vorticity $\mathcal{R}$ isosurfaces of mixed fluid (equation 4.1) in the local strain rate tensor eigenvector coordinate system for (*a*) $R = 5$ and (*b*) $R = 10$ at the highest Reynolds numbers attained for these density ratios, entering the fully developed turbulent regime.

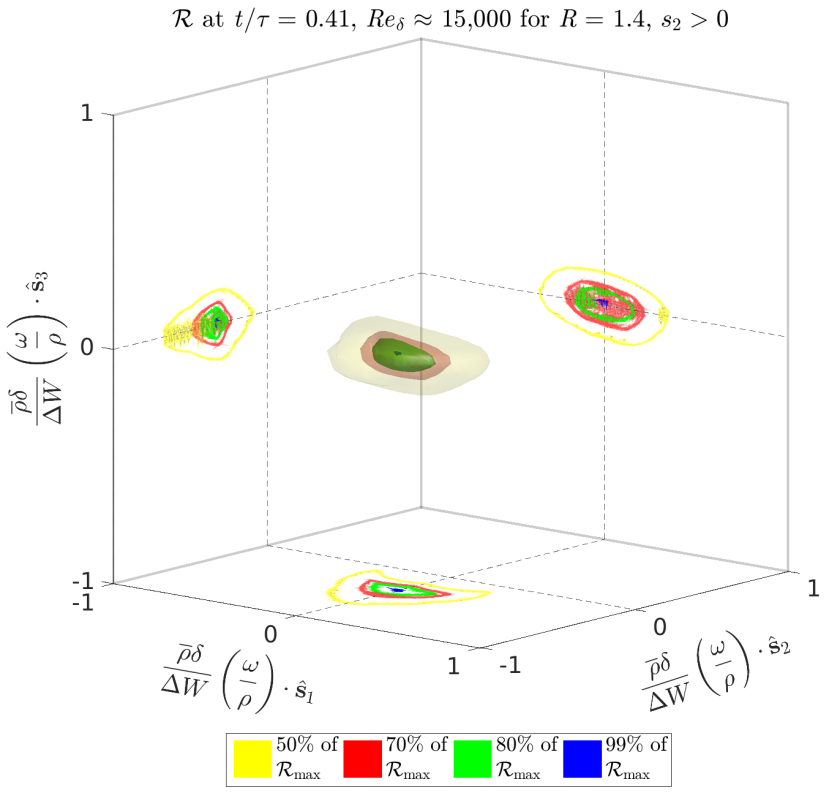

(a)

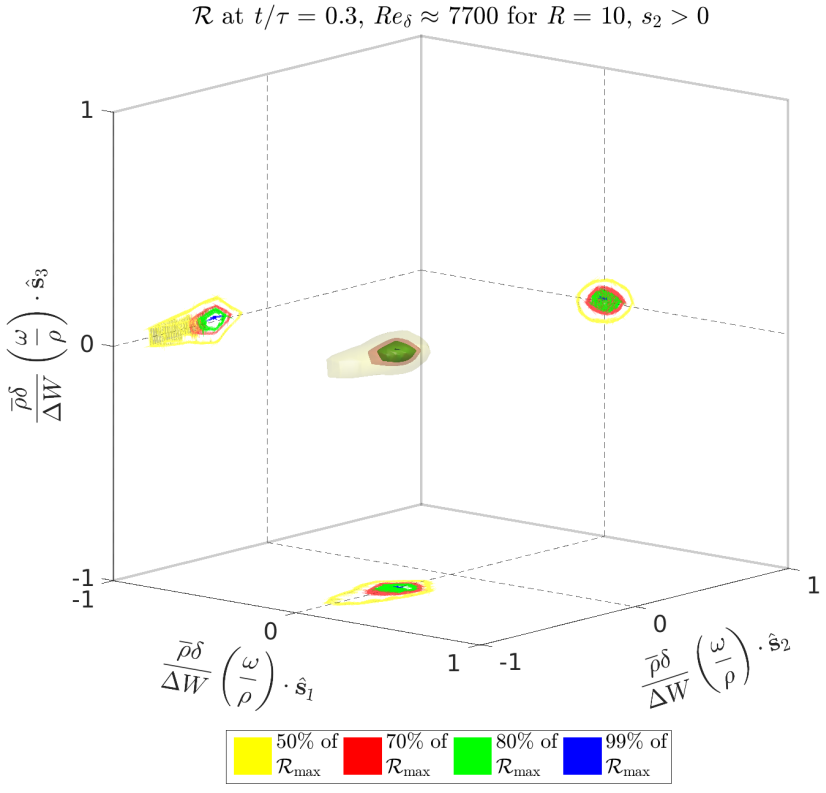

(b)

Figure 5.14: Conditional non-dimensional specific vorticity $\mathcal{R}$ isosurfaces of mixed fluid, in the local strain rate tensor eigenvector coordinate system for (*a*) $R = 1.4$ and (*b*) $R = 10$, at the same times as in figure 5.11. Statistics conditioned on the intermediate eigenvalue, $s_2 > 0$.

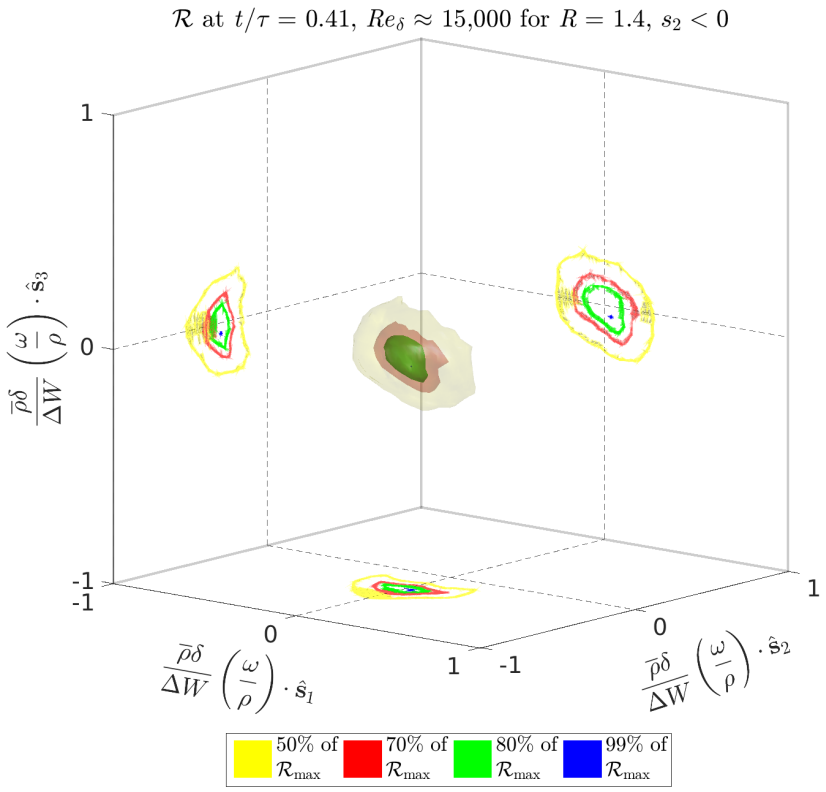

(a)

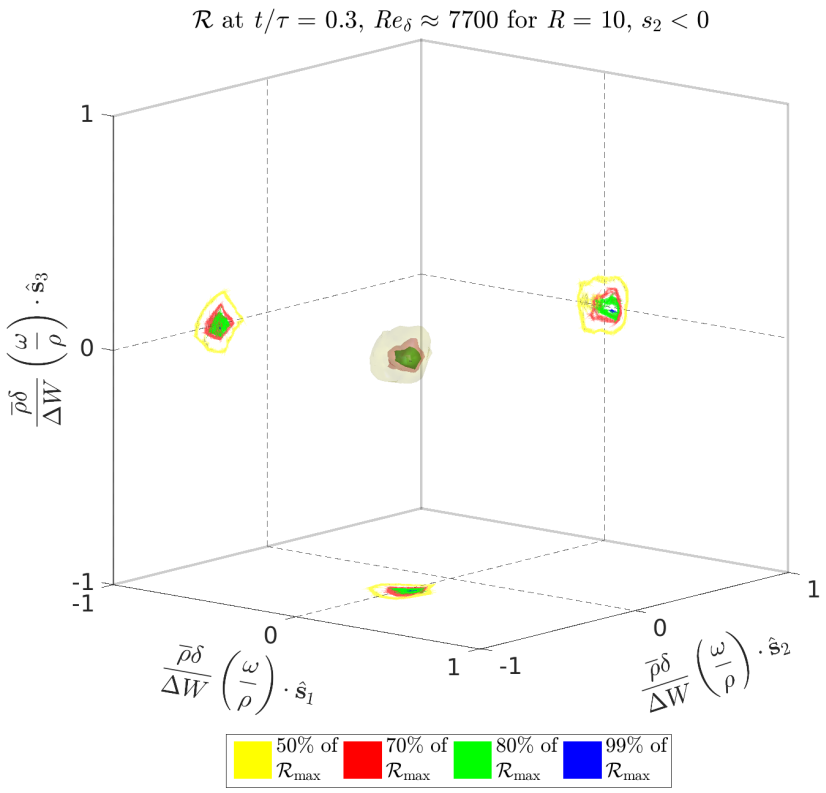

(b)

Figure 5.15: Conditional non-dimensional specific vorticity $\mathcal{R}$ isosurfaces of mixed fluid, in the local strain rate tensor eigenvector coordinate system for (*a*) $R = 1.4$ and (*b*) $R = 10$, at the same times as in figure 5.11. Statistics conditioned on the intermediate eigenvalue, $s_2 < 0$.

that negative intermediate eigenvalues should dominate and that there should be more variability when $s_2 > 0$. However, 'spaghetti' concepts describe stretching along the $\widehat{\boldsymbol{s}}_1$ axis only, but not vorticity alignment along the $\widehat{\boldsymbol{s}}_2$ axis. A $s_2 < 0$ strain rate contracts the vorticity vector inwards along $\widehat{\boldsymbol{s}}_2$ and $\widehat{\boldsymbol{s}}_3$ towards the origin, and outward along $\widehat{\boldsymbol{s}}_1$, resulting in a p.d.f. with a larger variance as vorticity is contracted inwards. When $s_2 > 0$, the strain elongates vorticity in the $\widehat{\boldsymbol{s}}_1$ and $\widehat{\boldsymbol{s}}_2$ directions. Since $s_2 > 0$ statistics have less variability, that configuration is more stable with respect to rolling up of a vortex sheet, and thus positive intermediate eigenvalues are expected to dominate, as confirmed in the simulated flow.

It has been shown that vorticity will align, generally, with the negative of the intermediate eigenvector of the local strain rate tensor, with the chosen eigenvector signs. There will be some variations, however they decrease as R increases. Thus, having a subgrid-scale model that may deviate vorticity from this alignment may be consistent, as long as that deviation decreases as R increases.

For uniform-density flow, the vorticity equation (4.23) simplifies to

$$\frac{\mathrm{D}\boldsymbol{\omega}}{\mathrm{D}t} \;=\; \boldsymbol{\omega}\cdot\boldsymbol{s} \;+\; \nabla\times\left[\frac{1}{\rho}\nabla\cdot\boldsymbol{\tau}\right] . \tag{5.25}$$

The main difference between this equation and equation 4.23 is the baroclinic torque: $-\left[\nabla\left(\frac{1}{\rho}\right)\right]\times(\boldsymbol{\Gamma}+\nabla p)$. It will be argued that in variable-density flow, the baroclinic torque will change the vorticity vector magnitude and its direction.

5.3 Baroclinic torque alignment

Figures 5.16 and 5.17 display $\mathcal{R}$ isosurfaces of non-dimensional baroclinic-torques in the local strain rate field, *i.e.*,

$$\boldsymbol{b} \;=\; (\boldsymbol{b}\cdot\widehat{\boldsymbol{s}}_1, \boldsymbol{b}\cdot\widehat{\boldsymbol{s}}_2, \boldsymbol{b}\cdot\widehat{\boldsymbol{s}}_3) \;=\; -\,\frac{\delta^2}{(\Delta W)^2}\left[\nabla\left(\frac{1}{\rho}\right)\right]\times(\boldsymbol{\Gamma}+\nabla p) , \tag{5.26}$$

which are used to investigate baroclinic torque affects on vorticity alignment.

Baroclinic-torques are seen to align with the intermediate eigenvector of the local strain rate tensor, or with $\pm\widehat{\boldsymbol{s}}_2$, although with a slightly stronger alignment to $-\widehat{\boldsymbol{s}}_2$. The stronger alignment of $\boldsymbol{b}$ with $-\widehat{\boldsymbol{s}}_2$ indicates $\boldsymbol{b}$ has a larger probability of aligning in the same direction as $\boldsymbol{\omega}$, with $\boldsymbol{b}$ amplifying vorticity when aligned. The oppositely aligned $\boldsymbol{b}$ with $\boldsymbol{\omega}$, *i.e.*, when $\boldsymbol{b} \parallel +\widehat{\boldsymbol{s}}_2$, $\boldsymbol{b}$ decreases $|\boldsymbol{\omega}|$.

Studying baroclinic torque effect on vorticity in the strain rate tensor eigenvector frame requires rotating the vorticity evolution equation (4.23) into the strain rate

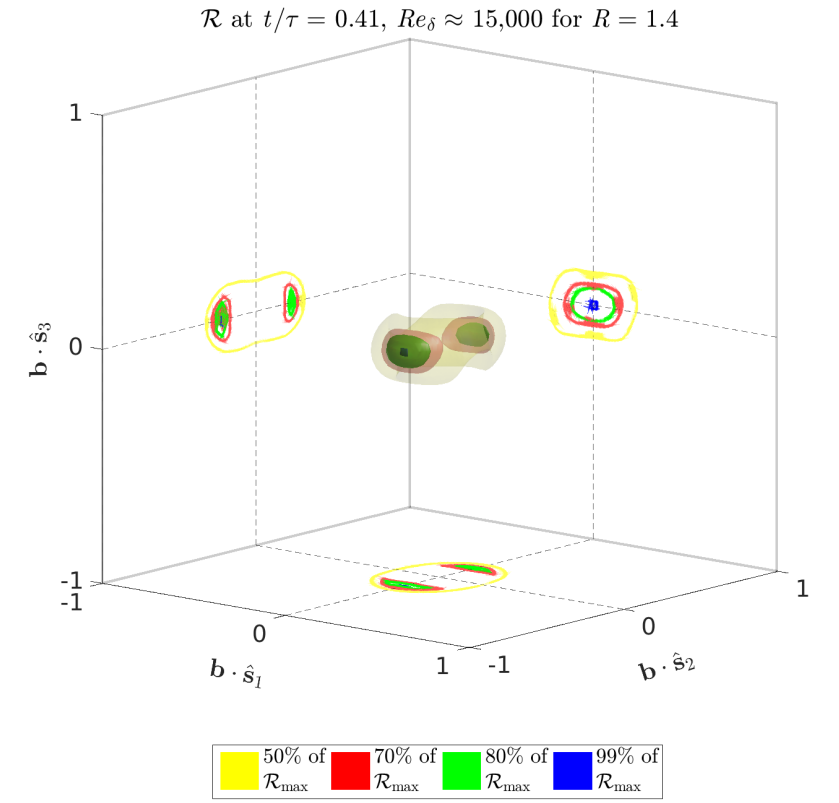

(a)

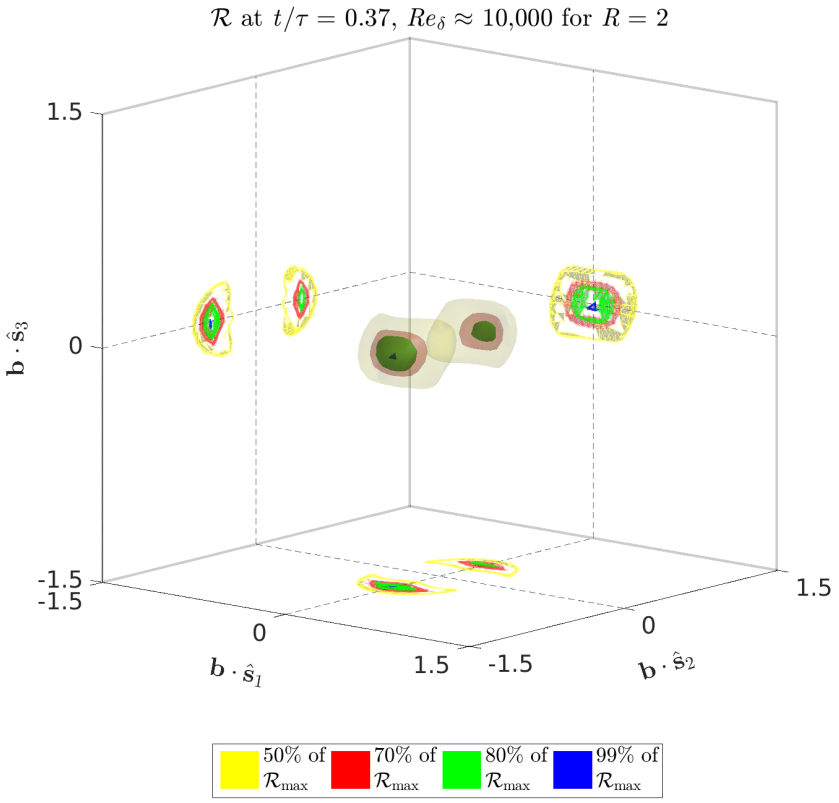

(b)

Figure 5.16: Non-dimensional baroclinic-torque $\mathcal{R}$ isosurfaces of mixed fluid (equation 4.1) in the local strain rate tensor eigenvector coordinate system for (*a*) $R = 1.4$ and (*b*) $R = 2$ at Reynolds numbers within the fully developed turbulent regime.

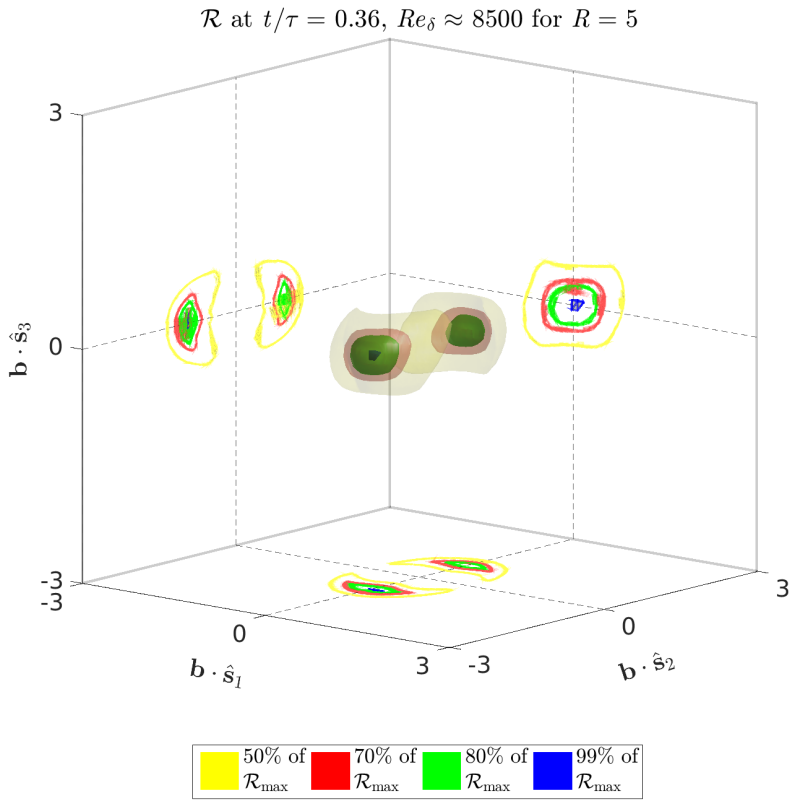

(a)

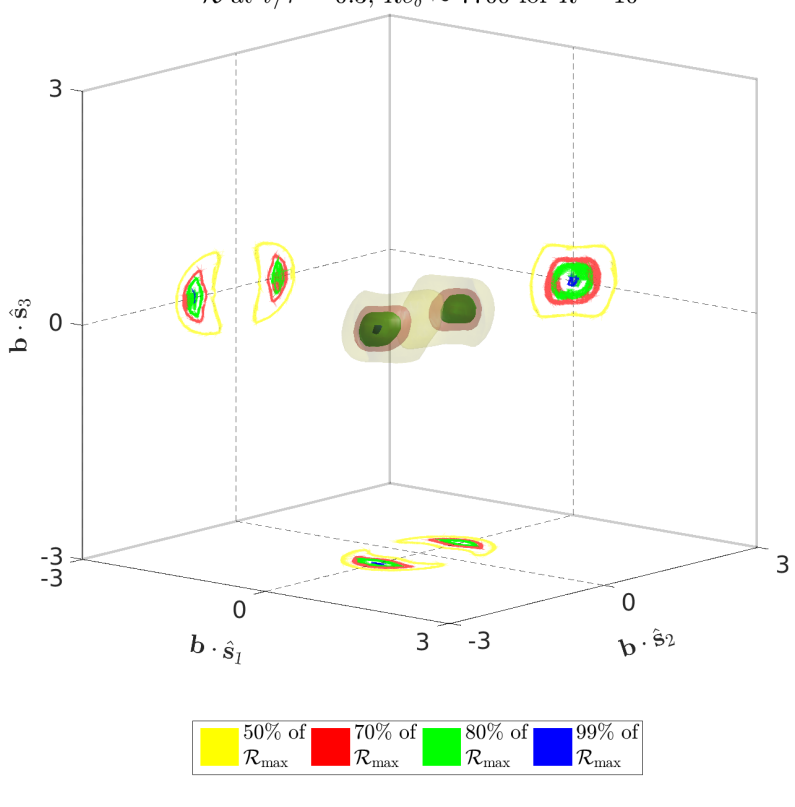

(b)

Figure 5.17: Non-dimensional baroclinic-torque $\mathcal{R}$ isosurfaces of mixed fluid (equation 4.1) in the local strain rate tensor eigenvector coordinate system for (*a*) $R = 5$ and (*b*) $R = 10$ at the highest Reynolds numbers attained for these density ratios, entering the fully developed turbulent regime.

tensor eigenvector frame. In doing so, the Lagrangian derivative and the Laplacian of $\widehat{\boldsymbol{s}}_i$ arise (Nomura and Post, 1998), along with other spatial derivatives from the viscous term, complicating the analysis. However, the relative alignments of $\boldsymbol{b}$ and $\boldsymbol{\omega}$ can be seen through their dot product, as shown in figure 5.18, which is independent of coordinate frame, but shows a similar relative alignment of figures 5.16 and 5.17 with figures 5.12 and 5.13.

Figure 5.18a displays the one dimensional p.d.f. of the cosine of the angle between $\boldsymbol{\omega}$ and $\boldsymbol{b}$ for $R = 1.4$ at various times. Bins are equally spaced in the cosine of the angle ensuring uniformly distributed data would correspond to a p.d.f. of $1/n$, where n is the number of bins. The fields are initially aligned, *i.e.*, $\boldsymbol{b} \parallel \boldsymbol{\omega}$, shown by the green line in figure 5.18a. As the flow evolves, baroclinic torques can also be oppositely aligned with vorticity, with just slightly less probability of occurrence. Note that if the absolute value of the dot product of $\boldsymbol{b}$ with $\widehat{\boldsymbol{s}}_i$ was studied, figure 5.18 could not be obtained from the vectors in the strain rate frame. However, using the chosen signs of the strain rate tensor eigenvectors (discussed in section 5.1), figure 5.18 can be calculated using vectors in the Cartesian frame, or the strain rate tensor eigenvector frame.

Figure 5.18b displays the late time alignment between $\boldsymbol{\omega}$ and $\boldsymbol{b}$ for various density ratios, showing again that in many locations, $\boldsymbol{b} \parallel \pm\boldsymbol{\omega}$. Note the larger probability of $\boldsymbol{\omega} \parallel \boldsymbol{b}$ (*i.e.*, when the cosine of the angle between the two is 1) than of $\boldsymbol{\omega} \parallel -\boldsymbol{b}$, which is also seen in the full three-dimensional plots of the baroclinic torque in figures 5.16 and 5.17, where the blue isosurface is aligned with $-\widehat{\boldsymbol{s}}_2$ (in the same direction as $\boldsymbol{\omega}$ alignment in figures 5.12 and 5.13). Additionally, the curves in figure 5.18b collapse for the wide range of density ratios studied, showing this alignment between $\boldsymbol{b}$ and $\boldsymbol{\omega}$ is independent of density ratio. $\boldsymbol{\Gamma}$ is included in $\boldsymbol{b}$, however $\boldsymbol{\Gamma}$ is not a dynamical quantity. It is set to ensure the mean momentum in the domain is constant and zero. Figure 5.18c shows the alignment of $\boldsymbol{\omega}$ with the baroclinic torque from the dynamic pressure gradient, ∇p, only, *i.e.*, $-\boldsymbol{\omega} \cdot [\nabla(1/\rho) \times \nabla p]$, estimating $\boldsymbol{\Gamma}$ as identically $-\widehat{\boldsymbol{z}}\rho_0 g$, which is not exact (*cf.*, section 3.2). Interestingly, the alignment of $\boldsymbol{\omega}$ with the baroclinic torque with and without $\boldsymbol{\Gamma}$ is similar. The behavior of ∇p is discussed further in section 5.3.2.

Integrating under the curves in figure 5.18b shows that $\boldsymbol{b} \parallel \pm\boldsymbol{\omega}$, *i.e.*, $\left|\frac{\boldsymbol{\omega}\cdot\boldsymbol{b}}{|\boldsymbol{\omega}||\boldsymbol{b}|}\right| < 0.95$, corresponding to $\cos^{-1}|\boldsymbol{\omega}\cdot\boldsymbol{b}| < 18°$, in less than 20% of the mixed-fluid locations. Baroclinic torques are not aligned with vorticity in approximately 80% of the mixed-fluid locations, with misalignments increasing slightly when $\boldsymbol{\Gamma}$ is not included in $\boldsymbol{b}$

(figure 5.18c). This is seen consistently regardless of density ratio, R, or Reynolds number, Re_δ, in the turbulent regime. Even though $\boldsymbol{b}$ and $\boldsymbol{\omega}$ are both most probably aligned with $\widehat{\boldsymbol{s}}_2$, they are misaligned with each other in the majority of the mixing region in the turbulent regime. In short, the role of baroclinic torques is to change vorticity direction and its magnitude.

The $\boldsymbol{b}$ alignment can be investigated further by studying the density gradient (or specific volume gradient) and pressure gradient alignments. Differing signs of baroclinic torques (*i.e.*, the alignment with $\pm\widehat{\boldsymbol{s}}_2$, as opposed to one sign of $\widehat{\boldsymbol{s}}_2$) has been previously seen (P. Miller, Lindstrom, and Cook, 2003) and will be shown to be from density-gradient sign variations.

5.3.1 Density-gradient alignment

Figures 5.19 and 5.20 display $\mathcal{R}$ isosurfaces of specific volume gradients, $\overline{\rho}\,\delta\,\nabla\,(1/\rho)$, within the mixed-fluid region for four density ratios in the strain rate tensor eigenvector frame. This section uses "specific volume gradient" and "density gradient" interchangeably; even though the latter refers to $\nabla\rho$, the two are linked.

Figures 5.19 and 5.20 illustrate the preferred alignment of $\nabla(1/\rho)$ to be close to 30° with $\pm\widehat{\boldsymbol{s}}_3$, 60° with $\pm\widehat{\boldsymbol{s}}_1$, and perpendicular to $\widehat{\boldsymbol{s}}_2$. This is similar to the preferred alignment of *passive* scalar gradients in shear-driven flows (Ashurst, Kerstein, et al., 1987; R. S. Miller et al., 1995). In isotropic turbulence, however, the angle of a passive scalar gradient with $\widehat{\boldsymbol{s}}_3$ decreases (and the angle with $\widehat{\boldsymbol{s}}_1$ increases), with the scalar gradient still perpendicular to the eigenvector corresponding to the intermediate eigenvalue of the local strain rate tensor (Ashurst, Kerstein, et al., 1987; R. S. Miller et al., 1995). Recently, Verma and Blanquart (2014) reported scalar gradients with high probabilities of aligning directly with $\widehat{\boldsymbol{s}}_3$. The present flow differs from those in the aforementioned studies in that the scalar gradient is of density as opposed to a passive scalar.

Note that figures 5.19 and 5.20 have negative specific volume gradients, *i.e.*, data in the $-\widehat{\boldsymbol{s}}_1 + \widehat{\boldsymbol{s}}_3$ direction, as opposed to the early-time specific volume gradients shown in section 5.1. This is from turbulent mixing, *i.e.*, $\nabla(1/\rho)$ can be positive or negative in both shear layers in the turbulent flow, allowing for a non-zero probability of aligning in the $-\widehat{\boldsymbol{s}}_1 + \widehat{\boldsymbol{s}}_3$ direction. However, there is a stronger probability of aligning with $\widehat{\boldsymbol{s}}_1 - \widehat{\boldsymbol{s}}_3$, the (approximate) direction of the mean specific volume gradient.

In discussing this alignment, it is helpful to consider statistics conditioned on the

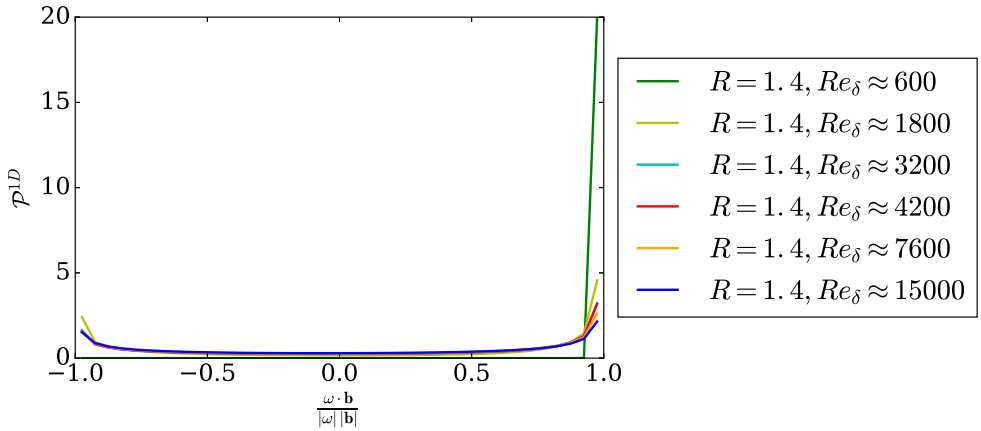

(a)

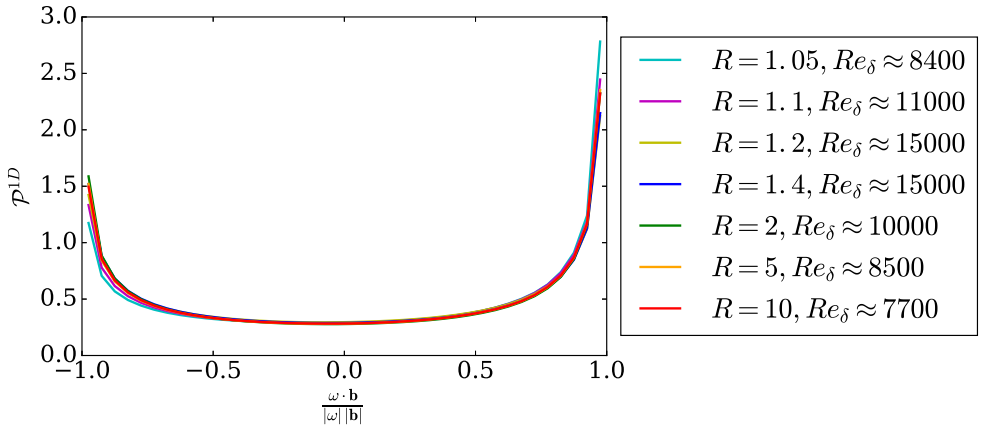

(b)

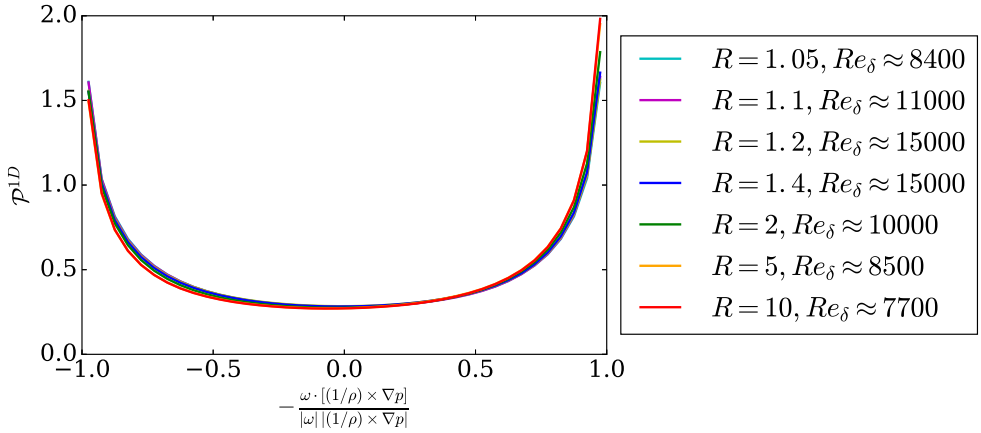

(c)

Figure 5.18: One-dimensional probability density function of the cosine of angles between $\boldsymbol{\omega}$ and $\boldsymbol{b}$ in figures a and b, and $\boldsymbol{\omega}$ with $-\nabla(1/\rho) \times \nabla p$ in figure c, in the mixed-fluid region (equation 4.1) for (a) $R = 1.4$ at various times, or various Re_δ (b and c) shown at late times for seven density ratios at close to the highest Reynolds numbers attained for these density ratios, entering the fully developed turbulent regime. The difference between figures b and c is the inclusion of $\boldsymbol{\Gamma}$ in the baroclinic torque in the former.

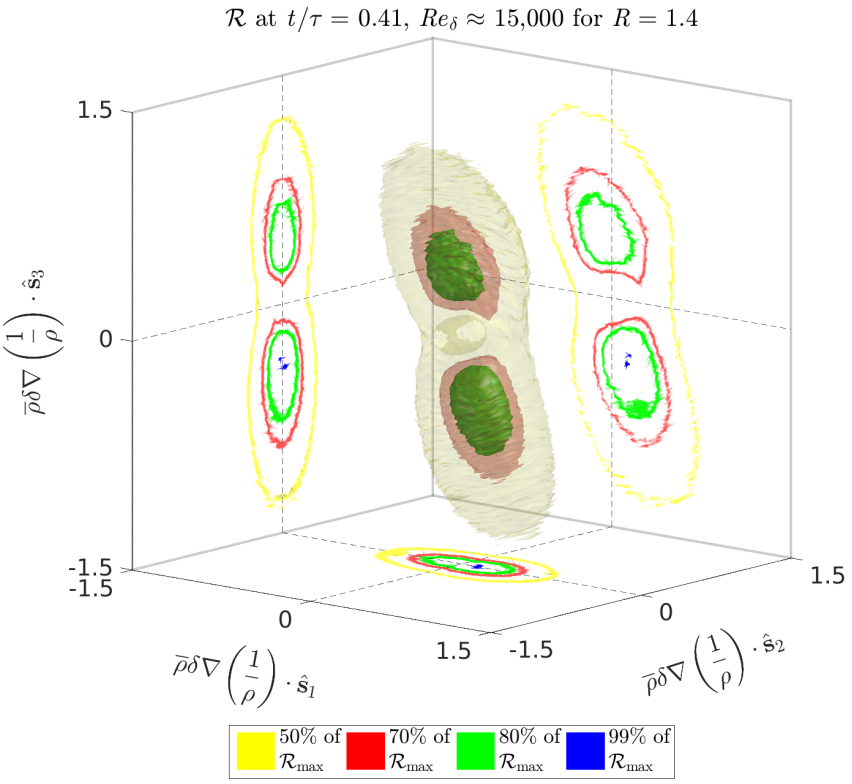

(a)

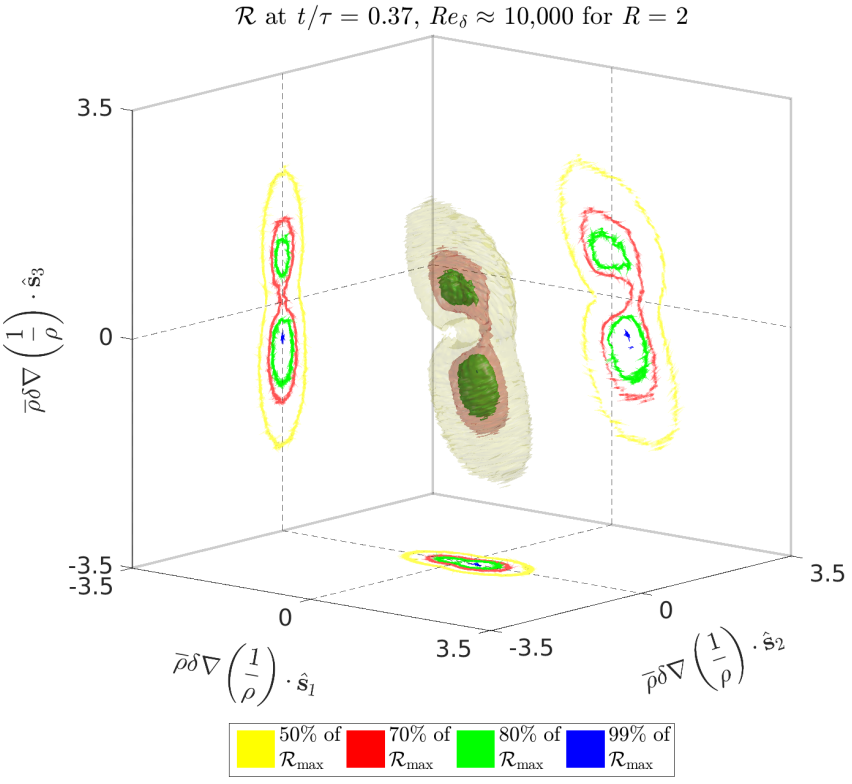

(b)

Figure 5.19: Non-dimensional specific volume gradient $\mathcal{R}$ isosurfaces of mixed fluid (equation 4.1) in the local strain rate tensor eigenvector coordinate system for (*a*) $R = 1.4$ and (*b*) $R = 2$ at Reynolds numbers within the fully developed turbulent regime.

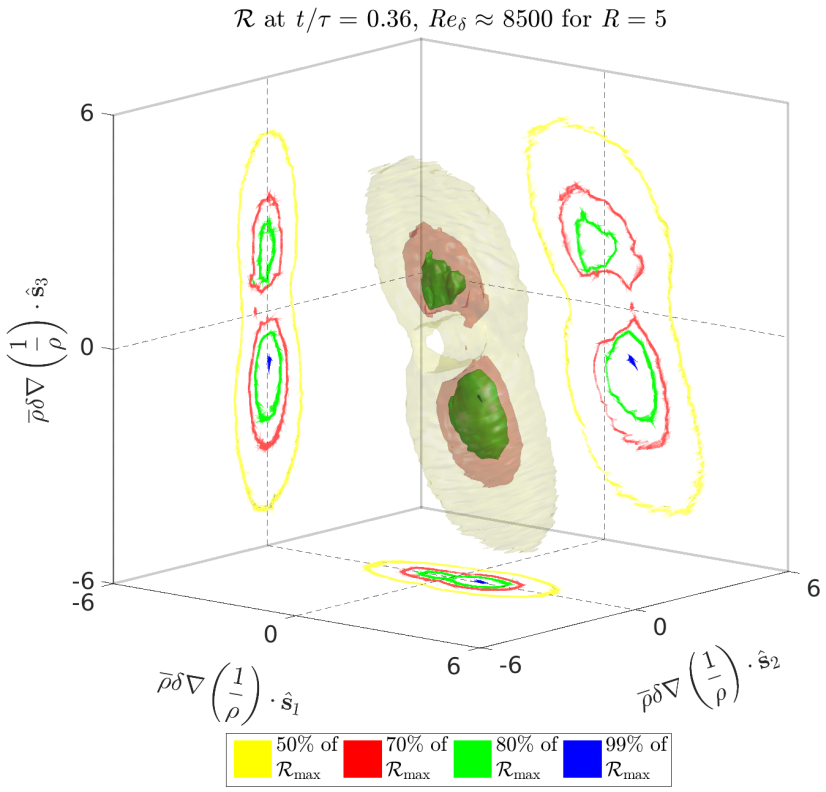

(a)

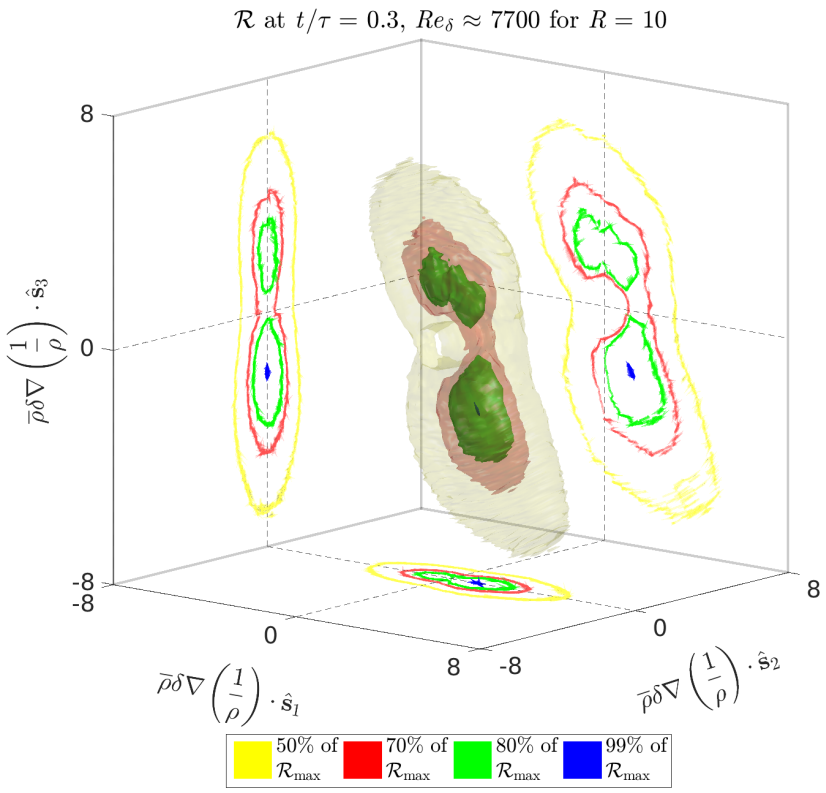

(b)

Figure 5.20: Non-dimensional specific volume gradient $\mathcal{R}$ isosurfaces of mixed fluid (equation 4.1) in the local strain rate tensor eigenvector coordinate system for (a) $R = 5$ and (b) $R = 10$ at the highest Reynolds numbers attained for these density ratios, entering the fully developed turbulent regime.

sign of s_2, *i.e.*, for locations where $s_2 > 0$ or $s_2 < 0$. Roughly 75% of locations within the mixed-fluid region have $s_2 > 0$; a bias mentioned earlier and previously reported for uniform-density flows (Ashurst, Kerstein, et al., 1987; Nomura and Elghobashi, 1992; Lund and Rogers, 1994). $\mathcal{R}$ isosurfaces of specific volume gradient conditioned on $s_2 > 0$ are shown in figure 5.21 for $R = 1.4$ and $R = 10$, with similar behavior for all density ratios studied. Figure 5.21 is similar to the unconditional $\mathcal{R}$ of figures 5.19 and 5.20 but with (slightly) less variation. Figure 5.22 displays isosurfaces of $\mathcal{R}$ conditioned on $s_2 < 0$ and shows stronger alignment along the ±45° lines, with more overall variation.

To explain this alignment, first consider uniform-density flow for which $s_1 + s_2 + s_3 = 0$. If $s_2 = 0$, then $-s_3 = s_1$ and matched strain rate amplitudes drive the fluid towards the local origin along $\widehat{\boldsymbol{s}}_3$ and away along $\widehat{\boldsymbol{s}}_1$, with no extension or contraction along $\widehat{\boldsymbol{s}}_2$. A scalar contracted and extended along those directions, respectively, will evolve a gradient perpendicular to that stream, *i.e.*, the scalar gradient will be at ±45° to $\widehat{\boldsymbol{s}}_1$ and $\widehat{\boldsymbol{s}}_3$, ignoring diffusion effects. This explains the initial behavior of the flow, seen in figure 5.8b which shows the specific volume gradient aligning perfectly at 45° to $\widehat{\boldsymbol{s}}_1$ and $-\widehat{\boldsymbol{s}}_3$. Note initially there is a zero probability of the specific volume gradient aligning with the other three components of ±45° to $\widehat{\boldsymbol{s}}_1$ and $\widehat{\boldsymbol{s}}_2$ because of the anisotropy of the flow, and the choice of eigenvector signs (section 5.1).

Since the majority of mixed-fluid locations in the unsteady/turbulent regime have $s_2 > 0$, then $-s_3 > s_1 > s_2$ generally. This asymmetry drives the scalar towards the local origin along $\widehat{\boldsymbol{s}}_3$ more strongly than it is being pulled away in the $\widehat{\boldsymbol{s}}_1$ or $\widehat{\boldsymbol{s}}_2$ directions. The strain field will then be steeper in the $\widehat{\boldsymbol{s}}_3$ direction than in the $\widehat{\boldsymbol{s}}_1$ direction, for example. The density gradient will be perpendicular to the strain field, and thus, the density gradient will be steeper with a smaller angle to $\widehat{\boldsymbol{s}}_3$ than it has to $\widehat{\boldsymbol{s}}_1$ (assuming $0 < s_2 \ll s_1$). If $s_2 < 0$, then $s_1 > -s_3$ and the scalar gradient favors aligning at angles less than ±45° to $\widehat{\boldsymbol{s}}_1$ and greater than ±45° to $\widehat{\boldsymbol{s}}_3$. If diffusion cannot be ignored, the scalar gradient will be weaker in the $\widehat{\boldsymbol{s}}_1$ direction, decreasing the scalar gradient angle with $\widehat{\boldsymbol{s}}_3$ (*e.g.* Batchelor, 1959; Ashurst, Kerstein, et al., 1987; Dimotakis, 1989). Thus, the scalar gradient will align at roughly ±45° to $\widehat{\boldsymbol{s}}_1$ and $\widehat{\boldsymbol{s}}_3$ where $s_2 < 0$, and will be at even smaller angles with $\widehat{\boldsymbol{s}}_3$ and larger to $\widehat{\boldsymbol{s}}_1$ where $s_2 > 0$. This discussion assumes $s_1 + s_2 + s_3 = 0$, however, it is found that $s_1 + s_2 + s_3 \ll \max(|s_1|, |s_3|)$, *i.e.*, $s_1 + s_2 + s_3 \approx 0$ for the variable-density flow discussed here. Thus, this argument holds for the present flow, and is consistent with the conditional statistics for specific volume gradients in figures 5.21 and 5.22,

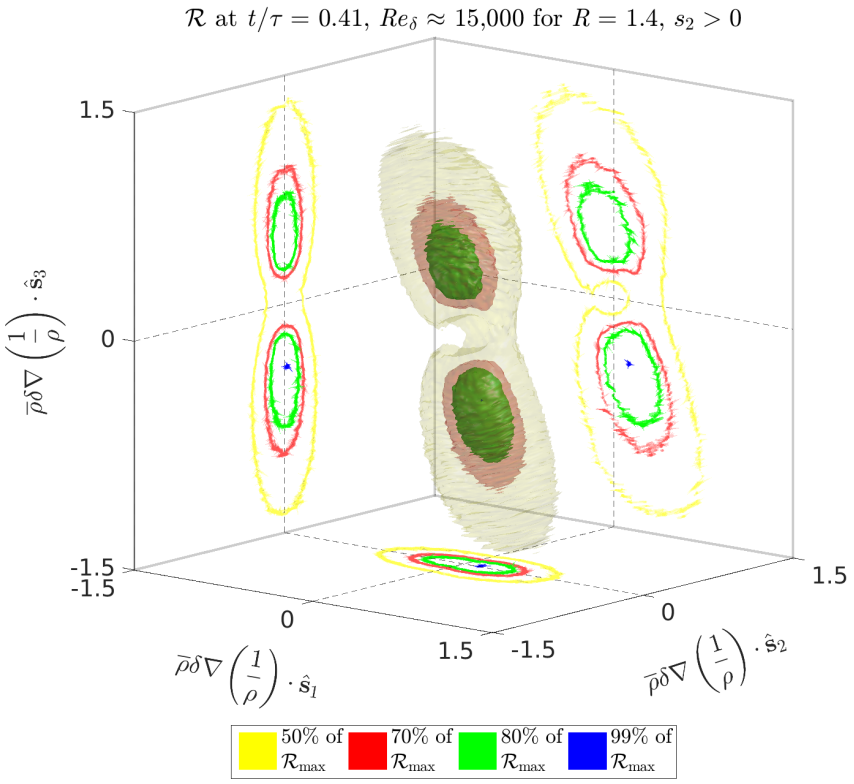

(a)

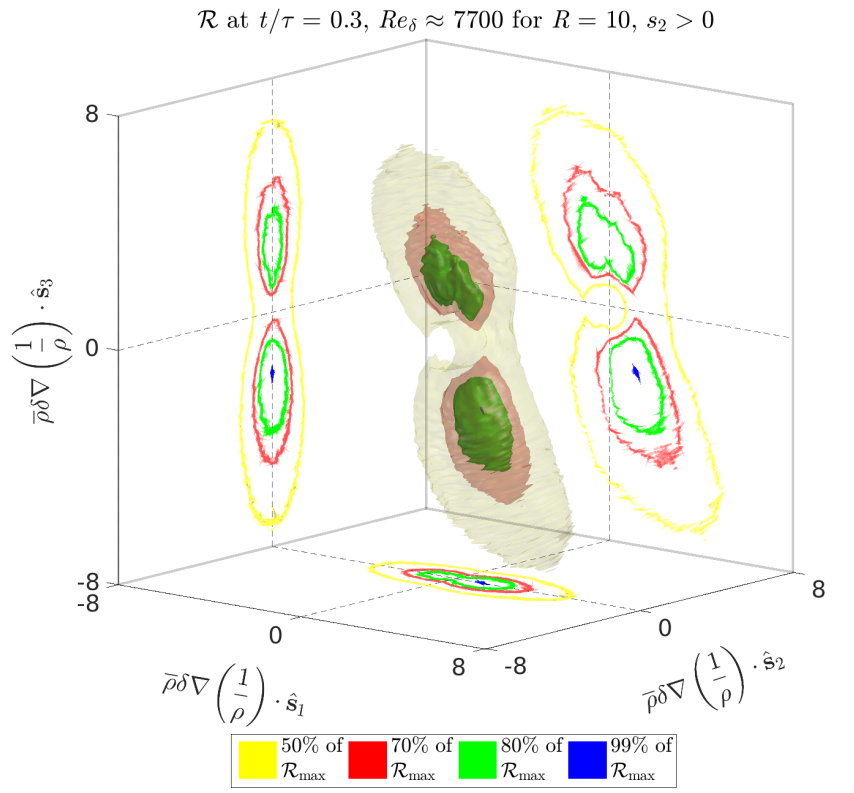

(b)

Figure 5.21: Conditional non-dimensional specific volume gradient $\mathcal{R}$ isosurfaces of mixed fluid (equation 4.1) in the local strain rate tensor eigenvector coordinate system for (*a*) $R = 1.4$ and (*b*) $R = 10$ at Reynolds numbers within or entering the fully developed turbulent regime. Statistics conditioned on the intermediate eigenvalue, $s_2 > 0$.

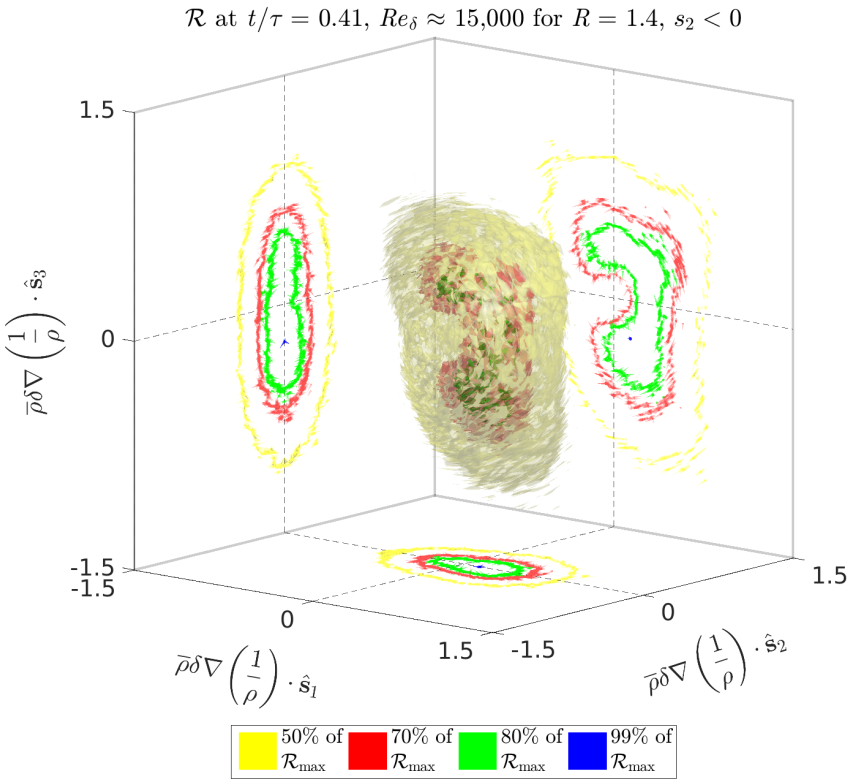

(a)

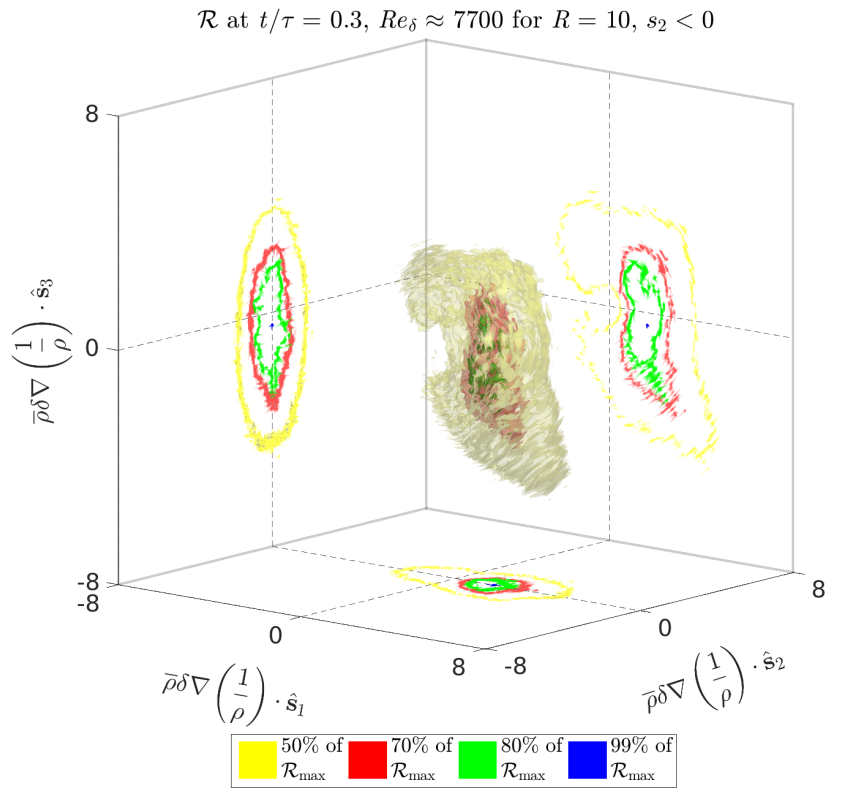

(b)

Figure 5.22: Conditional non-dimensional specific volume gradient $\mathcal{R}$ isosurfaces of mixed fluid (equation 4.1) in the local strain rate tensor eigenvector coordinate system for (*a*) $R = 1.4$ and (*b*) $R = 10$ at Reynolds numbers within or entering the fully developed turbulent regime. Statistics conditioned on the intermediate eigenvalue, $s_2 < 0$.

the unconditioned $\mathcal{R}$ statistics in figures 5.19 and 5.20, and with reported behavior for passive scalars in shear-driven flows.

The memory of flow initial conditions must be assessed. If the density gradient alignment is consistent in Cartesian coordinates from early-to-late times, then it is unclear that the flow is indeed in the fully developed turbulent regime. Figures 5.23 and 5.24 display the specific volume gradient $\mathcal{R}$ isosurface evolution in Cartesian coordinates for $R = 1.4$ in the diffusive regime (figure 5.23) through the unsteady transition (figure 5.24). As the flow becomes unsteady (figure 5.24), density gradients change significantly from the diffusive regime (figure 5.23), as the initial condition of $\nabla(1/\rho) \parallel \widehat{\boldsymbol{x}}$ is forgotten. Specific volume gradients in the unsteady regime are seen to align with $\pm\widehat{\boldsymbol{x}}$, instead of just with $\widehat{\boldsymbol{x}}$ in the diffusive regime, with larger variations in $\pm\widehat{\boldsymbol{y}}$.

Figure 5.25 displays the late-time $\mathcal{R}$ isosurfaces of specific volume gradients in Cartesian coordinates for $R = 1.4$ at a time well within the fully developed turbulent regime, and for $R = 10$ as the flow is entering fully developed turbulence. The specific volume gradient for both is in the $+\widehat{z}$ half-plane generally, *i.e.*, roughly parallel to $-\boldsymbol{g}$ as expected for a flow in a uniform acceleration field (buoyancy effects). However, aside from the gravitational driving force, the specific volume gradients show no affinity to the initial specific volume gradient field which is purely in $\widehat{\boldsymbol{x}}$ (figure 5.23a). This is inferred by the projection of the $\mathcal{R}$ isosurfaces onto the $(\widehat{\boldsymbol{x}}, \widehat{\boldsymbol{y}})$–plane being circular around the origin. No preferential alignment in this plane is observed.

Lastly, the specific volume gradients discussed in this section can be used to verify the assumption in section 5.2 that the irrotational component of velocity, equation 5.21 in equation 5.18, will be perpendicular to vorticity, *i.e.*, $\nabla(1/\rho) \perp \widehat{\boldsymbol{s}}_2$. With specific volume gradients mostly in the $(\widehat{\boldsymbol{s}}_1, \widehat{\boldsymbol{s}}_3)$–plane, the specific volume gradient is approximately perpendicular to $\widehat{\boldsymbol{s}}_2$, and this assumption is seen to hold, with some variations.

5.3.2 Pressure-gradient alignment

Pressure plays a different role than density, yet similar conditional behavior is observed. The pressure gradient can be separated into the hydrostatic, $\boldsymbol{\Gamma}$, and non-hydrostatic, ∇p, components. $\boldsymbol{\Gamma} \cong -\widehat{z}\rho_0 g$ to ensure the mean momentum is constant (and presently set to zero) in the presence of fluctuations. Initially, $|\boldsymbol{\Gamma}| \gg |\nabla p|$ and the hydrostatic component dominates the pressure-gradient field, corresponding to

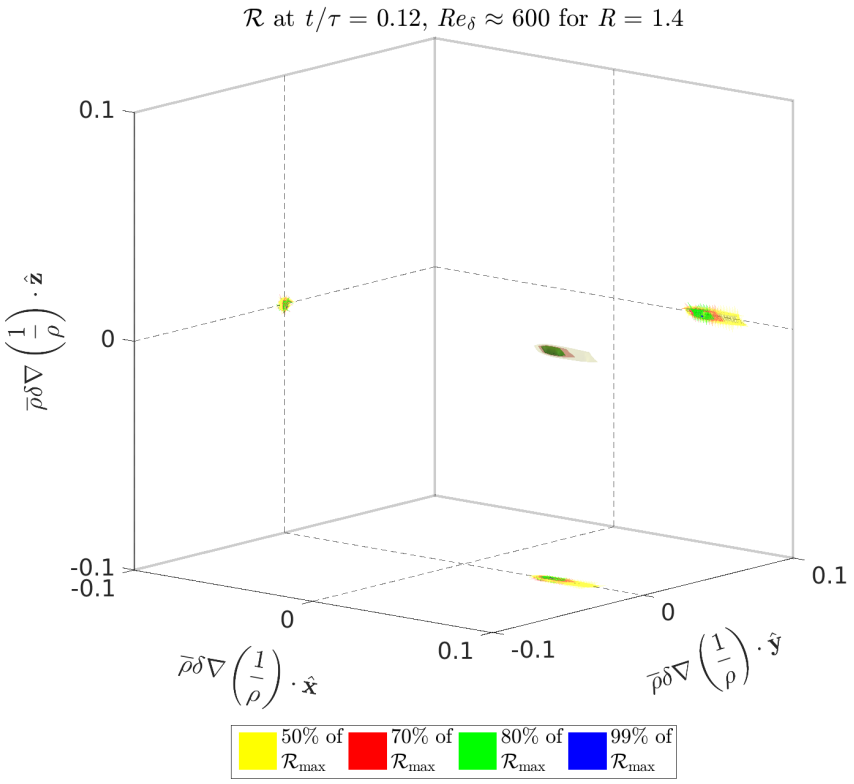

(a)

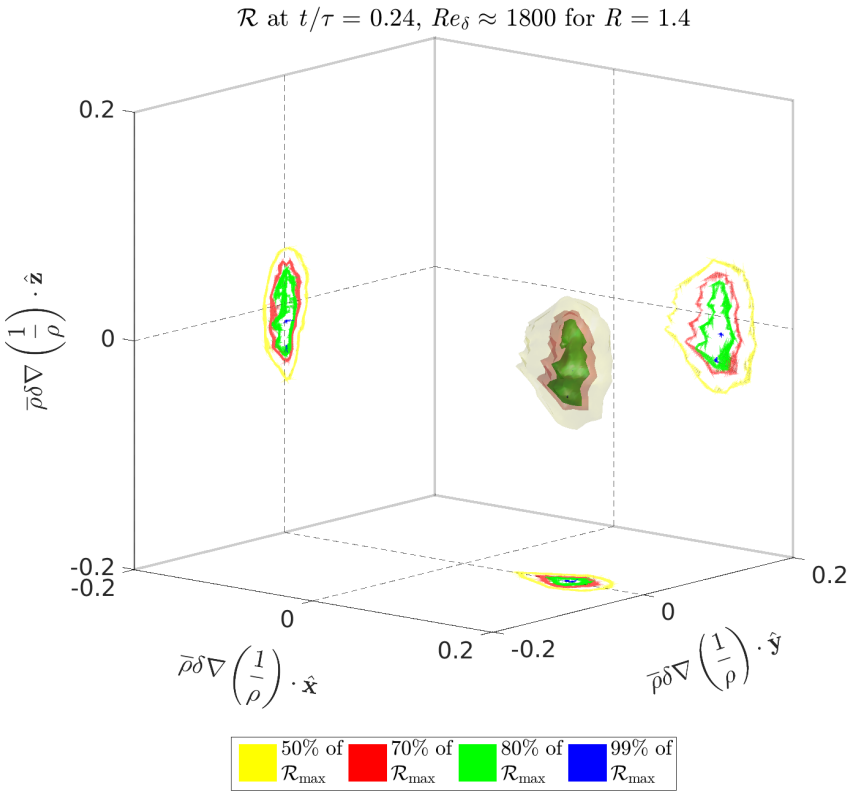

(b)

Figure 5.23: Non-dimensional specific volume gradient $\mathcal{R}$ isosurfaces of mixed fluid (equation 4.1) in Cartesian coordinates for $R = 1.4$ at (a) $t/\tau = 0.12$ and (b) $t/\tau = 0.24$ *i.e.*, early in the flow development. Plot in (a) is also in figure 5.6b.

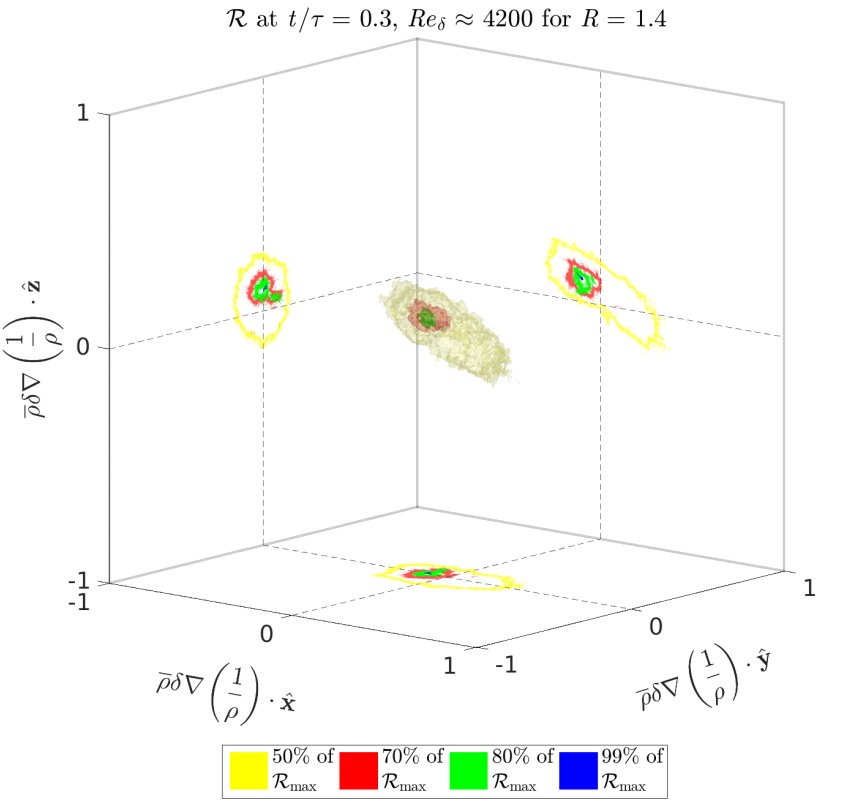

(a)

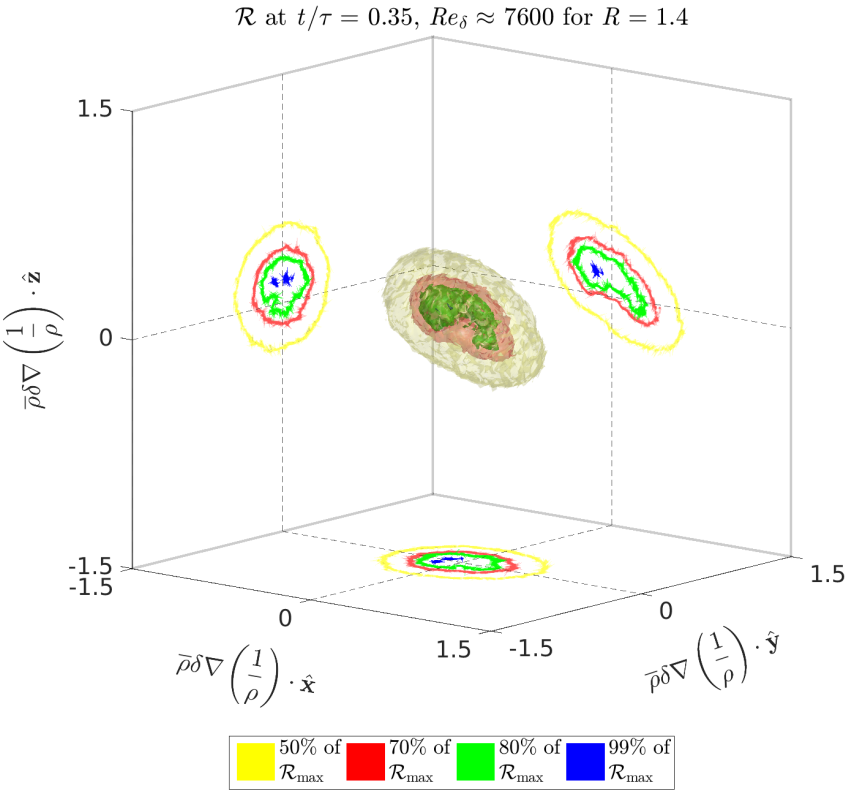

(b)

Figure 5.24: Non-dimensional specific volume gradient $\mathcal{R}$ isosurfaces of mixed fluid (equation 4.1) in Cartesian coordinates for $R = 1.4$ at (*a*) $t/\tau = 0.3$ and (*b*) $t/\tau = 0.35$ *i.e.*, around the unsteady regime transition.

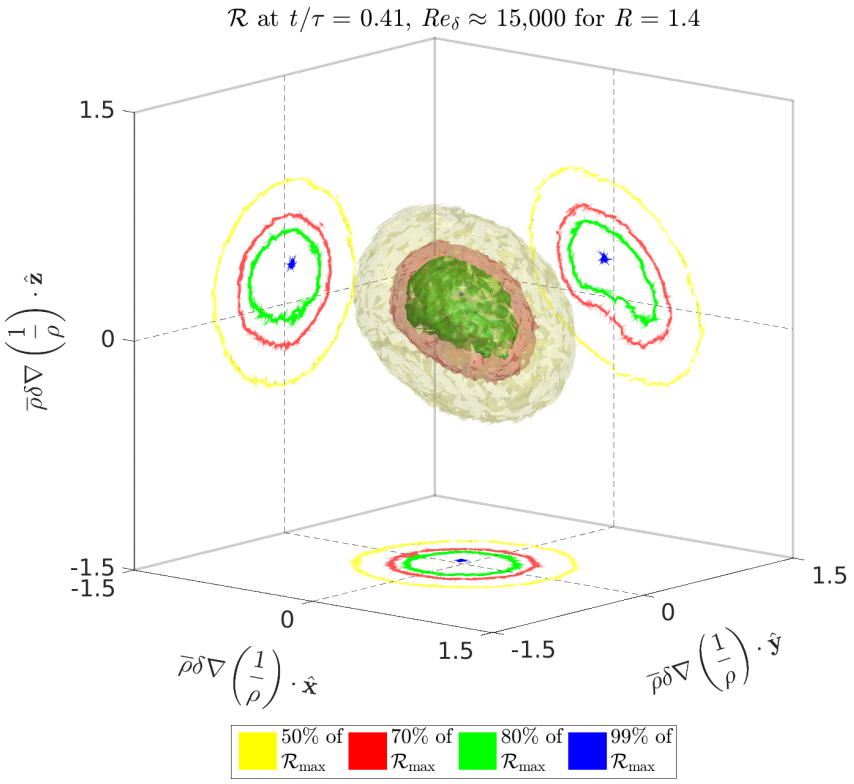

(a)

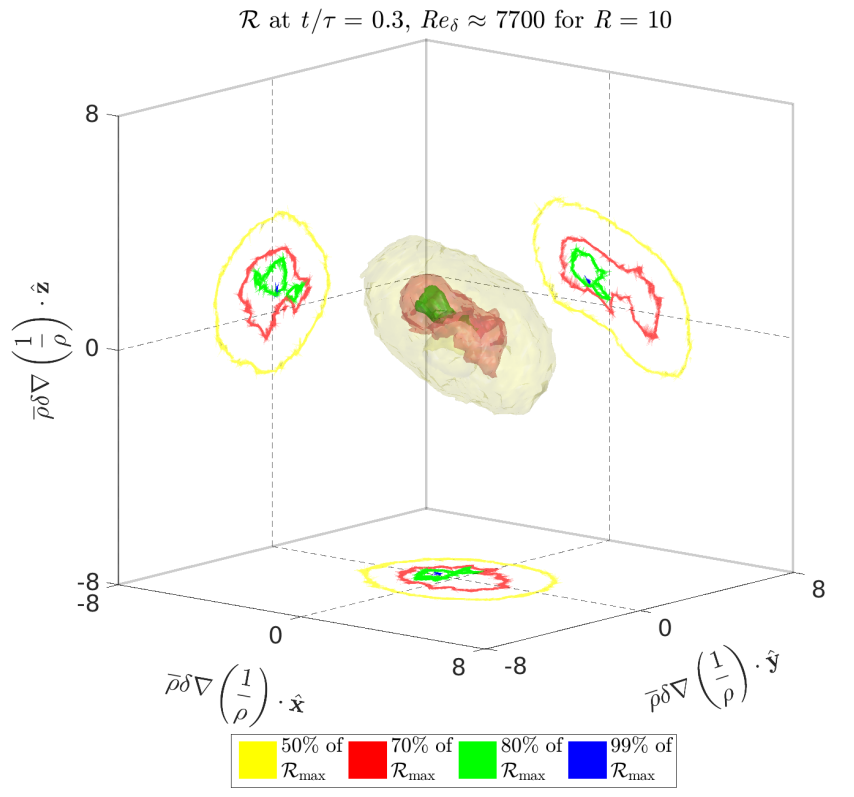

(b)

Figure 5.25: Non-dimensional specific volume gradient $\mathcal{R}$ isosurfaces of mixed fluid (equation 4.1) in Cartesian coordinates for (*a*) $R = 1.4$ and (*b*) $R = 10$ at Reynolds numbers within or entering the fully developed turbulence regime.

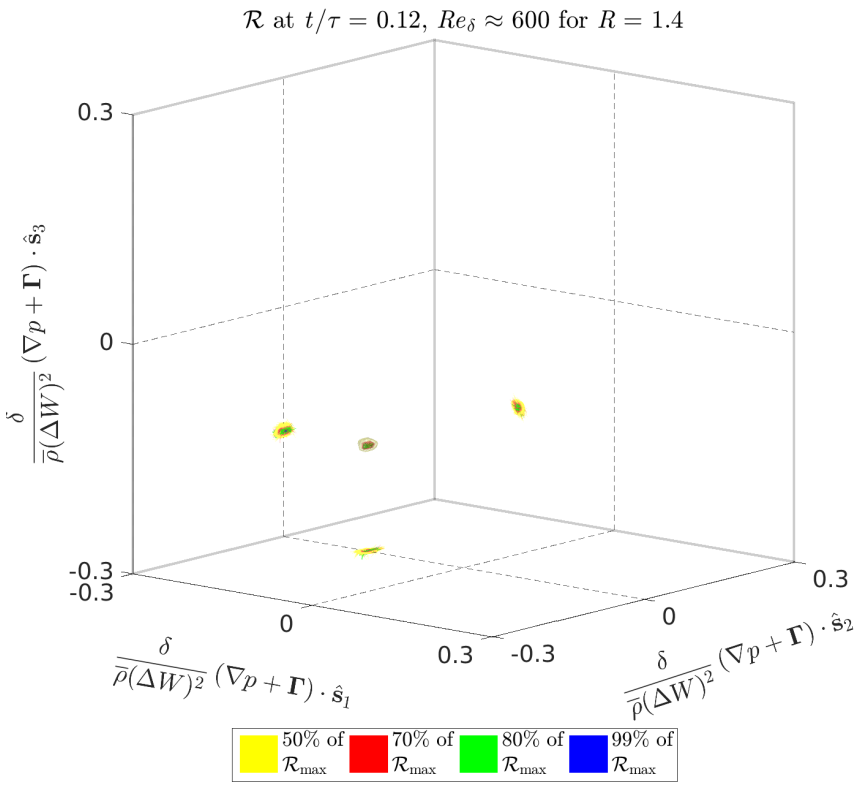

Figure 5.26: Non-dimensional pressure gradient $\mathcal{R}$ isosurfaces of mixed fluid (equation 4.1) in Cartesian coordinates for $R = 1.4$ at $t/\tau = 0.12$, *i.e.*, early in the flow development.

$\mathbf{\Gamma} + \nabla p \approx \mathbf{\Gamma} \parallel -(\widehat{s}_1 + \widehat{s}_3)/\sqrt{2}$, shown in figure 5.26 and is consistent with equation 5.14f, where the pressure gradient has been non-dimensionalized by $\delta/\overline{\rho}(\Delta W)^2$, double the dynamic pressure gradient scaling.

As the flow evolves to turbulence, the balance between ∇p and $\mathbf{\Gamma}$ changes in the shear layer as ∇p increases with respect to $\mathbf{\Gamma}$, depending on density ratio. $\mathbf{\Gamma}$ is (approximately) the hydrostatic component of the pressure gradient field, and as $R \to 1$, $\mathbf{\Gamma}$ should remain dominant over ∇p, as that is the sole pressure gradient contribution to the baroclinic torque in the Boussinesq approximation. Note that $\mathbf{\Gamma}$ is set to maintain a zero mean momentum, and is not a dynamic quantity like ∇p. To investigate the relative behavior of $\mathbf{\Gamma}$ with ∇p, $\mathbf{\Gamma}$ is approximated as $-\widehat{z}\rho_0 g$, which is not exact, as discussed in section 3.2. Only 'mixed-fluid' (equation 4.1) is considered since the free-streams will maintain $\mathbf{\Gamma} + \nabla p \approx \mathbf{\Gamma}$ until a shear layer has encroached across it, when the simulation is ended.

Figure 5.27a displays the ratio of mean magnitudes of ∇p to $\mathbf{\Gamma} + \nabla p$ versus At-

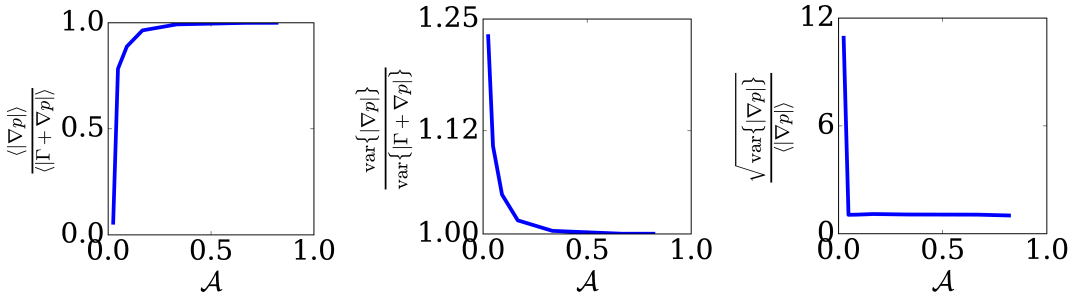

(a) (b) (c)

Figure 5.27: Ratio of (*a*) mean magnitude and (*b*) magnitude variance of ∇p to $\mathbf{\Gamma} + \nabla p$, and (*c*) square root of ∇p magnitude variance to its mean magnitude versus Atwood number, $\mathcal{A}$ (equation 3.9d). As $R \to \infty$, $\mathcal{A} \to 1$. Data shown are at the same Re_δ as in figure 5.18a, *i.e.*, differing for each R, but entering the fully-developed turbulent regime. Only mixed fluid (equation 4.1) is used in these statistics.

wood number, $\mathcal{A} = (R-1)/(R+1)$, equation 3.9d, for fluid considered 'mixed' (equation 4.1). As R increases, ∇p is seen to dominate $\mathbf{\Gamma} + \nabla p$ with the ratio of the mean magnitudes limiting to unity. This is also seen in figure 5.27b, which displays the ratio of magnitude variances of ∇p to $\mathbf{\Gamma} + \nabla p$ versus Atwood number. As R increases, the variance in ∇p equals that of $\mathbf{\Gamma} + \nabla p$, showing ∇p is the dominating term. Note that $\mathbf{\Gamma}$ is uniform across varying R and approximately constant. The magnitude variance of ∇p is larger than the magnitude variance of $\mathbf{\Gamma} + \nabla p$ at smaller R because $|\mathbf{\Gamma}| \gg |\nabla p|$, and when $\mathbf{\Gamma}$ is removed, so is the dominant direction of the total pressure gradient, increasing the variance. In short, ∇p grows to dominate $\mathbf{\Gamma}$ in the total pressure gradient in the turbulent regime as R increases.

Figure 5.27c displays the square root of the magnitude variance of ∇p to its magnitude. For $R \geq 1.1$, $\sqrt{\mathrm{var}\{|\nabla p|\}} \approx \langle|\nabla p|\rangle$, indicative of an exponential p.d.f. The $R = 1.05$ simulation was slightly too diffusive and did not reach the same turbulent behavior as the other density ratios, despite reaching $Re_\delta \approx 8400$. Figure 5.28a displays the one-dimensional p.d.f., $\mathcal{P}^{1D}$, of $|\nabla p|$ for seven density ratios at the same Re_δ as the data in figure 5.27, and an exponential p.d.f. is observed (note the logarithmic axes scaling). Data for the different density ratio simulations collapse when non-dimensionalized by the dynamic pressure scaling $\overline{\rho}\,(\Delta W)^2/\delta$.

When $\mathbf{\Gamma}$ is included in $\mathcal{P}^{1D}$ (figure 5.28b), the exponential distribution is only observed for the larger density ratios, since $\mathbf{\Gamma}$ has a larger effect on the lower density ratios, consistent with data shown in figure 5.27. $\mathbf{\Gamma}$ increases the most-probable

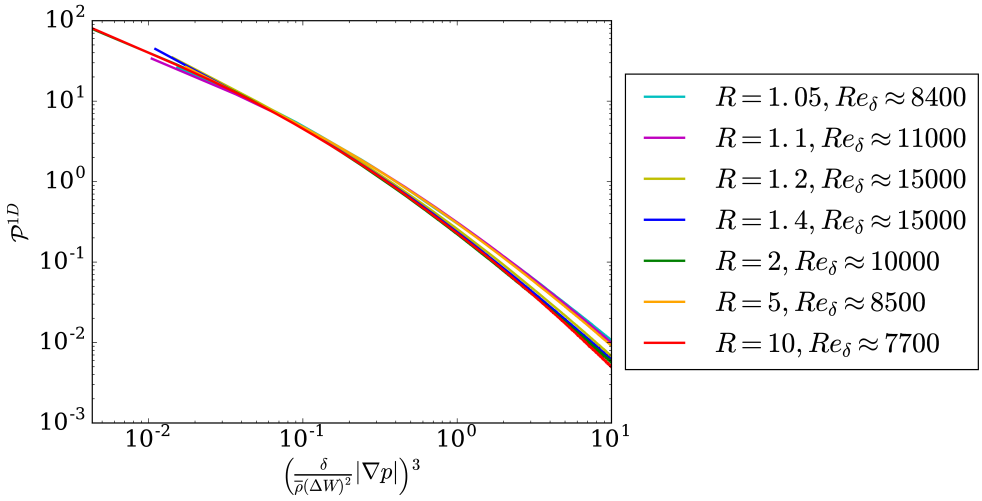

(a)

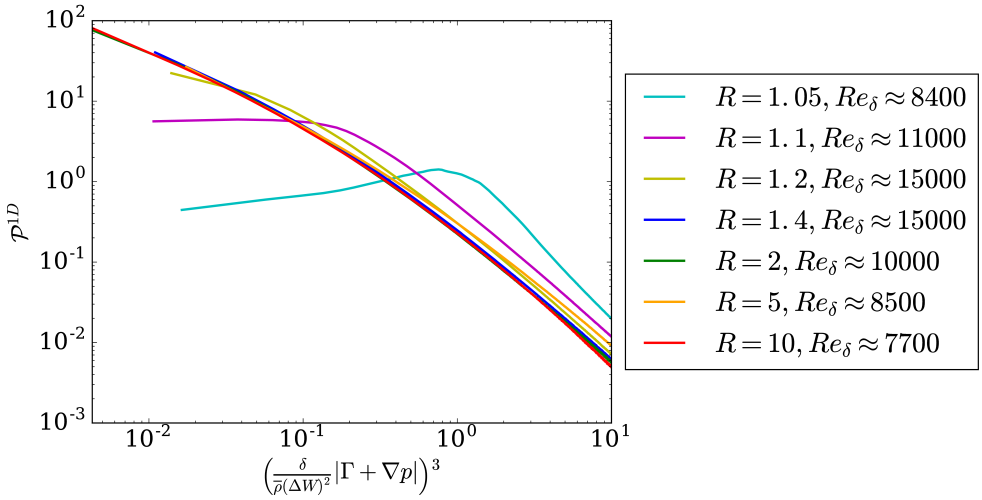

(b)

Figure 5.28: One-dimensional p.d.f.s of (*a*) ∇p and (*b*) $\mathbf{\Gamma} + \nabla p$ magnitudes within the mixed-fluid region (equation 4.1), non-dimensionalized by twice the dynamic pressure gradient scaling for seven density ratios.

magnitude of $\mathbf{\Gamma} + \nabla p$ as R decreases, widening those p.d.f.s. $\mathcal{P}^{1D}$ of the full pressure gradient magnitude for $R = 1.05$ shows a most-probable value at unity, or at $|\mathbf{\Gamma} + \nabla p| \approx |\mathbf{\Gamma}| \cong 1$, again displaying $|\mathbf{\Gamma}| \gg |\nabla p|$ at these lower-R simulations. At the Reynolds numbers plotted in figure 5.28b, the dynamic pressure scaling $\frac{\delta}{\overline{\rho}(\Delta W)^2} \sim 1$ for $R = 1.05$, and decreases as R increases since $(\Delta W)^2$ increases with R faster than $\overline{\rho}$ decreases with R, with similar shear-layer widths, δ, for the simulations at these Reynolds numbers, (variables discussed in chapter 4). As the scaling decreases, so does the location of $\frac{\delta}{\overline{\rho}(\Delta W)^2}|\mathbf{\Gamma}|$, seen with the most-probable hump location of $R = 1.1$ at a lower magnitude than that of $R = 1.05$, with a lower most-probable magnitude yet for $R = 1.2$. As ∇p begins to overtake $\mathbf{\Gamma}$, the hump from $\mathbf{\Gamma}$ becomes less visible (*i.e.*, for $R > 2$ in figure 5.28b).

Both plots in figure 5.28 show one-dimensional p.d.f.s calculated with bins spaced cubically in $|\nabla p|$. This is required to ensure no bias is imparted on the data from bin spacing, discussed further in appendix C. The p.d.f.s in figure 5.28, and all p.d.f.s in this work, normalize to unity when properly integrated (magnitude density functions $\mathcal{R}$, used throughout, do not normalize to unity). Additionally, only mixed fluid is used, *i.e.*, locations that satisfy the requirement in equation 4.1. Free-stream fluid that has not been encroached across by a shear layer has $\mathbf{\Gamma} \gg \nabla p$, with $\nabla p \approx 0$, but mixed fluid develops non-zero dynamic pressure gradients. If free-stream fluid was included in the p.d.f.s in figure 5.28, the p.d.f.s would continue to increase as $|\nabla p|$ reached zero.

Considering the behavior difference of $\mathbf{\Gamma} + \nabla p$ with R seen in figures 5.27 and 5.28, it may seems surprising that the alignment of $\boldsymbol{b}$ (a function of $\mathbf{\Gamma} + \nabla p$) with $\boldsymbol{\omega}$ is seen to be independent of R in figure 5.18b. To understand this, the alignment of $\mathbf{\Gamma} + \nabla p$ is investigated.

It has been reported that pressure gradients, ∇p, in homogeneous isotropic flows preferentially align at $\pm 45^\circ$ with the $\widehat{\boldsymbol{s}}_1$ and $\widehat{\boldsymbol{s}}_3$ eigenvectors, and at 90° with $\widehat{\boldsymbol{s}}_2$ (Ashurst, Kerstein, et al., 1987; Ashurst, Chen, and Rogers, 1987), with some variations (Kalelkar, 2006). As ∇p overtakes $\mathbf{\Gamma}$ as R increases in the present flow, pressure gradients agree somewhat with these studies, even though this setup is anisotropic in all three Cartesian directions and homogeneous in only two dimensions. $\mathcal{R}$ pressure gradient isosurfaces are shown in figures 5.29 and 5.30 for four density ratios at late times. As R increases, $\mathbf{\Gamma} + \nabla p$ aligns with other 45° lines with the $\widehat{\boldsymbol{s}}_1$ and $\widehat{\boldsymbol{s}}_3$ eigenvectors, aside from that which aligns with $\mathbf{\Gamma}$. This indicates that ∇p is starts to overtake $\mathbf{\Gamma}$ as R increases, consistent with data in figure 5.27.

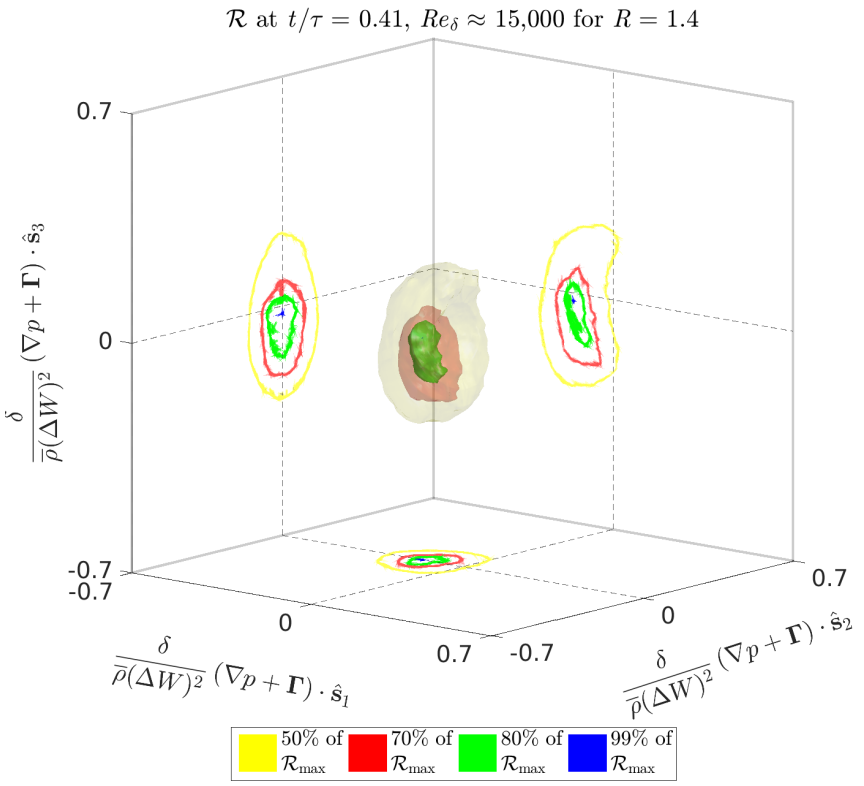

(a)

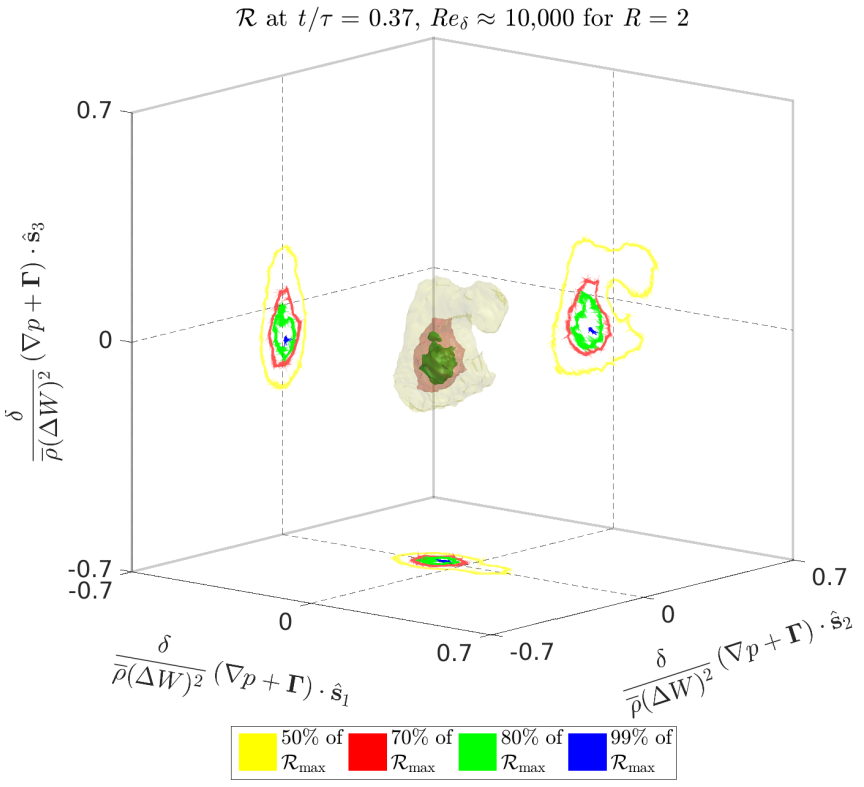

(b)

Figure 5.29: Non-dimensional pressure gradient $\mathcal{R}$ isosurfaces of mixed fluid (equation 4.1) in the local strain rate tensor eigenvector coordinate system for (*a*) $R = 1.4$ and (*b*) $R = 2$ at Reynolds numbers within the fully developed turbulent regime.

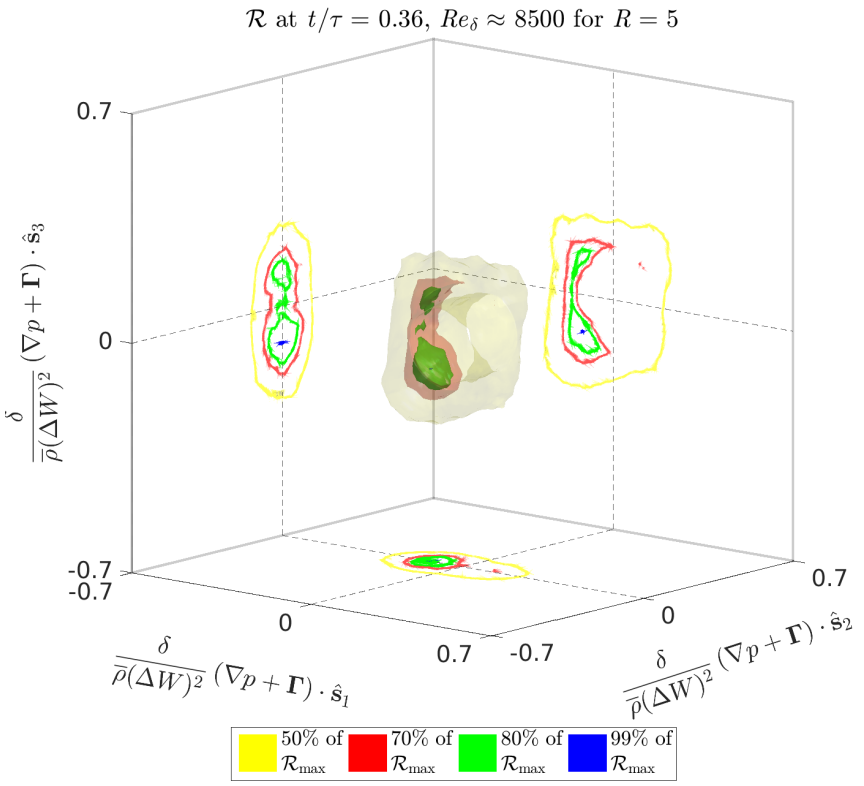

(a)

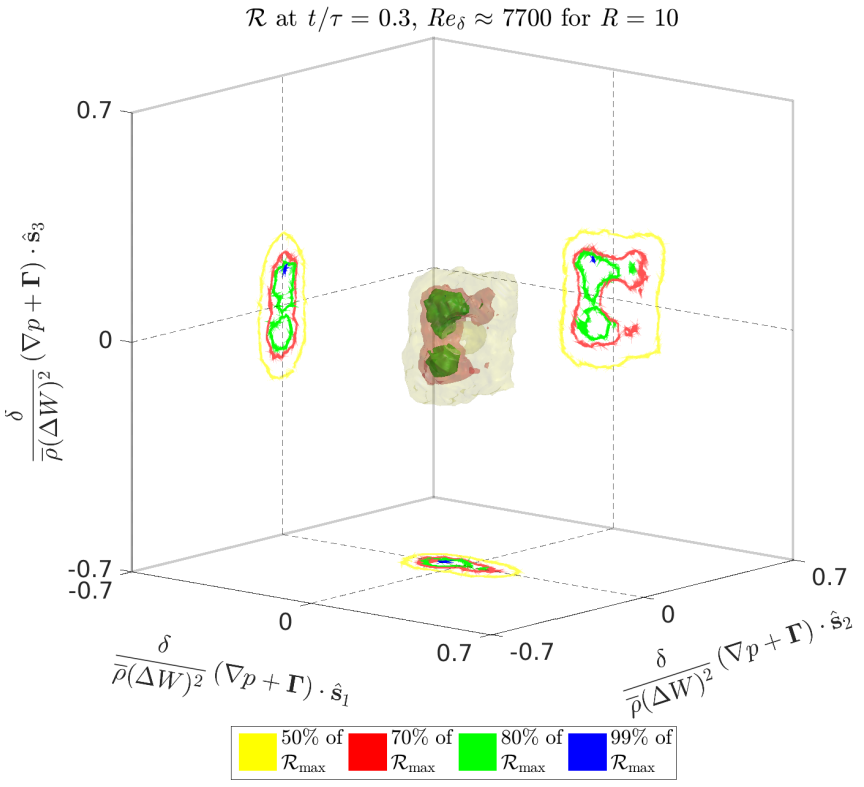

(b)

Figure 5.30: Non-dimensional pressure gradient $\mathcal{R}$ isosurfaces of mixed fluid (equation 4.1) in the local strain rate tensor eigenvector coordinate system for (*a*) $R = 5$ and (*b*) $R = 10$ at the highest Reynolds numbers attained for these density ratios, entering the fully developed turbulent regime.

Pressure gradient alignments can be explained in terms of the momentum equation. First, assume that in high-Reynolds-number turbulent regime, the viscous terms are negligible. Next, in the mixing region, away from the free streams, the Lagrangian time derivative,

$$\frac{\partial \rho \boldsymbol{u}}{\partial t} + \nabla \cdot \rho \boldsymbol{u}\boldsymbol{u} \sim \frac{\overline{\rho}(\Delta W)^2}{\delta}, \tag{5.27}$$

which will be balanced by the fluctuating pressure gradient since the mean pressure gradient, $\boldsymbol{\Gamma}$ balances the body force term, *i.e.*, $\boldsymbol{\Gamma} \sim O(\widehat{\boldsymbol{z}}\,\rho g)$. $\nabla p \sim \overline{\rho}(\Delta W)^2/\delta$, where $(\Delta W)^2$ increases quadratically with R, *i.e.*, the ∇p contribution to the total pressure gradient, $\boldsymbol{\Gamma} + \nabla p$ will increase with R. Using the mass conservation equation,

$$\frac{\partial \rho \boldsymbol{u}}{\partial t} + \nabla \cdot \rho \boldsymbol{u}\boldsymbol{u} = \rho \left(\frac{\partial \boldsymbol{u}}{\partial t} + \boldsymbol{u} \cdot \nabla \boldsymbol{u} \right), \tag{5.28}$$

which can be analyzed in the strain rate field eigenvector frame using equation 5.20 with $\boldsymbol{\omega}(\boldsymbol{x}) = \omega_0(\boldsymbol{x})\widehat{\boldsymbol{s}}_2$ and equation 5.18 without the gradient, *i.e.*,

$$\boldsymbol{u}(\boldsymbol{x}, t) = \frac{1}{4\pi} \int_{\boldsymbol{x}'} \boldsymbol{\omega}(\boldsymbol{x}', t) \times \frac{\boldsymbol{x} - \boldsymbol{x}'}{|\boldsymbol{x} - \boldsymbol{x}'|^3} \mathrm{d}^3\boldsymbol{x}' + \nabla\phi, \tag{5.29}$$

which yields

$$\boldsymbol{u} = \begin{bmatrix} \checkmark & 0 & \checkmark \end{bmatrix} \tag{5.30}$$

and then

$$\boldsymbol{u} \cdot \nabla \boldsymbol{u} = \begin{bmatrix} \checkmark & 0 & \checkmark \end{bmatrix}, \tag{5.31}$$

where again the check-marks denote non-zero components of the vectors. Since ρ enters equation 5.28 as a scalar, it does not rotate the Lagrangian derivative alignment, and since the attendant alignment of $\boldsymbol{\omega}$ with $\widehat{\boldsymbol{s}}_2$ is seen to be relatively constant in time (section 5.2), $\partial \boldsymbol{u}/\partial t$ should also follow the alignment of 5.30. Depending on the signs of $\nabla \boldsymbol{u}$ and $\boldsymbol{u}$, ∇p (and thus, $\boldsymbol{\Gamma} + \nabla p$) will align at $\pm 45°$ angles in the $(\widehat{\boldsymbol{s}}_1, \widehat{\boldsymbol{s}}_3)$–plane, with alignments other than $-(\widehat{\boldsymbol{s}}_1 + \widehat{\boldsymbol{s}}_3)/\sqrt{2}$, *i.e.*, $-\widehat{\boldsymbol{z}}$, dominating as R increases, as seen in figures 5.29 and 5.30. Since ∇p aligns in the $(\widehat{\boldsymbol{s}}_1, \widehat{\boldsymbol{s}}_3)$–plane, as does $\boldsymbol{\Gamma}$, cross products with $\nabla(1/\rho)$ with $\boldsymbol{\Gamma} + \nabla p$ will align in $\widehat{\boldsymbol{s}}_2$, independently of R. Magnitudes of $\boldsymbol{b}$ may change with R from ∇p, but not directions, as indicated in figure 5.18b, which displays relative directional alignments between $\boldsymbol{b}$ and $\boldsymbol{\omega}$.

Figures 5.31 and 5.32 display the conditional $\mathcal{R}$ isosurfaces of pressure gradients based on the strain rate intermediate eigenvalue sign for $R = 1.4$ and 10. As with the conditional density-gradient statistics, when $s_2 < 0$ (figure 5.32), the pressure gradient is more contracted, aligning at larger angles to $\pm\widehat{\boldsymbol{s}}_3$ and smaller angles to

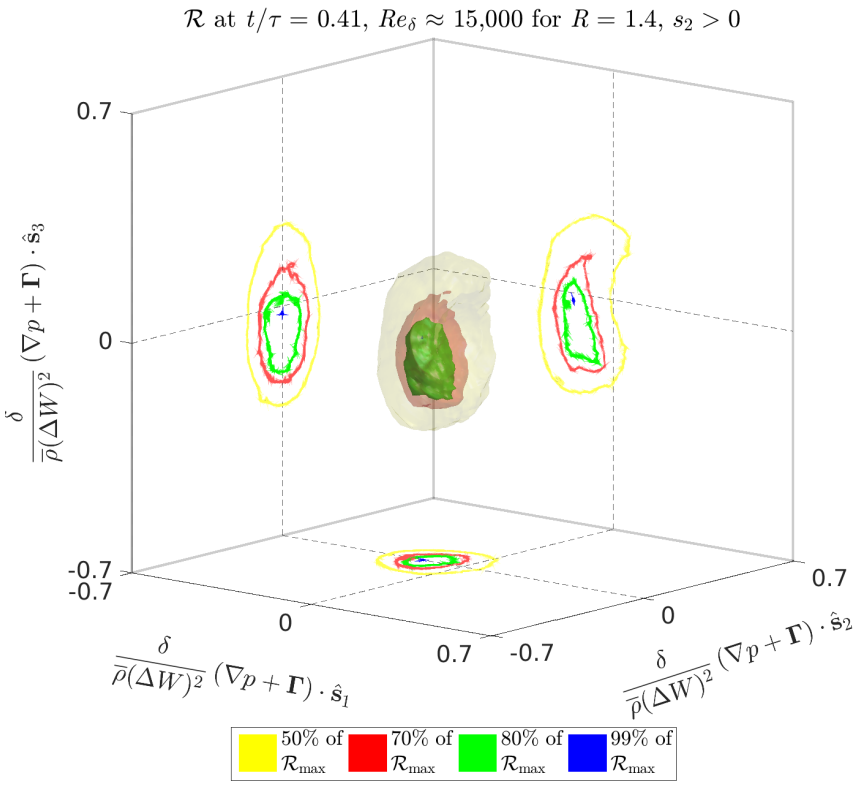

(a)

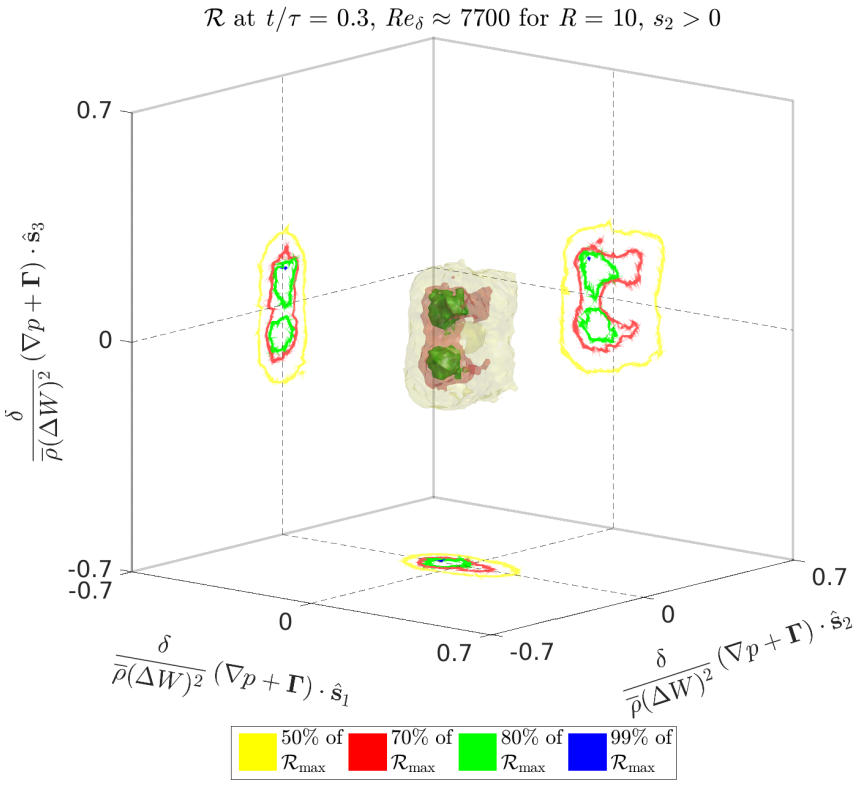

(b)

Figure 5.31: Conditional non-dimensional pressure gradient $\mathcal{R}$ isosurfaces of mixed fluid (equation 4.1) in the local strain rate tensor eigenvector coordinate system for (*a*) $R = 1.4$ and (*b*) $R = 10$ at Reynolds numbers within or entering the fully developed turbulent regime. Statistics conditioned on the intermediate eigenvalue, $s_2 > 0$.

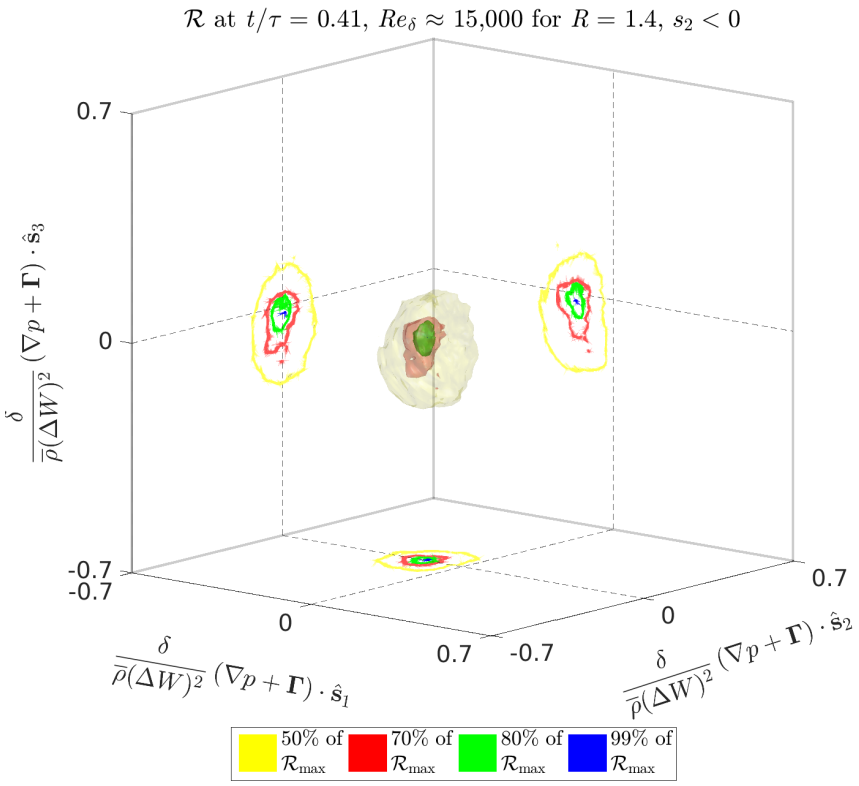

(a)

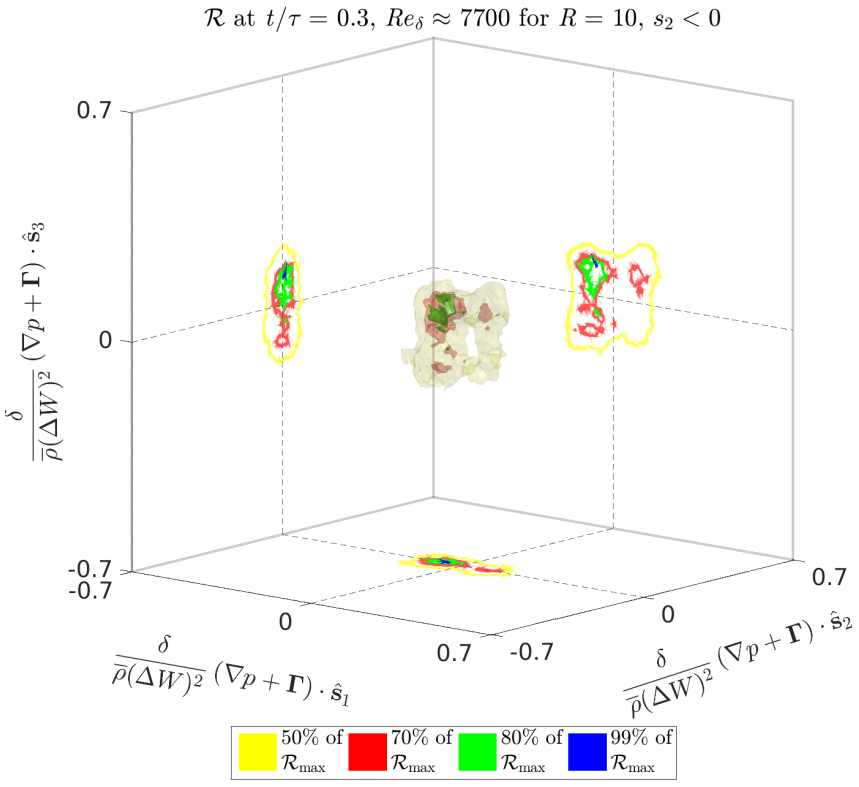

(b)

Figure 5.32: Conditional non-dimensional pressure gradient $\mathcal{R}$ isosurfaces of mixed fluid (equation 4.1) in the local strain rate tensor eigenvector coordinate system for (*a*) $R = 1.4$ and (*b*) $R = 10$ at Reynolds numbers within or entering the fully developed turbulent regime. Statistics conditioned on the intermediate eigenvalue, $s_2 < 0$.

$\pm\widehat{\boldsymbol{s}}_1$ than the pressure gradients conditioned on $s_2 > 0$ (figure 5.31). Pressure is seen here to have a dynamic role, *i.e.*, the dynamic component of the pressure gradient, ∇p, is affected by the strain rate field in a similar way to the specific volume gradient, and similar arguments on the conditional alignment statistics can be made.

With density gradients and pressure gradients statistically aligning in the $(\widehat{\boldsymbol{s}}_1, \widehat{\boldsymbol{s}}_3)$–plane, it can be inferred that their cross product, $\nabla\,(1/\rho) \times (\boldsymbol{\Gamma} + \nabla p)$, *i.e.*, baroclinic torques, will align with $\pm\widehat{\boldsymbol{s}}_2$, as seen in figures 5.16 and 5.17. The different signs of baroclinic torques are consequences of the density gradient signs in the turbulent regime.

Vorticity has been shown to align with $\widehat{\boldsymbol{s}}_2$ for flows without strong externally imposed shear in uniform density flows, *i.e.*, no baroclinic torques (*e.g.*, Ashurst, Kerstein, et al., 1987; Verma and Blanquart, 2014) and the argument for that, extending to variable-density flow has been discussed above. We have shown that, when the degeneracy of the strain rate tensor eigenvectors is exploited for vector field comparisons, vorticity aligns with $-\widehat{\boldsymbol{s}}_2$, the chosen sign for $\widehat{\boldsymbol{s}}_2$ with $\boldsymbol{\omega}$, collapsing data and creating a reference between Cartesian and strain rate eigenvector coordinates, as well as between $\boldsymbol{\omega}$ and other variables like baroclinic torques. Baroclinic torques, $\boldsymbol{b}$, are seen to align with $\pm\widehat{\boldsymbol{s}}_2$, however, $\boldsymbol{b}$ and $\boldsymbol{\omega}$ are actually misaligned in the majority of the mixed-fluid locations in the turbulent regime. The attendant role of baroclinic torques is thus to change vorticity magnitude, and its direction.

Chapter 6

CONCLUSIONS

Results of direct numerical simulation (DNS) of a variable-density flow at zero Mach number subject to a uniform acceleration field are presented in a novel configuration, with density ratios in the range $1.005 \leq R \leq 10$. The downward acceleration acts on initially vertical slabs of high-density fluid, in between vertical slabs of low-density fluid, in a triply periodic cubic flow domain. Initially horizontal density gradients are acted on by the acceleration-induced vertical pressure gradient, producing baroclinic torques that generate vorticity and shear-layer growth. The simulated flow attains Reynolds numbers that are approaching the fully developed turbulent regime with $Re_{\delta,\max} \approx 20{,}000$.

Simulations are in an accelerating frame in which the mean momentum is constant and maintained to be zero, facilitating imposed force accounting. In that frame, the acceleration dictates the vertical shear-layer large-scale structure convection velocity, W_c. An empirical relation obtained for W_c predicts the observed entrainment ratio and dominant mixed-fluid composition statistics, in accord with the self-similar mass conservation equation.

An equation for $\Delta W = |W_1 - W_2|$, the difference of the free-stream vertical velocities as a function of time, $\Delta W(t/\tau)/(\ell/\tau) = \underline{\mathrm{fn}}(t/\tau; R, \beta)$, is derived and solved. The theory is confirmed by simulation for all values of R studied, provided unmixed free-stream fluid remains on both sides of the shear layers.

Two phenomena cause shear-layer growth: diffusion and turbulent eddy growth. Diffusion dominates in a first regime, yielding a growth rate of $\delta/\delta_i = \sqrt{(t + t_i)/t_i}$. A subsequent regime is dominated by unsteady eddy growth, leading to turbulence. Shear-layer growth in this regime is found to scale approximately as the cube of time, *i.e.*, $\delta(t)/\delta_{tr} \simeq [(t + t_i)/(t_{tr} + t_i)]^3$, where δ_{tr} is the shear-layer thickness at the transition time to the unsteady/turbulent regime, t_{tr}.

The cubic shear-layer growth time dependence represents a new result, to the best of our knowledge. This unsteady/turbulent shear-layer growth is traceable to a fixed length scale, ℓ, that in turn defines a fixed characteristic flow time, τ. The

Chapter adapted from Gat et al., 2017

(horizontal width) growth rate then becomes, $\mathrm{d}\delta/\mathrm{d}(t/\tau) \propto \mathcal{A}\, g\, t^2$, consistent with the observed cubic growth in time. Notably, the vertical extent of a Rayleigh–Taylor mixed-fluid region grows quadratically in time, *i.e.*, a linear growth of its derivative, $\mathrm{d}h_{\mathrm{RT}}/\mathrm{d}t \propto t$, as with the linear growth in time of all vertical velocities in the flow studied here.

In the unsteady/turbulent regime, composition p.d.f.s within the shear layers exhibit a slightly tilted and constant in time ('non-marching') hump, (approximately) corresponding to the most probable mole fraction. The shear layers preferentially entrain low-density fluid by volume, as noted previously (Dimotakis, 1986; Livescu and Ristorcelli, 2007, 2008), and this is reflected in the mixed-fluid composition observed for all density ratios investigated in this flow.

For non-uniform-density flows, spectra of the kinetic energy must include the local density, *i.e.*, ρu^2, as opposed to the specific kinetic energy, u^2 (ignoring factors of $1/2$). This is addressed via the spatial autocorrelation of $\boldsymbol{j} = \rho^{1/2}\boldsymbol{u}$ and its spectra. Scaling the latter with $\overline{\rho}$, the mean density in the shear-layer mixed-fluid region, yields spectra similar to specific kinetic energy spectra. The specific vorticity, $\boldsymbol{\omega}/\rho$, obviating dealing with dilatation as a separate effect in flows extending to high density ratios, was also studied. Spectra of fluctuating specific vorticity are found to be very nearly similar to scaled fluctuating vorticity spectra. Other statistics, such as entrainment ratio and shear-layer composition p.d.f.s, that depend on density ratio are found to be in accord with previous theory predictions.

Previous work suggests that vorticity in uniform-density flows is preferentially aligned with the intermediate eigenvector of the local strain rate tensor (*e.g.*, Ashurst, Kerstein, et al., 1987; Ohkitani, 2002; Lüthi, Tsinober, and Kinzelbach, 2005; Guala et al., 2005; Hamlington, Schumacher, and Dahm, 2008; Meneveau, 2011; Verma and Blanquart, 2014). The same preferential alignment of vorticity is found in the present flow, at all density ratios, with some variability that decreases as R increases.

Alignment statistics are displayed in terms of three-dimensional plots that depict relevant information in a compact manner. Vorticity in variable-density flow is subject to baroclinic torques that are absent in uniform-density flows. A new finding is that baroclinic torques are also preferentially aligned with the eigenvector corresponding to the intermediate eigenvalue of the local strain rate tensor; however, they preferentially align with $\pm\boldsymbol{\omega}$. Even with this preferential alignment between $\boldsymbol{b}$ and $\boldsymbol{\omega}$, the two are misaligned in the majority of the mixed-fluid locations.

Density- and pressure-gradient statistics are studied in terms of the baroclinic torque alignments. Even though the studied flow has variable density, density-gradient alignments bear similarities to those of passive scalar gradients in uniform-density shear-driven flows. Pressure-gradient alignments follow behavior reported for isotropic and homogeneous flows, when R increases and ∇p grows to dominate $\mathbf{\Gamma}$. The cross product of the two fields, or the baroclinic torque, aligns with $\pm\widehat{\boldsymbol{s}}_2$, with a stronger affinity to $-\widehat{\boldsymbol{s}}_2$, similarly to vorticity. Again, signs of the strain rate tensor eigenvectors are chosen, since the strain rate tensor eigenvectors form lines in space, not directions. Even though $\boldsymbol{b}$ and $\boldsymbol{\omega}$ preferentially align with $\widehat{\boldsymbol{s}}_2$, they are misaligned with each other in the majority of the flow locations. The main dynamic role of baroclinic torque is to change vorticity magnitude and direction, which is important for turbulence modeling.

In conclusion, the baroclinic-vorticity-generated flow described in this work exhibits novel dynamics in the mean-flow statistics. Some attributes, such as the mixed-fluid statistics, can be mapped to those for uniform-density flows, such as spectral scaling and density-gradient alignments (in terms of passive scalars), regardless of the density ratio, R, extending to the Boussinesq limit, *i.e.*, $R = 1 + \varepsilon$, as $\varepsilon \to 0$. The mean-flow statistics are unique to the flow topology, whereas the mixed-fluid statistics have similarities to other flows and are less sensitive to flow topology. This confirms the premise for small-scale modeling, like in LES: large scales are unique and must be directly computed, while small scales are less unique and are amenable to modeling.

Chapter 7

FUTURE WORK

Further analysis of the flow studied can be done, especially with regards to relative alignments of $\boldsymbol{b}$ and $\boldsymbol{\omega}$. It was shown that their relative alignments were independent of density ratio, R, in figure 5.18b. This insensitivity to R can be investigated further. Additionally, understanding the alignment of $\boldsymbol{b}$ with $\boldsymbol{\omega}$ conditioned on kinetic energy dissipation would be of interest in understanding their relative behaviors. The role of ∇p in $\boldsymbol{b}$ can also be studied in more depth. Particularly, the decomposition of the pressure gradient into a mean pressure gradient, $\boldsymbol{\Gamma}$ and a fluctuating component, ∇p can be studied in more depth. $\boldsymbol{\Gamma}$ is not a dynamical quantity, whereas the fluctuating component, ∇p, is. A better understanding of the influence of $\boldsymbol{\Gamma}$ on the flow is needed, as well as a more in-depth investigation into the reasoning behind the exponential probability density function of $|\nabla p|$ (figure 5.28a).

The work described throughout this thesis provides details of variable-density turbulence which can be applied to variable-density SGS augmentations in LES modeling. As noted, there are many variable-density effects that can be scaled out, such as the spectral scaling, but some that cannot, such as shear-layer growth. To test a SGS model on this flow, the following metrics could be used: the eye norm (does the flow look smooth?), correct mean shear-layer density obtainment, and correct shear-layer width growth rates.

There are some corrections to the Smagorinsky model and SVM for buoyancy-driven flow (Lilly, 1962; Chung and Matheou, 2014; Matheou and Chung, 2014; Matheou, 2016). However, in the flow studied, the relative accelerations can be much larger than the imposed uniform acceleration fields. For example, the Lagrangian acceleration, $\boldsymbol{a}$,

$$\boldsymbol{a} = \frac{\mathrm{D}\boldsymbol{u}}{\mathrm{D}t} \tag{7.1}$$

has a magnitude density function, $\mathcal{R}$, shown in figure 7.1. For the $R = 1.4$ case, figure 7.1a, there is some degree of alignment of $\boldsymbol{a}$ at $\pm 45^\circ$ with the $(\widehat{\boldsymbol{s}}_1, \widehat{\boldsymbol{s}}_3)$–plane, which can partially be explained by the uniform acceleration field, $\boldsymbol{g}$, with differing directions for the light fluid moving up and heavy fluid moving downwards. However, as density ratio increases to $R = 10$, figure 7.1b, there are no such alignments. The Lagrangian acceleration has been studied in some detail for isotropic

homogeneous turbulence (*e.g.*, Monin and Yaglom, 1975; Voth, Satyanarayan, and Bodenschatz, 1998; Vedula and Yeung, 1999; Tsinober, Vedula, and Yeung, 2001; Sawford et al., 2003; Hill, 2002; Pope, 2002; Beck, 2003; Friedrich, 2003; Mordant, Crawford, and Bodenschatz, 2004; Biferale et al., 2004; Liberzon et al., 2012), with some showing that it is possible for $|\boldsymbol{a}| = 1{,}500|\boldsymbol{g}|$ (La Porta et al., 2001). However, in these cases, $\boldsymbol{a}$ is reported to align with $\pm 45^\circ$ in the $(\widehat{\boldsymbol{s}}_1, \widehat{\boldsymbol{s}}_3)$–plane (Liberzon et al., 2012), as seen for the $R = 1.4$ case (figure 7.1a), but not for $R = 10$. The $\boldsymbol{a}$ alignments at large R still need to be understood. As in the main text, the degeneracy of the strain rate tensor eigenvectors has been exploited in figure 7.1, with eigenvector signs chosen as discussed in section 5.1.

The alignment variation with R of Lagrangian acceleration can be used to extend the SGS buoyancy models to account for relative accelerations, as noted by Professor Paul Dimotakis.

In addition to the SGS acceleration implementation into SGS models, there may be other augmentations needed to account for variable-density affects. For example, the SVM relies on the Lundgren spiral vortex solution (Lundgren, 1982), and assumes uniform-density flow at the subgrid scale with equally distributed kinetic energy around the vortex, which is uniform in the vortex direction (Pullin and Saffman, 1994). The uniform-density flow assumption can be relaxed. The SVM uses the simplification that the spectrum of vorticity can be related to energy spectra, $S_{\omega\cdot\omega} = k^2 S_{\boldsymbol{u}\cdot\boldsymbol{u}}$, which is not the case when $\nabla \cdot \boldsymbol{u} \neq 0$, as it is in variable-density flow. In variable-density flow, following equation 4.20, and extending to three-dimensional Fourier transforms,

$$\begin{aligned} S_{\omega_i\omega_i} &= k_j k_j \mathcal{F}\{u_i(\boldsymbol{x},t)\}\mathcal{F}^*\{u_i(\boldsymbol{x},t)\} - k_j k_i \mathcal{F}\{u_i(\boldsymbol{x},t)\}\mathcal{F}^*\{u_j(\boldsymbol{x},t)\} \\ &= k^2 S_{u_i u_i} - k_j k_i S_{u_i u_j} \end{aligned} \tag{7.2}$$

where the latter term can be set to zero if $\nabla \cdot \boldsymbol{u} = 0$, with surface integrals of the velocity field being zero in the periodic domain. The above equation can be obtained by noting that the autocorrelation of vorticity is related to velocity with

$$\begin{aligned} \overline{\omega_i'(\boldsymbol{x}+\boldsymbol{x}',t)\omega_i'(\boldsymbol{x},t)} &= \int_{\boldsymbol{x}} \omega_i'(\boldsymbol{x}+\boldsymbol{x}',t)\omega_i'(\boldsymbol{x},t)\mathrm{d}\boldsymbol{x} \\ &= \int_{\boldsymbol{x}} \left\{ \left[\frac{\partial}{\partial x_j} u_k'(\boldsymbol{x}+\boldsymbol{x}',t)\right]\left[\frac{\partial}{\partial x_j} u_k'(\boldsymbol{x},t)\right] \right. \\ &\qquad \left. - \left[\frac{\partial}{\partial x_j} u_k'(\boldsymbol{x}+\boldsymbol{x}',t)\right]\left[\frac{\partial}{\partial x_k} u_j'(\boldsymbol{x},t)\right] \right\} \mathrm{d}\boldsymbol{x}\,, \end{aligned} \tag{7.3}$$

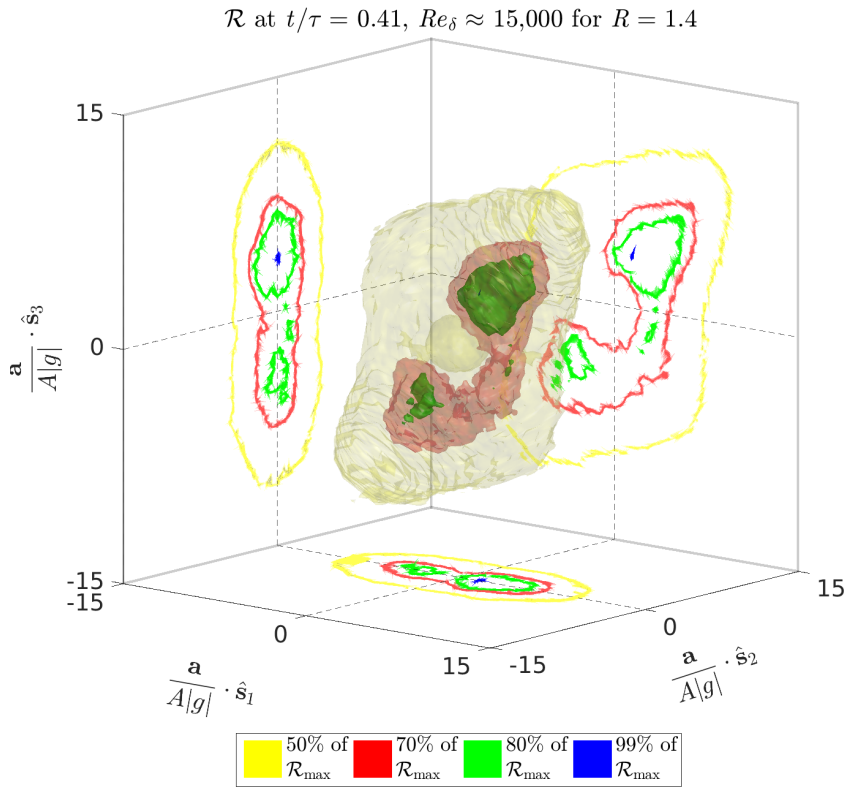

(a)

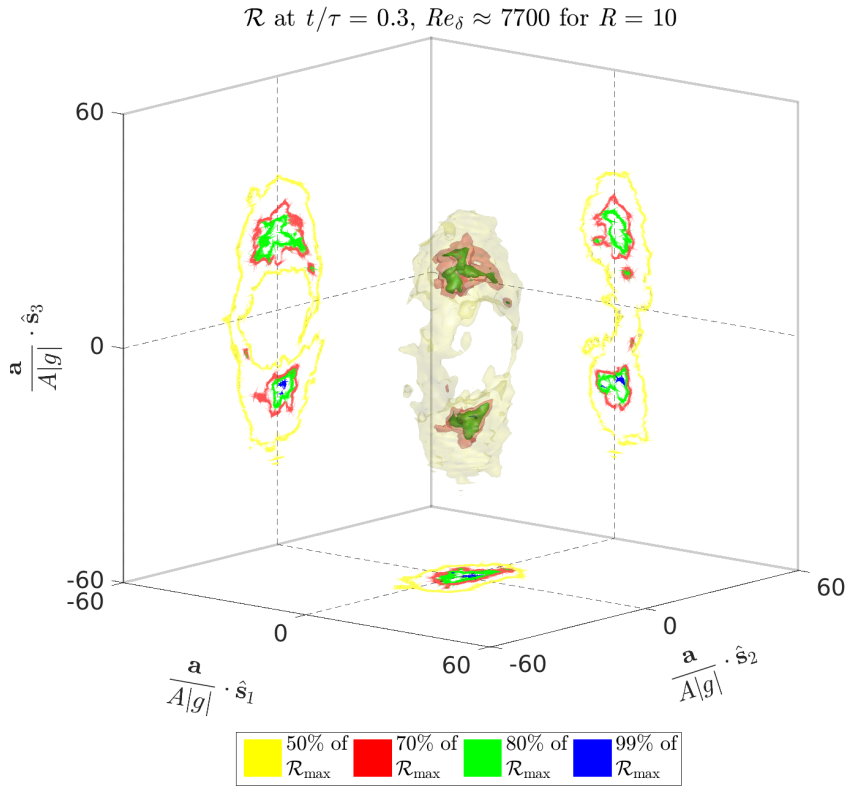

(b)

Figure 7.1: Non-dimensional Lagrangian acceleration $\mathcal{R}$ isosurfaces of mixed fluid, in the local strain rate tensor eigenvector coordinate system for (*a*) $R = 1.4$ and (*b*) $R = 10$, at the same times as in figure 5.11.

where the latter term is zero for divergence-free flow in a periodic domain, since u'_k can be moved into the x_k derivative, converting that volume integral into a surface integral that is zero with periodic boundaries. Taking the Fourier transform of the above equation and integrating in $\boldsymbol{x}'$, yields equation 7.2.

The incompressible relation between vorticity and velocity spectra, *i.e.*, $S_{\omega_i\omega_i} = k^2 S_{u_i u_i}$, can be studied in terms of variable-density flow by quantifying the relative magnitude of the off-diagonal terms, $k_j k_i S_{u_i u_j}$, in wavenumber space. If they are small at large wavenumbers (small scales), the relation $S_{\omega_i\omega_i} = k^2 S_{u_i u_i}$ may be a valid model approximation. This has yet to be tested in the studied flow.

In variable-density flow, the spectrum of $\boldsymbol{j} = \rho^{1/2}\boldsymbol{u}$ is needed to reproduce kinetic energy (section 4.2.2). A simple mathematical identity between vorticity spectra and kinetic energy spectra like in equation 7.2, however, is not known.

The assumption of equally distributed kinetic energy around the vortex may also be challenged in variable-density flow. Section 5.3.1 showed that there are density gradients at approximately $\pm(\widehat{\boldsymbol{s}}_1 - \widehat{\boldsymbol{s}}_3)$, which are perpendicular to the total vorticity direction, $\boldsymbol{\omega}$. Large-scale velocity will preferentially align approximately with $\pm(\widehat{\boldsymbol{s}}_1 + \widehat{\boldsymbol{s}}_3)$, *i.e.*, aligned with or oppositely to gravity depending on the fluid parcel. However, small-scale velocity may be less sensitive to this flow topology, and thus could be less anisotropic. This could challenge the argument that the kinetic energy is equally distributed around a vortex, since the velocity and density fields may not be equally distributed in the strain rate eigenvector space. Additionally, if the small scale vorticity, $\boldsymbol{\omega}'$, is not perpendicular to density gradients because of its alignment with $\widehat{\widetilde{\boldsymbol{s}}}_1$, then kinetic energy could vary in the vortex alignment direction.

The SVM uses the Lundgren (1982) spiral vortex and many authors assume the Lundgren (1982) spiral vortex aligns with the most extensional eigenvector of the resolved strain rate field, $\widehat{\widetilde{\boldsymbol{s}}}_1$. This assumption challenges the observations in chapter 5 that the total vorticity, $\boldsymbol{\omega} = \overline{\boldsymbol{\omega}} + \boldsymbol{\omega}' \parallel \widehat{\boldsymbol{s}}_2$. It was shown mathematically that aligning the SGS vorticity, $\boldsymbol{\omega}'$ with $\widehat{\widetilde{\boldsymbol{s}}}_1$ imparts variability in the total vorticity vector alignment. While there is variability in vorticity alignment, seen in section 5.2 with $\boldsymbol{\omega}$ not perfectly aligned with $\widehat{\boldsymbol{s}}_2$, the consistency of the SGS model vorticity alignment assumption with the observed vorticity alignment would need to be studied.

This is an area of ongoing research. In the studied flow, mixing occurs because of density gradients, *i.e.*, a uniform-density case would have no movement, providing an ideal testing ground to study small-scale variable-density effects.

Appendix A

NUMERICAL METHOD

A.1 Time integration

The time integration method used is a low-storage semi-implicit Runge–Kutta scheme from Spalart, Moser, and Rogers (1991), with an adaptive time step, discussed in Chung (2009) and Chung and Pullin (2010). The numerical scheme has been documented in those works described, with augmentations in the present work to account for $\mathbf{\Gamma} \cong -\widehat{z}\rho_0 g$ and variable diffusivity, $\mathcal{D}(\boldsymbol{x}, t)$. The updated equations are below, with the method described for completeness.

The adaptive time step consists of three substeps, each weighted differently denoted with constants $(\alpha, \beta, \gamma, \zeta)$. Note that α, β, and ζ were used in the main text with a different meaning. They are used again in this section only with a different meaning, to be consistent with what is done in Spalart, Moser, and Rogers (1991). The time step is solved with (Spalart, Moser, and Rogers, 1991)

$$f' = f^n + \Delta_t[L(\alpha_1 f^n + \beta_1 f') + \gamma_1 N(f^n)] \tag{A.1a}$$

$$f'' = f' + \Delta_t[L(\alpha_2 f' + \beta_2 f'') + \gamma_2 N(f') + \zeta_1 N(f^n)] \tag{A.1b}$$

$$f^{n+1} = f'' + \Delta_t[L(\alpha_3 f'' + \beta_3 f^{n+1}) + \gamma_3 N(f'') + \zeta_2 N(f')] \tag{A.1c}$$

with linear terms represented by L, non-linear by N, fields solved ($\boldsymbol{u}$ and ρ) represented by f, and time step Δ_t. The momentum equation (3.1b) and scalar transport equation (3.4) are partitioned as such.

$$\frac{\partial \boldsymbol{u}}{\partial t} = N(\boldsymbol{u}) + L(\boldsymbol{u}) \tag{A.2a}$$

with

$$N(\boldsymbol{u}) = -(\boldsymbol{u}\cdot\nabla)\,\boldsymbol{u} + \frac{\mu}{\rho_0}\left[\left(\frac{\rho_0}{\rho} - 1\right)\nabla^2\boldsymbol{u} + \frac{1}{3}\frac{\rho_0}{\rho}\nabla\left(\nabla\cdot\boldsymbol{u}\right)\right] - \widehat{z}g \tag{A.2b}$$

$$L(\boldsymbol{u}) = \frac{\mu}{\rho_0}\nabla^2\boldsymbol{u} - \frac{1}{\rho}\left(\mathbf{\Gamma} + \nabla p\right) \tag{A.2c}$$

and

$$\frac{\partial \rho}{\partial t} = N(\rho) + L(\rho) \tag{A.3a}$$

Chapter adapted from Gat et al., 2017

$$N(\rho) \;=\; -\left(\boldsymbol{u}\cdot\nabla\right)\rho + \frac{\mu}{\rho_0}\left(\frac{\rho_0}{\rho}-1\right)\nabla^2\rho - 2\frac{\mu}{\rho^2}\left|\nabla\rho\right|^2 \tag{A.3b}$$

$$L(\rho) \;=\; \frac{\mu}{\rho_0}\nabla^2\rho, \tag{A.3c}$$

where equation 3.4 has been rewritten to

$$\frac{\mathrm{D}\rho}{\mathrm{D}t} \;=\; \frac{\mu}{\rho}\nabla^2\rho - 2\frac{\mu}{\rho^2}\left|\nabla\rho\right|^2, \tag{A.3d}$$

which differs from previous implementations. Additionally (Spalart, Moser, and Rogers, 1991)

$$\alpha \;=\; \left\{\frac{29}{96}, -\frac{3}{40}, \frac{1}{6}\right\} \tag{A.4a}$$

$$\beta \;=\; \left\{\frac{37}{160}, \frac{5}{24}, \frac{1}{6}\right\} \tag{A.4b}$$

$$\gamma \;=\; \left\{\frac{8}{15}, \frac{5}{12}, \frac{3}{4}\right\} \tag{A.4c}$$

$$\zeta \;=\; \left\{0, -\frac{17}{60}, -\frac{5}{12}\right\} \tag{A.4d}$$

with

$$\alpha+\beta \;=\; \gamma+\zeta\,. \tag{A.4e}$$

Equations A.2 and A.3 are solved in wavenumber space, linearizing the spatial derivatives, *i.e.*,

$$\widehat{\rho}^{n+1} \;=\; \frac{1}{\left(-k^2 - \dfrac{1}{\beta\nu_0\Delta_t}\right)}\left[-\frac{\alpha}{\beta}\left(-k^2+\frac{1}{\alpha\nu_0\Delta_t}\right)\widehat{\rho}^{n} - \frac{\gamma}{\beta\nu_0}\widehat{H}_\rho^{n} - \frac{\zeta}{\beta\nu_0}\widehat{H}_\rho^{n-1}\right] \tag{A.5a}$$

$$\widehat{\boldsymbol{u}}^{n+1} \;=\; \frac{1}{\left(-k^2 - \dfrac{1}{\beta\nu_0\Delta_t}\right)}\left[-\frac{\alpha}{\beta}\left(-k^2+\frac{1}{\alpha\nu_0\Delta_t}\right)\widehat{\boldsymbol{u}}^{n} - \frac{\gamma}{\beta\nu_0}\widehat{\boldsymbol{H}}_{\boldsymbol{u}}^{n} - \frac{\zeta}{\beta\nu_0}\widehat{\boldsymbol{H}}_{\boldsymbol{u}}^{n-1} + \frac{\alpha+\beta}{\beta\nu_0}\widehat{\boldsymbol{P}}\right] \tag{A.5b}$$

$$\nabla\cdot\boldsymbol{u}^{n+1} \;=\; -\nabla\cdot\left(\frac{\mu}{\left(\rho^{n+1}\right)^2}\nabla\rho^{n+1}\right) \tag{A.5c}$$

with

$$\boldsymbol{H}_{\boldsymbol{u}} \;=\; -\left(\boldsymbol{u}\cdot\nabla\right)\boldsymbol{u} + \nu_0\left[\left(\frac{\rho_0}{\rho}-1\right)\nabla^2\boldsymbol{u} + \frac{1}{3}\frac{\rho_0}{\rho}\nabla\left(\nabla\cdot\boldsymbol{u}\right)\right] - \widehat{z}g \tag{A.5d}$$

$$\boldsymbol{P} \;=\; \frac{1}{\rho^{(*)}}\left(\boldsymbol{\Gamma}+\nabla p\right) \tag{A.5e}$$

$$\frac{\alpha+\beta}{\rho^{(*)}} \equiv \frac{\alpha}{\rho^n} + \frac{\beta}{\rho^{n+1}} \tag{A.5f}$$

$$H_\rho = -\boldsymbol{u}\cdot\nabla\rho + \nu_0\left(\frac{\rho_0}{\rho}-1\right)\nabla^2\rho - 2\frac{\mu}{\rho^2}\left|\nabla\rho\right|^2, \tag{A.5g}$$

where the n superscript can represent the intermediate prime superscripts of equation A.1, $\widehat{()}$ stands for the Fourier transform of the parenthetical value, $\nu_0 = \mu/\rho_0$, $\boldsymbol{k} = (k_x, k_y, k_z)$, the wavenumber, with $k^2 = k_x^2 + k_y^2 + k_z^2$.

The discrete time mass conservation equation in Chung (2009, equation 2.20a) differs from the implementation in this work (equation A.5a) to account for a variable diffusivity, $\mathcal{D}(\boldsymbol{x},t) = \mu/\rho(\boldsymbol{x},t)$, as opposed to $\mathcal{D}(\boldsymbol{x},t) = \mathcal{D} = const.$ in Chung (2009) and Chung and Pullin (2010). The variable diffusion coefficient here requires solving for ρ instead of $\log(\rho/\rho_0)$ with additional terms in the equation for H_ρ in Chung (2009, section 2.3.2), which are solved explicitly. The momentum equation solution method above (equations A.5b through A.5f) are consistent with Chung (2009), except for the meaning of $\boldsymbol{\Gamma}$, discussed in section 3.2, and the uniform dynamic viscosity.

A.2 Pressure term

Chung and Pullin (2010) decompose the pressure term into Lagrange multipliers $(\phi, \boldsymbol{\psi}, \boldsymbol{f})$:

$$\boldsymbol{P} = \frac{1}{\rho^{(*)}}\left(\boldsymbol{\Gamma} + \nabla p\right) = \nabla\phi + \boldsymbol{h} + \boldsymbol{f}, \tag{A.6}$$

where $\rho^{(*)}$ is a weighted average density over the time step (equation A.5f), $\boldsymbol{h} = \nabla\times\boldsymbol{\psi}$, and $\boldsymbol{f} = \boldsymbol{f}(t)$ is a harmonic component.

With this decomposition, ϕ is solved exactly from the divergence of the momentum equation, combined with the mass conservation equation, *i.e.*, equation A.5c.

The zero volume-averaged momentum is constrained with $\boldsymbol{f}$ by imposing $\left\langle \rho^{n+1}\boldsymbol{u}^{n+1}\right\rangle = 0$, as discussed in section 3.2. This is similar to Chung (2009), but with a volume-averaged momentum here, as opposed to a mid-plane-averaged velocity field in Chung (2009).

Lastly, $\boldsymbol{\psi}$ is calculated iteratively, as described in Chung (2009, section 2.3.1), with a convergence error set to be less than 10^{-6} in the present simulations.

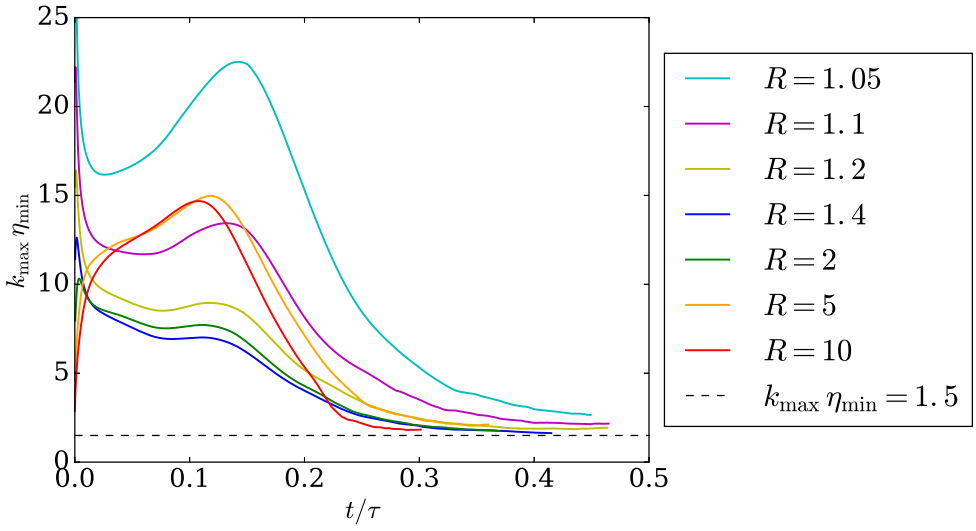

(a)

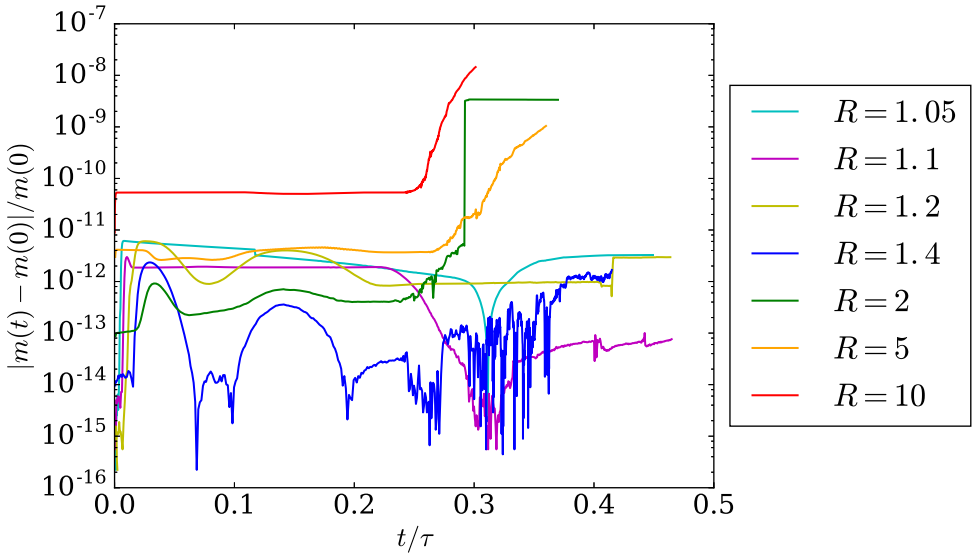

(b)

Figure A.1: (*a*) $k_{\max}\,\eta_{\min}$ for seven simulations, and (*b*) total mass error (see text).

A.3 Grid resolution

The value of the uniform viscosity, μ, is set in the simulations to ensure that they remain well resolved, *i.e.*, $k_{\max}\,\eta_{\min} > 1.5$ (Donzis and Yeung, 2010), with

$$\eta_{\min} = \min_{x}\left\{\left(\frac{\nu^3}{\epsilon}\right)^{1/4}\right\}, \tag{A.7}$$

where $\nu = \mu/\langle\rho\rangle_{y,z}$ and $\epsilon = 2\nu\,\langle \boldsymbol{D} : \boldsymbol{D}\rangle_{y,z}$ is the (y, z)–plane averaged specific kinetic energy dissipation rate, also used in scaling the spectra, with $\boldsymbol{D} = \boldsymbol{s} - (\nabla \cdot \boldsymbol{u})\,\mathbf{I}/3$, the traceless strain rate tensor, ensuring that $\eta > 0.7\Delta x$. Viscosities, μ, were set by first running lower grid resolutions for the desired density ratios and iterating until the late-time flow behavior maintained $k_{\max}\,\eta_{\min} > 1.5$. If that condition was not met, the viscosity was updated

$$\mu_{\text{new}} = \mu_{\text{old}}\left(\frac{1.5}{k_{\max,\text{old}}\,\eta_{\min,\text{old}}}\right)^{4/3}. \tag{A.8}$$

Once the desired condition was met, higher resolution simulations were run by decreasing the viscosity such that

$$\frac{\mu_1}{\mu_2} = \left(\frac{n_2}{n_1}\right)^{4/3}, \tag{A.9}$$

where the subscripts denote one resolution versus another, assuming $n = n_x = n_y = n_z$, which holds for the performed simulations. Equation A.9 is not exact, since turbulence is a non-linear problem. However, this method approximates the optimal viscosities for desired resolutions.

Figure A.1a plots $k_{\max}\,\eta_{\min}$ for seven density ratios. The simulations conserve mass to a fractional error of $\delta m/m \lesssim 10^{-8}$, as shown in figure A.1b, where $m(t)$ is the total mass in the domain at time t and $\delta m(t) = |m(t) - m(0)|$.

Appendix B

FLOW SENSITIVITY TO INITIAL CONDITIONS

To probe flow dependence on initial conditions, various initial density and velocity profiles, and perturbations were tested. These tests were performed on 512^3 grids.

Initial density perturbations were chosen to be isotropic and calculated similarly to Cook and Dimotakis (2001), implemented by Professor Georgios Matheou, however velocity perturbations were calculated differently than Cook and Dimotakis (2001), as discussed below. A discrete two-dimensional random number field (*e.g.*, figure B.1a) is convolved with a spatial Gaussian filter. The resulting field (figure B.1b) is Fourier transformed (figure B.1c) and filtered with a radial Gaussian function (figure B.1d). The Fourier coefficients (figure B.1e) are then inverse transformed (figure B.1f) and used as the perturbation field, $\xi(y, z)$, to offset x locations of the initial density profile (equation 3.8). The ratio of perturbation root mean square to initialized shear-layer width is in the range $0.36 < (20\,\Delta x\,\xi_{\mathrm{RMS}})/\delta_{\mathrm{i}} < 0.44$, depending on grid size and density ratio, as referenced in the main text.

Spectra of the isotropic perturbation fields are taken in the radial direction and averaged in the polar direction. Three perturbation spectra were tested, labeled: 'Pert1', 'Pert2', and 'Pert3', in figure B.2a. The spectra (in figure B.2a) use different initial discrete random number fields and spectral Gaussian filter widths. The flow in this paper was initialized with Pert3.

To investigate the effects of the initial density profile, an error function (chosen for the simulations shown throughout this paper), a hyperbolic tangent function, and a numerical fit to the solution of equation 4.5 were used to represent density interfaces.

The sensitivity of the flow to the various initial conditions, is assessed in terms of the shear-layer width growth (figure B.2b). This illustrates that initial diffusive growth rates are similar in all cases studied. The shear-layer width slopes in this diffusive regime are very nearly 0.5, as predicted in section 4.1.1, with actual slopes in the range 0.4802 to 0.4881.

Transition times when the flow enters the turbulent regime depend on perturbations and initial profiles, with variations in t_{tr} less than 10%. The growth in the

Chapter adapted from Gat et al., 2017

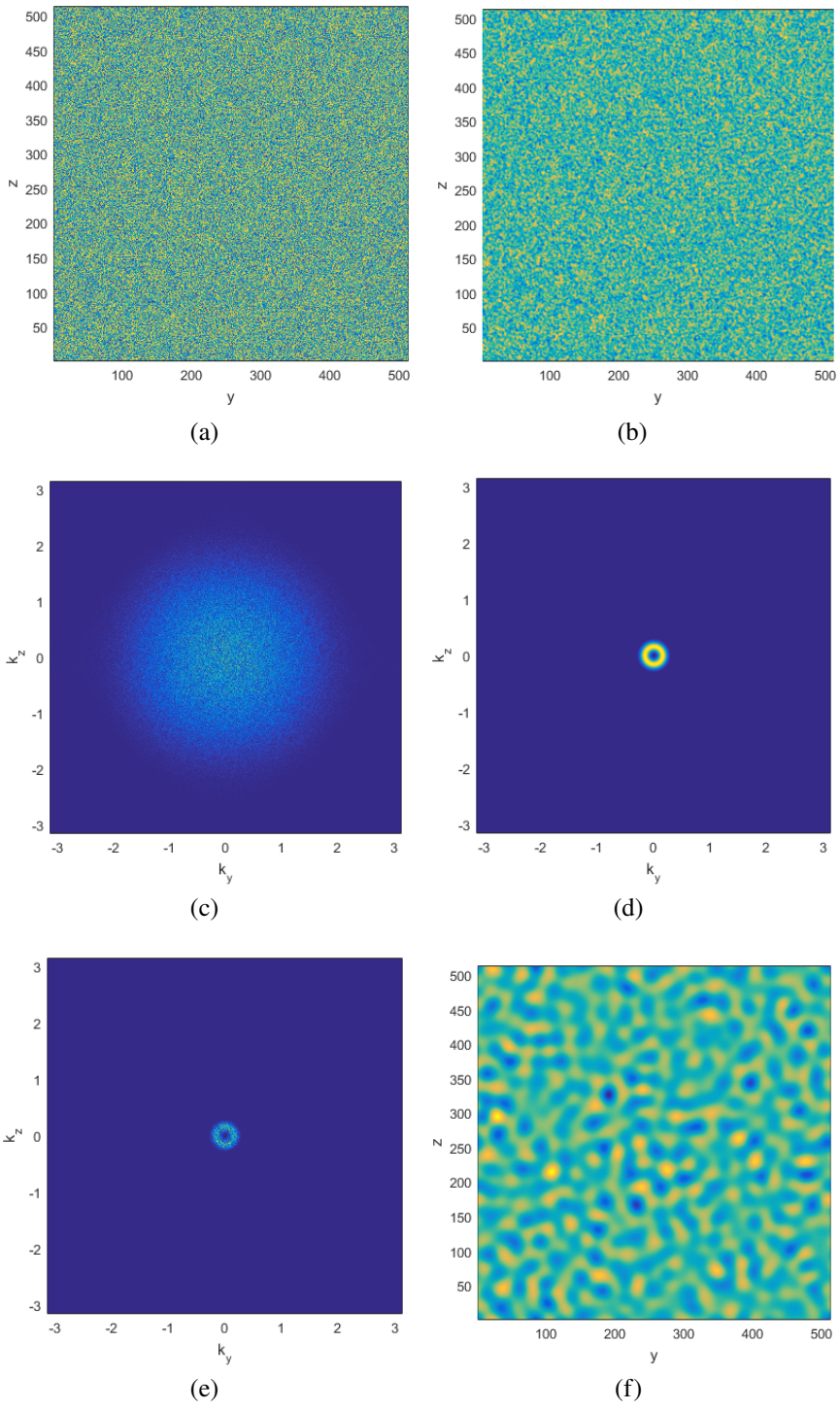

Figure B.1: (*a*) Discrete random number field for a 512^3 simulation. (*b*) Field from (*a*) convolved with spatial Gaussian periodic filter. (*c*) Fourier transform of field in (*b*). (*d*) Example Gaussian filter used in Fourier space corresponding to "Pert3." (*e*) Field from (*c*) filtered with field from (*d*). (*f*) Inverse Fourier transform of (*e*), and is the field used as the initial perturbation of "Pert3."

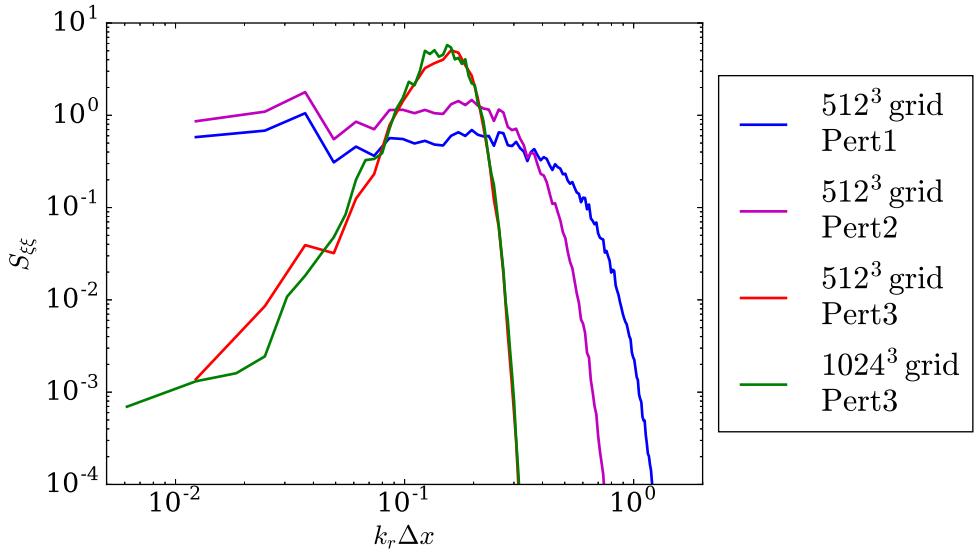

(a)

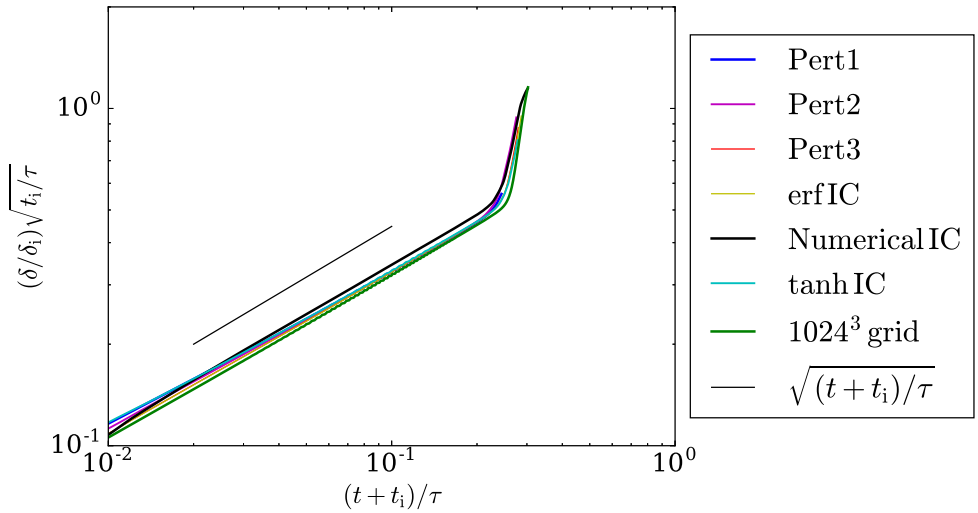

(b)

Figure B.2: (*a*) Radial spectra of three initial perturbation fields tested in 512^3 simulations, along with the initial perturbation spectra in the 1024^3 simulations. (*b*) Shear-layer width growth in time for initial perturbations and initial profiles tested with 512^3 grids. 1024^3 result shown for comparison. Blue, magenta, red, and green solid lines are from error function initial profiles with different perturbations. Yellow and red lines differ only by initial random number fields of the perturbation profiles. Yellow, cyan, and green lines are initialized with Pert3. Results plotted derive from $R = 10$ simulations.

unsteady/turbulent regime depends weakly on initial conditions and differs (somewhat) between 512^3 and 1024^3 simulations. Other flow statistics studied, *e.g.*, shear-layer composition p.d.f., mean shear-layer density, *etc.*, are found to be statistically independent (or only weakly dependent) on the initial condition choices described above.

While testing the effects of the initialized density field as the numerical fit to equation 4.5, the initial velocity field dependence was specifically probed. This was motivated by initial condition effects documented in Cook and Dimotakis (2001), in which the flow was initialized with a diffusion-induced velocity deduced from their three-dimensional initial density profiles. Simulations were run with a zero initial velocity field, *i.e.*, $\boldsymbol{u}_\mathrm{i} = 0$, as in the simulations documented in the main text, as well as with $\boldsymbol{u}_\mathrm{i} = \mu\nabla(1/\rho)$ — the three-dimensional equivalent to equation 4.3 required by continuity by the initial three-dimensional density field. In the case of $\boldsymbol{u}_\mathrm{i} = 0$, the pressure Lagrange multiplier generates the required fields after the first time step to satisfy continuity. The study below assesses the differences on the flow from the two initial velocity fields.

A discrete pointwise L_2-norm was employed to study the sensitivity to the initial velocity, shown in figure B.3a, with

$$L_{2,F}(t) \;=\; \left[\left(\frac{\Delta x}{L}\right)^3 \sum_{l,m,n} \left|F_{lmn}(t)_{\boldsymbol{u}_\mathrm{i}=\mu\nabla(1/\rho)} - F_{lmn}(t)_{\boldsymbol{u}_\mathrm{i}=0}\right|^2\right]^{1/2}. \tag{B.1a}$$

Each component of the velocity field and the density field were tested, with

$$F(t) \;=\; \left\{\frac{u_i(t)}{\Delta W}, \frac{\rho(t)}{\Delta\rho}\right\}, \tag{B.1b}$$

where $\Delta\rho$ is the difference between free-stream densities. The error is seen to decrease in the diffusive regime, but diverges as the flow enters the turbulent regime. Pointwise statistics, however, do not provide the appropriate error metric in the high-Lyapunov-exponent unsteady/turbulent regime. In that regime, a scaled difference of averaged quantities, such as shear-layer widths, rather than a pointwise metric, is computed,

$$\Delta G(t) \;=\; \left|G(t)_{\boldsymbol{u}_\mathrm{i}=\mu\nabla(1/\rho)} - G(t)_{\boldsymbol{u}_\mathrm{i}=0}\right|, \tag{B.2a}$$

with

$$G(t) \;=\; \frac{\delta^*(t)}{\overline{\delta^*(t)}}, \quad \delta^*(t) \;=\; \frac{\delta(t)}{\delta_\mathrm{i}}\sqrt{\frac{t_\mathrm{i}}{\tau}}, \tag{B.2b}$$

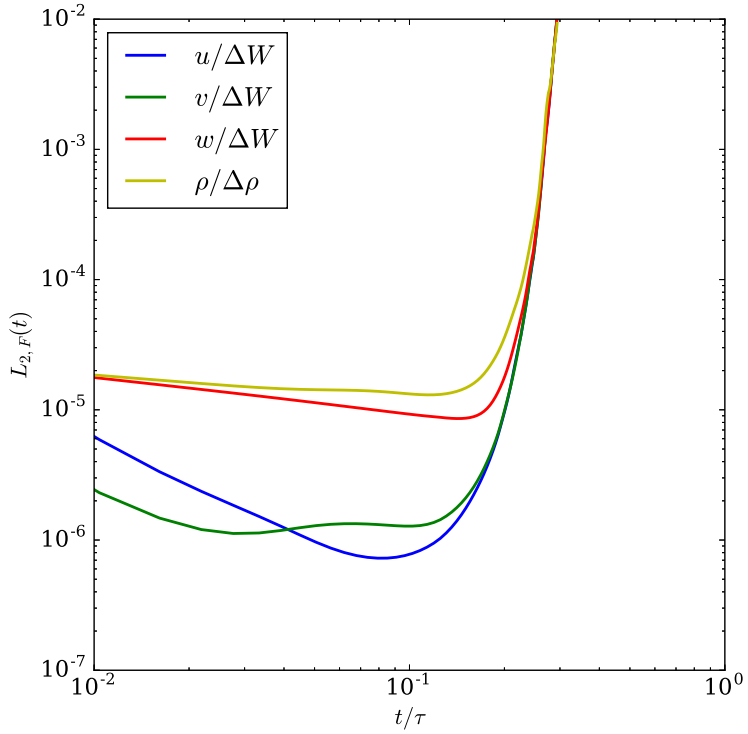

(a)

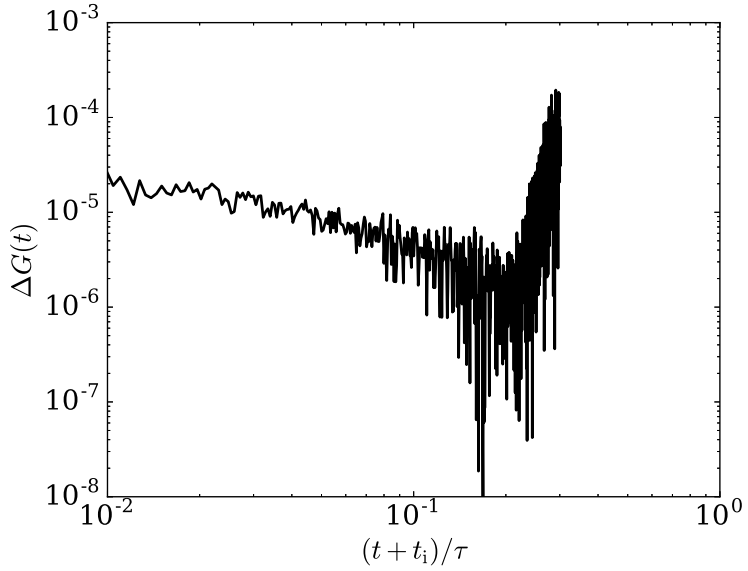

(b)

Figure B.3: Differences in statistics between two simulations with the same initial density field, but different initial velocity fields. (*a*) Pointwise L_2-norms of the evolving velocity and density fields. (*b*) Evolving shear-layer width difference (equation B.2a). Results in plots are for $R = 10$ simulations with 512^3 grids.

and

$$\overline{\delta^*}(t) \;=\; \frac{1}{2}\left[\delta^*(t)_{\boldsymbol{u}_\mathrm{i}=\mu\nabla(1/\rho)} + \delta^*(t)_{\boldsymbol{u}_\mathrm{i}=0}\right]. \tag{B.2c}$$

The results are plotted in figure B.3b. The quantities differenced criss-cross each other in the turbulent regime, indicating the absence of a systematic statistical difference in time, with only a small fractional amplitude difference, even towards the end of the simulations, when rapid shear-layer growth occurs.

Effects from the differences in the initial velocity field are seen to be small, especially when compared to those resulting from the different initial density fields discussed above, which are also small.

There are many possible initialization choices. This section quantified the relative lack of initialization sensitivity of this flow, which may not hold for other flows. Investigation of the sensitivity to various initial condition choices was undertaken because a zero initial velocity does not satisfy the continuity equation (3.4). The initial condition choice was simple to implement and the inconsistency is lifted after the first $1-2$ time steps through strict mass conservation, leaving no significant imprint on the flow.

Appendix C

VECTOR ALIGNMENT PROBABILITY DENSITY FUNCTION CALCULATION

The display of three-dimensional statistical information throughout this work is facilitated by three-dimensional magnitude density functions of vector fields, which are essentially three-dimensional probability density functions (p.d.f.s) multiplied by magnitudes. This appendix details the probability density function calculation method.

C.1 Methodology

Consider a three-dimensional vector field, $\boldsymbol{\xi}$, of size (n_x, n_y, n_z) in Cartesian space. At each point in space, $\boldsymbol{\xi}$ has a magnitude, r_ξ, and a direction (θ_ξ, ϕ_ξ), where the polar angle, θ, ranges from $(0, \pi)$, and the azimuthal angle ϕ ranges from $(-\pi, \pi)$. The three dimensional probability density function of $\boldsymbol{\xi}$ is then $\mathcal{P}(r_\xi, \theta_\xi, \phi_\xi)$, where

$$1 \;=\; \int_{-\pi}^{\pi}\int_{0}^{\pi}\int_{0}^{\infty} \mathcal{P}(r_\xi, \theta_\xi, \phi_\xi)\, r_\xi^2 \,\mathrm{d}r_\xi \sin\theta_\xi \,\mathrm{d}\theta_\xi \,\mathrm{d}\phi_\xi \,. \tag{C.1}$$

A two-dimensional p.d.f. can be defined as

$$\mathcal{P}^{2D}(\theta_\xi, \phi_\xi) \;=\; \int_{0}^{\infty} \mathcal{P}(r_\xi, \theta_\xi, \phi_\xi)\, r_\xi^2 \,\mathrm{d}r_\xi \tag{C.2}$$

such that

$$1 \;=\; \int_{-\pi}^{\pi}\int_{0}^{\pi} \mathcal{P}^{2D}(\theta_\xi, \phi_\xi) \sin\theta_\xi \,\mathrm{d}\theta_\xi \,\mathrm{d}\phi_\xi \,. \tag{C.3}$$

Additionally, a magnitude density function, $\mathcal{R}(r_\xi, \theta_\xi, \phi_\xi)$, as seen in the main text, can be defined as

$$\mathcal{R}(r_\xi, \theta_\xi, \phi_\xi) \;=\; r_\xi\, \mathcal{P}(r_\xi, \theta_\xi, \phi_\xi) \tag{C.4}$$

such that

$$\bar{r}_\xi \;=\; \int_{-\pi}^{\pi}\int_{0}^{\pi}\int_{0}^{\infty} \mathcal{R}(r_\xi, \theta_\xi, \phi_\xi)\, r_\xi^2 \,\mathrm{d}r_\xi \sin\theta_\xi \,\mathrm{d}\theta_\xi \,\mathrm{d}\phi_\xi \,. \tag{C.5}$$

Lastly, the variance is defined as

$$\sigma_\xi^2 \;=\; \int_{-\pi}^{\pi}\int_{0}^{\pi}\int_{0}^{\infty} \mathcal{P}(r_\xi, \theta_\xi, \phi_\xi)\, r_\xi^4 \,\mathrm{d}r_\xi \sin\theta_\xi \,\mathrm{d}\theta_\xi \,\mathrm{d}\phi_\xi \;-\; \bar{r}_\xi^2 \,. \tag{C.6}$$

$\mathcal{R}$ is advantageous for displaying mean magnitudes when p.d.f.s are extremely skewed (asymmetric), as they are in the studied flow. The most probable magnitude

may be an order of magnitude smaller than the mean magnitude. For a more accurate depiction of the mean magnitudes in these cases, $\mathcal{R}$, is used.

To calculate $\mathcal{P}$ or $\mathcal{R}$, the data is binned such that no biases are imparted on the data. This is done by ensuring each volume element of the bin grid, $\mathcal{V}$, is uniform, *i.e.*, if the bins in $r_{\boldsymbol{\xi}}$ are indexed in i, $\theta_{\boldsymbol{\xi}}$ in j, and $\phi_{\boldsymbol{\xi}}$ in k, then

$$\begin{aligned}\mathcal{V} \equiv \mathcal{V}_{ijk} &= \int_{\phi_{\boldsymbol{\xi},k}}^{\phi_{\boldsymbol{\xi},k+1}} \int_{\theta_{\boldsymbol{\xi},j}}^{\theta_{\boldsymbol{\xi},j+1}} \int_{r_{\boldsymbol{\xi},i}}^{r_{\boldsymbol{\xi},i+1}} r_{\boldsymbol{\xi}}^2 \, \mathrm{d}r_{\boldsymbol{\xi}} \sin\theta_{\boldsymbol{\xi}} \, \mathrm{d}\theta_{\boldsymbol{\xi}} \, \mathrm{d}\phi_{\boldsymbol{\xi}} \\ &= \frac{1}{3} \left(\phi_{\boldsymbol{\xi},k+1} - \phi_{\boldsymbol{\xi},k}\right) \left(\cos\theta_{\boldsymbol{\xi},j} - \cos\theta_{\boldsymbol{\xi},j+1}\right) \left(r_{\boldsymbol{\xi},i+1}^3 - r_{\boldsymbol{\xi},i}^3\right) \\ &= \frac{1}{3} \, \Omega \left(r_{\boldsymbol{\xi},i+1}^3 - r_{\boldsymbol{\xi},i}^3\right) ,\end{aligned} \tag{C.7}$$

where

$$\Omega \equiv \Omega_{jk} = \left(\phi_{\boldsymbol{\xi},k+1} - \phi_{\boldsymbol{\xi},k}\right) \left(\cos\theta_{\boldsymbol{\xi},j} - \cos\theta_{\boldsymbol{\xi},j+1}\right) \tag{C.8}$$

and is the solid angle.

The number of bins in $\theta_{\boldsymbol{\xi}}$ is n_θ, and in $r_{\boldsymbol{\xi}}$ is n_r.

To maintain uniform Ω with reasonable aspect ratios, the number of bins in $\phi_{\boldsymbol{\xi}}$ varies with $\theta_{\boldsymbol{\xi}}$, *i.e.*, there are $n_{\phi,j}$ bins in $\phi_{\boldsymbol{\xi}}$ at each j bin in $\theta_{\boldsymbol{\xi}}$. These are calculated by first limiting the bin spacing in $\theta_{\boldsymbol{\xi}}$ to a uniform A_θ

$$A_\theta = \frac{\pi}{n_\theta - 1} = \theta_{\boldsymbol{\xi},j+1} - \theta_{\boldsymbol{\xi},j} \, . \tag{C.9}$$

Pole locations are alloted half A_θ since they span $-\pi \leq \phi_{\boldsymbol{\xi}} < \pi$. Polar cap solid angles are used as the preliminary solid angle for all locations with $\Omega = 2\pi \left(1 - \cos\frac{A_\theta}{2}\right)$. At each j bin in $\theta_{\boldsymbol{\xi}}$, $n_{\phi,j}$ is calculated

$$n_{\phi,j} = \mathrm{ceil} \left\{ \frac{2\pi}{\Omega} \left[\cos\left(\theta_{\boldsymbol{\xi},j}\right) - cos\left(\theta_{\boldsymbol{\xi},j} + A_\theta\right)\right] \right\} , \tag{C.10}$$

where "ceil" returns the largest integer value closest to the bracketed term. The solid angle, Ω is redefined with new $n_{\phi,j}$ values

$$\Omega = \frac{4\pi}{\sum_j n_{\phi,j}} , \tag{C.11}$$

which ensures for n_θ and $n_{\phi,j}$ bins, $\theta_{\boldsymbol{\xi},n_\theta} = \pi$. $\theta_{\boldsymbol{\xi}}$ bin boundaries are calculated as

$$\theta_{\boldsymbol{\xi},j+1} = \cos^{-1}\left(\cos\theta_{\boldsymbol{\xi},j} - \frac{n_{\phi,j}\Omega}{2\pi}\right) \tag{C.12}$$

with $\theta_{\boldsymbol{\xi},j=0} = 0$.

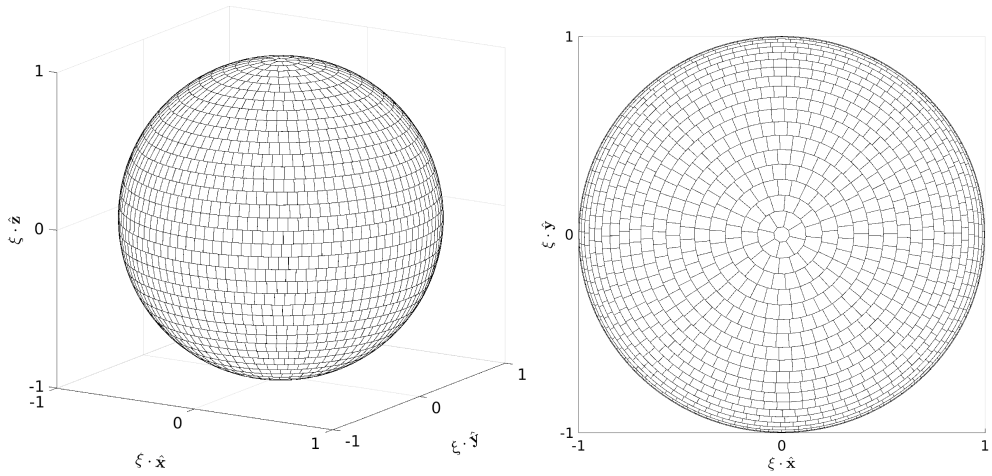

(a) (b)

Figure C.1: Illustration of angular binning grid on a unit sphere showing (*a*) side view and (*b*) top down view, for $n_\theta = 40$.

At every j location, $\phi_{\boldsymbol{\xi}}$ bin boundaries are

$$\phi_{\boldsymbol{\xi},j,k} \;=\; -\pi + k\frac{2\pi}{n_{\phi,j}} + \phi_{\boldsymbol{\xi},j,\text{init}}\,, \tag{C.13}$$

where $\phi_{\boldsymbol{\xi},j,\text{init}} = \text{rand}\,2\pi/n_{\phi,j}$, and rand is a random number between 0 and 1, preventing data biasing imparted by a grid with $\pm\pi$ bin edges at every polar angle.

Figure C.1 displays the described bin grid methodology for $n_\theta = 40$. The values of n_θ used in the main text vary to ensure smooth p.d.f.s that meet validation criterion discussed below.

Radial bins are linearly spaced in $r_{\boldsymbol{\xi}}^3$, *i.e.*

$$r_{\boldsymbol{\xi},i+1} \;=\; \left(r_{\boldsymbol{\xi},\text{init}}^3 + i\Delta r\right)^{1/3}\,, \tag{C.14}$$

where $r_{\boldsymbol{\xi},\text{init}} = \min r_{\boldsymbol{\xi}}$, $\Delta r = (\max {r_{\boldsymbol{\xi}}}^3 - \min {r_{\boldsymbol{\xi}}}^3)/(n_r - 1)$, and $r_{\boldsymbol{\xi},0} = -r_{\boldsymbol{\xi},1}$ to allow proper closure of the p.d.f.

Spacing radial bins linearly in cubic space results in increased resolution as $r_{\boldsymbol{\xi}}$ increases. In some cases, the opposite is required since p.d.f.s may have larger gradients at smaller magnitudes, resulting in an ill-refined p.d.f. that does not meet verification criteria (discussed below), even with large n_r. In these cases, the smaller magnitude bins are split. For example if originally $n_r = 10{,}000$, then the bins between $r_{\boldsymbol{\xi},0}$ and $r_{\boldsymbol{\xi},10}$ are split into 10,000 more bins resulting in $n_r = 19{,}990$. This

bin splitting methodology was seen to increase accuracy, even though in these cases, there are two $\mathcal{V}$ – one for smaller magnitudes and another for larger magnitudes.

Each data point is looped through and put into the appropriate bin to form a counting vector, C_{ijk}. C_{ijk} contains integers in each component representing the number of times the field, $\boldsymbol{\xi}$, has that magnitude and direction. Three-dimensional p.d.f.s are then calculated as

$$\mathcal{P}_{ijk} \;=\; \frac{C_{ijk}/\mathcal{V}_{ijk}}{\sum_k \sum_j \sum_i C_{ijk}}\,, \tag{C.15}$$

where

$$1 \;=\; \sum_i \sum_j \sum_k \mathcal{P}_{ijk}\mathcal{V}_{ijk}\,, \tag{C.16}$$

the discretized version of equation C.1. The two-dimensional p.d.f., equation C.2, is discretized as

$$\mathcal{P}^{2D}_{jk} \;=\; \sum_i \mathcal{P}_{ijk}\frac{\left(r^3_{\xi,i+1} - r^3_{\xi,i}\right)}{3}\,. \tag{C.17}$$

Data is plotted at the center of mass of each bin, $(r_{c,i}, \theta_{c,j}, \phi_{c,k})$, with

$$\begin{aligned} r_{c,i} \;&=\; \frac{1}{\mathcal{V}_{ijk}}\int_{\phi_{\xi,k}}^{\phi_{\xi,k+1}}\int_{\theta_{\xi,j}}^{\theta_{\xi,j+1}}\int_{r_{\xi,i}}^{r_{\xi,i+1}} r_\xi^3\,\mathrm{d}r_\xi\,\sin\theta_\xi\,\mathrm{d}\theta_\xi\,\mathrm{d}\phi_\xi \\ &=\; \frac{3}{4}\frac{\left(r^4_{\xi,i+1} - r^4_{\xi,i}\right)}{\left(r^3_{\xi,i+1} - r^3_{\xi,i}\right)} \end{aligned} \tag{C.18a}$$

$$\begin{aligned} \theta_{c,j} \;&=\; \frac{1}{\mathcal{V}_{ijk}}\int_{\phi_{\xi,k}}^{\phi_{\xi,k+1}}\int_{\theta_{\xi,j}}^{\theta_{\xi,j+1}}\int_{r_{\xi,i}}^{r_{\xi,i+1}} \theta_\xi\, r_\xi^2\,\mathrm{d}r_\xi\,\sin\theta_\xi\,\mathrm{d}\theta_\xi\,\mathrm{d}\phi_\xi \\ &=\; \frac{-\theta_{\xi,j+1}\cos\theta_{\xi,j+1} + \sin\theta_{\xi,j+1} + \theta_{\xi,j}\cos\theta_{\xi,j} - \sin\theta_{\xi,j}}{\cos\theta_{\xi,j} - \cos\theta_{\xi,j+1}} \end{aligned} \tag{C.18b}$$

$$\begin{aligned} \phi_{c,k} \;&=\; \frac{1}{\mathcal{V}_{ijk}}\int_{\phi_{\xi,k}}^{\phi_{\xi,k+1}}\int_{\theta_{\xi,j}}^{\theta_{\xi,j+1}}\int_{r_{\xi,i}}^{r_{\xi,i+1}} \phi_\xi\, r_\xi^2\,\mathrm{d}r_\xi\,\sin\theta_\xi\,\mathrm{d}\theta_\xi\,\mathrm{d}\phi_\xi \\ &=\; \frac{\phi_{\xi,k+1} + \phi_{\xi,k}}{2}\,. \end{aligned} \tag{C.18c}$$

The magnitude density function is computed as

$$\mathcal{R}_{ijk} \;=\; r_{c,i}\mathcal{P}_{ijk}\,, \tag{C.19}$$

which is the discretized equivalent to equation C.4. It is important to note that

$$\overline{r} \;=\; \sum_k \sum_j \sum_i \mathcal{R}_{ijk}\mathcal{V}_{ijk} \tag{C.20a}$$

and that

$$\sum_k \sum_j \sum_i \mathcal{R}_{ijk}\mathcal{V}_{ijk} \equiv \sum_k \sum_j \sum_i \frac{1}{4}\mathcal{P}_{ijk}\,\Omega\left(r^4_{\xi,i+1} - r^4_{\xi,i}\right), \tag{C.20b}$$

the discretized version of equation C.5 with equation C.4.

C.2 Verification

The three-dimensional p.d.f. calculation was verified using two random number fields:

1. Generated in Cartesian space (and only including values within the sphere $0 \leq \sqrt{x^2 + y^2 + z^2} \leq r_{\max}$) called R_{C}
2. Generated in spherical space with magnitudes ranging from $0 \leq r \leq r_{\max}$ called R_{S},

where the maximum magnitude, $r_{\max} = 100$, for performed tests.

The R_{C} field was generated by looping through x, y, and z n times to generate a vector field of size n with

$$\begin{aligned} x &= 200\mathrm{rand} - 100 \\ y &= 200\mathrm{rand} - 100 \\ z &= 200\mathrm{rand} - 100, \end{aligned} \tag{C.21}$$

where again rand is a random number between 0 and 1. This field is then converted to spherical space, with only $\pi/6$ of the domain kept to ensure uniformity in spherical space (only locations with $0 \leq \sqrt{x^2 + y^2 + z^2} \leq 100$ are used).

Next, the R_{S} field, $f(r, \theta, \phi)$, is generated such that

$$1 = \int_{-\pi}^{\pi}\int_{0}^{\pi}\int_{0}^{r_{\max}} f(r,\theta,\phi)\, r^2\, \mathrm{d}r\, \sin\theta\, \mathrm{d}\theta\mathrm{d}\phi, \tag{C.22}$$

where again $r_{\max} = 100$. To ensure equation C.22 is met

$$f(r,\theta,\phi) = \frac{3}{4\pi r^3_{\max}}. \tag{C.23}$$

To generate random numbers in (r, θ, ϕ) space using random numbers between 0 and 1, the cumulative distribution functions are used (Simon, 2015).

$$\begin{aligned} F(r) &= \int_{-\pi}^{\pi}\int_{0}^{\pi}\int_{0}^{r} \frac{3}{4\pi r_{\max}^3}\, r'^2\, \mathrm{d}r'\, \sin\theta\, \mathrm{d}\theta\, \mathrm{d}\phi \\ &= \frac{r^3}{r_{\max}^3} \end{aligned} \tag{C.24a}$$

$$\begin{aligned} F(\theta) &= \int_{-\pi}^{\pi}\int_{0}^{\theta}\int_{0}^{r_{\max}} \frac{3}{4\pi r_{\max}^3}\, r^2\, \mathrm{d}r\, \sin\theta'\, \mathrm{d}\theta'\, \mathrm{d}\phi \\ &= \frac{1}{2}\left(1 - \cos\theta\right) \end{aligned} \tag{C.24b}$$

$$\begin{aligned} F(\phi) &= \int_{-\pi}^{\phi}\int_{0}^{\pi}\int_{0}^{r_{\max}} \frac{3}{4\pi r_{\max}^3}\, r^2\, \mathrm{d}r\, \sin\theta\, \mathrm{d}\theta\, \mathrm{d}\phi' \\ &= \frac{\phi + \pi}{2\pi}, \end{aligned} \tag{C.24c}$$

yielding a uniformly random number field (r, θ, ϕ) in spherical space

$$r = F(r)^{1/3} r_{\max} \tag{C.24d}$$

$$\theta = \cos^{-1}\left[1 - 2F(\theta)\right] \tag{C.24e}$$

$$\phi = 2\pi F(\phi) - \pi\,, \tag{C.24f}$$

where $F(r)$, $F(\theta)$, and $F(\phi)$ contain n random numbers between 0 and 1.

Both R_{C} and R_{S} generate discretely uniform random fields in spherical space. As the number of points, n, increases, $\mathcal{P}$ becomes uniform and equal to $f(r, \theta, \phi)$,

$$\mathcal{P}_{ijk} = \frac{3}{4\pi r_{\max}^3} = 2.39 \times 10^{-7}\,. \tag{C.25a}$$

Additionally, the mean magnitude tends to

$$\overline{r} = \frac{3}{4} r_{\max} = 75 \tag{C.25b}$$

with a variance

$$\sigma^2 = \left[\frac{3}{5} - \left(\frac{3}{4}\right)^2\right] r_{\max}^2 = 375 \tag{C.25c}$$

and

$$\mathcal{P}_{jk}^{2D} = \frac{1}{4\pi} = 0.0796 \tag{C.25d}$$

$$\mathcal{P}_{i}^{1D} = \frac{3}{r_{\max}^3} = 3 \times 10^{-6}, \tag{C.25e}$$

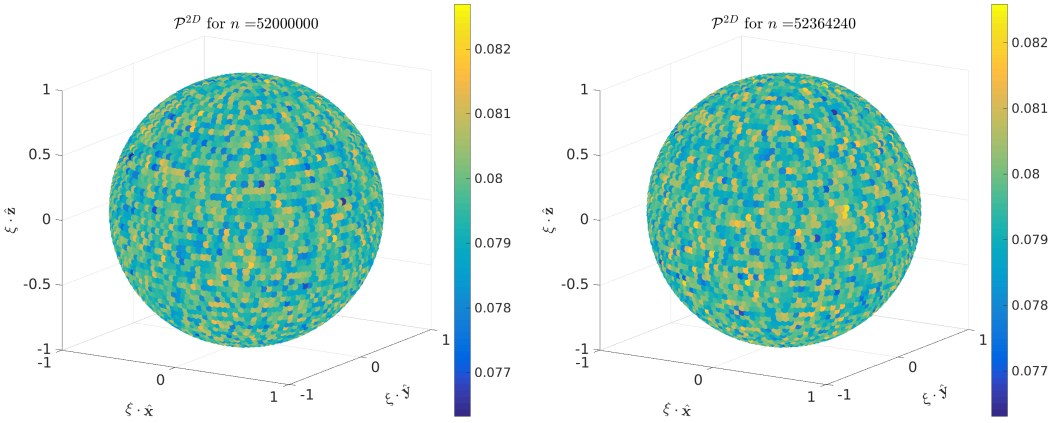

(a) (b)

Figure C.2: Scatter plot of $\mathcal{P}^{2D}$ for (*a*) R_{S} and (*b*) R_{C} fields, $\boldsymbol{\xi}$, with $n \approx 52 \times 10^6$ data points and $n_\theta = 62$.

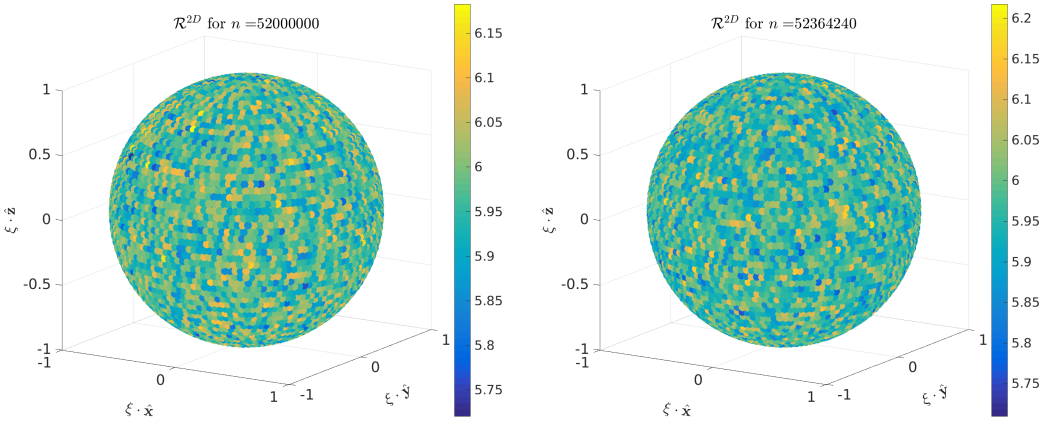

(a) (b)

Figure C.3: Scatter plot of $\mathcal{R}^{2D}$ for (*a*) R_{S} and (*b*) R_{C} fields, $\boldsymbol{\xi}$, with $n \approx 52 \times 10^6$ data points and $n_\theta = 62$.

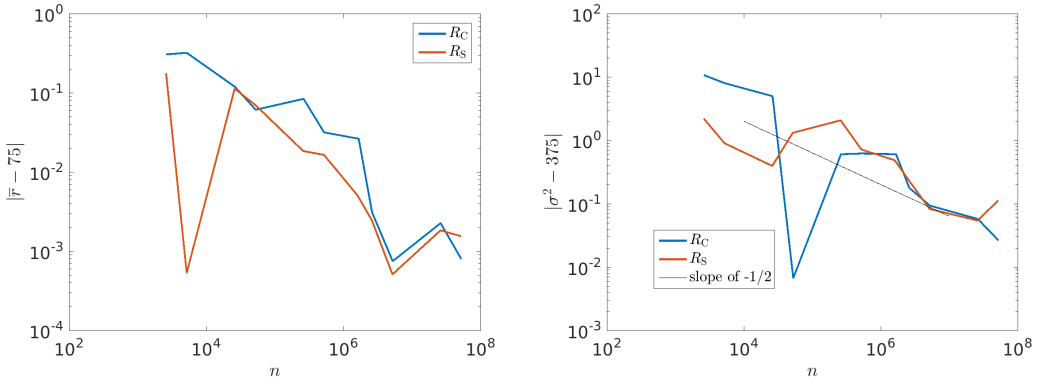

(a) (b)

Figure C.4: Deviations of calculated (*a*) $\bar{r}$ from the theoretical value, equation C.25b, and (*b*) σ^2 from equation C.25c for R_C (blue) and R_S (red). Slope of $-1/2$ is shown for reference.

where $\mathcal{P}_i^{1D}$ is the one-dimensional p.d.f. in r by integrating over the sphere. Lastly,

$$\mathcal{R}_{jk}^{2D} = \frac{3}{16\pi} r_{\max} = 5.9683\,. \tag{C.25f}$$

Example $\boldsymbol{\xi}$ p.d.f.s for R_S and R_C are shown in figure C.2, with magnitude density functions in figure C.3. The values of $\mathcal{P}^{2D}$ and $\mathcal{R}^{2D}$ fluctuate around the theoretical limits (equations C.25d and C.25f). Variations seen decrease as n increases (quantified in figure C.4b). Both R_C and R_S generate fields with $\bar{r}$ and σ^2 close to the theoretical values (figure C.4) with errors decreasing with increasing n. All tests for differing n were done with $n_\theta = 62$ and $n_r = 120$. If those were to decrease with decreasing n, the variations would also decrease.

The full three-dimensional p.d.f., $\mathcal{P}$, oscillates around the theoretical value (equation C.25a), seen in figure C.5a. The one dimensional p.d.f. in magnitude, $\mathcal{P}^{1D}$, also matches the theoretical value of equation C.25e (figure C.5b). As n increases, the oscillations seen decrease, like the other statistics studied. Both plots in figure C.5 show the zeroth bin in magnitude, required for proper closure, but with no data, resulting in a value inconsistent with the theoretical limit, as expected.

With both random fields (R_C and R_S) matching the theoretical values of equation C.25, the algorithm has been verified.

For non-random number fields, *i.e.*, data used in this thesis, the algorithm is measured against how well $\bar{r}$ and σ^2, calculated with $\mathcal{P}$ and $\mathcal{R}$, *i.e.*, equations C.5 and C.6,

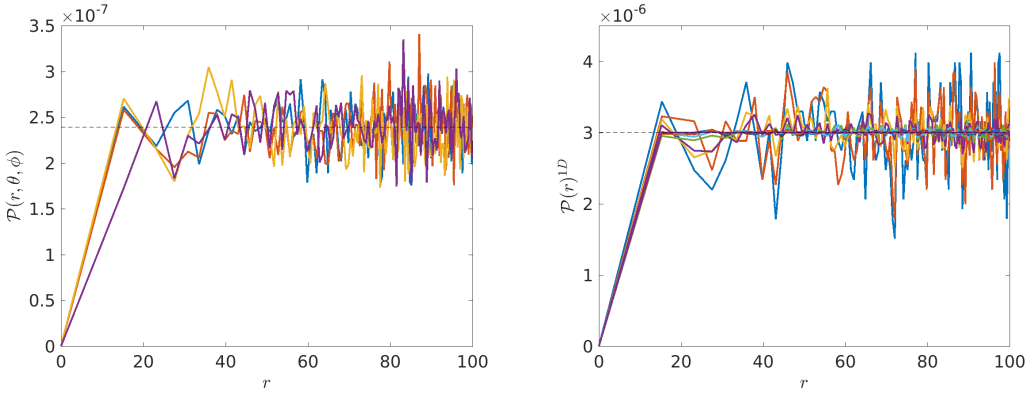

(a) (b)

Figure C.5: (*a*) $\mathcal{P}(r_{\xi}, \theta_{\xi}, \phi_{\xi})$ for $R_{\rm S}$ with $n = 52 \times 10^6$ at random $(\theta_{\xi}, \phi_{\xi})$ bins. Dashed line denotes theoretical value, equation C.25a. (*b*) $\mathcal{P}(r_{\xi})^{1D}$ for $R_{\rm S}$ with colors representing various n values used. Dashed line denotes theoretical value, equation C.25e.

match $\overline{r}$ and σ^2 calculated with the raw data. The binning grid is refined until they match to within approximately 3%.

BIBLIOGRAPHY

Anuchina, N. N., Y. A. Kucherenko, V. E. Neuvazhaev, V. N. Ogibina, L. I. Shibarshov, and V. G. Yakovlev (1978). "Turbulent mixing at an accelerating interface between liquids of different density". In: *Fluid Dyn.* 13.6, pp. 916–920.

Ashurst, W. T., J. Y. Chen, and M. M. Rogers (1987). "Pressure gradient alignment with strain rate and scalar gradient in simulated Navier-Stokes turbulence". In: *Phys. Fluids* 30.10, pp. 3293–3294.

Ashurst, W. T., A. R. Kerstein, R. M. Kerr, and C. H. Gibson (1987). "Alignment of vorticity and scalar gradient with strain rate in simulated Navier–Stokes turbulence". In: *Phys. Fluids* 30.8, pp. 2343–2353.

Batchelor, G. K. (1959). "Small-scale variation of convected quantities like temperature in turbulent fluid Part 1. General discussion and the case of small conductivity". In: *J. Fluid Mech.* 5 (01), pp. 113–133.

Batchelor, G. K., V. M. Canuto, and J. R. Chasnov (1992). "Homogeneous buoyancy-generated turbulence". In: *J. Fluid Mech.* 235, pp. 349–378.

Beck, C. (2003). "Lagrangian acceleration statistics in turbulent flows". In: *Europhys. Lett.* 64.2, p. 151.

Bellman, R. and R. H. Pennington (1954). "Effects of surface tension and viscosity on Taylor instability". In: *Q. Appl. Math.* 12.2, pp. 151–162.

Biferale, L., G. Boffetta, A. Celani, B. J. Devenish, A. Lanotte, and F. Toschi (2004). "Multifractal statistics of Lagrangian velocity and acceleration in turbulence". In: *Phys. Rev. Lett.* 93.6, p. 064502.

Bradshaw, P. (1977). "Compressible turbulent shear layers". In: *Annu. Rev. Fluid Mech.* 9.1, pp. 33–52.

Brown, G. L. and A. Roshko (1974). "On density effects and large structure in turbulent mixing layers". In: *J. Fluid Mech.* 64.4, pp. 775–816.

– (2012). "Turbulent shear layers and wakes". In: *J. Turbul.* 13, N51.

Chandrasekhar, S. (1961). *Hydrodynamic and hydromagnetic stability*. Oxford University Press.

Chung, D. (2009). "Numerical simulation and subgrid-scale modeling of mixing and wall-bounded turbulent flows". PhD thesis. California Institute of Technology.

Chung, D. and G. Matheou (2012). "Direct numerical simulations of stationary homogeneous stratified sheared turbulence". In: *J. Fluid Mech.* 696, pp. 434–467.

– (2014). "Large-Eddy Simulation of Stratified Turbulence. Part I: A Vortex-Based Subgrid-Scale Model". In: *J. Atmos. Sci.* 71.5, pp. 1863–1879.

Chung, D. and D. I. Pullin (2010). “Direct numerical simulation and large-eddy simulation of stationary buoyancy-driven turbulence”. In: *J. Fluid Mech.* 643, pp. 279–308.

Cook, A. W. and P. E. Dimotakis (2001). “Transition stages of Rayleigh–Taylor instability between miscible fluids”. In: *J. Fluid Mech.* 443, pp. 69–99.

Diamessis, P. J. and K. K. Nomura (2004). “The structure and dynamics of overturns in stably stratified homogeneous turbulence”. In: *J. Fluid Mech.* 499, pp. 197–229.

Dimotakis, P. E. (1986). “Two-dimensional shear-layer entrainment”. In: *AIAA J.* 24, pp. 1791–1796.

– (1989). “Turbulent Shear Layer Mixing With Fast Chemical Reactions”. In: *Turbulent Reactive Flows*. Ed. by R. Borghi and S. N. B. Murthy. New York, NY: Springer US, pp. 417–485. ISBN: 978-1-4613-9631-4.

– (2000). “The mixing transition in turbulent flows”. In: *J. Fluid Mech.* 409, pp. 69–98.

– (2005). “Turbulent Mixing”. In: *Annu. Rev. Fluid Mech.* 37.1, pp. 329–356.

Domaradzki, J. A., W. Liu, and M. E. Brachet (1993). “An analysis of subgrid-scale interactions in numerically simulated isotropic turbulence”. In: *Phys. Fluids A* 5.7, pp. 1747–1759.

Donzis, D. A. and P. K. Yeung (2010). “Resolution effects and scaling in numerical simulations of passive scalar mixing in turbulence”. In: *Physica D* 239, pp. 1278–1287.

Drazin, P. G. and W. H. Reid (2004). *Hydrodynamic stability*. Cambridge University Press.

Ferziger, J. H. and M. Peric (2012). *Computational methods for fluid dynamics*. Springer Science & Business Media.

Friedrich, R. (2003). “Statistics of Lagrangian velocities in turbulent flows”. In: *Phys. Rev. Lett.* 90.8, p. 084501.

Gad-el-Hak, M. (2000). *Flow Control: Passive, Active, and Reactive Flow Management*.

Garnier, E., N. Adams, and P. Sagaut (2009). *Large eddy simulation for compressible flows*. Springer Science & Business Media.

Gat, I., G. Matheou, D. Chung, and P. E. Dimotakis (2016). “Acceleration-driven variable-density turbulent flow”. In: *Proceedings of the VIIIth International Symposium on Stratified Flows (ISSF)*. San Diego, CA.

– (2017). “Incompressible variable-density turbulence in an external acceleration field”. In: *"J. Fluid Mech."* 827, pp. 506–535.

Germano, M., U. Piomelli, P. Moin, and W. H. Cabot (1991). “A dynamic subgrid-scale eddy viscosity model”. In: *Phys. Fluids A* 3.7, pp. 1760–1765.

Gerz, T., U. Schumann, and S. E. Elghobashi (1989). “Direct numerical simulation of stratified homogeneous turbulent shear flows”. In: *J. Fluid Mech.* 200, pp. 563–594.

Gerz, T. and H. Yamazaki (1993). “Direct numerical simulation of buoyancy-driven turbulence in stably stratified fluid”. In: *J. Fluid Mech.* 249, pp. 415–440.

Ghosal, S. (1999). “Mathematical and physical constraints on large-eddy simulation of turbulence”. In: *AIAA J.* 37.4, pp. 425–433.

Guala, M., B. Lüthi, A. Liberzon, A. Tsinober, and W. Kinzelbach (2005). “On the evolution of material lines and vorticity in homogeneous turbulence”. In: *J. Fluid Mech.* 533, pp. 339–359.

Hamlington, P. E., J. Schumacher, and W. J. A. Dahm (2008). “Direct assessment of vorticity alignment with local and nonlocal strain rates in turbulent flows”. In: *Phys. Fluids* 20.11, p. 111703.

Higgins, C. W., M. B. Parlange, and C. Meneveau (2003). “Alignment trends of velocity gradients and subgrid-scale fluxes in the turbulent atmospheric boundary layer”. In: *Boundary-Layer Meteorol.* 109.1, pp. 59–83.

Hill, R. J. (2002). “Scaling of acceleration in locally isotropic turbulence”. In: *J. Fluid Mech.* 452, pp. 361–370.

Hirschfelder, J. O., C. F. Curtiss, and R. B. Bird (1964). *Molecular Theory of Gases and Liquids*. John Wiley, NY.

Ho, C. M. and P. Huerre (1984). “Perturbed free shear layers”. In: *Annu. Rev. Fluid Mech.* 16.1, pp. 365–422.

Holt, S. E, J. R Koseff, and J. H. Ferziger (1992). “A numerical study of the evolution and structure of homogeneous stably stratified sheared turbulence”. In: *J. Fluid Mech.* 237, pp. 499–539.

Horiuti, K. (2003). “Roles of non-aligned eigenvectors of strain-rate and subgrid-scale stress tensors in turbulence generation”. In: *J. Fluid Mech.* 491, pp. 65–100.

Jacobitz, F. G., S. Sakar, and C. W. Van Atta (1997). “Direct numerical simulations of the turbulence evolution in a uniformly sheared and stably stratified flow”. In: *J. Fluid Mech.* 342, pp. 231–261.

Jiménez, J. (1992). “Kinematic alignment effects in turbulent flows”. In: *Phys. Fluids A* 4.4, pp. 652–654.

Jiménez, J., A. A. Wray, P. G. Saffman, and R. S. Rogallo (1993). “The structure of intense vorticity in isotropic turbulence”. In: *J. Fluid Mech.* 255, pp. 65–90.

Kalelkar, C. (2006). “Statistics of pressure fluctuations in decaying isotropic turbulence”. In: *Phys. Rev. E* 73 (4), p. 046301.

Kerr, R. M. (1985). “Higher-order derivative correlations and the alignment of small-scale structures in isotropic numerical turbulence”. In: *J. Fluid Mech.* 153, pp. 31–58.

Kida, S. and S. A. Orszag (1992). “Energy and spectral dynamics in decaying compressible turbulence”. English. In: *J. Sci. Comput.* 7.1, pp. 1–34.

Kolmogorov, A. N. (1941). “Local Structure of Turbulence in an Incompressible Viscous Fluid at Very High Reynolds Numbers”. In: *Dokl. Akad. Nauk SSSR* 30. Translated 1968 into English in Sov. Phys. Usp 10(6):734–736, pp. 301–305.

– (1962). “A refinement of previous hypotheses concerning the local structure of turbulence in a viscous incompressible fluid at high Reynolds number”. In: *J. Fluid Mech.* 13. Translated by the author at the Colloque International du C.N.R.S de Méchanique de la Turbulence, Marseilles, 28 Aug – 2 Sep 1961., pp. 82–85.

Koochesfahani, M. M. and P. E. Dimotakis (1986). “Mixing and chemical reactions in a turbulent liquid mixing layer”. In: *J. Fluid Mech.* 170, pp. 83–112.

Kosović, B., D. I. Pullin, and R. Samtaney (2002). “Subgrid-scale modeling for large-eddy simulations of compressible turbulence”. In: *Phys. Fluids* 14.4, pp. 1511–1522.

La Porta, A., G. A. Voth, A. M. Crawford, J. Alexander, and E. Bodenschatz (2001). “Fluid particle accelerations in fully developed turbulence”. In: *Nature* 409 (6823), pp. 1017–1019.

Leonard, A (1975). “Energy cascade in large-eddy simulations of turbulent fluid flows”. In: *Advances in geophysics* 18, pp. 237–248.

Lesieur, M. (2012). *Turbulence in fluids*. Vol. 40. Springer Science & Business Media.

Lesieur, M. and O. Metais (1996). “New trends in large-eddy simulations of turbulence”. In: *Annu. Rev. Fluid Mech.* 28.1, pp. 45–82.

Liberzon, A., B. Lüthi, M. Holzner, S. Ott, J. Berg, and J. Mann (2012). “On the structure of acceleration in turbulence”. In: *Physica D: Nonlinear Phenomena* 241.3, pp. 208–215.

Lilly, D. K. (1962). “On the numerical simulation of buoyant convection”. In: *Tellus* 14.2, pp. 148–172.

Livescu, D. (2013). “Numerical simulations of two-fluid turbulent mixing at large density ratios and applications to the Rayleigh–Taylor instability”. In: *Phil. Trans. R. Soc* 371.2003, p. 20120185.

Livescu, D. and J. R. Ristorcelli (2007). “Buoyancy-driven variable-density turbulence”. In: *J. Fluid Mech.* 591, pp. 43–71.

Livescu, D. and J. R. Ristorcelli (2008). "Variable-density mixing in buoyancy-driven turbulence". In: *J. Fluid Mech.* 605, pp. 145–180.

Livescu, D., J. R. Ristorcelli, R. A. Gore, S. H. Dean, W. H. Cabot, and A. W. Cook (2009). "High-Reynolds number Rayleigh–Taylor turbulence". In: *J. Turbul.* 10, N13.

Lumley, J. L. (1992). "Some comments on turbulence". In: *Phys. Fluids A* 4.2, pp. 203–211.

Lund, T. S. and M. M. Rogers (1994). "An improved measure of strain state probability in turbulent flows". In: *Phys. Fluids* 6.5, pp. 1838–1847.

Lundgren, T. S. (1982). "Strained spiral vortex model for turbulent fine structure". In: *Phys. Fluids* 25.12, pp. 2193–2203.

Lüthi, B., A. Tsinober, and W. Kinzelbach (2005). "Lagrangian measurement of vorticity dynamics in turbulent flow". In: *J. Fluid Mech.* 528, pp. 87–118.

Matheou, G. (2016). "Numerical discretization and subgrid-scale model effects on large-eddy simulations of a stable boundary layer". In: *Q. J. R. Meteorol. Soc.* 142.701, pp. 3050–3062.

Matheou, G. and D. Chung (2014). "Large-Eddy Simulation of Stratified Turbulence. Part II: Application of the Stretched-Vortex Model to the Atmospheric Boundary Layer". In: *J. Atmos. Sci.* 71.12, pp. 4439–4460.

Mattner, T. W. (2011). "Large-eddy simulations of turbulent mixing layers using the stretched-vortex model". In: *J. Fluid Mech.* 671, pp. 507–534.

Meneveau, C. (2011). "Lagrangian Dynamics and Models of the Velocity Gradient Tensor in Turbulent Flows". In: *Annu. Rev. Fluid Mech.* 43.1, pp. 219–245.

Meneveau, C. and J. Katz (2000). "Scale-invariance and turbulence models for large-eddy simulation". In: *Annu. Rev. Fluid Mech.* 32.1, pp. 1–32.

Métais, O. and J. R. Herring (1989). "Numerical simulations of freely evolving turbulence in stably stratified fluids". In: *J. Fluid Mech.* 202, pp. 117–148.

Meyer, T. R., J. C. Dutton, and R. P. Lucht (2006). "Coherent structures and turbulent molecular mixing in gaseous planar shear layers". In: *J. Fluid Mech.* 558, pp. 179–205.

Miller, P., P. Lindstrom, and A. W. Cook (2003). "Visualizations of the dynamics of a vortical flow". In: *Phys. Fluids* 15.9, S13–S13.

Miller, R. S., F. A. Jaberi, C. K. Madnia, and P. Givi (1995). "The structure and the small-scale intermittency of passive scalars in homogeneous turbulence". In: *J. of Sci. Comp.* 10.1, pp. 151–180.

Misra, A. and D. I. Pullin (1997). "A vortex-based subgrid stress model for large-eddy simulation". In: *Phys. Fluids* 9.8, pp. 2443–2454.

Moin, P. and K. Mahesh (1998). “DIRECT NUMERICAL SIMULATION: A Tool in Turbulence Research”. In: *Annu. Rev. Fluid Mech.* 30.1, pp. 539–578.

Moin, P., K. Squires, W. Cabot, and S. Lee (1991). “A dynamic subgrid-scale model for compressible turbulence and scalar transport”. In: *Phys. Fluids A* 3.11, pp. 2746–2757.

Monin, A. S. and A. M Yaglom (1975). *Statistical Fluid Mechanics II*. MIT Press.

Mordant, N., A. M. Crawford, and E. Bodenschatz (2004). “Three-dimensional structure of the Lagrangian acceleration in turbulent flows”. In: *Phys. Rev. Lett.* 93.21, p. 214501.

Mydlarski, L. and Z. Warhaft (1996). “On the onset of high-Reynolds-number grid-generated wind tunnel turbulence”. In: *J. Fluid Mech.* 320, pp. 331–368.

Nomura, K. K. and S. E. Elghobashi (1992). “Mixing characteristics of an inhomogeneous scalar in isotropic and homogeneous sheared turbulence”. In: *Phys. Fluids A* 4.3, pp. 606–625.

Nomura, K. K. and G. K. Post (1998). “The structure and dynamics of vorticity and rate of strain in incompressible homogeneous turbulence”. In: *J. Fluid Mech.* 377, pp. 65–97.

Ohkitani, K. (2002). “Numerical study of comparison of vorticity and passive vectors in turbulence and inviscid flows”. In: *Phys. Rev. E* 65 (4), p. 046304.

Pawlak, G. and L. Armi (1998). “Vortex dynamics in a spatially accelerating shear layer”. In: *J. Fluid Mech.* 376, pp. 1–35.

Piomelli, U. (1999). “Large-eddy simulation: achievements and challenges”. In: *Prog. in Aero. Sc.* 35.4, pp. 335–362.

Piomelli, U., W. H. Cabot, P. Moin, and S. Lee (1991). “Subgrid-scale backscatter in turbulent and transitional flows”. In: *Phys. Fluids A* 3.7, pp. 1766–1771.

Pope, S. B. (2002). “A stochastic Lagrangian model for acceleration in turbulent flows”. In: *Phys. Fluids* 14.7, pp. 2360–2375.

– (2004). “Ten questions concerning the large-eddy simulation of turbulent flows”. In: *New Journal of Physics* 6.1, p. 35.

Prathama, A. H. and C. Pantano (2017). “Inviscid linear stability analysis of two vertical columns of different densities in a gravitational acceleration field”. In: *J. Fluid Mech.* 826, R4.

Pullin, D. I. (2000). “A vortex-based model for the subgrid flux of a passive scalar”. In: *Phys. Fluids* 12.9, pp. 2311–2319.

Pullin, D. I. and T. S. Lundgren (2001). “Axial motion and scalar transport in stretched spiral vortices”. In: *Phys. Fluids* 13.9, pp. 2553–2563.

Pullin, D. I. and P. G. Saffman (1994). "Reynolds stresses and one-dimensional spectra for a vortex model of homogeneous anisotropic turbulence". In: *Phys. Fluids* 6.5, pp. 1787–1796.

– (1998). "VORTEX DYNAMICS IN TURBULENCE". In: *Annu. Rev. Fluid Mech.* 30.1, pp. 31–51.

Rayleigh, Lord (1882). "Investigation of the Character of the Equilibrium of an Incompressible Heavy Fluid of Variable Density". In: *Proc. London Math. Soc.* s1-14.1, pp. 170–177.

Read, K. I. (1984). "Experimental investigation of turbulent mixing by Rayleigh–Taylor instability". In: *Physica D* 12, pp. 45–58.

Reynolds, O. (1883). "An experimental investigation of the circumstances which determine whether the motion of water shall be direct or sinuous, and of the law of resistance in parallel channels." In: *Proc. R. Soc. Lond.* 35.224-226, pp. 84–99.

Riley, J. J. and S. M. deBruynKops (2003). "Dynamics of turbulence strongly influenced by buoyancy". In: *Phys. Fluids* 15.7, pp. 2047–2059.

Rogallo, R. S. and P. Moin (1984). "Numerical simulation of turbulent flows". In: *Annu. Rev. Fluid Mech.* 16.1, pp. 99–137.

Rogers, M. M. and R. D. Moser (1994). "Direct simulation of a self-similar turbulent mixing layer". In: *Phys. Fluids* 6.2, pp. 903–923.

Sandoval, D. L. (1995). "The Dynamics of Variable-Density Turbulence". PhD thesis. University of Washington.

Sawford, B. L., P. K. Yeung, M. S. Borgas, P. Vedula, A. La Porta, A. M. Crawford, and E. Bodenschatz (2003). "Conditional and unconditional acceleration statistics in turbulence". In: *Phys. Fluids* 15.11, pp. 3478–3489.

She, Z. S., E. Jackson, and S. A. Orszag (1990). "Intermittent vortex structures in homogeneous isotropic turbulence". In: *Letters to Nature* 344, pp. 226–228.

Shih, L. H, J. R Koseff, J. H. Ferziger, and C. R Rehmann (2000). "Scaling and parameterization of stratified homogeneous turbulent shear flow". In: *J. Fluid Mech.* 412, pp. 1–20.

Sidharth, G. S., A. Kartha, and G. V. Candler (2016). "Filtered velocity based LES of mixing in high speed recirculating shear flow". In: *46th AIAA Fluid Dynamics Conference*. American Institute of Aeronautics and Astronautics.

Siggia, E. D. (1981). "Numerical study of small-scale intermittency in three-dimensional turbulence". In: *J. Fluid Mech.* 107, pp. 375–406.

Simon, C. (2015). *Generating uniformly distributed numbers on a sphere*. URL: `http://corysimon.github.io/articles/uniformdistn-on-sphere/`.

Slessor, M. D., C. L. Bond, and P. E. Dimotakis (1998). "Turbulent shear-layer mixing at high Reynolds numbers: effects of inflow conditions". In: *J. Fluid Mech.* 376, pp. 115–138.

Smagorinsky, J. (1963). “GENERAL CIRCULATION EXPERIMENTS WITH THE PRIMITIVE EQUATIONS”. In: *Mon. Weather Rev.* 91.3, pp. 99–164.

Spalart, P. R., R. D. Moser, and M. M. Rogers (1991). “Spectral methods for the Navier–Stokes equations with one infinite and two periodic directions”. In: *J. Comput. Phys.* 96.2, pp. 297–324.

Speziale, C. G., G. Erlebacher, T. A. Zang, and M. Y. Hussaini (1988). “The subgrid-scale modeling of compressible turbulence”. In: *Phys. Fluids* 31.4, pp. 940–942.

Sreenivasan, K. R. and R. A. Antonia (1997). “THE PHENOMENOLOGY OF SMALL-SCALE TURBULENCE”. In: *Annu. Rev. Fluid Mech.* 29.1, pp. 435–472.

Staquet, C. and F. S. Godeferd (1998). “Statistical modelling and direct numerical simulations of decaying stably stratified turbulence. Part 1. Flow energetics”. In: *J. Fluid Mech.* 360, pp. 295–340.

Taylor, G. I. (1935). “Statistical theory of turbulence”. In: *Proc. Royal Soc. A*. Vol. 151. 873. The Royal Society, pp. 421–444.

– (1950). “The Instability of Liquid Surfaces when Accelerated in a Direction Perpendicular to their Planes. I”. In: *Proc. Roy. Soc. London A* 201.1065, pp. 192–196.

Tennekes, H. and J. L. Lumley (1972). *A first course in turbulence*. The Massachusetts Institute of Technology.

Thorpe, S. A. (1968). “A method of producing a shear flow in a stratified fluid”. In: *J. Fluid Mech.* 32 (04), pp. 693–704.

– (1978). “On internal gravity waves in an accelerating shear flow”. In: *J. Fluid Mech.* 88 (04), pp. 623–639.

Tsinober, A., P. Vedula, and P. K. Yeung (2001). “Random Taylor hypothesis and the behavior of local and convective accelerations in isotropic turbulence”. In: *Phys. Fluids* 13.7, pp. 1974–1984.

Turner, J. S. (1979). *Buoyancy effects in fluids*. Cambridge University Press.

Vedula, P. and P. K. Yeung (1999). “Similarity scaling of acceleration and pressure statistics in numerical simulations of isotropic turbulence”. In: *Phys. Fluids* 11.5, pp. 1208–1220.

Verma, S. and G. Blanquart (2014). “Subfilter scalar-flux vector orientation in homogeneous isotropic turbulence”. In: *Phys. Rev. E* 89 (6), p. 063015.

Vincent, A. and M. Meneguzzi (1991). “The spatial structure and statistical properties of homogeneous turbulence”. In: *J. Fluid Mech.* 225, pp. 1–20.

Voelkl, T., D. I. Pullin, and D. C. Chan (2000). “A physical-space version of the stretched-vortex subgrid-stress model for large-eddy simulation”. In: *Phys. Fluids* 12.7, pp. 1810–1825.

Voth, G. A., K. Satyanarayan, and E. Bodenschatz (1998). “Lagrangian acceleration measurements at large Reynolds numbers”. In: *Phys. Fluids* 10.9, pp. 2268–2280.

Wilke, C. R. (1950). “A viscosity equation for gas mixtures”. In: *J. Chem. Phys.* 18.4, pp. 517–519.

Yoshizawa, A. (1986). “Statistical theory for compressible turbulent shear flows, with the application to subgrid modeling”. In: *Phys. Fluids* 29.7, pp. 2152–2164.

Youngs, D. L. (1984). “Numerical simulation of turbulent mixing by Rayleigh–Taylor instability”. In: *Physica D* 12, pp. 32–44.

– (1989). “Modelling turbulent mixing by Rayleigh–Taylor instability”. In: *Physica D* 37, pp. 270–287.

Zang, T. A., R. B. Dahlburg, and J. P. Dahlburg (1992). “Direct and large-eddy simulations of three-dimensional compressible Navier–Stokes turbulence”. In: *Phys. Fluids A* 4.1, pp. 127–140.